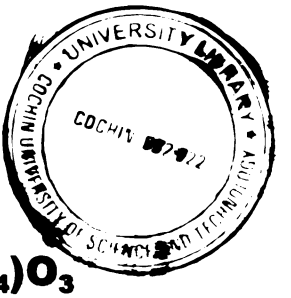

NOVEL LOW LOSS $A(A_{1/4}B_{2/4}C_{1/4})O_3$ DIELECTRICS AND THEIR APPLICATIONS IN BROADBAND ANTENNAS

THESIS SUBMITTED TO COCHIN UNIVERISTY OF SCIENCE AND TECHNOLOGY IN PARTIAL FULFILMENT OF REQUIREMENT FOR THE DEGREE OF DOCTOR OF PHILOSOPHY IN PHYSICS

P. V. BIJUMON

Under the guidance and supervision of
Dr. M. T. Sebastian (Supervisor)
Prof. P. Mohanan (Co-supervisor)

REGIONAL RESEARCH LABORATORY (CSIR)
THIRUVANANTHAPURAM

AUGUST 2005

DECLARATION

I hereby declare that the matter presented in the thesis entitled "NOVEL LOW LOSS $A(A_{1/4}B_{2/4}C_{1/4})O_3$ DIELECTRICS AND THEIR APPLICATIONS IN BROADBAND ANTENNAS" is the outcome of investigations carried out by me under the supervisions of Dr. M. T. Sebastian, Scientist, Ceramic Technology Division, Regional Research Laboratory, Trivandrum and Prof. P. Mohanan, Centre for Research in Electromagnetics and Antennas, Department of Electronics, Cochin University of Science and Technology, Kochi, India and the results embodied here has not been submitted elsewhere for the award of any other degree.

Trivandrum
Dated 5th August 2005

P. V. Bijumon

Fax : ++ 91- (0) 471 - 2491712
Phone : 471- 2515294 (O), 471- 2446901 (R)
Email : mailadils@yahoo.com
Council of Scientific & Industrial Research
REGIONAL RESEARCH LABORATORY
THIRUVANANTHAPURAM - 695 019, INDIA

Dr. M. T. SEBASTIAN
Deputy Director

CERTIFICATE

This is to certify that this thesis entitled "NOVEL LOW LOSS $A(A_{1/4}B_{2/4}C_{1/4})O_3$ DIELECTRICS AND THEIR APPLICATIONS IN BROADBAND ANTENNAS" is an authentic record of the investigations carried out by Mr. P. V. Bijumon at the Ceramic Technology Division of Regional Research Laboratory (CSIR), Trivandrum and Centre for Research in Electromagnetics and Antennas, Department of Electronics, Cochin University of Science and Technology, Kochi, India, under my supervision and guidance. This thesis or any part thereof has not been submitted elsewhere for the award of any other degree.

Sebastian

Trivandrum

Dated 5/8/2005

Supervisor

CERTIFICATE

This is to certify that this thesis entitled "NOVEL LOW LOSS $A(A_{1/4}B_{2/4}C_{1/4})O_3$ DIELECTRICS AND THEIR APPLICATIONS IN BROADBAND ANTENNAS" is an authentic record of the investigations carried out by Mr. P. V. Bijumon at the Ceramic Technology Division of Regional Research Laboratory (CSIR), Trivandrum and Centre for Research in Electromagnetics and Antennas, Department of Electronics, Cochin University of Science and Technology, Kochi, India, under my supervision and guidance. This thesis or any part thereof has not been submitted elsewhere for the award of any other degree.

Kochi

Dated 5/08/2005

Prof. P. Mohanan
(Thesis Co – Supervisor)
Centre for Research in
Electromagnetics and Antennas
Department of Electronics
Cochin University of Science and
Technology (CUSAT)
Kochi - 682 022, India.

CONTENTS

PREFACE
ACKNOWLEDGEMENTS

CHAPTER 1
DIELECTRIC RESONATORS AND ANTENNAS

1.1 MICROWAVE DIELECTRIC RESONATORS 2
1.1.1 Introduction 2
1.1.2 An overview of Dielectric Resonator (DR) Research 3
1.1.3 Working principle of Dielectric Resonators 5
1.1.4 Modes and Mode Nomenclature 8

1.2 MATERIAL REQUIREMENTS 11
1.2.1 High dielectric constant 11
1.2.2 High unloaded Quality Factor 12
1.2.3 Small Temperature Coefficient of Resonant Frequency 14

1.3 APPLICATIONS OF DIELECTRIC RESONATORS 15
1.3.1 Dielectric Resonator Oscillators 16
1.3.2 Dielectric Resonator Filters 17

1.4 DIELECTRIC RESONATOR ANTENNAS (DRAs) 17
1.4.1 Introduction 17
1.4.2 History of Dielectric Resonator Antennas 18
1.4.3 Various Geometries of DRAs 20
1.4.4 Excitation Techniques of DRA 22

1.5 BASIC DRA PARMETERS 24
1.5.1 Input Impedance of the Antenna 24
1.5.2 Resonant Frequencies 25
1.5.3 Radiation Q-Factor and Impedance Bandwidth 26
1.5.4 Dielectric Resonator Antenna Gain 28
1.5.5 Radiation Efficiency 28
1.5.6 Pattern Beamwidth 29

1.6 PROGRESS IN DIELECTRIC RESONATOR ANTENNA RESEARCH 29

1.7 REFERENCES 32

CHAPTER 2

FABRICATION AND CHARACTERIZATION

2.1	SYNTHESIS OF DIELECTRIC RESONATORS	39
	2.1.1 Introduction	39
	2.1.2 Solid State Synthesis of Ceramics	41
	2.1.2.1 Weighing of Raw Materials	41
	2.1.2.2 Stoichiometric Mixing	42
	2.1.2.3 Calcination	42
	2.1.2.4 Grinding	43
	2.1.2.5 Addition of Polymeric Binder	43
	2.1.2.6 Forming or Shaping	43
	2.1.2.7 Solid State Sintering	44
	2.1.2.8 Effect of Dopants in Sintering	44
	2.1.2.9 Liquid Phase Sintering	45
2.2	STRUCTURAL AND MICROSTRUCTURAL CHARACTERIZATION OF DIELECTRIC RESONATORS	
	2.2.1 X-Ray Diffraction Methods	45
	2.2.2 Scanning Electron Microscopic Methods	46
2. 3	MICROWAVE CHARACTERIZATION OF DRs	
	2.3.1 Introduction	46
	2.3.1.1 Network Analyzer	48
	2.3.2 Measurement of Dielectric Constant (ε_r)	49
	2.3.3 Measurement of Unloaded Quality Factor (Q_u)	52
	2.3.4 Measurement of Temperature Coefficient of Resonant Frequency (τ_f)	54
	2.3.5 Error Calculations in Dielectric Property Measurements	54
2.4	DESIGN METHODOLOGY AND FABRICATION OF DRAs	55
2.5	MEASUREMENT TECHNIQUES OF ANTENNAS	
	2.5.1 Measurement of return loss, resonant frequency and bandwidth	56
	2.5.2 Measurement of Radiation Pattern	57
	2.5.3 Measurement of Gain	58
2.6	SIMULATION OF DRs AND DRAs	
	2.6.1 Introduction	59
	2.6.2 Transmission Line Matrix (TLM) Method	60
2.7	REFERENCES	66

CHAPTER 3

$Ca(Ca_{1/4}B_{2/4}Ti_{1/4})O_3$ (B = Nb, Ta) CERAMICS: EFFECT OF DOPANTS ON THE MICROWAVE DIELECTRIC PROPERTIES

3.1 SIMPLE AND COMPLEX PEROVSKITES
- 3.1.1 Introduction 71
- 3.1.2 ABO_3 Structure 71
- 3.1.3 Complex Perovskite Structured Compounds 73

3.2 $Ca(Ca_{1/4}B_{2/4}Ti_{1/4})O_3$ (B = Nb, Ta) COMPLEX PEROVSKITES
- 3.2.1 Milestones in the Research of $Ca(Ca_{1/4}B_{2/4}Ti_{1/4})O_3$ (B = Nb, Ta) Ceramics 75

3.3 SYNTHESIS CHARACTERIZATION AND MICROWAVE DIELECTRIC PROPERTIES OF $Ca(Ca_{1/4}B_{2/4}Ti_{1/4})O_3$ (B = Nb, Ta) AND $Ca_5Nb_{2-x}Ta_xTiO_{12}$ CERAMICS
- 3.3.1 Experimental 79
- 3.3.2 Results and Discussion 80

3.4 $Ca_5Nb_{2-x}Ta_xTiO_{12}$ [$0 \leq x \leq 2$] CERAMICS 83

3.5 EFFECT OF DOPANTS IN $Ca(Ca_{1/4}B_{2/4}Ti_{1/4})O_3$ (B = Nb, Ta) CRERAMICS
- 3.5.1 Introduction 84
- 3.5.2 Experimental 85
- 3.5.3 Results and Discussion
  - 3.5.3.1 Phase Analysis 86
  - 3.5.3.2 Densification and Microstructural Analysis 86
  - 3.5.3.3 Microwave Dielectric Properties 91
    - 3.5.3.3.1 Divalent dopants 91
    - 3.5.3.3.2 Trivalent dopants 93
    - 3.5.3.3.3 Tetravalent dopants 94
    - 3.5.3.3.4 Pentavalent dopants 96

3.6 CONCLUSIONS 99

3.7 REFERENCES 101

CHAPTER 4

INFLUENCE OF GLASS ADDITION IN $Ca(Ca_{1/4}B_{2/4}Ti_{1/4})O_3$ [B = Nb, Ta] CERAMICS

4.1 INTRODUCTION 106

4.2 EXPERIMENTAL 108

4.3 RESULTS AND DISCUSSION 109
4.3.1 Phase Analysis 109
4.3.2 Sintering and Densification 112
4.3.3 Microstructural Analysis 115
4.3.4 Microwave Dielectric Properties 117
4.3.4.1 Primary Glasses 117
4.3.4.2 Binary Glasses 119
4.3.4.3 Ternary Glasses 121

4.4 CONCLUSIONS 124

4.5 REFERENCES 126

CHAPTER 5

TAILORING THE PROPERTIES OF $Ca(Ca_{1/4}Nb_{2/4}Ti_{1/4})O_3$ CERAMICS BY CATIONIC SUBSTITUTIONS

5.1 INTRODUCTION 131

5.2 $Ca_{5-x}A_xNb_2TiO_{12}$ (A = Ba, Sr) CERAMICS 133
5.2.1 Experimental 133
5.2.2 Results and Discussion 134
5.2.2.1 Structural Characterization 134
5.2.2.2 Microstructural Analysis 139
5.2.2.3 Microwave Dielectric Properties 140
5.2.2.4 Raman Spectroscopic Studies 142
5.2.2.5 FTIR Analysis 147

5.3 $Ca_{5-x}A'_xNb_2TiO_{12}$ (A' = Mg, Zn, Ni & Co) CERAMICS 149
5.3.1 Experimental 149
5.3.1.1 Ceramic synthesis and characterization 149
5.3.1.2 Simulation procedure 150
5.3.2 Results and Discussion 152
5.3.2.1 XRD Analysis 152
5.3.2.2 Densification and Microstructural Analysis 155
5.3.2.3 Simulation Results 158
5.3.2.4 Microwave Dielectric Properties 160
5.3.3 $(5-x)CaO$-$xA'O$–Nb_2O_5–TiO_2 ($2 \leq x \leq 5$) [A'=Mg, Zn, Ni & Co] Ceramics 163

5.4 $Ca_5Nb_2Ti_{1-x}C_xO_{12}$ (C = Zr, Hf) CERAMICS 166
5.4.1 Experimental 166
5.4.2 Results and Discussion 166
5.4.2.1 Phase Analysis 166
5.4.2.2 Densification and Microstructural Analysis 167
5.4.2.3 Microwave Dielectric Properties 170

5.5 CONCLUSIONS 172

5.6 REFERENCES 175

CHAPTER 6

CATIONIC SUBSTITUTIONS IN $Ca(Ca_{1/4}Ta_{2/4}Ti_{1/4})O_3$ CERAMICS

6.1 INTRODUCTION 180

6.2 $Ca_{5-x}A_xTa_2TiO_{12}$ (A = Ba, Sr) CERAMICS 181
6.2.1 Experimental 181
6.2.2 Results and Discussion 181
6.2.2.1 Structural characterization 181
6.2.2.2 Microstructural Analysis 186
6.2.2.3 Microwave Dielectric Properties 187
6.2.2.4 Raman Spectroscopic Studies 189
6.2.2.5 FTIR Analysis 193

6.3 $Ca_{5-x}A'_xTa_2TiO_{12}$ (A' = Mg, Zn, Ni & Co) CERAMICS 195
6.3.1 Experimental Procedure 195
6.3.2 Results and Discussion 196
6.3.2.1 XRD Analysis 196
6.3.2.2 Densification and Microstructural Analysis 199
6.3.2.3 Microwave Dielectric Properties 201
6.3.2.4 Simulation Results 204
6.3.3 $(5-x)CaO-xA'O-Ta_2O_5-TiO_2$ $(2 \le x \le 5)$ [A'=Mg, Zn, Ni & Co] Ceramics 206

6.4 $Ca_5Ta_2Ti_{1-x}C_xO_{12}$ (C = Zr, Hf) CERAMICS 208
6.4.1 Experimental 208
6.4.2 Results and Discussion 208
6.4.2.1 Phase Analysis 208
6.4.2.2 Densification and Microstructural Analysis 209
6.4.2.3 Microwave Dielectric Properties 212

6.5 CONCLUSIONS 214

6.6 REFERENCES 216

CHAPTER 7

DIELECTRIC RESONATOR LOADED WIDEBAND MICROSTRIP PATCH ANTENNAS

7.1 INTRODUCTION 221

	7.1.1	History of Microstrip Antennas	221
	7.1.2	Basic operation of the Microstrip Antenna	222
	7.1.3	Rectangular Microstrip Antennas	223
	7.1.4	Advantages and Disadvantages of Microstrip Antennas	225
	7.1.5	Bandwidth Enhancement of Microstrip Antennas	225
	7.1.6	DR loaded Microstrip Antennas	228
7.2	ANTENNA GEOMETRY		229
7.3	EXPERIMENTAL RESULTS		229
	7.3.1	DR over the patch surface	229
	7.3.2	DR on the feed line	235
7.4	CONCLUSIONS		237
7.5	REFERENCES		239

CHAPTER 8

BROADBAND DIELECTRIC RESONATOR ANTENNAS

8.1	INTRODUCTION		243
	8.1.1	Bandwidth Enhancement Techniques of DRA	244
8.2	CYLINDRICAL DIELECTRIC RESONATOR ANTENNAS		246
	8.2.1	Antenna Geometry	246
	8.2.2	Experimental Results	247
8.3	ELLIPTICAL DIELECTRIC RESONATOR ANTENNAS		255
	8.3.1	Antenna Geometry	255
	8.3.2	Experimental Results	255
8.4	RECTANGULAR DIELECTRIC RESONATOR ANTENNAS		263
	8.4.1	Antenna Geometry	263
	8.4.2	Experimental Results	265
8.5	CONCLUSION		271
8.5	REFERENCES		274

CHAPTER 9

CONCLUSIONS AND SCOPE FOR FUTURE WORK 277

PREFACE

Dielectric resonators (DRs) are an inevitable component in microwave telecommunication devices and are extensively used as filters, oscillators and dielectric resonator antennas (DRAs). To meet the requirements for use in such practical applications, the materials should posses stringent properties like (i) high dielectric constant (ε_r) for miniaturization, (ii) high unloaded quality factor (Q_u) or low dielectric loss for better selectivity and (iii) low temperature coefficient of resonant frequency (τ_f) for frequency stability with thermal variations of the circuit.

Open dielectric resonators can radiate energy through their lower order modes and hence act as effective antennas. These DRAs have the advantages like reduced size, lower ohmic loss, mechanical simplicity, relatively large bandwidth, simple coupling schemes to nearly all commonly used transmission lines and different radiation characteristics using different modes of the resonator. The search for new DR materials with optimum balance of microwave dielectric properties for antenna applications and the fabrication of wide band DRAs with reasonable gain and radiation performances is one of the challenging problems in telecommunication field.

This thesis entitled "NOVEL LOW LOSS $A(A_{1/4}B_{2/4}C_{1/4})O_3$ DIELECTRICS AND THEIR APPLICATIONS IN BROADBAND ANTENNAS" is the outcome of a detailed investigation made on the synthesis, characterisation and microwave dielectric properties of $A(A_{1/4}B_{2/4}C_{1/4})O_3$ (A = Ca, Ba, Sr, Mg, Zn, Ni, Co; B = Nb, Ta; C = Ti, Zr and Hf) ceramics, tailoring their dielectric properties by different techniques, verification of the experimental results using theoretical modelling and fabrication of wide band antennas using the developed DR materials. Accordingly these results are classified into 9 chapters in the thesis.

Chapter 1 is a general introduction about low loss dielectric resonator materials, and a brief survey of their technological and industrial applications, especially as DRAs. A consolidated introduction about DRAs, their merits over other conventional patch antennas and the major developments in this area of research have been discussed.

Chapter 2 illustrates the experimental method of conventional solid-state ceramic route for the synthesis of DRs. The information about instrumental techniques adopted for the structural, microstructural and microwave dielectric properties of DRs have also been summarised. The design and measurement methods employed for the fabrication of DRAs have been described in this chapter. Furthermore, a brief introduction about the theoretical modelling adopted for checking the validity of experimental results has been discussed. The experimental set up for measuring Q_u, ε_r and DRA geometry was modelled using a complete software tool for 3D electromagnetic analysis (Micro – stripes 6.5). The time domain solver based on the Transmission Line Matrix (TLM) technique was adopted which allowed an efficient way of solving Maxwell's equations without suffering the drawbacks of other techniques such as FDTD and finite elements.

Chapter 3 presents the preparation, characterization and microwave dielectric properties of $Ca_5B_2TiO_{12}$ (B = Nb, Ta) [or $Ca(Ca_{1/4}B_{2/4}Ti_{1/4})O_3$ in perovskite form] ceramics. The synthesizing conditions were optimised for best dielectric properties. Two novel DR materials were reported in which, $Ca_5Nb_2TiO_{12}$ has ε_r = 48, $Q_u \times f$ > 26000 GHz and τ_f = +40 ppm/°C, whereas $Ca_5Ta_2TiO_{12}$ has ε_r = 38, $Q_u \times f$ > 33000 GHz and τ_f = +10 ppm/°C. The effects of various dopants on the dielectric properties of these ceramics have been investigated. It is found that dopants such as MgO, ZnO, CuO, Co_3O_4, Sb_2O_3, Cr_2O_3, In_2O_3 and SnO_2 improve the microwave dielectric properties. A correlation between the microwave dielectric properties of the matrix and ionic radii of the dopant has been established.

The effect of glass additives on the sintering temperature, density and microwave dielectric properties of $Ca_5B_2TiO_{12}$ [B = Nb, Ta] ceramics have been described in Chapter 4. It is found that small amount (0.1 wt %) addition of glasses improved the density, dielectric constant and quality factor. Al_2O_3 and SiO_2 glasses are more effective in reducing τ_f whereas B_2O_3 based glasses better aids the lowering of sintering temperature. Higher wt % of all glasses deteriorated the density and microwave dielectric properties of these ceramics though they effectively reduced the sintering temperature.

Chapter 5 deals with tailoring the microwave dielectric properties of $Ca_5Nb_2TiO_{12}$ by partial substitution of Ca^{2+} with Ba, Sr, Mg, Zn, Ni, and Co and Ti^{4+} with Zr and Hf. Consequently, solid solutions such as $Ca_{5-x}Ba_xNb_2TiO_{12}$, $Ca_{5-x}Sr_xNb_2TiO_{12}$, Ca_{5-x}

$Mg_xNb_2TiO_{12}$, $Ca_{5-x}Zn_xNb_2TiO_{12}$, $Ca_{5-x}Ni_xNb_2TiO_{12}$, $Ca_{5-x}Co_xNb_2TiO_{12}$, $Ca_5Nb_2Ti_{1-x}Zr_xO_{12}$, $Ca_5Nb_2Ti_{1-x}Hf_xO_{12}$ have been prepared and characterised. It is found that Ba and Sr substitution increased ε_r and τ_f whereas all other compounds form temperature stable compositions for $0 < x$ 1. Moreover the quality factor increased and dielectric constant decreased with x. The experimental values were compared with that obtained by simulation. Excellent agreement between experiment and theory was observed.

Tuning of microwave dielectric properties of $Ca_5Ta_2TiO_{12}$ ceramics by solid solution formations like $Ca_{5-x}Ba_xTa_2TiO_{12}$, $Ca_{5-x}Sr_xTa_2TiO_{12}$, $Ca_{5-x}Mg_xTa_2TiO_{12}$, $Ca_{5-x}Zn_xTa_2TiO_{12}$, $Ca_{5-x}Ni_xTa_2TiO_{12}$, $Ca_{5-x}Co_xTa_2TiO_{12}$, $Ca_5Ta_2Ti_{1-x}Zr_xO_{12}$ and $Ca_5Ta_2Ti_{1-x}Hf_xO_{12}$ are illustrated in Chapter 6. As in the case of their niobium analogue Ba and Sr substitution increased the ε_r and τ_f with gradual decrease in quality factor. Mg, Zn, Ni, Co, Ti and Zr substitution yielded temperature stable ceramics with slightly less ε_r and high quality factor compared with the parent material. The experimental data is compared with simulated results and a very good agreement is observed between the two.

The results of experimental investigation made on DR loaded microstrip patch antennas are given in Chapter 7. The effect of ε_r and resonant frequency of DR on the gain, bandwidth and radiation performance of microstrip patch antennas have been studied. Cylindrical DRs of ε_r varying from 9 to 92 were loaded over the patch antenna. It was observed that ε_r in the range 40 – 50 was best suited for bandwidth enhancement of antennas. When a dielectric resonator of $\varepsilon_r = 48$ and resonant frequency close to that of the microstrip antenna was loaded over the patch, a five fold increase in the percentage bandwidth of the antenna was observed without much affecting its gain and radiation performance. A much more improved bandwidth was obtained when the dielectric resonator was placed on the feed line close to the patch antenna.

Chapter 8 probes the fabrication of broadband dielectric resonator antennas with different geometries. A compromise between size, operating frequency and antenna performance can be made only if the ε_r of the DR material is around 50. Hence cylindrical, elliptical and rectangular DRAs have been fabricated using $Ca_5Nb_2TiO_{12}$ ceramics ($\varepsilon_r = 48$) and excited with microstripline mechanisms. The experimental results were compared with simulated values and excellent agreement was observed. Cylindrical DRAs have higher gain and bandwidth compared with other two geometries. It was

observed that the antenna as well as feed line geometry plays a major role in controlling the gain, radiation performance and bandwidth. With this view the effects of feed line geometry on the antenna characteristics have also been investigated. The antenna makes a better performance with the branching of feed line.

The ninth chapter gives the conclusion of the thesis and scope for future work. It is proposed to synthesize $Ca_5B_2TiO_{12}$ (B = Nb, Ta) ceramics at low temperatures through chemical methods and development of single crystals with improved performance. Fabrication of DRA array using temperature stable DRs, miniaturized ceramic antennas employing LTCC technology and beam steerable DRAs using tunable dielectrics are proposed to improve antenna performance.

ACKNOWLEDGEMENTS

I present this report, in the name of God, the Almighty, who kindly showers HIS unperturbed concern, grace and blessings throughout my life.

It is with great pleasure that I place on record my deepest sense of gratitude to Dr. M. T. Sebastian, Scientist, Regional Research Laboratory, Trivandrum, for his efficient guidance, creative discussions and constant encouragement provided to me. His wide knowledge, serious research attitude and enthusiasm in work deeply impressed me.

This work could not have been completed, without the creative suggestions and great help rendered by my co-supervisor Prof. P. Mohanan, Department of Electronics, Cochin University of Science and Technology (CUSAT), Kochi. I am very much indebted to his efficient guidance, constant encouragement and moral support.

I am grateful to Prof. T. K. Chandrasekhar, Director, Regional Research Laboratory (RRL), Trivandrum, for kindly providing the facilities.

My sincere gratitude is also due to Dr. G. Vijay Nair, Dr. K. G. Satyanarayana, Prof. Javed Iqbal and Dr. B. C. Pai (Former Directors, RRL, Trivandrum) for their encouragement during the period of my research.

I am thankful to Prof. K. Vasudevan and Prof. K. G. Balakrishnan (Present and former Heads, Department of Electronics, CUSAT) for extending the microwave laboratory facilities for antenna characterization. I am also thankful to Dr. C. K. Anandan for his kind co-operation and help during the microwave measurements.

The invaluable support and immense favours provided by Dr. Manoj Raama Varma, Scientist, RRL, Trivandrum, is highly acknowledged.

I would like to thank all my colleagues and friends in the Ceramic Technology Division of RRL, especially Dr. N. Santha, Mr. L. A. Khalam, Ms. Anjana Gopakumar, Mr. G. Subodh, Mr. P. C. Rajath Varma, Mr. S. Biju, Ms. R. Rejini, Ms. Sherin Thomas, Ms. B. R. Priya Rani, Ms. Asha Pramod and Ms. L. Shamla who helped me in many ways.

The creative suggestions and valuable advices given by my seniors in the lab, Dr. K. P. Surendran (IISc, Bangalore), Dr. I. N. Jawahar, Dr. R. Ratheesh (Scientist, C-MET, Thrissur), Dr. H. Sreemoolanadhan (Scientist, VSSC) and Dr. Sam Solomon are thankfully remembered.

I wish to express my heartiest thanks to all the present and past members of microwave electronics research lab, CUSAT, Kochi, who extended their support and help to me. The favours rendered by Mr. Rohith, Mr. Gijomon, Mr. Anupam, Mr. Shynu, Mr. Manoj, Mr. Praveen, Ms. Sreedevi, Ms. Suma, Ms. Mridula, Ms. Binu Paul and Ms. Lethakumari are greatly acknowledged.

I also wish to express my sincere thanks to Dr. R. Jose, Dr. Asha Mary John, Mr. M. Sankar and Mr. Senthil Kumar, former members of Ceramic Technology Division, for their help and support.

I am indebted to Dr. K. G. K. Warrier, Dr. U. Shyama Prasad, Prof. Jacob Koshy, Dr. Jose James, Dr. K. Ravindran Nair and Dr. Peter Koshy for their help given during the course of this work.

I am thankful to Mr. K. V. Oonnikrishnan Nair, Mr. P. Gurusamy, Mr. Prabhakar Rao, Mr. P. Mukundan and Mr. Sreekumar (SCTIMST) for extending the XRD and SEM facility for this research work.

The help provided by Prof. R. L. Moreira and Dr. Anderson Dias, UFMG, Brazil, in the recording and analysis of Laser Raman and FTIR spectra of dielectrics discussed in this thesis is sincerely acknowledged.

My special thanks are due to the Flomerics India Pvt. Ltd., Bangalore for providing an evaluation version of Micro Stripes 6.5, without which the simulation work described in this thesis could not have been performed.

The inspiration and constant encouragement from my teachers, especially Fr. John Kuzhimannil, Ms. V. Vasanthy and Dr. Sebastian Mathew are always remembered.

The financial support from Department of Science and Technology and Council of Scientific and Industrial Research, Government of India, New Delhi, is gratefully acknowledged.

I could never forget the invaluable support provided by my wife during the research tenure. She stood with me in my thick and thin, provided a lot of encouragements when it needed me most and her love, understandability and adjustability throughout these years helped me in the successful and comfortable completion of this work.

I owe an unlimited debt of gratitude to my parents and other family members who have enlighten my paths with their invaluable advice, support and encouragement that contributed a lot to shape my career. I also like to express my deepest sense of gratitude to my parents-in-law for the timely help and moral support.

Last but not least, I want to express my appreciation to all those who have helped me in many ways for the successful completion of this work. I remember that the care and support from all these people gave me the confidence, their encouragement means so much to me throughout those countless hard-working days and nights.

P. V. Bijumon

CHAPTER 1

DIELECTRIC RESONATORS AND ANTENNAS

This chapter gives an overview of introduction and progress of research in dielectric resonators and antennas. The fundamental physical aspects and working principle of dielectric resonators as well as the requirements of the material to act as efficient resonators are discussed. Out of the numerous applications of dielectric resonators, in this chapter special emphasis has been given to dielectric resonator antennas. Historical evolution of dielectric resonator antenna research to the forefront of wireless communication applications are discussed. The basic antenna parameters are also described briefly to aid the easier design of dielectric resonator antennas in microwave engineering.

1.1 MICROWAVE DIELECTRIC RESONATORS

1.1.1 Introduction

"*In this era of high-tech wizardry, every flashy new technology rises to the top*". The use of ceramics in electronic equipments is growing rapidly as a result of their superior physical properties and immense technological applications. The markets and material technologies, making use of ceramics as insulators, substrates and packages, components in microwave devices, capacitors, resistors, semiconductors, piezoelectric devices and superconductors have shown an outstanding growth during the past few decades. For each type of material market factor, segmentation and trends are strongly connected with technology developments. The electronic ceramics industry is a highly technological industry characterized by rapid innovation and technological changes. Among the various branches of functional ceramics, the electronic ceramic industry is of primary interest characterized by rapid innovations and technological advances. Recently released industry news in U. S. states that till 1990's 62 % of the total ceramic industry was led by electronic ceramics, 26% by structural ceramics and 12% by ceramic coatings. But at the end of last year electronic ceramic industry witnessed an exponential growth to occupy almost 80% of the total ceramic industry owing to the wide application of electroceramic materials in telecommunication devices. The report proceeds that the total investment in ceramic industry was 12 725 millions US $ in the year 2000, while it reached about more than 15 000 millions US $ with more than 25 % increase within 5 years.

One of the major achievements of electronic ceramics is the recognition of potential usefulness of dielectric materials as energy storage devices, in oscillators and filters for the microwaves carrying the desired information. The ceramic pieces are designated as dielectric resonators (DRs), which resonates at the frequency of the carrier signal to allow that to be efficiently separated from other frequencies in the microwave band[1]. When the transverse dimension of the dielectric rod is comparable to the wavelength of the electromagnetic wave passing through it, the material can sustain standing waves within its body by multiple internal reflections at the dielectric/air interface. Clearly, the smaller the resonating body, the higher the frequency. After the

utilization of microwaves (electromagnetic wave in the 1 to 30 GHz frequency range) as a communication media, especially for satellite and mobile phone systems, miniaturization and reduction of weight of devices were pointed out as the important subject for innovation.

The size of the resonator at any particular resonant frequency depends on the inverse of the square root of the dielectric constant (ε_r) of the material, and thus the larger the ε_r, smaller the ceramic component needed. Further, to optimize the signal intensity and the number of channels possible within a given microwave frequency range, the dielectric loss (tan δ) of the resonator must be low. In other words the DR material should posses high unloaded quality factor (Q_u = 1/ tan δ), better than 2000, or preferably an order of higher magnitude. To be useful in potential practical applications, the resonant frequency of DRs must not depend strongly on temperature. If that frequency were to be temperature dependent, then the carrier signal would drift in and out of resonance on hot and cold days. To be useful, the temperature coefficient of resonant frequency (τ_f) should be as low as possible. Hence for the practical requirements, a material using as dielectric resonator should have $\varepsilon_r > 30$, high $Q_u > 2000$ and $\tau_f \approx \pm 3$ ppm/°C[2,3]. These three stringent requirements pause the utilization of all available materials for dielectric resonator applications and make the development of advanced materials for microwave communications a challenging area of research.

1.1.2 An overview of Dielectric Resonator Research

From a historical perspective, guided electromagnetic wave propagation in dielectric media received widespread attention in the early days of researching microwaves. In 1894 Lord Rayleigh[4] discovered that dielectric structures can guide electromagnetic waves, and that fields of these waves extend partially into surrounding space. Surprisingly, substantial efforts in this area predate 1920 and include famous scientists of the era like, Sommerfield, Bose and Debye[5]. In 1935, in his U. S. patent entitled "Transmission of Guided waves" Southworth[6] disclosed that "The wave guiding structure may take a variety of forms: of which typical is a guide consisting of a rod of dielectric material having high ε_r and the specific dielectric guide he considered was a

cylindrical specimen of TiO_2 (rutile). The term dielectric resonator first appeared in 1939, when Ritchmyer[7] of Stanford University showed that, unmetallised dielectric objects in the form of 'toroids' can function as microwave resonators. However, his theoretical investigations failed to generate significant interest and practically nothing happened in this area for over 25 years. In 1953, Schlicke[8] reported the application of super-high dielectric constant materials ($\varepsilon_r \sim 1000$) as capacitors in low radio frequencies. In early 1960s, researchers from Columbia University, Okaya and Barash reported single crystal TiO_2 resonators. Their papers[9,10] provided the first analysis of modes and dielectric resonator design parameters. Nevertheless the DR was still far from practical applications.

In the mid 1960s, Cohn[11] and his co-workers at the Rantec Corporation performed the first extensive theoretical and experimental evaluation of DR. Rutile ceramics were used for experiments that had an isotropic dielectric constant of the order of 100. However, poor temperature stability prevented development of practical components. A real breakthrough in the dielectric ceramic industry occurred in the early 1970s when the first temperature-stable, low loss barium tetratitanate ceramics were developed by Masse *et al.*[12]. Temperature stable microwave DRs utilizing the composite structure of positive and negative temperature coefficients were reported by Konishi[13]. Later, a modified barium tetratitanate with improved performance was reported from Bell Laboratories[14]. These positive results led to actual implementations of DRs as microwave components. The materials, however were in scarce supply and thus were not commercially available. The next major breakthrough came from Japan when the Murata Manufacturing Company produced (Zr, Sn)TiO_4[15] ceramics. They offered adjustable compositions so that the temperature coefficient could be varied between +10 and -22ppm/°C. These components became commercially available at reasonable prices. Afterwards, the experimental and theoretical work as well as the use of DRs expanded rapidly.

The emergence of DR as a circuit element for several microwave wireless devices has injected tremendous interest in the research of such materials. A simple representation of the trend can be obtained from Fig. 1.1 showing the number of research papers published/patents filed in this area against year starting from 1980. It can be seen

from the figure that last decade has witnessed dramatic increase in the research of DRs, which can be attributed to the revolutionary progress in wireless communication and information access devices in which DRs find immense applications. A good number of reviews are available describing the properties and applications of DRs.[16,17,18,19,20,21,22]

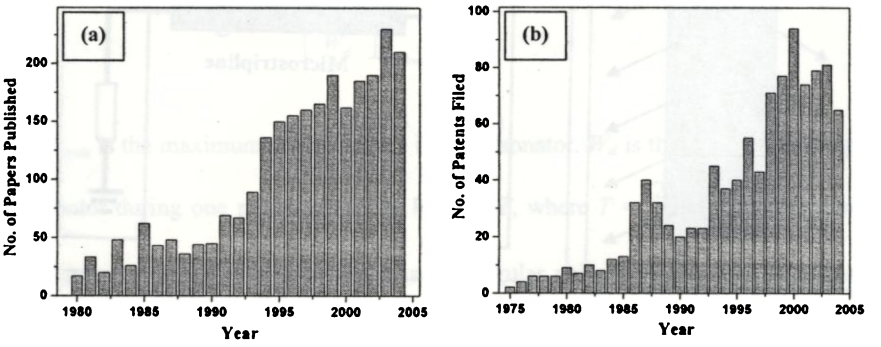

Fig. 1.1 Schematic representation of number of (a) research papers published and (b) patents filed in recent years in DRs.

Currently available materials[23] for practical purposes which posses excellent dielectric properties include, $MgTiO_3$-$CaTiO_3$[15], Ba(Sn, Mg, Ta)O_3[24], Ba(Zn, Ta)O_3[25], Ba(Zr, Zn, Ta)O_3[26], (Zr, Sn)TiO_4[27], $Ba_2Ti_9O_{20}$[28], (Ba, Sr)O-RE_2O_3-TiO_2[29], $Ba[(Zn_{0.7}Co_{0.3})_{1/3}Nb_{2/3}]O_3$[23] etc. Dielectric materials with $5 \leq \varepsilon_r \leq 140$ and $Q_u \times f > 6\ 00\ 000$ GHz and near zero τ_f have been developed[16]. It is noteworthy that still DR materials are needed with a wide variety of dielectric properties to meet the evergrowing demand in wireless devices. Hence search is going on for new materials as well as tailoring the properties of existing ones.

1.1.3 Working Principle of Dielectric Resonators

It was established[7] that through multiple internal reflections, a piece of dielectric with high dielectric constant can confine microwave energy at a few discrete frequencies, provided that the energy is fed in the appropriate direction. The electromagnetic wave moving from the electrically dense high dielectric region to the electrically thin air meets

very high impedance at the dielectric-air interface and reflects back to the dielectric itself. As the dielectric constant increases the impedance offered by the boundary also increase to allow better confinement of energy within the dielectric body. (See Fig. 1.2).

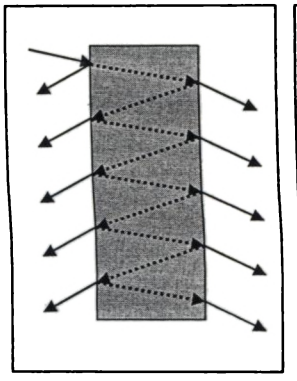

Fig. 1.2 Sketch of multiple Internal reflections in DR

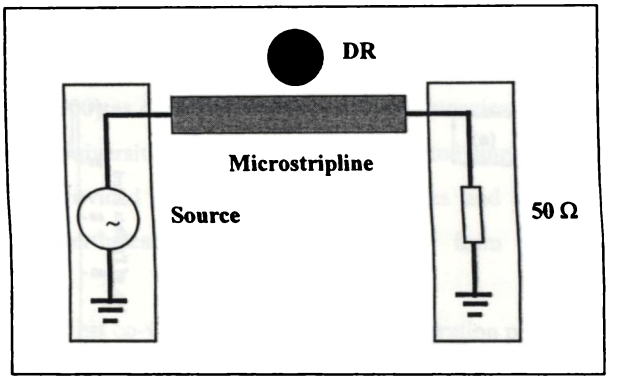

Fig.1.3 DR as circuit element coupled to a microstripline

The reflection coefficient approaches unity when the dielectric constant approaches infinity. The trapped electromagnetic waves will form standing waves to generate resonance. A high dielectric constant material can confine most of the standing electromagnetic wave within its volume. If the transverse dimensions of the dielectric are comparable to the wave length of the microwave, then certain field distributions or modes will satisfy Maxwell's equations and boundary conditions[30] and only those modes satisfying this condition will be excited. The frequency of the generated resonating modes depends on the dimensions and dielectric constant of the dielectric specimen. For microwaves the free space wavelength (λ_o) is of the order of a few centimeters and on entering the material with ε_r in the range 20-100, the wavelength (λ_d) inside the dielectric will be in millimeters. Hence proper resonance occurs only when the transverse dimensions of the dielectric sample are of the same order (in millimeters) for resonance to occur.

Further, to explain the theory of resonance in DRs, the schematic representation of a DR coupled to a microstrip line is depicted in Fig 1.3. This coupling is a result of

field interaction due to the microstrip line and DR. Let the fundamental $TE_{01\delta}$ resonance mode, is excited due to electromagnetic coupling between DR and microstrip line. The quality factor (Q), which is the ability to confine energy in a certain mode is to be calculated at resonant frequency[31]. Hence,

$$Q = 2\pi \left[\frac{W_{\max}}{W_d} \right]_{\omega=\omega_{res}} \tag{1.1}$$

where W_{max} is the maximum energy stored in the resonator. W_d is the dissipated energy in the resonator during one period given by $W_d = P_d T$, where $T = \frac{2\pi}{\omega}$, P_d is the average power dissipated in the resonator and ω is the angular velocity. Thus eqn. (1.1) can be rewritten as

$$Q = \left[\frac{\omega W_{\max}}{P_d} \right]_{\omega=\omega_{res}} \tag{1.2}$$

A bulk dielectric material excited for resonance using microwave energy is equivalent to a parallel *LCR* resonant circuit. Hence the alternating field will have inductive, capacitive and resistive components. From the fundamental rules of resonant electrical circuits, the electric energy stored in the capacitor is given as

$$W_e(t) = \frac{1}{2} C[v(t)]^2 = \frac{1}{2} C|V|^2 \cos^2(\omega t) \tag{1.3}$$

and magnetic energy stored in the inductor is

$$W_m(t) = \frac{1}{2} L\,[\mathrm{i}(t)]^2 = \frac{|V|^2}{2\omega^2 L} \sin^2(\omega t) \tag{1.4}$$

At resonance, capacitive and inductive reactances become equal and opposite to vanish. Hence the impedance of the circuit equals the ohmic resistance and maximum energy storage takes place within the body of the dielectric resonator.

At this condition

$$\omega = \omega_{res} = \frac{1}{\sqrt{LC}} \tag{1.5}$$

The maximum stored energy W_{max} will be the sum of that stored in capacitor (W_e) and inductor (W_m). Since the average energy values are equal to one half of their peak values,

$$W_{max} = 2W_e = 2W_m = W_e + W_m \tag{1.6}$$

Now using Eqn. (1.6) in (1.2), the definition of Q at resonance becomes[32]

$$Q = \left[\frac{\omega(W_e + W_m)}{P_d}\right]_{\omega=\omega_{res}} \tag{1.7}$$

If the operational frequency is not equal to the resonant frequency, the peak of the stored electric energy is not equal to the peak of the stored magnetic energy. Therefore the definition of Q is not unique[23] at any frequency other than ω_{res}.

1.1.4 Modes and Mode Nomenclature

A microwave resonator has infinite number of resonant modes, each of them corresponding to a particular resonant frequency, at which the electric stored energy is equal to the magnetic one. The excited modes can be classified into three distinct types: *TE, TM* and hybrid. The fields for *TE* and *TM* modes are axisymmetric whereas hybrid modes are azimuthally dependent. The hybrid modes can again be categorized into *HE* and *EH*. According to the mode nomenclature described by Kobayashi *et al.*,[33,34] the variation of fields along the azimuthal, radial and z-direction inside the resonator, are

denoted by adding mode indices as subscripts to each family of modes. This nomenclature is historically based on the mode nomenclature of cylindrical dielectric waveguides. The *TE, TM, HE* and *EH* modes are classified as $TE_{nmp+\delta}$, $TM_{nmp+\delta}$, $HE_{nmp+\delta}$ and $EH_{nmp+\delta}$ respectively. The first index denotes the number of full-period field variations in azimuthal direction, the index m (m = 1, 2, 3 .....) denotes the order of variation of the field along the radial direction and the index $p+\delta$ (p = 0, 1, 2.....) denotes the order of variation of the fields along the *Z*-direction.

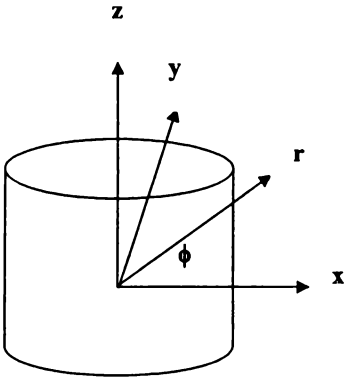

Fig. 1.4 Three dimensional view of an isolated cylindrical dielectric resonator

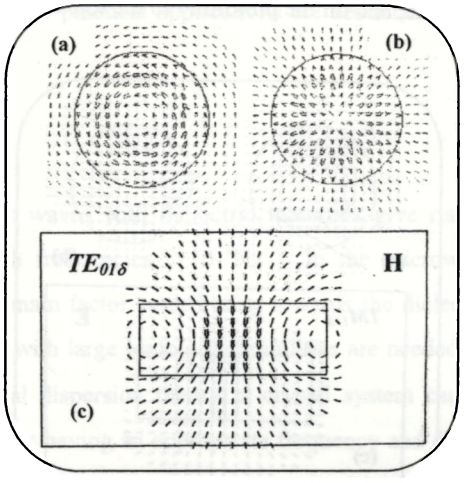

Fig. 1.5 Fields inside a cylindrical DR for $TE_{01\delta}$ mode with (a) Top view of E – Field (b) Top view of H – Field (c) H-Field in side view

An interesting feature of DR is the variation in field distribution of different modes, because the modes behave like electric and magnetic multipoles such as dipole, quadrupole, octupole etc. The mode nomenclature makes it congenial the accurate prediction of far field radiation of dielectric resonators in their application as antennas. For example, the $TE_{01\delta}$ mode radiates like magnetic dipole oriented along its axis and $TE_{011+\delta}$ radiates like an axial magnetic quadrupole. Similarly, the *TM* counterparts radiate like electric dipole and quadrupole respectively. Pictorial representations of field

distribution for various modes are shown in Figs. 1.5 - 1.7. In the cross sectional view, the field lines can be either concentric circles (like E field of the $TE_{01\delta}$ mode), or the radial straight line (like H field of the same mode).

The resonant mode most often used in shielded microwave circuits is $TE_{01\delta}$. In classical waveguide cavities, the third index is used to denote the number of half-wavelength variations in the axial direction of the waveguide. Here, the third index, denotes the fact that the dielectric resonator is shorter than one-half wavelength. The actual value of δ depends on the relative dielectric constant of the resonator and the substrate, and on the proximity to the top and bottom conductor planes.

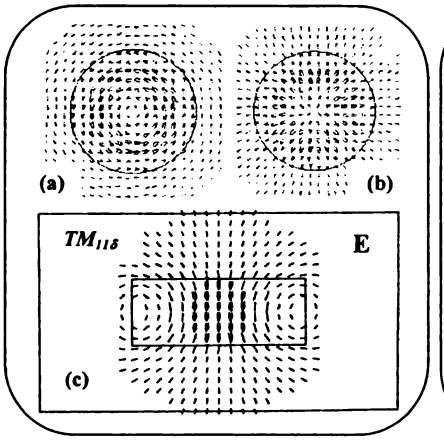

Fig.1.6 Fields inside a cylindrical DR for $TM_{11\delta}$ mode with (a) Top view of H – Field (b) Top view of E – Field (c) E-Field in side view

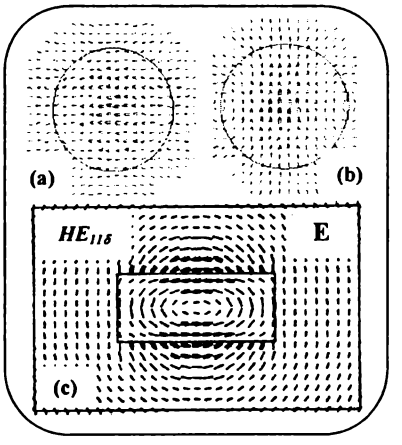

Fig. 1.7 Fields inside a cylindrical DR for $HE_{11\delta}$ mode with (a) Top view of E – Field (b) Top view of H – Field (c) E-Field in side view

Practically a part of the field in the z-direction will decay exponentially outwards to the flat surface of the DR and is termed as evanescent field. Hence it is customary to denote the fraction of the half cycle variation in the z-direction[35] with δ, which takes values between 0.5 to 1. For higher modes, the pure transverse electric or transverse magnetic fields cannot exist, so that both electric and magnetic field must have nonvanishing longitudinal components. Such modes are termed as hybrid modes and the lowest is being

$HE_{11\delta}$. Hybrid modes are frequently used in dielectric resonator filters and whispering gallery mode resonators at millimeter wave frequencies.

1.2 MATERIAL REQUIREMENTS

After the utilization of microwave as a common communication media, the miniaturization and reduction of weight of devices were pointed as the important thrust for further research. Improved performance of microwave goes hand in hand with the utilization of apt dielectric materials as circuit elements. The essential characteristics required for a dielectric resonator material for practical applications are described in the following sections.

1. 2. 1 High dielectric constant

The interaction of electromagnetic waves with dielectric materials give rise to ionic and electronic polarizations at high frequencies (>10^{11}Hz). In the microwave frequency range, ionic polarization is the main factor contributing towards the dielectric constant. Hence materials containing ions with large ionic polarizabilities are needed for sufficiently high ε_r. According to classical dispersion theory, a crystal system can be imagined as consisting of damped oscillators having an appropriate frequency and dipole moment. The complex dielectric constant as functions of ω (where $\omega = 2\pi\nu$) is given by

$$\varepsilon'(\omega) = \varepsilon_\infty + \sum_j \frac{4\pi\rho_j(\omega_j^{\,2} - \omega^2)\omega_j^{\,2}}{(\omega_j - \omega^2)^2 + (\gamma_j\omega)^2} \qquad (1.8)$$

where $4\pi\rho_j$ is the oscillator strength, ω_j is the resonant angular frequency of the j^{th} oscillator, ε_∞ is the dielectric constant caused by electronic polarization at higher frequencies and γ_j is the damping constant which is given by the width of the peak. The summation is over the j resonances in the spectrum. Each resonance is characterized by its dispersion parameters. For $\omega_j >> \omega$,

$$\varepsilon'(\omega) = \varepsilon_\infty + \sum_j 4\pi\rho_j \qquad (1.9)$$

From the above equation it is clear that the dielectric constant is independent of frequency in the microwave frequency region.

The experimental determination of ε_r at microwave frequency is done by resonance method and will be described in next chapter. It should be noted that, in polycrystalline ceramics, the experimental ε_r deviates more from the theoretical value because, the polarizability of the ceramics are affected by porosity, impurities and secondary phases to reduce ε_r.

1. 2. 2 High unloaded Quality Factor

The efficiency of a resonant circuit to confine electromagnetic energy is termed as its quality factor (Q - factor). This is the figure of merit for assessing the performance or quality of a resonator. In the case of bulk ceramics energized by electromagnetic wave, quality factor is roughly the inverse of dielectric loss of the material. Q factor is defined as a ratio of energy loss or dissipation per cycle to the energy stored in the fields inside the resonator. If W_0 is the stored energy per cycle, P is power dissipation and $\omega_o = 2\pi f_r$ is the angular velocity of the electromagnetic wave at resonant frequency f_r then Q- factor is given by[36]

$$Q = 2\pi \frac{Maximum\ \ Energy\ \ Stored\ \ per\ \ cycle}{Average\ \ Energy\ \ Dissipated\ \ per\ \ cycle} \qquad (1.10)$$

$$Q = \frac{2\pi W_0}{PT} = \frac{\omega_0 W_0}{P} \qquad (1.11)$$

In practical experiments the Q – factor is determined from the sharpness of the resonance curve, when the DR is connected in the transmission mode. If Δf_r is the 3 dB band width of the resonant curve from the resonant frequency, then

$$Q = \frac{\omega_o}{\Delta\omega} = \frac{f_r}{\Delta f} \tag{1.12}$$

Hence sharpness of the resonance curve and low insertion loss points towards higher quality factor of the ceramic material.

The total Q-factor of a DR loaded on a circuit is termed as loaded quality factor (Q_L) given as

$$\frac{1}{Q_L} = \frac{1}{Q_e} + \frac{1}{Q_u} \tag{1.13}$$

Where Q_e and Q_u represents the external and unloaded Q-factor of the DR respectively.

The unloaded Q-factor arises due to three individual components such as conductor loss ($1/Q_c$), dielectric loss ($1/Q_d$) and radiation loss ($1/Q_r$). Off these the conductor loss is due to the contact between the metallic cavity and DR, radiation loss is due to the evanescent field decaying out from the DR surface and dielectric loss is the intrinsic loss of the material.

Hence, the total unloaded Q-factor (Q_u) of a DR can be represented as

$$\frac{1}{Q_u} = \frac{1}{Q_c} + \frac{1}{Q_d} + \frac{1}{Q_r} \tag{1.14}$$

In polycrystalline ceramics, defects such as grain boundaries, stacking faults, chemical or structural disorder, point defects, planar defects, line defects, inclusions, secondary phases, twinning, porosity etc contribute towards the intrinsic dielectric losses. For an ideal DR devoid of all such intrinsic losses, an approximation can be made as

$$Q_d = \frac{1}{\tan\delta} \tag{1.15}$$

It should also be noted that in the case of an isolated DR, $Q_d = Q_u$ as a general convention. However, the quality factor of a DR can only be measured as the loaded

value (Q_L) by keeping in an external circuit. Hence it is necessary to have a relation between the two forms of quality factor (Q_u and Q_L) and is represented as

$$Q_u = Q_L(1+\beta) \tag{1.16}$$

Where β is termed as the coupling coefficient given by

$$\beta = \frac{P_e}{P_u} \tag{1.17}$$

P_e is the power loss due to external factors and P_u is the sum of that due to conductor, dielectric and radiation.

According to Classical dispersion theory,[37,38] in the microwave region the loss is mainly due to the interaction of the applied field with phonons. The microwave energy is transferred to transverse optical phonons. These optical phonons can then generate thermal phonons. This leads to damping of the optical lattice vibrations and therefore causes dielectric loss. There is a linear increase of loss with frequency which is a characteristic phonon effect. Hence the quality factor of a DR is normally represented as $Q_u \times f$ instead of Q_u as a general convention. In general the losses are lower for centro-symmetric crystals than the non centro-symmetric crystals. Normally a quality factor greater than 2000 is required for better selectivity and hence improved power handling capacity of the device comprising DR.

1. 2. 3 Small Temperature Coefficient of Resonant Frequency

The coefficient of temperature variation of resonant frequency (τ_f) determines the frequency drift with temperature variations of the DR. This is of prime importance while using a DR in a practical device to confirm the stability of the operating frequency. It is defined as

$$\tau_f = \frac{1}{f_r} \times \frac{\Delta f}{\Delta T} \qquad (1.18)$$

where f_r is the resonant frequency at room temperature, Δf is the variation of resonant frequency from room temperature for a change in temperature ΔT. The τ_f depends on the temperature variation of ε_r (τ_ε) and coefficient of linear thermal expansion according to the expression

$$\tau_f = -\alpha_L - \frac{\tau_\varepsilon}{2} \qquad (1.19)$$

The value of τ_f should be near to zero for practical applications. However often the device engineer requires a small positive or negative τ_f to compensate for the temperature variation of the resonant frequency due to the external circuit connected to DR.

1.3 APPLICATIONS OF DIELECTRIC RESONATORS

Dielectric Resonator materials are continuing to play a vital role in the microwave communication systems. Besides the electromagnetic energy storage resonators, in the present era these materials are key in the realization of low loss filters, oscillators etc. Dielectric resonators are inevitable components in microwave subsystems which are used in a range of consumer and commercial products. These products include satellite receiver modules and cellular telephones. DRs find applications in Low Noise Block converters (LNB) for digital broadcasting systems, microwave filters, security systems, detectors, Auto Cruise Control (ACC) radar systems, Wireless communication equipments, cellular base stations, collision avoidance systems, global positioning systems, Satellite multiplexing filter devices, High stability dielectric resonator oscillators, Microwave duplexers, Radio links, Wideband networks LMDS, MVDS, GSM, PCN/PCS etc. All these applications of DRs may be categorized based on their

ability to determine and stabilize the frequency of a microwave oscillator or as a resonant element in a microwave filter.

1.3.1 Dielectric Resonator Oscillators (DRO)

The performance of modern radar and communication systems are determined by the spectral purity of the local oscillators generating the microwave energy in the transmitters and receivers. It is known that[39] high Q_u DRs with low signal to noise ratio can confine most of the electromagnetic energy fed into it within itself and hence is suitable for high spectral purity oscillator applications. The application of DR as oscillator element was first proposed by Day in 1970[40]. Subsequently, in 1977, a 4 GHz $Ba_2Ti_9O_{20}$ resonator integrated with Si bipolar transistor was used as a fixed frequency oscillator. These fundamental fixed frequency oscillators are significantly simpler and efficient with 10 – 20 dB lower phase noise than conventional electronic oscillators[41]. Later efforts were made to design tunable frequency DR oscillators functioning in the *X*-band using metallic/dielectric rod to perturb the evanescent fields, by optical methods or by varactor connected circuits[42]. The schematic diagram of an oscillator using DR is shown in Fig. 1. 8.

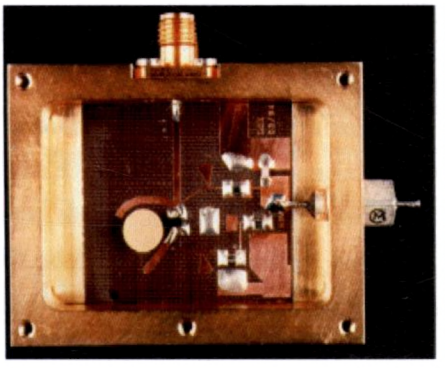

Fig. 1.8 Silicon bipolar mechanically tunable DRO at 10 GHz with parallel feed back stability

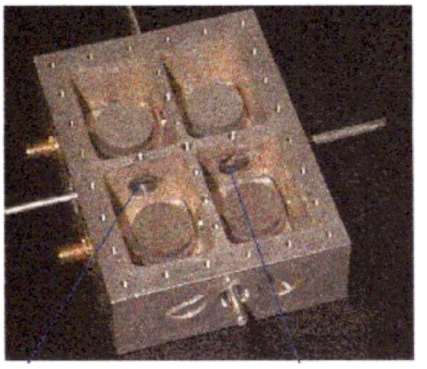

Fig. 1.9 Tunable fourth order DRF with bandwidth 0.2 MHz and centre frequency 3.6 GHz

1. 3.2 Dielectric Resonator Filters (DRF)

Microwave filters are widely used in radar, satellite, and mobile communication systems. They are typically narrow band bandpass devices with stringent specifications for passband insertion loss, stopband rejection, power handling and physical size. DRs have been widely used for the fabrication of high efficiency filters because of their inherent qualities like high Q_u, low τ_f and ability to bring miniaturization. The first DR filter was reported in 1975 by Wakino *et al.*[43] In its basic structure, a DR filter consists of a high ε_r material suspended remote from a metal enclosure. At the resonant frequency, most of the electromagnetic energy is stored within the dielectric. The enclosure stops radiation and because the enclosure is remote, the resonant frequency is largely controlled by the ε_r and dimensions of the DR sample. Practical filters are constructed by arranging coupled DRs to achieve specified frequency selective transfer function. The most commonly used DR structure is cylindrical one operated in $TE_{01\delta}$ mode. Consequent to the wide applications in wireless devices, a wide variety of DR structures and modes such as $TM_{01\delta}$, $HE_{11\delta}$ etc. are currently in use[44,45] to improve the rate of change of attenuation from passband to stopband (selectivity) and passband insertion loss. The major disadvantage of DR band pass filters is that the necessary encapsulation in a metal case to minimize radiation loss which makes them bulky, especially for medium and low frequencies. The schematic diagram of a filter using DR is shown in Fig. 1. 9.

Currently, DR materials of the BaO-TiO_2, SnO_2 – TiO_2 – ZrO_2, and BaO – ZnO/MgO – Ta_2O_5 systems offer the best combination of properties for microwave applications.

1.4 DIELECTRIC RESONATOR ANTENNAS (DRAs)

1.4.1 Introduction

The vast field of wireless communication has undergone a revolutionary progress in the last two decades. This can be attributed to the historic invention of portable mobile phones some 20 years back. The success of the second-generation (2G) cellular communication services motivated the development of wideband third generation (3G)

cellular phones and other wireless products and services. This includes wireless local area network (WLAN), global positioning systems (GPS), Bluetooth, wireless local loops, Local Multipoint Distributed Network (LMDS), Spatial Division Multiplex Access (SDMA) devices for base stations, radar and other technologies making use of a number of frequency (RF) circuits etc. The crucial component of any wireless network or device comprising them is the antenna. The antenna is the transition between a guiding device (transmission line, waveguide) and free space (or another usually unbounded medium). Its main purpose is to convert the energy of a guided wave into the energy of a free-space wave (or vice versa) as efficiently as possible, while in the same time the radiated power has a certain desired pattern of distribution in space. Hence the surprisingly enhanced progress in telecommunication industry demands the development of highly efficient, low profile and miniaturized antennas that can be embedded into devices. With this view, two classes of novel antennas have been widely investigated and extensively reported in literature. They are the microstrip patch antenna and the dielectric resonator antenna (DRA). Both are highly suitable for the development of modern wireless communication systems. Compared with the conventional microstrip patch antennas, dielectric resonator antennas are more suitable for mobile telecommunications, because they offer the possibility to drastically decrease the antenna size. Due to the wavelength scaling with $(\varepsilon_r)^{-1/2}$ the larger the permittivity of the material the smaller the antenna dimensions. Conventional antennas are usually connected exterior to the mobile device which can lead to reliability problems (eg. the antenna breaking of the device if it falls onto the ground). With an internal antenna this problem could be avoided. Moreover, it would be highly desirable to mount the antenna in a Surface Mount Process (SMD). This would substantially reduce the costs of the antenna placement onto the PCB of the mobile device.

1.4.2 History of Dielectric Resonator Antennas

Dielectric Resonators made of low loss materials and high dielectric constant have been used efficiently as shielded microwave components in the design of filters and oscillators because of their capability to store electromagnetic energy[17]. Therefore, many

engineers have doubted their suitability for use as a radiator, thinking that they would not be efficient radiators and that they would have a very small radiation bandwidth. It has, however, been shown that some modes of DRs have a small radiation Q-factor when placed in an open environment since power is lost in the radiated fields. This concept led to the exploration of DRs as antennas. Although open DRs were found to radiate many years ago[7,46,47] the real idea of using DR as a practical antenna was materialized in 1983, when Long *et al.*[48] published the first ever original paper on cylindrical DRA. Subsequently, rectangular[49] and hemispherical[50] DRAs were investigated by other researchers. These works laid the foundation for later extensive investigations[51,52,53] on various aspects of DRAs, which is still one of the promising and most challenged area of research in electromagnetics and antennas.

Compared with their conventional counterparts (eg. rod or whip antennas), DRAs offer many attracting features. The dimension of a Dielectric Resonator Antenna is of the order of $\lambda_o/\varepsilon_r^{1/2}$, where λ_o is the free space wavelength and ε_r is the dielectric constant of the DR. Thus by suitably choosing a high ε_r DR material, the size of DRA can be significantly reduced, which is highly essential for miniaturization of devices. As the resonator is constructed from a ceramic dielectric material, it has lower ohmic loss and hence high radiation than a conventional microstrip patch antenna, particularly at millimeter and near millimeter wave frequencies. At these frequencies, the conductor loss of metallic antennas becomes severe and the efficiency of the antenna is reduced significantly. Conversely, the only loss for a DRA is that due to the imperfect dielectric material, which could be very small in practice. DRAs also have the advantages like mechanical simplicity, relatively large bandwidth, simple coupling schemes to nearly all commonly used transmission lines and different radiation characteristics using different modes of the resonator. Moreover the operating bandwidth of a DRA can be varied by suitably choosing the dielectric constant of the resonator material and its dimensions. DRA has the ease of integration with other active or passive Microwave Integrated Circuit (MIC) components. Compared to the microstrip antenna, DRA has a much wider impedance bandwidth. This is because, the microstrip antenna radiates only through two narrow radiation slots, whereas the DRA radiates through the whole DRA surface except

the grounded part. Avoidance of surface waves is another attractive advantage of DRAs over the microstrip antenna. More recently dielectric resonator antennas have achieved much attention owing to their wide applicability in wireless communication techniques due to their inherent advantages over microstrip patch antennas. It has been established that DRA can replace microstrip patch antennas in almost all applications like mobile phones, satellite communications, phased array, electronic warfare, missile seekers, altimeters, biological telemetry, navigators, radars, radiometers, space and airborne microwave remote sensing devices etc. Nevertheless, many characteristics of the DRA and microstrip patch are common because both of them behave like identical resonant cavities.

1.4.3 Various Geometries of DRAs

One of the attracting features of a DRA is that it can assume any one of a number of shapes. Moreover the mode of operation and performance of a DRA can be varied by selecting a DR with desired structure. Hence a number of DRA geometries have been experimented (See Figs. 1.10 and 1.11). The first systematic, theoretical and experimental study was made on cylindrical[48] disk DRA geometry. Later geometries such as triangular[54], rectangular[49], conical[55], elliptical[56], spherical[50], hemispherical[53], spherical cap[57] and cylindrical rings[58] have been reported. It was found that[53] DRAs operating at their fundamental modes radiate like an electric or magnetic dipole, which depends on the mode of excitation and geometry of the bulk dielectric material. Out of the so many DRA structures reported the most common being ones with circular or rectangular cross sections. An interesting feature of cylindrical DR antennas is that, its design and analysis is very easy and hence it is the most popular type. Moreover the resonant frequency and radiation pattern of this antenna can be predicted quite accurately without any extensive computations. But cylindrical and spherical DRAs always support degenerate modes which are not desirable. Cylindrical ring resonators were designed[59] to increase the bandwidth of cylindrical DRAs. A ring DR supports the same type of modes as a cylindrical DR. However, the resonant frequency of ring resonator is higher than that of corresponding solid cylindrical DR as the effective dielectric constant of the antenna

system reduces by introducing an air cylinder at the centre of the DR. The radiation Q-factors (Q_r) of a ring DR are smaller to those of the corresponding cylindrical DR and hence ring resonators offer larger impedance bandwidth than the cylindrical DRs. This improvement in bandwidth offered by ring resonators over cylindrical DRA is quite substantial for certain modes[60]. DRA with rectangular cross section is the most versatile one as the antenna designer has more degrees of freedom with this structure than that with cylindrical or hemispherical one. Hence the resonant frequencies of different modes can be chosen to be different from each other by properly choosing the three dimensions of the resonator.

Simultaneously, rectangular DRAs are even more difficult to analyze than cylindrical one because of the increase in edge shaped boundaries.[61] In addition the modes of a rectangular DRA has not been analyzed and understood in detail though approximate methods for the computational analysis of rectangular DRAs do exist[62,63]. Hence DRAs of rectangular geometry has been less frequently used in practice.

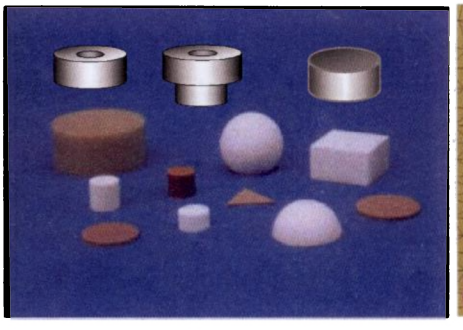

Fig. 1.10 Pictures of DRs with various shapes

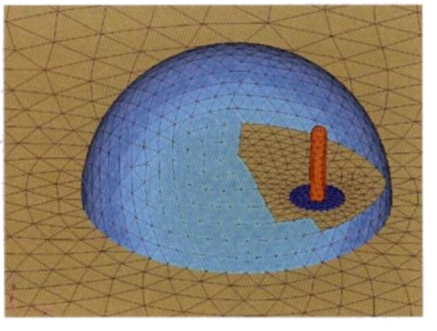

Fig. 1.11 Coaxial probe fed hemispherical DRA

Dielectric resonators of spherical shape are of special interest because this is the only shape for which an analytical solution is possible. But they have the disadvantage of low impedance bandwidth compared with other geometries. To overcome the inherent disadvantage (low impedance bandwidth) of a spherical DRA, the hemispherical

structure has been introduced. The modes of this structure can be derived on the basis of modes of an isolated spherical DR. In addition, the hemisphere offers an advantage over the rectangular and cylindrical shapes in that the easy solution for interference between the dielectric and air can be obtained. Another modification of spherical DRA was made in the form of spherical cap geometry for improved performance. Recently, triangular DRAs were tried[54] because for a given frequency and a dielectric constant, they are provide more miniaturization of the circuit devices compared with rectangular and cylindrical DRAs. Although this miniaturization comes at the cost of their bandwidth, they find application in antenna arrays. Conical[55] and elliptical[56] DRAs were also investigated for special purpose of miniaturization and multiband operations. Though several geometries have been introduced, the most studied and common structures are still the cylindrical and rectangular DRAs.

1.4.4 Excitation Techniques of DRAs

The operational mode of a DRA depends on the method of excitation employed. Moreover it is established that[53] the coupling mechanisms significantly affect the resonant frequency and radiation Q-factor of DRA. The coupling mechanism applied to a DRA, in addition of transferring energy has a loading effect, which will affect the radiation Q – factor (Q_r) of DRA. Hence after accounting for this, an external Q – factor (Q_{ext}) can be defined as

$$Q_{ext} = \frac{Q_r}{k} \tag{1.20}$$

and loaded Q – factor (Q_L) is given by

$$Q_L = \left[\frac{1}{Q} + \frac{1}{Q_{ext}}\right]^{-1} = \frac{Q}{1+k} \tag{1.21}$$

Maximum power transfer takes place between the coupling port and DRA when the coupling factor k is unity. This condition is termed as critical coupling. When $k < 1$, the DRA is said to be under coupled, while $k > 1$, the case is over coupled.

A number of excitation techniques have been adopted. These include coaxial probe,[64,65] aperture coupling with a microstrip feed line,[66,67] aperture coupling with a coaxial feedline,[68,69] direct microstrip feedline,[70,71] coplanar feed,[72] soldered through probe,[73] slotline,[74] conformal strip[75] and direct image guide.[76] Fig. 1.11 shows a coaxial probe fed hemispherical DR placed on a metallic plane. The probe is kept away from the geometric centre of the DR to excite the $HE_{11\delta}$ mode.

In aperture coupling methods, the aperture consists of a slot cut in the ground plane and fed by microstrip line beneath the ground plane. In this case the aperture behaves like a magnetic current running parallel to the length of the slot, which excites the magnetic fields in DRA. Here the coupling level can be adjusted by moving the DRA with respect to the slot. This method has the advantage of feeding networks kept below the ground plane and hence avoids the spurious modes. Moreover, slot aperture coupling is widely used for integrating DRAs with printed feed structures. However this coupling technique can be effective at frequencies above L – band, since the slot size becomes too large below L – band. In coaxial probe fed excitation, the probe can be either located adjacent to the DRA or can be embedded within the body. The extent of coupling can be adjusted by modifying the probe height. In this method, various modes are excited depending on the position of the probe. Another advantage of this method is that the antenna system can be directly connected to a 50 Ω circuit without the aid of any matching network. The excitation of DRs using coplanar wave guide lines appears to be highly promising as they enable easy coupling with MMICs. In this case coupling level can be adjusted by positioning the DRA over the co-planar loop. By moving the position of DR over the loop, the operational mode can be selected. Dielectric image guide excitation of DRAs offer advantages over microstrip line methods in such a way that they do not suffer from conductor losses especially at millimeter wave frequencies. Here the coupling between the guide and the DR is usually small, but can be increased by operating the guide closer to the cut - off frequency. Direct microstrip line mechanism is

the simplest method to energize DRAs. In this method, a DR placed over the dielectric substrate is excited by a microstrip line printed on the same substrate. The level of coupling can be adjusted by the lateral position of the DR with respect to the microstrip line and by using substrate with different permittivity. For wider bandwidth, the ε_r of the substrate should be kept low, but requires a reasonable value for better coupling. To have acceptable radiation efficiency, microstrip line excited DRA arrays are being used. Microstrip line offers advantage of easy and cost effective fabrication of DRA arrays as feed lines can be simply printed over the substrate. But these have the disadvantage that polarization of the array is dictated by the orientation of the microstrip line. Moreover, this excitation scheme may also generate surface waves in the dielectric substrate, which is highly undesirable.

1.5 BASIC DRA PARAMETERS

The antenna parameters describe the antenna performance with respect to space distribution of the radiated energy, power efficiency, matching to the feed circuitry, etc. The design of DRAs with any geometry needs to be specified with factors such as resonant frequency, gain, impedance bandwidth, field distribution inside the DR, radiated field etc. It is worth to mention that many of these parameters are inter-related and also with the mode selected for the operation of DRA.

1.5.1 Input Impedance of the Antenna

The input impedance of antenna is given by

$$Z_A = R_A + jX_A \tag{1.22}$$

Where R_A is the antenna resistance and X_A is the reactance.
Generally, the antenna resistance has two terms

$$R_A = R_r + R_l \tag{1.23}$$

Where R_r is the radiation resistance and R_l is the loss resistance.

The antenna impedance is related to the radiated power P_r, the dissipated power P_d and the stored reactive energy (W), in the following way

$$Z_A = \frac{p_r + p_d + 2j\omega(W_m - W_e)}{\frac{1}{2} I_0 I_0^*} \tag{1.24}$$

Here, I_0 is the current at the antenna terminals, W_m and We are the respective average magnetic and electric energy stored in the near-field region. When the stored magnetic and electric energy are equal, a condition of resonance occurs, and the reactive part of Z_A vanishes.

One of the commonly adopted methods for the graphical representation of input impedance of an antenna is in the form of Smith chart.[77] It is a polar plot of the complex reflection coefficient, Γ (also known as the one-port scattering parameter S or S_{11}) for reflections from a normalized complex load impedance.

1.5.2 Resonant Frequencies

It is the frequency at which maximum impedance matching between the source and antenna occurs to transfer maximum power to the antenna. Rigorous numerical methods[78] are required for the determination of resonant frequencies of DRAs. In this analysis, the DRA surface assumes perfect magnetic conductors and the effect of feed will be ignored. The resonant frequency depends on the height h, radius r and dielectric constant ε_r of the resonator. In the case of cylindrical DRA, the fundamental excited mode, which has the lowest resonant frequency will be TM_{110}. The resonant frequency of this mode employing the magnetic wall method (MWM) has been computed[79] and is given[53] as

$$f_{TM110} = \frac{c}{2\pi r\sqrt{\varepsilon_r}} \sqrt{X^2 + \left(\frac{\pi r}{2h}\right)^2} \tag{1.25}$$

This expression is valid in the range $0.33 \leq r/h \leq 5$. Where X is the coefficient of Bessel function of the first kind and is equal to 1.8411. However tolerances are admissible in the value of X with excitation mechanisms employed and coefficient of coupling.

For a rectangular DRA with dimensions a, $b > d$, the lowest order mode excited will be TE_{110}[53]. The dielectric waveguide model is used to analyse the performance of rectangular DRs and accordingly, the resonant frequency of TE_{110} mode of rectangular DRA is given by

$$f_{TE110} = \frac{c}{2\pi\sqrt{\varepsilon_r}}\sqrt{\left(\frac{\pi}{a}\right)^2 + \left(\frac{\pi}{2b}\right)^2 + \left(\frac{\pi}{d}\right)^2} \tag{1.26}$$

1.5.3 Radiation Q - Factor and Impedance Bandwidth

The radiation Q – factor (Q_r) of a DRA has an inverse relation with its bandwidth. If W_e and P_r are the stored energy and radiated power in a DR, the radiation Q is given[80] by

$$Q = \frac{2\omega W_e}{P_r} \tag{1.27}$$

The impedance bandwidth (BW) of an antenna is defined as the frequency range over which the input impedance of the antenna is less than a specified value, S.

$$BW = \frac{S-1}{Q_r\sqrt{S}} \tag{1.28}$$

Where S is the maximum acceptable voltage standing wave ratio (VSWR). The above equation also validates for the inverse proportionality between radiation Q and impedance bandwidth of DRAs. For DRAs, which has negligible dielectric and conductor losses compared to its radiated power, the unloaded quality factor of DRs is related to the radiation Q – factor by

$$Q_u \cong Q_r \tag{1.29}$$

Combining Eqns. (1.28) and (1.29), it is evident that ultra low loss dielectric resonator materials yield antennas with very narrow bandwidth. Conversely, Van Bladel[81] showed that for a given mode, the radiation Q – factor depends on the aspect ratio and dielectric constant of the DR sample. Q_r varies with ε_r as,

$$Q_r = (\varepsilon_r)^p \tag{1.30}$$

Where, p is an integer with values 1.5 for modes that radiate like magnetic dipole and 2.5 for modes radiate like electric dipole and magnetic quadrupole. This relation ensures that, high dielectric constant DR materials increases the radiation Q of DRAs and thereby reduces the bandwidth of antennas. Hence it can be concluded that low ε_r materials are preferable for the fabrication of enhanced bandwidth DRAs. Very low permittivity materials are not preferable as they make the antenna system bulky. In practice there is a lower limit on the value of ε_r required to sustain the fields within the DRA in order to resonate. Same is the case with very high permittivity materials with very high dielectric loss (low Q_u and hence low Q_r). Though they can provide miniaturization, it would be very difficult to couple electromagnetic energy into the body of the ceramic because of their ultra high dielectric loss and hence do not resonate. Hence materials with intermediate dielectric constants are preferable, as a compromise between bandwidth and miniaturization of DRAs. Moreover, considerable degree of control over bandwidth can be possible by suitable adjustments of aspect ratio of DRs. In general, simple geometries for wider bandwidths are[10] rectangular and cylindrical DRAs for a fixed volume of the antenna. It was found that as the DRA volume increases, the bandwidth initially decreases to reach a minimum value and then increases with volume. These trends will hold good only for aspect ratios in between 0.5 to 5, only where the dielectric waveguide model hols good.

1.5.4 Dielectric Resonator Antenna Gain

The gain G of an antenna is the ratio of radiation intensity U in a given direction to the radiation intensity that would be obtained, if the power (P_{in}) fed to the antenna were radiated isotropically.

$$G_{(\theta,\phi)} = 4\pi \frac{U_{(\theta,\phi)}}{P_{in}} \tag{1.31}$$

The gain is a dimensionless quantity, which is very similar to the directivity D. There are many factors that can worsen the transfer of energy from the transmitter to the antenna (or from the antenna to the receiver) like mismatch losses, losses in the transmission line and losses in the antenna: viz. dielectric losses, conduction losses, polarization losses etc. In a DRA the gain is also affected by the excitation mechanism, dimensions, geometry and dielectric properties of DR used.

1.5.5 Radiation Efficiency

Radiation efficiency is the ratio of radiated power to the input power of an antenna. Several methods are available in literature to measure the radiation efficiency of antennas. For physically small antennas like DRAs, a special technique like Wheeler cap[82] method is employed. In this method the radiation efficiency is measured as a function of Q – factor of the antenna (See eqn. 1.27). The total power (P) lost from the antenna system can be divided into (i) radiated power (P_r) and (ii) Power dissipated as heat (P_d).

$$P = P_r + P_d \tag{1.32}$$

Based on the above equation, the total Q – factor (Q_o) of the antenna can be decomposed into a radiation Q – factor (Q_r) and dissipation Q – factor (Q_d) with the given by,

$$\frac{1}{Q_o} = \frac{P_r + P_d}{\omega W} = \frac{1}{Q_r} + \frac{1}{Q_d} \tag{1.33}$$

The radiation efficiency (η) of the antenna is represented as

$$\eta = \frac{P_r}{P_r + P_d} = 1 - \frac{Q_o}{Q_d} \tag{1.34}$$

Q_o and Q_d can be calculated using eqn (1.33) by measuring the return loss with and without the radiation shield. When the DRA is covered by a metal shield, the radiation is suppressed and the measured Q represents Q_d.

1.5.6 Pattern Beamwidth

The practical DRAs are directional. ie, the antenna radiates (receives) much more efficiently in some directions than in others. The principal radiation patterns are normally linearly polarized and measured in the *E*-plane (a plane parallel to the *E* - vector and containing the direction of maximum radiation) and in the *H*-plane (a plane parallel to the *H* - vector, orthogonal to the *E*-plane, and containing the direction of maximum radiation). Circular polarizations can be obtained by modified excitation mechanisms. One of the most common and important parameter to be defined in an antenna pattern is its Half Power Beam Width (HPBW). It is the angular width of the radiation pattern where the radiation intensity is half its maximum value. The HPBW is the best parameter to describe the antenna resolution properties. In radar technology as well as in radio astronomy, the antenna resolution capability is of primary importance.

1.6 PROGRESS IN DRA RESEARCH

Earlier DRAs have only been an object of investigation in academic laboratories, so that their field application was not demonstrated properly. However in the ongoing era of adiabatic expansion in the growth of wireless devices, low profile and miniaturized dielectric resonator antennas are of prime importance to meet applications in mobile devices such as cellular phones, notebook computers, personal digital assistant (PDA) etc. Hence recent years have witnessed intense researches[83,84] in the area of dielectric

resonator antennas due to their inherent advantages prior to the above mentioned applications.

The prime importance has been given to bandwidth enhancement techniques[53] (See Chapter 8) including the reduction of radiation Q – factor by loading effect, the employment of matching networks and use of multiple resonators in array as well as stacked structures. Low profile, wide band DRAs have been designed[85] using a very high permittivity material (ε_r = 100) for application in notebook computer connected to a wireless computer network. Efforts were also being made to fabricate circularly polarized DRAs for better applications in satellite communications.

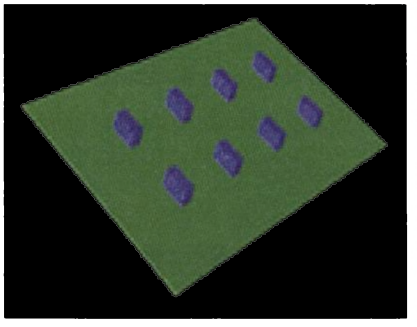

Fig. 1.13 Microstrip fed DRA array

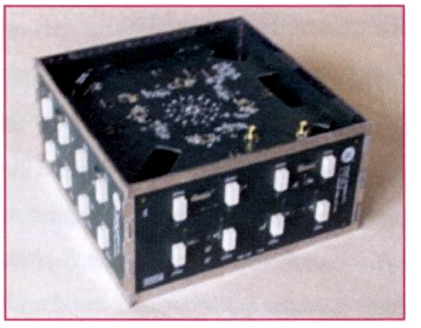

Fig. 1.14 DRA array in an active circuit

This has been achieved by modifying the excitation as well as DRA geometries. Circular sector DRAs have been reported[86] for circular polarizations as well as dual frequency applications. Efficient use of several high permittivity DRAs as diversity antennas for multipurpose applications located on one handset has also been reported[87,88]. Lot of researches were being made[89,90,91,92,93] in the direction of appropriate feed arrangements to couple a number of DRA elements to form DRA arrays with directional radiation pattern and enhanced gain for terrestrial communication and radar applications. The schematic diagram of a microstrip fed DRA array is depicted in Fig. 1.13 where as Fig. 1.14 shows one such antenna array in active circuit. Efforts were also made to form adaptive or functional DRA arrays with beam steering capability. Recently investigations

are being made on leaky-wave dielectric resonator antennas based on non-radiative dielectric guides (NRD)[94,95] because of their compact size, low loss and ease of fabrication and finds application in wideband millimeter wave devices.

1.7 REFERENCES

[1] P. C. Osbond, R. W. Whatmore and F. W. Ainger, *Br. Ceram. Soc. Proc.* **36** (1985) 167.

[2] S. J. Fiedziuszko, I. C. Hunter, T. Itoh, Y. Kobayashi, T. Nishikawa, S. N. Stitzer and K. Wakino, *IEEE Trans. Microwave Theory Tech.* **MTT-50** (2002) 706.

[3] P. L. Wise, I. M. Reaney, W. E. Lee, D. M. Iddles, D. S. Cannel and T. J. Price, *J. Mater. Res.* **17** (2002) 2033.

[4] Rayleigh, *Phil. Mag.* **43** (1892) 123.

[5] K. S. Packard, *IEEE Trans. Microwave Theory Tech.* **MTT-32** (1984) 961.

[6] G. C. Southworth, "*Transmission of guided wave*", U. S. Patent 2 106 769, Aug. 23, 1935.

[7] R . D. Ritchmyer, "Dielectric Resonators", *J. Appl. Phys.* **10** (1939) 391.

[8] H. M. Schlicke, *J. Appl. Phys.* **24** (1953) 187.

[9] A. Okaya, *Proc. IRE.* **48** (1960) 1921.

[10] A. Okaya and L. F. Barash, *Proc. IRE.* **50** (1962) 2081.

[11] S. B. Cohn, *IEEE Trans. Microwave Theory Tech.* **MTT-16** (1968) 218.

[12] D. J. Masse, R.A. Purcel, D. W. Ready, E. A. Maguire and C. D. Hartwig, *Proc. IEEE.* **59** (1971) 1628.

[13] Y. Konishi, "*Microwave dielectric resonators*" (in Japanese), NHK, Tokyo, Japan, Techn. Rep. 1971.

[14] J. K. Plourde, D. F. Linn, H. M. O'Bryan, Jr., and J. Thompson, Jr., *J. Am. Ceram. Soc.* **58** (1975) 418.

[15] K. Wakino, M. Katsube, H. Tamura, T. Nishikawa and Y. Ishikawa, "*Microwave dielectric materials*" (in Japanese), in IEE Four Joint Conv. Rec. 1977, Paper 235.

[16] W. Wersing, "*Electronic Ceramics*" Ed. B. C. H. Steele, Elsevier Pub. Co. Inc. (1991) p. 67.

[17] D. Kajfez and P. Guillon, *Dielectric Resonators*, Noble Publishing Corp. Atlanta (1998).

[18] J. K. Plourde and C. L. Ren, *IEEE Trans. Microwave Theory Tech.* **MTT-29** (1981) 754.

[19] R. Freer, *Silicates Industriels* **9-10** (1993) 191.

[20] S. Nomura, *Ferroelectrics* **49** (1983) 61.

[21] K. Wakino, T. Nishikawa, Y. Ishikawa and H. Tamura, *Br. Cera. Trans. J.* **89** (1990) 39.

[22] K. Wakino and H. Tamura, *Ceram. Trans.* **15** (1990) 305.

[23] Internet data: http://www.lsbu.ac.uk/dielectric-materials

[24] H. Tamura, T. Konoike, and K. Wakino, *Proc of 3rd U.S – Japan Seminar Dielectric Piezoelectric Ceram.* (1984) 69.

[25] S. Kawashima, M. Nishida, I. Ueda, and H. Ouchi, *J. Am. Ceram. Soc.* **66** (1983) 421.

[26] H. Tamura, T. Konoike, and K. Wakino, *J. Am. Ceram. Soc.* **67** (1984) C59.

[27] K. Wakino, K. Minai, and H. Tamura, *J. Am. Ceram. Soc.* **67** (1984) 278.

[28] H. M. O'Bryan Jr., J. Thompson, Jr., and J. K. Plourde, *J. Am. Ceram. Soc.* **57** (1974) 450.

[29] S. Nishikawa, Y. Ishikawa, J. Hattori and Y. Ida, *J. Inst. Electron. Inf. Commun. Eng.* **J27-C-1** (1989) 650.

[30] D. Kajfez, *Q Factor*, Vector Fields, Oxford (1994).

[31] R. Beringer, "*Resonant cavities as microwave circuit elements*", Ch.7 in *Principles of Microwave Circuits*. Edited by C.G. Montgomery, R.H.Dicke and E.M. Purcell, Dover, New York (1965).

[32] M. Sucher, *Measurement of Q in Handbook of Microwave Measuremens*, 3rd Edition, Editted by M. Sucher and J. Fox, Polytechnic Press, Brooklyn (1963).

[33] Y. Kobayashi and T. Tanaka, *IEEE Trans. Microwave Theory Tech.* **MTT – 28** (1980) 1077.

[34] Y. Kobayashi and M. Miura, *IEEE MTT-S Int. Microwave Symp. Dig.*, San Fransico, (1984) 184.

[35] P. Vincent, *Appl. Phys.* **A-31** (1983) 51.

[36] I. J. Bahl and P. Bhartia, *Microwave Solid State Circuit Design*, New York, Wiley, (1988).

[37] R. Kudesia, *PhD Thesis*, Alfred University (1992).

[38] K. Fukuda, R. Kotoh and I. Awai, *Jpn. J. Appl. Phys.* **32** (1993) 4584.

[39] J-S. Sun and Y-L Huang, *Microwave J.* **11** (1999) 93.

[40] W. R. day, Jr. *IEEE MTT-S Int. Microwave Symp. Dig.* (1970) 24.

[41] J. K. Plourde, D. F. Linn, I. Tatsuguchi and C. B. Swan, *IEEE MTT-S Int. Microwave Symp. Dig.* (1977) 273.

[42] K. Wakino, T. Nishikawa, S. Tamura and H. Tamura, *37th Annu. Freq. Contr. Symp.* Japan, 1983.

[43] K. Wakino, T. Nishikawa, S. Tamura, and Y. Ishikawa, *IEEE MTT-S Int. Microwave Symp. Dig.* (1975) 63.

[44] S. J. Fiedziuszko, *IEEE Trans. Microwave Theory. Tech.* **MTT-30** (1982) 1311.

[45] I. C. Hunter, J. D. Rhodes and V. Dassonville, *IEEE Trans. Microwave Theory. Tech.* **MTT- 42** (1998) 2501.

[46] M. Gastine, L. Courtois and J. L. Dormann, *IEEE Trans. Microwave Theory Tech.* **MTT – 15** (1967) 694.

[47] O. Sager and F.Tisi, *Proc. IEEE*, Sept. (1968) 1593.

[48] S. A. Long, M. McAllister and L. C. Shen, *IEEE. Trans. Antennas. Propagat.* **AP-31** (1983) 406.

[49] M. McAllister, S. A. Long and G.L Conway, *Electron. Lett.* **19** (1983) 219.

[50] M. McAllister and S. A. Long, *Electron. Lett.* **24** (1988)1156.

[51] R. K. Mongia and P. Bhartia, *Intrenational Jour. Microwave and Millimeter-Wave Computer-Aided Engineering* **4** (1994) 230.

[52] A. Petosa, D. J. Roscoe, A. Ittipibon and M. Cuhaci, *IEEE Antennas Propag. Mag.* 7 (1996) 7.

[53] K. M. Luk and K. W. Leung, "*Dielectric Resonator Antennas*", Ed. J. R. James (Resrach Studies Press Ltd. Baldock, Hertfordshire, U. K.), 2003.

[54] A. Ittipiboon, R. K. Mongia, Y. M. M. Antar, P. Bhartia and M. Cuhaci, *Electron. Lett.* **29** (1993) 2001.

[55] A. A. Kishk, Y. Yin and A. W. Glisson, *IEEE Trans. Antennas Propagat.* **AP-50** (2002) 469.

[56] B. Paul, S. Mridula, P. Mohanan, P.V. Bijumon, and M. T. Sebastian, *Microwave Opt. Technol. Lett.* **43** (2004) 118.

[57] K. W. Leung, K. M. Luk and E. K. N. Yung, *Electron. Lett.* **30** (1994) 1366.

[58] R. K. Mongia, A. Ittipiboon, P. Bhartia and M. Cuhaci, *Electron. Lett.* **29** (1993) 1530.

[59] Y. Ge and K. P. Esselle, *IEEE Tarns on Microwave Theory and Tech.* (in press).

[60] M. Verplanken and J. Van Bladel, *IEEE Trans. Microwave Theory Tech.* **MTT-27** (1979) 328.

[61] Y. M. M. Antar and Z. Fan, *IEE Proc. Microwave Antennas Propag.* **143** (1996) 113.

[62] A. Okaya and L. F. Barash, *Proc. IRE* **50** (1962) 2081.

[63] R. K. Mongia, *IEE Proc. H* **139** (1992) 98.

[64] S. M. Shum and K. M. Luk, *IEEE Trans. Antennas Propagat.* **46** (1998) 325.

[65] G. P. Junker, A. A. Kishk and A. W. Glisson, *IEEE Trans Antennnas Propagat.* **42** (1994) 960.

[66] J. T. H. St. Martin, Y. M. M. Antar, A. A. Kishk and A. Ittipiboon, *Electron. Lett.* **26** (1990) 2015.

[67] K. W. Leung, *IEEE Trans Antennnas Propagat.* **48** (2000) 1005.

[68] K. Y. Chow and K. W. Leung, *IEEE Trans Electromagnetic Compactibility* **42** (2000) 290.

[69] K. Y. Chow, K. W. Leung, K. M. Luk and E. K. N. Yung, *IEEE Trans Antennnas Propagat.* **49** (2001) 307.

[70] R. A. Kranenburg and S. A. Long, *Electron. Lett.* **24** (1988) 1156.

[71] K. W. Leung, K. Y. Chow, K. M. Luk and E. K. N. Yung, *Electron. Lett.* **33** (1997) 1004.

[72] R. A. Kranenburg, S. A. Long and J. T. Williams, *IEEE Trans Antennas Propagat.* **39** (1991) 119.

[73] K. M. Leung, K. Y. Chow, K. M. Luk and E. K. N. Yung, *Electron. Lett.* **33** (1997) 349.

[74] H. Y. Lo, K. W. Leung and K. M. Luk, *Microwave and Opt. Technol. Lett.* **29** (2001) 230.

[75] H. Y. Lo and K. W. Leung, *Microwave and Opt. Technol. Lett.* **29** (2001) 317.

[76] M. T. Birand and R. V. Gelsthorpe, *Electron. Lett.* **17** (1981) 633.

[77] "Philip Smith, Electrical Engineer," an oral history conducted in 1973 by Frank A. Polkinghorn, IEEE History Center, Rutgers University, New Brunswick, NJ. www.ieee.org/organizations/history_center/ oral_histories/transcripts/smith3.html.

[78] W. Zheng, *IEEE Trans. Microwave Theory Tech.* **MTT-34** (1989) 953.

[79] M. Tsuji, H. Shigesawa and K. Takiyama, *IEEE Trans. Microwave Theory Tech.* **MTT-32** (1984) 628.

[80] R. K. Mongia, and A. Ittipiboon, *IEEE Trans. Antennas Propagat.* **45** (1997) 1348.

[81] J. Van Bladel, *IEEE Trans. Microwave Theory Tech.* **MTT-23** (1975) 199.

[82] H. A. Wheeler, *Proc. IRE* **47** (1959) 1325.

[83] A. A. Kishk, A. W. Glisson and G. P. Junker, *Progress in Electromagnetic Research, PIER* **33** (2001) 97.

[84] I.S. Ghosh, A. Hilgers, T. Schlenker, R. Porath, *J. Eur. Ceram. Soc.* **21** (2001) 2621.

[85] R. K. Mongia, A. Ittipiboon and M. Cuhaci, *Electron. Lett.* **30** (1994) 1362.

[86] K. P. Esselle, *IEEE Antennas Propagat. Society Int. Symp.* **1**(1996) 577.

[87] S. C. K. Ko and R. D. Murch, *IEEE Trans. Antennas Propagat.* **49** (6) (2001) 954.

[88] S. C. K. Ko and R. D. Murch, *IEEE Trans. Antennas Propagat.***49** (5) (2001) 840.

[89] A. Petosa, R. K. Mongia, A. Ittipiboon and J. S. Wight, *Proc. of IEEE AP-S Conf.* California, USA, pp. 1982 – 1985 (1995).

[90] H. M. Neshati, "*Numerical modeling and application studies of rectangular dielectric resonator antennas*", PhD thesis, University of Manchester, UK, 2001.

[91] Z. Wu, *IEE Internatioanl Conference on Antennas and Propagat.*, Manchester, UK, pp. 668 – 671 (April 2001).

[92] K. K. Pang, H. Y. Lo, K. W. Leung, K. M. Luk and E. K. N. Yung, *Microwave and Opt. Technol. Lett.* **27** (2000) 377.

[93] B. J. Fasefest, A. G. Walsh, C. S. De Yong, T. F. Kennedy, S. A. Long and J. T. Williams, *Electron. Lett.* **39** (2003) 12.

[94] S. J. Xu, X. Y. Zeng, K. Wu and K. M. Luk, *IEEE Trans. Microwave Theory Tech.* **MTT – 46** (1998) 2450.

[95] M. Yamamoto and K. Itoh, *Electron. Lett.* **35** (1999) 857.

CHAPTER 2

FABRICATION AND CHARACTERIZATION OF DIELECTRIC RESONATORS AND ANTENNAS

The sequential description of various steps involved in the synthesis of low loss dielectric resonator materials are described in this chapter. A qualitative discussion on the structural as well as microwave characterization tools to determine the dielectric constant, quality factor and temperature coefficient of resonant frequency of ceramics are given. The design, fabrication and characterization of dielectric resonator antennas are also included in this chapter. A brief introduction about the importance and applications of 3D Transmission Line Matrix simulation method and its adaptation for modeling the cavity shielded dielectric resonators and antennas are introduced.

2.1 SYNTHESIS OF DIELECTRIC RESONATORS

2. 1. 1 Introduction

The miniaturization of devices and the development of new components have made possible many interesting advances and innovative concepts in material fabrication technology. The focus of attention in this regard has not only been on the improved microstructure and property of the products but also in the design and development of potential engineering applications. Along with the revolutionary development of electronics in the second half of the twentieth century, the huge potential of ceramic materials has been unfolded and introduced into a fascinatingly wide spectrum of electrical and microelectronic devices and applications. Obviously, oxide ceramics cover a huge area of functionalities. Hardly any other class of materials (semiconductors, metals, polymers) offers such a broad variety of properties which can be exploited for electronic applications. Nowadays, the synthesis technique for the fabrication of electroceramic powders has generated considerable interest mainly focusing on improving the physical and electronic properties of the final ceramic products. Different methods can be applied to ceramic powder materials to form the commercial ceramic products like Dielectric resonators that are diverse in size, shape, material composition, structure and property[1]. Hence to the shaped body of DR with desired property, the ceramic processing steps have to be carefully monitored.

Ceramics, by definition, comprise inorganic, non-metallic, non-water-soluble compounds that show ionic contributions in their chemical bonds. These are the product of solid compounds, which are formed into desired shapes initially and then hardened by the application of heat and sometimes heat and pressure simultaneously[2]. Ceramic fabrication techniques generally include various powder processing methods with powder synthesis, forming and sintering. The powder synthesis process of ceramics involve several techniques like (a) solid state reaction methods (b) mechanical methods and (c) chemical methods[3]. Powders with different properties can be produced using different processing methods. A careful selection of the preparation technique is necessary to prepare powders consisting of particles with specific properties to yield the bulk component. The synthesis of specific powders and the better control of chemical and

physical characteristics of ceramic powders allow obtaining improved and/or reproducible properties.

The most common method of preparing ceramic powders is by solid-state reaction methods, because it is the simplest, easier and cost effective method to make bulk amount of ceramics. However it is established that[4] the surface area of the ceramic powder derived through solid state reaction technique is relatively lower and hence the particles can offer lesser points of contacts which are vital for effective sintering reactions to take place. In addition to that the homogeneity of particle size distribution and high temperature of formation makes the solid state ceramic techniques unpopular for the synthesis of advanced dielectric ceramics.[5] In the mechanical methods, small particles are produced from larger ones by mechanical forces, a process referred to as comminution. The process of comminution involves operations such as crushing, grinding and milling. Mechanical treatment of ceramic powders can reduce particle size and enables to obtain nano-structured powders, which are of the main interest in the current trend of miniaturization and integration of electronic components. However this technique lacks the synthesis of phase pure ceramics, which is essential for the fabrication of DRs with optimum dielectric properties. Hence alternate chemical techniques[6,7] like molten salt, precipitation, sol-gel, hydrothermal and combustion methods have been worked out in the synthesis of complex perovskite ceramics. But the sinterability of bulk ceramics prepared using chemically derived powders was found to be very poor and hence none of these techniques could fetch a higher quality factor for dielectric resonators than that obtained through solid state technique. Moreover the stringent operation conditions involved in the reaction sequence as well as the high cost of chemicals, limit the usage of chemical methods for the fabrication of DRs in industry. Hence in the present study we have employed the conventional solid state synthesis of ceramics for the fabrication of DRs, because this method lead to better dielectric properties, which is the primary interest in the fabrication of devices employing DRs.

2. 1. 2 Solid State Synthesis of Ceramics

The conventional ceramic approach involves basically four steps (a) intimate mixing of the stoichiometric oxides, (b) high temperature firing/calcination (c) intermediate grinding and (d) sintering.

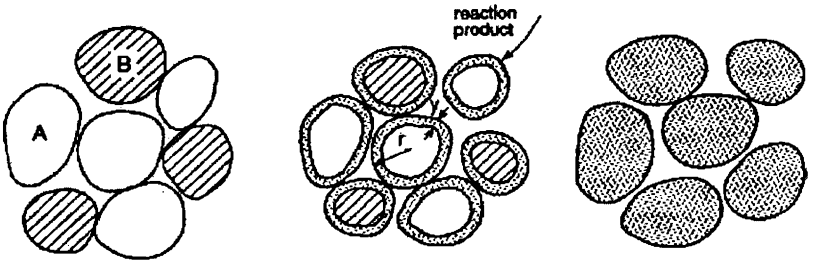

Fig. 2. 1 Reaction between two kinds of particles to form a product at the points of contact

On heating at high temperatures, a new material is formed (See Fig. 2.1) to reduce the free energy, at the points of contact through solid state diffusion. This new product layer (of a few Å) eventually acts as a potential barrier between the two grains and thus impeding further grain to grain material transport. This demands the need of new points of contacts to be introduced which is usually achieved though grinding or ball milling. This frequent grinding coupled with multiple calcination maximizes the product to reactant ratio.

The solid-state reaction method, which is employed in the present work, involves the following steps:

2. 1. 2. 1 Weighing of Raw Materials

The first step in the solid-state reaction method is to weigh the different oxides/carbonates which act as reactants according to the stoichiometry with due allowance to impurity and moisture content. The presence of impurities in the raw

materials can affect reactivity as well as dielectric properties of the fired ceramics. Hence very high purity oxides (> 99.9 %) are essential for obtaining phase pure compounds. Electronic balance is used to obtain accuracy up to four decimal places.

2. 1. 2. 2 Stoichiometric Mixing

The raw materials need to be intimately mixed to increase the points of contacts between reactant oxides, which in turn act as 'product layer formation centres'. Hence the raw materials constituting the batch must be intimately mixed. The mixing and milling eliminates agglomerates and reduces particle size. If agglomerates are present they densify more rapidly resulting in pores. During the mixing process agglomerates are broken and defects are introduced into the grains that enhance diffusion mechanism. Therefore in the present investigation, the mixture of constituent powders taken in polythene bottles were ball milled for sufficient duration in distilled water medium using Yttria Stabilized Zirconia (YSZ) balls. In the milling process, the particles experience mechanical stresses at their contact points due to compression, impact or shear with the milling medium or with other particles[8]. The mechanical stress leads to elastic and inelastic deformation. If the stresses exceed ultimate strength of the particle, it will fracture the particles. The mechanical energy supplied to the particle is used not only to create new surfaces but also to produce other physical changes in the particle[9].

2. 1. 2. 3 Calcination

Calcination is the intermediate heat treatment at a lower temperature prior to sintering. Calcination involves chemical decomposition reactions, in which a solid reactant is heated to produce a new solid plus a gas which are commonly used for the production of powders of simple oxides. The calcination conditions such as temperature, duration and heating atmosphere are important factors controlling densification during sintering. Though calcination does not yield the final phases of interest, consistent products may form during the process.

2.1.2.4 Grinding

The grinding of calcined powder helps to reduce the particle size and hence to increase the surface area to promote densification during sintering. Grinding also aids to homogenize the compositional variations that may still exist or that may arise during calcination. If the grind is coarser the ceramic can have larger intergranular voids and lower sintered density. If grinding is too fine, the colloidal properties may interfere with subsequent forming operations[10]. Generally, grinding up to a grain size of about 5 μm is advisable. Generally for grinding purpose ball mill or agate mortar with pestle is used. In large scale production of ceramics a grinding medium is chosen that suffers very little wear.

2.1.2.5 Addition of Polymeric Binder

The main objective of adding polymer binder is to impart sufficient strength and appropriate mechanical properties for handling and shaping the ceramic during the post forming stage. The polymeric dispersions and organic binders provide the pressed ceramic powders with optimal properties for thickening abilities and mechanical strength of the pressed samples[11]. Hence in modern ceramics technology, a narrow range of water-soluble organic binders, such as poly vinyl alcohol (PVA) or poly ethylene glycol (PEG) is most often applied to improve the rheological properties of the powder compact[12]. The recent research trends suggest that small amount (3 – 4 wt %) of the PVA and PEG are ideal binder additives for fabrication of microwave dielectric ceramics[13]. Optimal addition of the binder will not affect the dielectric properties as it will burn out at low temperatures (400 – 500°C).

2.1.2.6 Forming or Shaping

Forming or shaping is the process of making the powder in the desired form or shape. Various methods like dry uniaxial pressing, isostatic pressing, calendaring, extrusion, jiggering, injection moulding, slip casting, band casting, silk screening etc. are available for shaping bulk ceramic specimens. In the present study the fine powder is compacted into cylindrical specimen by uniaxial dry-pressing. Compaction is done

slowly to facilitate the escape of the entrapped air. Internal lubricants such as Stearic Acid dissolved in Propan 2-ole, was used to reduce the friction between the powder and die wall. Pressures of the range 50-150 MPa is ideal in low loss ceramic forming.

2.1.2.7 Solid State Sintering

Sintering is the heat treatment of powder compacts at elevated temperatures, where diffusional mass transport is appreciable which results in a dense polycrystalline solid[14]. The purpose of sintering is the reduction of compact porosity. The development of microstructure and densification during sintering is a direct consequence of mass transport through several possible paths and one of these paths is usually predominant at any given stage of sintering[15,16]. The normal sintering method is also termed as standard pressure sintering and is used in the present investigation. The pressed ceramic green sample is loaded over cleaned platinum plates and kept in high temperature furnaces. In this method at a certain temperature the ceramic begin to diffuse and shrinkage occurs resulting in densification[17]. Usually the sintering temperature is a little below the melting point of the ceramic. In solid state sintering mechanism, the bulk material transport can be by (i) volume diffusion, (ii) grain boundary diffusion, (iii) surface diffusion or by (iv) evaporation-condensation.

During sintering, the surface energy is reduced by transferring matter from the interior of grains to adjacent pores. Grain boundaries serve as vacancy sinks. Grain growth also takes place in parallel with densification[18], which is favoured by reduction in the area of grain boundaries. Rapid growth of discontinuous grains during sintering will trap porosity,[19] which in turn will deteriorate the dielectric properties. On the otherhand, if the material contains a large fraction of low-melting vitreous phases, then densification is accelerated by liquid-phase sintering[20]. For microwave dielectric resonator applications, ceramics sintered by solid-state diffusion show better quality factor.

2.1.2.8 Effect of Dopants in Sintering

Dopants can significantly affect the sintering process. They can act either as (i) substitution ions (ii) grain boundary pinning to form secondary phase or (iii) as solute

segregation to grain boundaries inhibiting discontinuous grain growth. In the first case bulk material transport is enhanced due to the introduction of vacancies when a solute of different valancy is added[21]. The presence of vacancies (or defects) speed up the transport mechanism. In the second mechanism, formation of second phase particles at grain boundaries acts to pin up the grain boundaries and thereby prevents discontinuous grain growth. The third mechanism is similar to the second one, but the grain growth inhibitor is an adsorbed solute. The role and effect of dopants on the densification and microwave dielectric properties of low loss ceramics are described in detail in Chapter 3.

2.1.2.9 Liquid Phase Sintering

When a wetting liquid is present during the process of sintering, bulk viscous flow can result in volume shrinkage. When the liquid coats each grain, the material can often be sintered to a higher density at a lower temperature with less tendency for exaggerated grain growth. The liquid phase wets the surface of solid phase, partially dissolves and pulls the mass of particles together so that a large fraction of pores is filled with glass. The role and effect of glass additives on the densification and microwave dielectric properties of low loss ceramics are explained in Chapter 4.

2.2 STRUCTURAL AND MICROSTRUCTURAL CHARACTERIZATION OF DIELECTRIC RESONATORS

2.2.1 X-Ray Diffraction Methods

The structure of the powdered ceramic specimens in this investigation were analyzed by X-Ray diffraction (XRD) techniques. The X-Ray diffraction method is most useful for qualitative, rather than quantitative, analysis (although it can be used for both). An X-Ray diffractometer utilizes a powdered sample, a goniometer, and a fixed-position detector to measure the diffraction patterns of unknowns. The powdered sample provides (theoretically) all possible orientations of the crystal lattice, the goniometer provides a variety of angles of incidence, and the detector measures the intensity of the diffracted beam. The resulting analysis is described graphically as a set of peaks with percentage intensity on the Y-axis and goniometer angle on the X-axis. The exact angle and intensity

of a set of peaks is unique to the crystal structure being examined[22]. A monochromator is used to ensure a specific wavelength reaches the detector, eliminating fluorescent radiation. The resulting trace consists of a recording of the intensity against counter angle (2θ). The trace can then be used to identify the phases present in the sample. Diffraction data from many materials have been recorded in a computer searchable Powder Diffraction File (PDF/JCPDS File). Comparing the observed data with that in the PDF allows the phases in the sample to be identified[23,24]. In this investigation XRD spectra were recorded using CuKα radiations employing Philips X-ray Diffractometer (Model-Expert Pro).

2.2.2 Scanning Electron Microscopic Methods

Scanning Electron Microscopic (SEM) methods were adopted in the present study to analyze the microstructure of sintered and thermally etched surface of ceramic samples. In this method, an electron beam is produced at the top of the microscope by an electron gun. The electron beam follows a vertical path through the microscope, which is held within a vacuum atmosphere. The beam travels through electromagnetic fields and lenses, which focus the beam down toward the sample. Once the beam hits the sample, electrons and X-Rays are ejected from the sample. Detectors collect these X-Rays, backscattered electrons, and secondary electrons to convert them into a signal that is sent to a screen similar to a television screen. This produces the final image[25]. All metals are conductive and require no preparation before being used. All non-metals need to be made conductive by covering the sample with a thin layer of conductive material like gold[26]. In this study we have used a Scanning Electron Microscope of Model S – 2400, Hitachi, Japan for the microstructural evolution of ceramic samples prepared.

2. 3 MICROWAVE CHARACTERIZATION OF DRs

2. 3.1 Introduction

The generally adopted methods for the measurement of dielectric and magnetic properties of materials at microwave frequencies can be classified into (i) perturbation

methods, (ii) optical methods, (iii) transmission line methods, (iv) reflection methods and (v) exact resonance methods. The choice of method or combination of methods will depend on the value of ε_r and loss factor, the amount of material available, the accuracy required, and whether the technique is required for research or routine measurements.

Perturbation Technique: The perturbation methods are highly suitable for materials of small size since the material should not alter the field configuration considerably. These techniques are suitable for dielectric constants less than 10, although this range can be extended by an exact solution of the resonator containing the specimen[27]. Hence this technique is not commonly used for DR characterization.

Optical Methods: Optical methods are applicable for wavelength of below one centimetre. Since this method requires large amount of material it is not suitable for DRs[28].

Transmission line techniques: This technique has a serious disadvantage of the very small waveguide size used below 4 mm, which gives rise to practical difficulties[29]. More over imperfections in the sample dimensions produce errors in the measurement. It was reported that the accuracy of transmission mode measurements of the dielectric properties is more in weak coupling conditions[30].

Reflection methods: In reflection methods, waves reflected from the dielectric are studied. When the dielectric constant becomes large, there occurs considerable error in the measurement of complex voltage reflection coefficient[31].

Exact Resonance methods: Exact resonance method is the most accurate method as compared to the above-mentioned methods for the measurement of DRs. In this method, the exact resonant frequency of the resonator is measured using different techniques[32]. From the resonant characteristics, parameters like ε_r, Q_u etc are determined. Special techniques of exact resonance methods are used in the present study, which are described in detail in the following sections.

2.3.1.1 Network Analyzer

This is the major instrument used in this investigation for the characterization DRs and DRAs. Network Analyzer is a swept frequency measurement equipment to completely characterize the complex network parameters in comparatively less time, without any degradation in accuracy and precision. Two types of network analyzers are available, scalar and vector network analyzers. Scalar network analyzer measures only the magnitude of reflection and transmission coefficients while the vector network analyzer measures both the magnitude and phase.

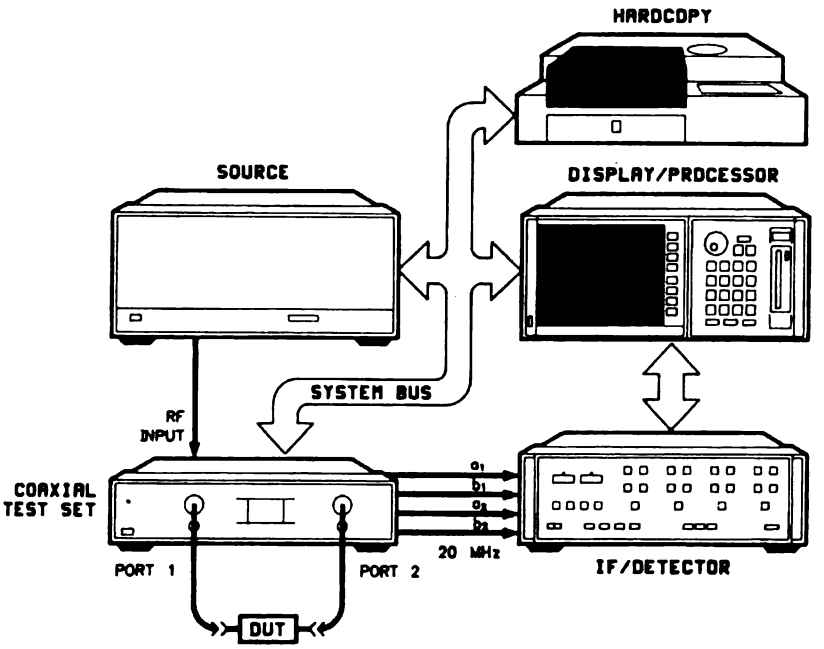

Fig. 2.2 Schematic diagram of HP 8510C network Analyzer

A vector Network Analyzer consists of the following system

1) Microwave Source
2) Test Set

3) Signal Processor

4) Display Unit

The schematic diagram of the network analyzer controlled by IBM PC is shown in Fig.2.2. The synthesized source or the sweep oscillator provides the RF stimulus. The sweep oscillator drives the network under test and two receivers. The first receiver is used to accurately measure the Reflection or input voltage to the network. The second receiver is called the Transmission channel and is used to measure the output of the network under test. The ratio of the output to the input level is displayed as dB and is the voltage gain or loss of the network. The analyzer can operate in ramp or in step mode. In the ramp mode the analyzer directs the source to sweep in a linear ramp over the frequency and in the step mode, it provides maximum precision.

2. 3. 2 Measurement of Dielectric Constant (ε_r)

In this method developed by Hakki and Coleman[33] a circular disc of material whose ε_r to be measured is inserted between two mathematically infinite conducting plates, as shown in Fig 2.3.

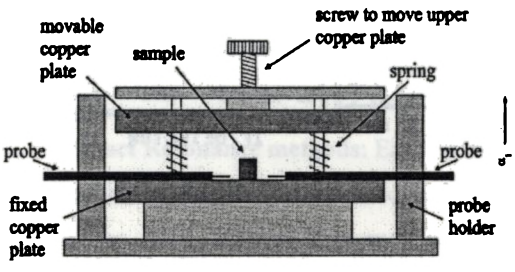

Fig. 2. 3 Hakki-Coleman method for measuring ε_r by end shorted method

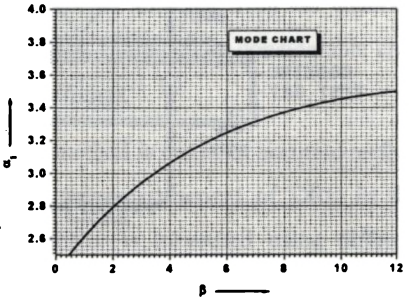

Fig. 2. 4 Mode charts of Hakki -Coleman giving α_1 as functions of β.

If the dielectric material is isotropic then the characteristic equation for this resonant structure operating in the TE_{0ml} mode is written as

$$\alpha \frac{J_0(\alpha)}{J_1(\alpha)} = -\beta \frac{K_0(\beta)}{K_1(\beta)} \tag{2.1}$$

where $J_0(\alpha)$ and $J_1(\alpha)$ are Bessel functions of the first kind of orders zero and one respectively. The $K_0(\beta)$ and $K_1(\beta)$ are the modified Bessel functions of the second kind of order zero and one respectively. The parameters α and β depend on the geometry, the resonant wavelength inside and outside the DR respectively and dielectric properties. Thus

$$\alpha = \frac{\pi D}{\lambda_o} \left[\varepsilon_r - \left(\frac{l\lambda_o}{2L} \right)^2 \right]^{1/2} \tag{2.2}$$

$$\beta = \frac{\pi D}{\lambda_o} \left[\left(\frac{l\lambda_o}{2L} \right)^2 - 1 \right]^{1/2} \tag{2.3}$$

where

l = the longitudinal variations of the field along the axis

L = Length of the DR

D = Diameter of the DR

λ_0 = free space resonant wave length

The characteristic equation is a transcendental equation and hence a graphical solution is necessary. Corresponding to each value of β there are infinite number of (α_n) that solves the characteristic equation. Hakki and Coleman obtained a mode chart showing the variation of α values as a function of β and are shown in Fig. 2. 4.

The dielectric constant of the resonator can be calculated using the mode chart parameters (α_1 and β_1), the resonant frequency (f_r) and the dimensions of the dielectric puck using the equation

$$\varepsilon_r = 1 + \left[\frac{c}{\pi D f_r}\right]^2 \left(\alpha_1^2 + \beta_1^2\right) \qquad (2.4)$$

The horizontally oriented E-field probes for coupling microwaves to the DRs, was proposed by Courtney[34] which enabled to span a wide range of frequencies, since there is no cut-off frequency for coaxial lines. The $TE_{01\delta}$ mode is used for the measurements since this mode propagates inside the sample but is evanescent out side the geometry of DR. Therefore a large amount of electrical energy can be stored in the high Q dielectric resonators[35]. However, in the open space post resonators setup, a part of electrical energy is radiated out as evanescent field and hence the axial mode number is usually expressed as δ since it is less than 1 (i.e. $TE_{01\delta}$). In the end shorted condition the E-field becomes zero close to the metal wall and electric energy vanishes in the air gap[36].

In the experimental setup, a Vector Network Analyzer, HP 8510 C is used for taking measurements at microwave frequencies. The HP 9000, 300 series instrumentation computer, interfaced with network analyzer makes the measurement quicker and accurate. The specimen is placed approximately symmetrical with the two E-probes. The resonant modes are visualized by giving a wide frequency range by adjusting the Network Analyzer. To select the $TE_{01\delta}$ resonance from the several modes having non zero E_z components, the upper metal plate is slightly tilted to introduce an air gap. As the plate is tilted the entire TM modes move rapidly to the higher frequencies while the $TE_{01\delta}$ mode remains almost stationary. It is well known that in exact resonance technique, $TE_{01\delta}$ is least perturbed by the surroundings. After identifying the $TE_{01\delta}$ resonant frequency or central frequency (f_r), the span around f_r is reduced as much as possible to get maximum resolution. The 3 dB bandwidth of the curve decreases and a stage of saturation is reached when the width will remain the least possible. The coupling loops are fixed at

this position and the centre frequency can be noted corresponding to the maxima as f_r. By knowing the diameter 'D' and length 'L' of the sample β is calculated using equation 2. 3. From the mode chart, the value of α_l corresponding to β_l value is noted. The dielectric constant ε_r is calculated using Eqn. 2.4.

2. 3. 3 Measurement of Unloaded Quality Factor (Q_u)

Various methods[37,38,39,40] are available in literature for measurement of Q-factors of microwave resonators. However, all these methods failed to account for the practical effects such as noise, crosstalk, coupling losses, transmission line delay, and impedance mismatch introduced by a real measurement system. Moreover the microwave loss factors of DRs are affected by many other intrinsic and extrinsic factors (See section 1.2.2 of Chapter 1). Inadequate accounting of these effects may lead to significant uncertainty in the measured quality factor of the DRs. End-shorted method applied for the measurement of ε_r can also be used for measuring the unloaded quality factor (Q_u). But the quality factor measured for the TE_{011} mode using the parallel plate rod resonator is very low since there occurs losses due to conducting plates, radiation etc.

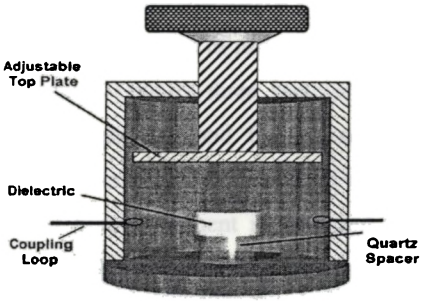

Fig. 2. 5 The cavity set up for the measurement of Q factor

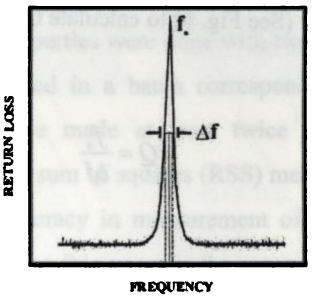

Fig. 2. 6 The method of calculating Q from resonant mode using Eqn. 2.5

In the present study the Q_u of the DR samples are measured by using a method proposed by Krupka *et al.*[41] (See Fig. 2.5). In this method, the DR specimen to be characterized is placed inside a cylindrical copper/invar cavity whose inner surface is

silver coated to reduce radiation loss. The diameter of the cavity is designed almost four times than that of the sample diameter to reduce the effect of cavity shielding. Samples with diameter/length (D/L) ratio of 1.8 - 2.2 is preferable to get maximum mode separation and to avoid interference from other modes. The DR specimen is kept over a quartz spacer placed at the inner bottom surface, which enables to avoid the conduction loss. The cavity is provided with a tunable upper lid. This enables to tune the height of air layer in the metallic cavity and hence more accuracy in the determination of the resonant mode and Q_u can be attained and also allows to measure samples with various dimensions. Microwaves are fed into the sample using two loop coaxial antennas which provides a magnetic coupling to excite the transmission mode resonance spectrum of dielectric cylinder. The coupling is adjusted to be optimum (weak coupling for high Q_u and strong coupling for lossy samples). Observe S_{21} versus frequency spectrum. In principle the cavity has infinite number of modes, when excited with microwave spectrum of frequencies. $TE_{01\delta}$ mode is identified as the fundamental mode with least perturbation when the tunable top lid is adjusted properly. After identifying the desired mode, the lid is fine tuned to get maximum separation between $TE_{01\delta}$ and any nearby cavity modes, to attain maximum possible accuracy in the Q_u measurement. Measure $TE_{01\delta}$ mode frequency and the unloaded and the 3 dB bandwidth from the resonance spectrum (See Fig. 6) to calculate the Q factor as

$$Q = \frac{f_o}{\Delta f} \tag{2.5}$$

One can assume that for low loss dielectrics, the unloaded Q factor is equal to loaded Q factor if coupling is weak. In the microwave frequency range the dielectric loss increases with frequency and hence there exists an inverse relationship between quality factor and resonant frequency. Hence the quality factor of dielectric resonators are conventionally represented in units of $Q_u \times f$, rather than Q_u.

2. 3. 4 Measurement of Temperature Coefficient of Resonant Frequency (τ_f)

Stability of resonant frequency with temperature is an important property of a DR to operate in microwave devices. τ_f is defined as

$$\tau_f = \frac{1}{f}\frac{\Delta f}{\Delta T} \tag{2.6}$$

The unit of τ_f is part per million per degree Celsius. In order to measure τ_f, DR is kept in the Hakki-Coleman end-shorted position between two copper plates. This is then kept on a hot plate and the entire system is insulated in an isothermal enclosure. The *E*-field probe is kept near the DR in such a way to get the TE_{011} resonant mode excited. The set up is then slowly heated (~ 1°C/minute) in the range 25 to 80°C. The probe of the thermocouple is kept just inside the isothermal enclosure so that it does not disturb the resonant frequency. Shift in the resonant frequency of TE_{011} is noted at every 2°C increment in temperature. The variation of resonant frequency is plotted as function of temperature and the τ_f is calculated from the slope of the curve using eqn. 2.6.

2. 3. 5 Error Calculations in Dielectric Property Measurements

The measurement of microwave dielectric properties were done with two decimal point accuracy. Usually three samples were prepared in a batch corresponding to a particular composition and the measurements were made at least twice per each specimen. The error in ε_r is calculated using the root sum of squares (RSS) method. The accuracy of ε_r measurement is restricted to the accuracy in measurement of resonant frequency and dimensions of the sample. Hence the possible errors in the measured value of dielectric constant of a sample of height (L), radius (r) and resonant frequency (f_r) given by

$$\Delta\varepsilon_r = \left[\left(\frac{\partial\varepsilon_r}{\partial L}\ \Delta L\right)^2 + \left(\frac{\partial\varepsilon_r}{\partial r}\ \Delta r\right)^2 + \left(\frac{\partial\varepsilon_r}{\partial f_r}\ \Delta f_r\right)^2\right]^{1/2} \tag{2.7}$$

If the independent sources of error corresponds to one standard deviation, then the error in ε_r will also corresponds to one standard deviation[42]. The errors in unloaded quality factor (Q_u) and temperature coefficient of resonant frequency (τ_f) were calculated using RSS method by taking partial derivative of these parameters with respect to independent variables.

2.4 DESIGN METHODOLOGY AND FABRICATION OF DRAs

The building block for dielectric resonator antenna is a block of dielectric material. Various shapes are possible for the antenna solely depending on the geometry of the DR sample. The physical dimensions and ε_r of the dielectric block determines the resonant frequency of the antenna. Due to the ease of fabrication and better performance reported, in the present work investigations were mainly concentrated on cylindrical, rectangular and elliptical DRAs.

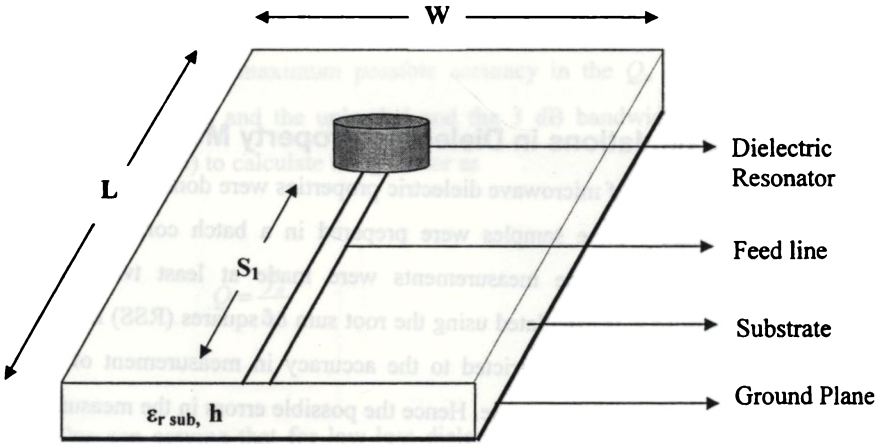

Fig. 2.7 Geometry of a cylindrical DRA configuration

The geometry of a representative DRA studied in this investigation is depicted in Fig. 2.7. The geometry comprises a dielectric disk resonator of specific shape (cylinder, ellipsoid/rectangular) synthesized through solid-state ceramic route as explained in sections 2.1 and the dielectric properties are characterized as described in section 2.3 of

this chapter. The dielectric constant and dimensions of the DR disk are controlled to operate the antenna in the desired frequency range. The DR is electromagnetically coupled with a 50 Ω microstrip feed line of width 3 mm and length S_1 = 50 mm, fabricated on a low loss, low dielectric constant ($\varepsilon_{r\ sub}$) substrate material (glass epoxy) of dielectric constant $\varepsilon_r = 4.28$ and thickness h = 1.6 mm backed by a conducting plane.

2.5 MEASUREMENT TECHNIQUES OF ANTENNAS

2.5.1 Measurement of return loss, resonant frequency and bandwidth

Network Analyzer is calibrated to one full port and the test antenna is connected to PORT 1 of the S-parameter test set. The measured S_{11} in 'LOGMAG' data is acquired

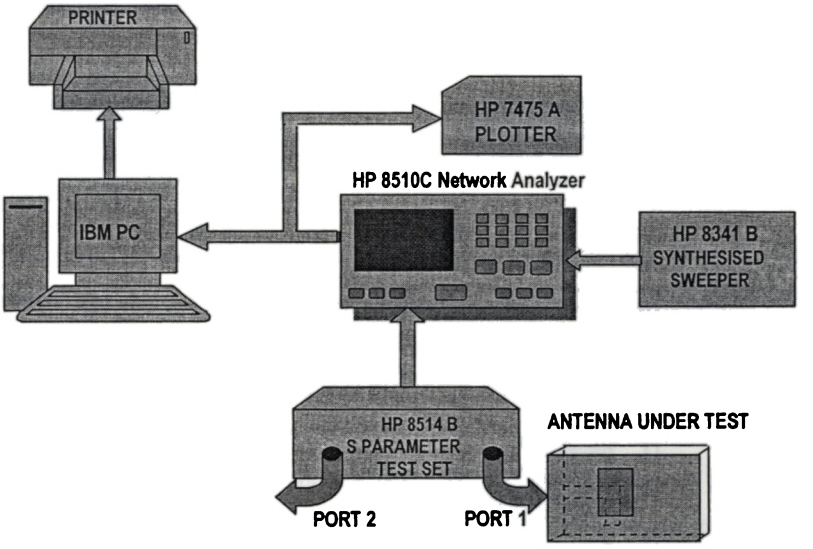

Fig. 2.8 Experimental setup for the measurement of return loss and resonant frequency

and stored in ASCII format in the computer interfaced with the network analyzer (Fig. 2.8), using 'MERL Soft'. The resonant frequency is determined from the dip of the return loss curve. The impedance bandwidth is measured by taking the range of frequencies

(Δf) over which the return loss is greater than or equal to 10 dB. Percentage bandwidth can be calculated using the expression ($\Delta f/f_r$) x 100, where f_r is the centre frequency of the operating band.

2.5.2 Measurement of Radiation Pattern

Antenna radiation pattern is the spatial distribution of the electromagnetic field radiated by the antenna. Generally patterns in two-principle plane, E and H planes are taken. The principal plane patterns (co-and cross-polar) of the test antenna are measured

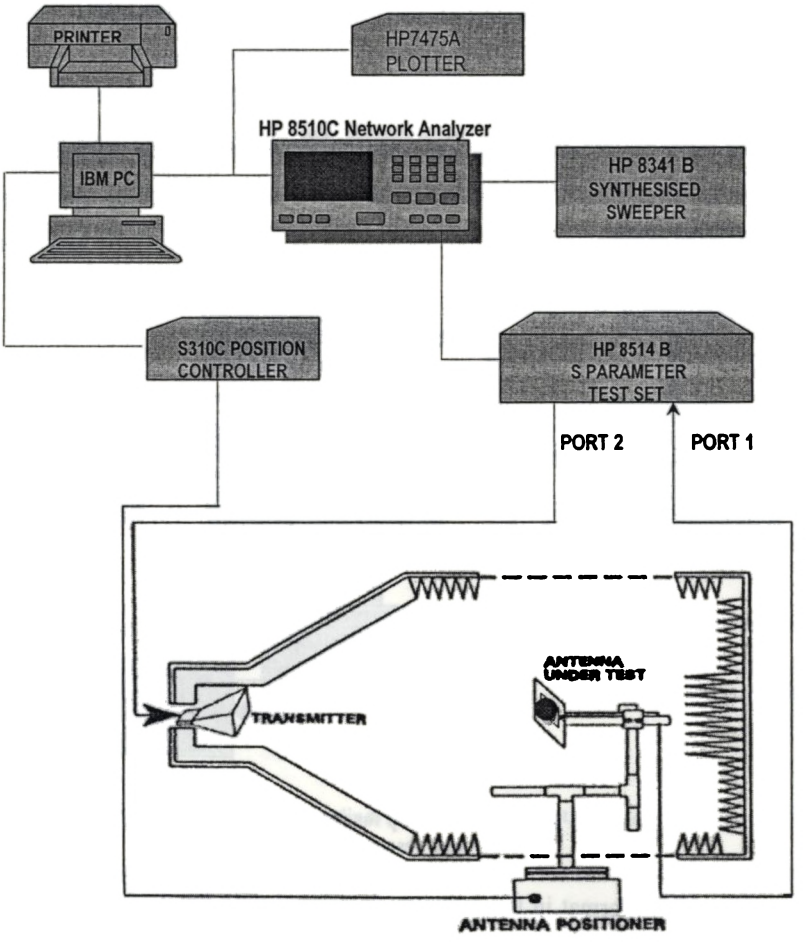

Fig. 2.9 Experimental setup for the measurement of radiation pattern

by keeping the antenna in receiving mode inside an anechoic chamber. The experimental setup for the measurement of radiation pattern is shown in Fig. 2.9. HP 8510C Network Analyzer, interfaced to an IBM PC, is used for the pattern measurement. The PC is attached to a STIC 310C position controller. The test antenna is mounted on the antenna positioner kept inside the anechoic chamber at a distance $R > 2D^2/\lambda$ from a wideband horn antenna (transmitter), where D is the maximum dimension of the antenna and λ is the wavelength. The test antenna and the transmitting antenna are connected to Port 2 and Port 1 of the network analyzer respectively.

Radiation patterns of the antenna at multiple frequency points can be measured in a single rotation of the test antenna by using MERL Soft. The positioner will stop at each step angle and take S_{21} measurement at different frequency points in the operating band. The process will repeat till it reaches the stop angle. The entire measured data is stored in ASCII format and can be used for further processing. The different radiation pattern characteristics like half power beam width, cross-polar level etc. are obtained after the analysis of the radiation pattern.

2.5.3 Measurement of Gain

The setup for the measurement of gain is the same as that used for pattern measurement. The relative gain of the new antenna is measured with a standard circular patch antenna operating at the same frequency and fabricated on the same substrate. The standard circular microstrip antenna is kept inside the anechoic chamber and connected to Port 2 of the Network Analyzer. The test antenna in the transmitting mode is connected to Port 1.The antenna is bore-sighted and a THRU RESPONSE calibration is performed in the Network Analyzer and stored in the CAL SET. This is the reference gain response. The standard antenna is now replaced with the test antenna and the plot displayed on the Network Analyzer will directly give the relative gain of the test antenna with respect to the standard circular antenna.

2.6 SIMULATION OF DRs AND DRAs

2.6.1 Introduction

The traditional process for solving EM (Electromagnetic) problems was to build a prototype, accumulate performance test data by subjecting the prototype to various experiments, correct deficiencies, and retesting, which normally require several cycles. With the advent of 3D-EM (Three Dimensional Electro-Magnetic) simulation techniques, these problems became efficient and simplified. However, these methods were generally not economically feasible since they required the use of supercomputers as well as a substantial knowledge of EM theory and advanced numerical techniques. During the last decade, the three dimensional electromagnetic simulation capabilities have significantly advanced due to the tremendous progress in computer hardware technology combined with an improvement in numerical techniques. Most of the electromagnetic problems can now be analyzed and understood by 3D-EM simulation which is performed by solving Maxwell's equations numerically. Recent advances in computer hardware technology and EM simulation algorithm enabled to visualize 3D EM wave propagation, even with personal computers. The following are very important criteria to be considered when selecting a 3D- EM software tool: (i) Consistently reliable results (ii) Relatively short computational time, compatible with the development schedule (iii) Simplicity of operation, particularly the ease of CAD input and mesh generation (iv) Compatibility with the requirements (v) Compatibility with other CAD tools and (vi) Versatility and expandability. Various numerical methods have been used to solve different EM problems. These methods include mode matching technique,[43] the finite element method (FEM)[44], the finite-difference method (FDM)[45], the finite-difference time-domain method (FDTD)[46] the moment method (MoM)[47] and Transmission Line Matrix (TLM) method. Each method has got its own advantages and deficiencies and hence a single method can not be used to solve all the problems related with EM wave propagation. In this work the 3D TLM technique has been employed to describe the interaction of EM wave with dielectric resonators and the characteristics of DRAs.

2.6.2 Transmission Line Matrix (TLM) Method

Transmission Line Modeling (TLM) or Transmission Line Matrix/ Modeling (TLM) is a general numerical simulation technique suitable for solving field problems. In 1971, Johns & Beurle[48] have introduced the principles of TLM time domain methods in electromagnetics. Subsequently, this method was pioneered by the microwave engineering community. Its main application has been in electromagnetics, but it has also been applied to thermal or diffusion problems[49] as well as acoustics[50]. The TLM method belongs to the general class of differential time-domain numerical modeling methods. The basic approach of the TLM method is to obtain a discrete model which is then solved exactly by numerical means; approximations are only introduced at the discretisation stage. This is to be contrasted with the traditional approach in which an idealized continuous model is first obtained and then this model is solved approximately. For electromagnetic systems, the discrete model is formed by conceptually filling space with a network of transmission-lines in such a way that the voltage and current give information on the electric and magnetic fields. The point at which the transmission-lines intersect is referred as a node and the most commonly used node for 3-dimensional work is the symmetrical condensed node. At each time step, voltage pulses are incident upon the node from each of the transmission-lines. These pulses are then scattered to produce a new set of pulses which become incident on adjacent nodes at the next time step. Each 3D node[51] is the combination of three shunt and three series nodes. The three shunt nodes represent the E-field, and the three series nodes represent the H-field in the three coordinate directions as shown in Fig. 2.10 (a). To accommodate discontinuities such as metallic boundaries and slabs of dielectric or magnetic material, open-circuited and short-circuited stubs of admittance Y_o and impedance Z_o are added to shunt and series nodes respectively. The 3D node is further equipped with stubs of infinite length and normalized characteristic admittance G_o to facilitate any dielectric losses which may be required. The 3D geometry of a problem is set up by connecting many such 3D nodes together. The relationship between the incident pulses and the scattered pulses at each node is determined by the scattering matrix, which is set to be consistent with the

following set of Maxwell's equations. Additional elements, such as transmission-line stubs, can be added to the node so that different material properties can be represented.

$$\frac{\partial H_z}{\partial y} - \frac{\partial H_y}{\partial z} = \varepsilon_o \varepsilon_r \frac{\partial E_x}{\partial t} + \sigma E_x \tag{2.8}$$

$$\frac{\partial H_x}{\partial z} - \frac{\partial H_z}{\partial x} = \varepsilon_o \varepsilon_r \frac{\partial E_y}{\partial t} + \sigma E_y \tag{2.9}$$

$$\frac{\partial H_y}{\partial x} - \frac{\partial H_x}{\partial y} = \varepsilon_o \varepsilon_r \frac{\partial E_z}{\partial t} + \sigma E_z \tag{2.10}$$

$$\frac{\partial E_z}{\partial y} - \frac{\partial E_y}{\partial z} = -\mu_o \mu_r \frac{\partial H_x}{\partial t} \tag{2.11}$$

$$\frac{\partial E_x}{\partial z} - \frac{\partial E_z}{\partial x} = -\mu_o \mu_r \frac{\partial H_y}{\partial t} \tag{2.12}$$

$$\frac{\partial E_y}{\partial x} - \frac{\partial E_x}{\partial y} = -\mu_o \mu_r \frac{\partial H_z}{\partial t} \tag{2.13}$$

In these equations, the following equivalences apply:

E_x = the common voltage at shunt node E_x

E_y = the common voltage at shunt node E_y

E_z = the common voltage at shunt node E_z

H_x = the common current at series node H_x

H_y = the common current at series node H_y

H_z = the common current at series node H_z

ε_o and μ_o are the permittivity and permittivity of free space, ε_r and μ_r are their relative values and σ is the conductivity. It should be noted that the values of ε_r, μ_r and σ can assign values depending on the material properties.

For the purpose of analysis, any of the six electromagnetic field components is excited by introducing impulses at various points in the network model. The impulses travel along the ideal TEM lines and are scattered at the individual nodes. In this way the time-domain propagation of all six EM field components is obtained simultaneously. A solution of any (or all) of the field components is available anywhere within the geometry of the problem. The output consists of a stream of impulse amplitudes corresponding to the output impulse function for the particular field component under consideration. Finally, the Fourier transform of this function is taken to yield the response to an excitation varying sinusoidally with time.

In general, models can be described as low, medium or high loss systems. For low loss systems, the spectral content of the truncated time series is required since the amplitude of any resonances will increase in proportion to the number of time steps (tending to infinity in the limit). For high loss systems, in which the signal effectively decays to zero within the simulation time, the actual spectral content of the complete time series is obtained. Moderately damped systems present a problem since an excessive number of time steps would be required for the signal to decay significantly. In this case, the spectral content of the truncated time series is obtained as an estimation of the spectral content of the complete time series.

One of the advantages of TLM is that the core algorithm is very straightforward. Each time step can be divided into two processes: scatter and connect. During the "scatter" stage, voltage pulses incident on the node are scattered to produce a new set of outgoing voltage pulses. During the "connect" stage, voltage pulses are transferred to the adjacent nodes. It is possible to combine both processes together but it is simpler to consider them separately. Nowadays 3D-TLM methods are popular measurement technique[52,53,54,55] because of their accuracy, efficiency and ability to provide broadband data over a wide frequency range. In the present investigation, we have used a Computer Aided Simulation (CAD) package named Micro-stripes 6.5[56] based on 3D-TLM techniques.

- Aided Simulation (CAD) package named Micro-stripes 6.5[56] based on 3D-TLM techniques.

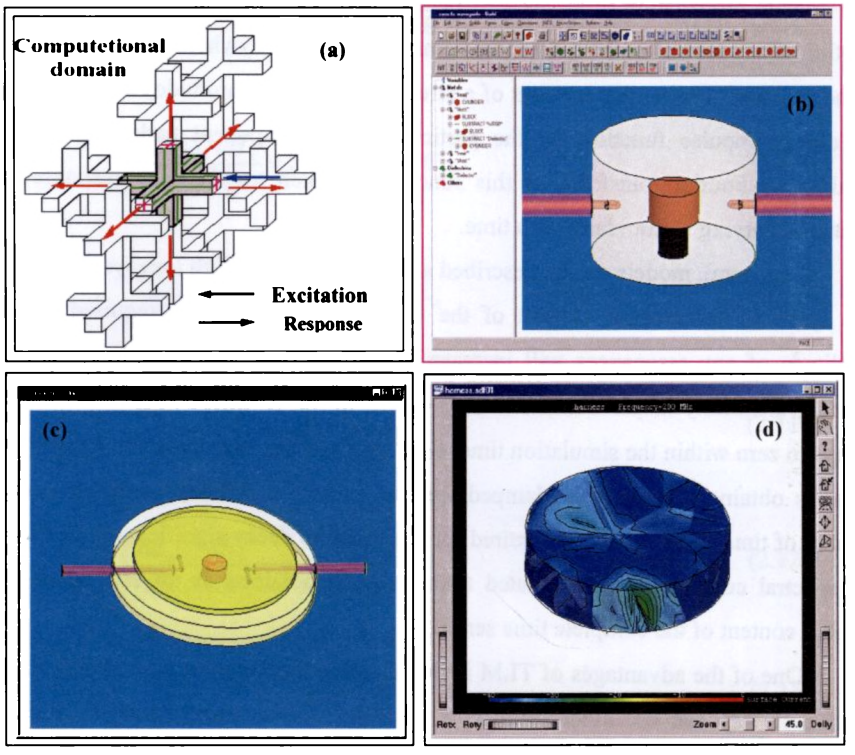

Fig. 2.10 Schematic diagram of various steps involved in the simulation using Micro-stripes 6.5

Micro-Stripes is a complete software tool for the 3D electromagnetic analysis and design of devices and structures required in the high frequency range. The design process follows five easy steps: (i) Define the geometry using a versatile and intuitive solid modeler based on the ACIS kernel, or import the geometric model from another CAD package (ii) Assign the material properties to the geometry (iii) Choose the type of excitation (e.g. port or plane wave) (iv) Definition of the results indented to obtain and (v) Let the efficient processing of time domain solver based on the TLM to yield the results. Examples for various processes involved in the simulation process using Micro-stripes is shown in Fig. 2.10 (b) to 2.10 (d). The geometric structure for simulation was made using solid modeler based on ASCIs Kernel plotting software. Fig. 2.10 (b) shows the main application window from which all the tools of the CAD can be accessed.

Projects are created using this window, and system designs held within the projects are studied. The advanced build module provided allows the 3D solid modelling, which is used to create the geometry or import it from other CAD tools. Most industry standard CAD formats can be imported. Within Build the electromagnetic parameters and results required are set. Material properties like conductivity, relative permittivity and dielectric loss as well as excitation mechanisms can be assigned properly. TLM has multigrid mesh capability to assign isotropic as well as anisotropic properties of different materials. The mesh size can be manually assigned or it can be automized. Fig. 2.10 (b) and 2.10 (c) shows the model of a three dimensional geometric structure (Cavity and Hakki-Colemann set up) for the measurement of microwave dielectric properties of a dielectric resonator (See Chapter 5, Section 5.3.1.2) designed using Micro-stripes 6.5.

To run the simulation program, the Build module of Micro-stripes divides the model and space it occupies (the work space) into a large number of spatial elements or cells. These cells are small rectangular blocks arranged on a Cartesian mesh. The accuracy and time step of simulation depends on cell size. The duration for the process can be reduced by lumping or multigriding. The 3D-TLM simulator considers the EM field to be uniform within each cell. It is therefore necessary for the cells to be small on the scale of distance over which the field varies. Build chooses the default cell-size to be $1/10^{th}$ of the free space wavelength at the requested maximum model frequency. Auto-mesh facility takes into account the material properties and reduces the cell-size within dielectric bodies. Build sets a sensible default duration. Build monitor the response after every multigriding analysis and display a graph of the time-domain response which is updated as the simulation proceeds. Simulation terminates after completing all the time domain truncation and verifying the results with the input given by the user.

TLM has the feasibility for the calculation and displaying of field distributions (Electric, Magnetic fields, surface currents, power flows, power densities, power loss densities and SAR) at specified frequencies after a single run. This enables the resonant mode identification of DRs and DRAs. Two such examples are illustrated in Figs. 2.10 (d). After finishing the simulation, the graph plotter of TLM provides a view of time and frequency domain results assigned to it. In this thesis TLM method was adopted for the

simulation of transmission mode resonance spectra of cavity shielded and end-shorted dielectric resonators (See Chapters 5 and 6) to predict their microwave dielectric properties. In addition the simulation technique was also applied to simulate the antenna characteristics (See Chapter 8) and to identify the excited modes of DRA.

2.7 REFERENCES

[1] R. Rice, *Ceramic Fabrication Technology*, Marcel Dekker, Boston (2003).

[2] M. Barsoum, "Fundamentals of Ceramics", McGraw-Hill. Companies, Singapore (1997).

[3] Y. Arai, "*Chemistry of powder production*" Chapman & Hall, London (1996).

[4] H. Schmalzried, *Sold State Reactions*, Academic Press, New York (1974)

[5] P. Nanni, M. Viviani and V. Buscaglia, *Synthesis of Dielectric Ceramic Materials, Handbook of Low and High dielectric Constant and their Applications,* Ed. H.S. Nalwa, Vol.1, Materials and Processing, Academic Press, New York, (1999).

[6] M. Thirumal, P. Jain and A. K. Ganguli, *Mater. Chem. Phys.* **70** (2001) 7.

[7] D. W. Johnson Jr., *Am. Ceram. Soc. Bull.* **64** (1985) 1597.

[8] C. C. Harris, *Trans. AIME.* **238** (1967) 17.

[9] B. Beke, *Principles of Communition*, Akademi Kiado, Budapest (1964).

[10] L. M. Sheppard, *Ceram. Ind.* **149** (1999) 51.

[11] P. Winiewski, M. Szafran, G. Rokicki, *Key Engineering Materials, Euro Ceramics – VIII.* **264** (2000) 428-32.

[12] G. Y. Onoda and L. L. Hench, *Ceramic Processing before Firing*, Wiley Interscience, New York (1973).

[13] N. McN. Alford, X. Wang, S. J. Penn, M. Poole and A. Jones, *Br. Ceram. Trans.* **99** (2000) 212.

[14] S-J. L. Kang, *Sintering, Densification, Grain Growth and Microstructure*, Elsevier, Amsterdam (2002).

[15] R. L. Coble, *J. Appl. Phys.* **32** (1961) 789.

[16] W. D. Kingery and M. Berg, *J. Appl. Phys.* **26** (1955) 1205.

[17] C. Herring, *J. Appl. Phys.*, **21** (1950) 301.

[18] T. K. Gupta, *J. Am. Ceram. Soc.* **61** (1978) 191.

[19] W. D. Kingery, *J. Am. Ceram. Soc.* **37** (1954) 42.

[20] H. M. Shirey, "*Low temperature synthesis of the microwave dielectric material Barium Magnesium Tantalate (BMT)*", M. S. Thesis, University of Pittsburg (2002).

[21] A. D. Lidiard "*Deffects and their structure in non-metallic solids*" NATO Advances study series B Physics, Vol. 19, Ed. B. Henderson and A. E. Hughes.

[22] G. E. Bacon, *X-ray and Neutron Diffraction*, Pergamon Press, Amsterdam, (1966).

[23] B. D. Cullity and S. R. Stock, *Elements of X-ray diffraction*, Prentice Hall, New Delhi, (2001).

[24] D. L. Bish and J. E. Post, *Modern Powder Diffraction. Reviews in Mineralogy,* **20**, Mineralogical Association of America, Boston (1989).

[25] Internet File: *http://www.mse.iastate.edu/microscopy/college.html*

[26] Ian M. Watt, *The Principles and Practice of Electron Microscopy-* 2nd Edn., Cambridge University Press, Cambridge (1997).

[27] G. Birnbaum and J. Franeaue, *J. Appl. Phys.* **20** (1949) 817.

[28] J. Mussil and F. Zacek, *Microwave Measurement of Complex Permittivity by Free Space Methods And Applications*, Elsevier, New York, (1986).

[29] K. Leong, *Precise Measurements of Surface Resistance of HTS Thin Films using A Novel Method of Q-Factor Computations for Sapphire Dielectric Resonators in the Transmission Mode*, Ph. D. thesis, James Cook University (2000).

[30] K. Leong and J. Mazierska, *J. Supercond.* **14** (2001) 93.

[31] D. Kajfez, *Q Factor*, Vector Fields, Massachusetts (1994).

[32] K. Wakino, *Proc. of The Second Sendai Inter. Conference*, YAGI Symposium on Advanced Technology Bridging the Gap between Light and Microwaves, pp. 187–196 (1990).

[33] B. W. Hakki and P.D. Coleman, *IRE Trans. Microwave Theory Tech.* **MTT-8** (1960) 402.

[34] W. E. Courtney, *IEEE Trans. on Microwave Theory Tech.* **MTT-18** (1970) 476.

[35] Y. Kobayashi, *IEEE Trans. Microwave Theory Tech.* **MTT-28** (1980) 1077.

[36] S. B. Cohn and K. C. Kelly, *IEEE Trans. Microwave Theory Tech.* **MTT-14** (1966) 406.

[37] E. L. Ginzton, *Microwave Measurements*, McGraw Hill Book Co., Boston, (1957).

[38] E. J. Vanzura, J. E. Rogers: *Proceedings of the IEEE Conference on Instrumentation and Measurement Technology*, May 14-16, Atlanta, (1991).

[39] T. Miura, T. Takahashi, M. Kobayashi, *IEICE Transactions on Electronics,* **E7 7-C** (1994) 900.

[40] M. C. Sanchez, *IEE Proceedings*, Part. H, **134** (1987) 243.

[41] J. Krupka, K. Derzakowski, B. Riddle, and J. B. Jarvis, *Meas. Sci. Technol.* **9** (1998) 1751.

[42] J. B. Jarvis, R.G. Gayer, J. H. Grosvenor Jr., M. D. Janezic, C. A. Jones, B.Riddle, C. M. Weil and J. Krupka, *IEEE Trans. Dielec. Electrical Insul.* **5** (1998) 571.

[43] K. A. Zakki and A. E. Atia, *IEEE Trans. Microwave Theory Tech.* **MTT-31** (1983) 1039.

[44] M. Mohammad-Taheri and D. Mirshelkar-Syahkal, *IEEE Trans. Microwave Theory Tech.* **MTT-39** (1989) 1536.

[45] J. M. Guan C. C. Su, *IEEE Trans. Microwave Theory Tech.* **MTT-45** (1997) 1767.

[46] Y. X. Guo, K. M. Luk and K. W. Leung, *IEE Proc. Microwave Antennas Propagat.* **146** (1999) 292.

[47] B. Widenberg, "*A general mode matching technique applied to bandpass radomes*", Ed. Gerhard, Kristensson, Lund, Sweden (2001).

[48] P. B. Johns and R. L. Beurle, "*Numerical solution of two-dimensional scattering problems using a transmission-line matrix*", *Proc. IEE.* **118** (1971)1203.

[49] J. Paul, V. Podliozny, D. W. P. Thomas and C. Chrstopoulos, *Turk. J. Elec. Engin.* **10** (2002) 185.

[50] X. Pelorson, P. Badin, K. Motoki, N. Miki and M. Plique, *Proc. 15th International Congress on Acoustics,* Trondheim, Norway, **4** (1995) 497.

[51] S. Akhtarzad, "*Analysis of lossy microwave structures and microstrip resonators by the TLM method*", PhD dissertation, University of Nottingham, Nottingham, England,

May 1975.

[52] S. Akhtarrzad and P. B. Johns, *IEEE Trans. Microwave Theory Tech.* **MTT-23** (1975) 990.

[53] J. Baker-Jarvis, M. D. Janezic, P. D. Domich and R. G. Geyer, *IEEE Trans., Instrum. Meas.* **43** (1994)711.

[54] J. Chuma, C. W. Sim and D. Mirshekar-Syahkal, *Electron. Lett.* **35** (1999) 1712.

[55] W. J. R. Hoefer, *IEEE Trans. Microwave Theory Tech.* **MTT -40** (1992) 1517.

[56] Micro-stripes 6.5 Reference manual, Flomerics Limited, Surrey, UK.

CHAPTER 3

$Ca(Ca_{1/4}B_{2/4}Ti_{1/4})O_3$ (B = Nb, Ta) CERAMICS: EFFECT OF DOPANTS ON THE MICROWAVE DIELECTRIC PROPERTIES

This chapter discusses in detail about the complex perovskite type dielectric resonator materials and the introduction of a novel system: $Ca_5B_2TiO_{12}$ (B = Nb, Ta) into this family. $Ca_5Nb_2TiO_{12}$ and $Ca_5Ta_2TiO_{12}$ have been prepared by conventional solid-state ceramic route. The structure and microstructure were studied by X-Ray diffraction and Scanning Electron Microscopic techniques. The dielectric properties of the materials were measured in the 3-5 GHz microwave frequency range. Linear variations of microwave dielectric properties were observed in $Ca_5Nb_{2-x}Ta_xTiO_{12}$ solid solution system. The effect of various amounts of di-, tri-, tetra-, penta- and hexavalent impurities on the structure, microstructure, density and microwave dielectric properties of $Ca_5B_2TiO_{12}$ (B = Nb, Ta) complex perovskites have been investigated. Structure of the parent materials remained unchanged while slight increase in density was observed with small amount of certain dopants. Improvement in dielectric constant, quality factor and temperature coefficient of resonant frequency was observed with the doping of small amounts of MgO, ZnO, NiO, CuO, Co_3O_4, Cr_2O_3, SnO_2 and Sb_2O_5. A correlation between the microwave dielectric properties of $Ca(Ca_{1/4}B_{2/4}Ti_{1/4})O_3$ [B = Nb, Ta] ceramics and ionic radius of the dopant has been observed.

3.1 SIMPLE AND COMPLEX PEROVSKITES

3.1.1 Introduction

Among the vast majority of mixed metal oxides used in modern chemical industry, perovskite-type oxides remain prominent. The perovskite oxides have the general formula ABO_3 (A cation is larger in size than B). Although most of the numerous and interesting compounds with the perovskite structure are oxides, some carbides, nitrides, halides, and hydrides also crystallize in this structure. The first material reported in this family was $CaTiO_3$ later named as mineral perovskite by Gustav Rose in 1830's and named it after the memory of famous Russian mineralogist Count Lev Aleksevich von Perovski[1]. The broad diversity of properties that these class of compounds exhibit is derived from the fact that around 90% of the metallic natural elements of the Periodic Table are known to be stable in a perovskite type oxide structure and also from the possibility of synthesizing multicomponent perovskites by partial substitution of cations in positions A and B, giving rise to substituted compounds with formula of $A_{1-x}A'_xB_{1-x}B'_xO_3$. These characteristics account for the large variety of reactions in which they are used as catalysts as well as applications in material science and electronics. Other important aspects of perovskites are related to the stability of mixed oxidation states or unusual oxidation states in the crystal structure.

3.1.2 ABO_3 Structure

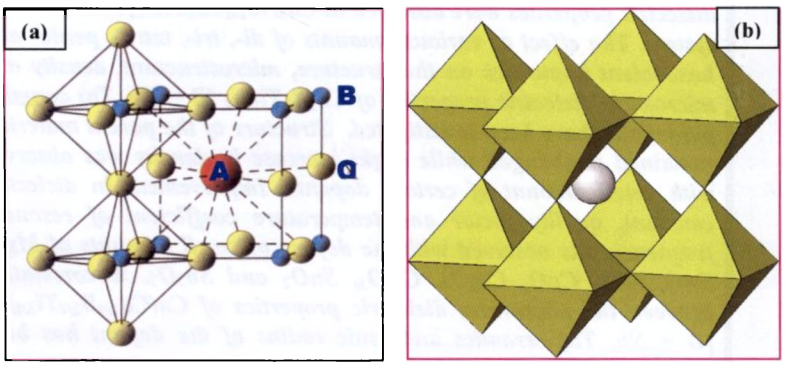

Fig. 3.1 (a) Ideal Perovskite (ABO_3) structure showing 6-fold coordination of B-site and 12-fold coordination of A- site cations (b) Unit cell of ABO_3 perovskite featuring the A-site enclosed by eight BO_6 octahedra

The ideal perovskite-type structure is cubic with space group $Pm\bar{3}m$. The unit cell formula of perovskite-type oxides is ABO_3, where A is the larger and B is the smaller cation. Fig. 3.1 (a) depicts the corner shared octahedra that form the skeleton of the structure, in which the centre position is occupied by the A cation. In the unit cell, A cations are located at position [0, 0, 0], the B at [½, ½, ½] and three O ions at [0, ½, ½]; [½, 0, ½]; [½, ½, 0]. Alternatively, this structure can be viewed with the B cation placed at the center of the octahedron and the A cation is at the center of the cube. The perovskite structure is thus a superstructure with an REO_3-type (RE = Rare earth ions) framework built up by the incorporation of A cations into the BO_6 octahedra. Hence in the ABO_3 structure, the B cation is 6-fold coordinated and the A cation is 12-fold coordinated with the oxygen anions. Besides the ionic radii requirements, another condition to be fulfilled for the stability of the structure is electroneutrality, ie., the sum of charges of A and B equals the total charge of oxygen anions. This is attained by means of appropriate charge distribution of the form $A^{1+}B^{5+}O_3$ [eg. $LiNbO_3$], $A^{2+}B^{4+}O_3$ [eg. $CaTiO_3$], $A^{3+}B^{3+}O_3$ [eg. $LaAlO_3$] and $A^{0}B^{+6}O_3$ [eg. REO_3] while $A^{4+}B^{2+}O_3$ is rare for columbic reasons[2]. In addition to this, partial substitution of A and B ions is allowed, thus yielding a plethora of compounds while preserving the perovskite structure. However, deficiencies of cations at the A- or B-sites or of oxygen anions are frequent, which results in defective perovskites. The nonstoichiometry in perovskites has been widely discussed in several reviews[3,4,5].

In the ideal structure, where the atoms are touching one another, the B-O distance is equal to $a/\sqrt{2}$ (a is the cubic unit cell parameter) while the A-O distance is $a/\sqrt{2}$ and the following relationship between the ionic radii holds: $R_A + R_O = \sqrt{2}\,(R_B + R_O)$. However, it was found that the cubic structure was still retained in ABO_3 compounds, even though this equation is not exactly obeyed. As a measure of the deviation from the ideal situation, Goldschmidt[6] introduced a parameter named tolerance factor (t), defined by the equation:

$$t = \frac{R_O + R_A}{\sqrt{2}\,(R_O + R_B)} \qquad (3.1)$$

which is applicable at room temperature to the empirical ionic radii. Although for an ideal perovskite t is unity, this structure is also found for lower t-values ($0.75 < t < 1.0$). The ideal cubic perovskite structure appears in a few cases for t-values very close to unity at high temperatures. In most cases, different distortions of the perovskite structure appear. The naturally occurring compound $CaTiO_3$ was originally thought to be cubic, but its true symmetry was later shown to be orthorhombic[7] whereas $SrTiO_3$ was found to be more symmetric with cubic structure and $t = 1.002$[8]. Deviations from the ideal structure with orthorhombic, rhombohedral, tetragonal, monoclinic, and triclinic symmetry are known, although the latter three ones are scarce and poorly characterized[9,10,11]. The distorted structure may exist at room temperature, but it transforms to the cubic structure at high temperature. This transition may occur in several steps through intermediate distorted phases. These deviations from the cubic perovskite structure may proceed from a simple distortion of the cubic unit cell, or an enlargement of the cubic unit cell, or a combination of both.

3.1.3 Complex perovskite structured compounds

Derivatives of simple perovskite structures are formed when either or both of the *A*- and *B*-site cations are replaced by combination of other cations located at specific crystallographic sites. Accordingly perovskites with general formula $A(BB')O_3$, $(AA')BO_3$ and $(AA')(BB')O_3$ are possible. In these types of compositions, change in temperature increases or decreases the amplitude of thermal vibrations and will not alter the positions of ions in their respective crystallographic positions and compositions is assumed to be in an ordered state. But there are some solid solutions in perovskite family, in which the random structure of cations exists only at elevated temperatures. If cations are ordered at only one site the compounds are commonly termed as double perovskite, whereas if ordering occurs at both sites they are referred to as complex or quadruple perovskites. Because of the potential to tolerate a wide range of elements of differing size and charge there exist a large number of permutations employing various cations in perovskite structure. Interestingly because of the industrial importance as dielectric resonators at microwave frequencies most of the perovskite compounds studied are not simple systems, but rather complex perovskite type with 1:1, 1:2 or 1:3 type of *A* and/or *B*-site ordering.

Ideal 1:1 ordered oxide perovskite comprises $A^{2+}{}_2B^{3+}B'^{5+}O_6$ (eg. Sr_2DyRuO_6), $A^{2+}{}_2B^{4+}B'^{4+}O_6$ (eg. Ba_2CePtO_6), $A^{2+}{}_2B^{2+}B'^{6+}O_6$ (eg. Ba_2NiMoO_6), and $A^{2+}{}_2B^{1+}B'^{7+}O_6$ (eg. Ba_2NaReO_6) compositions with the occupancy of divalent cation in the *A*-site. When *A* cation is trivalent two combinations of *B*-site cations are possible: $A^{3+}{}_2B^{2+}B'^{4+}O_6$ (eg. La_2MgHfO_6) and $A^{3+}{}_2B^{1+}B'^{5+}O_6$ (La_2LiIrO_6). In a completely ordered 1:1 perovskite, the *B* and *B'* sublattices are occupied only by *B* or *B'* cations respectively and are ordered along $[111]_p$ planes or the vector $\frac{1}{2}[111]^*_p$. However for a completely random distribution (disorder) the sublattices can not be distinguished.

A genuine effort to make double perovskites with the general formula $A_3B^{2+}B'^{5+}{}_2O_9$ or $A(B^{2+}{}_{1/3}B'^{5+}{}_{2/3})O_3$ was first made by Rustam Roy[12] based on complex perovskite compositions in $Ba(B_{1/2}B'_{1/2})O_3$ and $Ba(B_{1/3}B'_{2/3})O_3$. Later, Galasso *et al.*[13, 14,15,16] studied the effect of substitution of different ions such as Ba, Sr, Ca and Pb on the *A*-site and Zn, Co, and Ni on the *B* site in the $A_3B^{2+}B'^{5+}O_9$ complex perovskites using powder diffraction methods, where the B'-site was occupied by niobium or tantalum ions. It was observed[15] that ideal 1:2 double perovskites are formed when the *B*-cations are ordered along $[111]_p$, or the vector $1/3[111]^*_p$ of the original cubic cell, and BO_6 and $B'O_6$ ployhedra are not tilted.

Perovskites which exhibit 1:3 ordering are relatively rare as most of the attempts to synthesize such compounds[17,18] have resulted in ternary disordered perovskites. The 1:3 *A*-site ordered compounds have the general formula $AA'B_4O_{12}$ and include materials like $CaCu_3Ge_4O_{12}$[19] and $NdCu_3Ti_4O_{12}$[20]. The 1:3 *B*-site ordered compounds have the general formula $A_4BB'_3O_{12}$ like $Ba_4LiSb_3O_{12}$ compound reported[17] by Alonsa *et al.* in 1987. It was observed that majority of ordered perovskites studied to date are oxide perovskites which exhibit 1:2 *B*-site ordering[13].

An unusual composition with the complex perovskite structure was reported by Cava *et al.*[21] in the $Ca(Ca_{1/4}B_{2/4}Ti_{1/4})O_3$ (B = Nb, Ta) system, where mixing of three cations takes place in the *B*-site of the material. The material is actually a composition derived from $CaTiO_3$ - $Ca_4B_2O_9$ (B = Nb, Ta) polymorhs where the *B*-site of the latter was incorporated with Ti^{4+} ions. High temperature phases of both $Ca(Ca_{1/4}Nb_{2/4}Ti_{1/4})O_3$ and $Ca(Ca_{1/4}Ta_{2/4}Ti_{1/4})O_3$ ceramics were disordered, whereas low temperature phase of tantalum based material exhibited 1:2 type ordering and a mixing of 1:1 + 1:3 ordering for the

niobium analogue. Consequent to the complexity in ordering, the materials showed interesting variation in dielectric properties measured at 1 MHz[21].

3.2 $Ca(Ca_{1/4}B_{2/4}Ti_{1/4})O_3$ (B = Nb, Ta) COMPLEX PEROVSKITES

3.2.1 Milestones in the research of $Ca(Ca_{1/4}B_{2/4}Ti_{1/4})O_3$ (B = Nb, Ta) Ceramics

Complex perovskite type titania and Nb/Ta based ceramics are of special interest as dielectric resonators for use in wireless communications[22]. These materials exhibit a combination of high dielectric constant (ε_r) and low dielectric loss (high unloaded quality factor, Q_u). But they suffer from the drawback of relatively high temperature coefficient of resonant frequency (τ_f), which is not preferable from the application point of view. Investigations were made to tune the τ_f of these ceramics by solid solution formation between them[23,24,25,26,27]. The $CaTiO_3$ – $Ca_4Nb_2O_9$ polymorphs has drawn much attention because of the opposite signs of τ_f for $CaTiO_3$[22] [ε_r = 162, $Q_u \times f$ = 13000 GHz and τ_f = + 859ppm/°C] and $Ca_4Nb_2O_9$[22] [ε_r = 28, $Q_u \times f$ = 17000 GHz and τ_f = - 22ppm/°C], which suggests the possibility of tuning τ_f to zero. The crystal structure of $CaTiO_3$ (the mineral perovskite) has been extensively studied[28,29,30,31] and exists in several polymorphic forms which differ by a distortion of the framework of corner-connected [TiO_6] octahedra. The distortion originates from a large mismatch in the size of the *A*-type (Ca^{2+}) and *B*-type (Ti^{4+}) cations. Nevertheless, the room temperature phase is well established and belongs to orthorhombic symmetry with *Pnma* space group. In contrast only limited information is available on the structure of $Ca_4Nb_2O_9$ ceramics, though the dielectric properties were reported[32] by Kagata *et al.* In 1997, Hervieu *et al.*[33] reported the existence of a high temperature orthorhombic and low temperature monoclinic structure for $Ca_4Nb_2O_9$. They proposed that both the $Ca_4Nb_2O_9$ polymorphs are derivatives of the perovskite structure with one fourth of the Ca ions occupying the *B*-site, when represented in $Ca(Ca_{1/3}Nb_{2/3})O_3$ form. Recently Levin *et al.*[34] made a detailed investigation about the octahedral tilting and cation ordering in $Ca(Ca_{1/3}Nb_{2/3})O_3$ polymorphs. They suggested that four distinct perovskite related polymorphs exist in $Ca(Ca_{1/3}Nb_{2/3})O_3$, which was identified with structures that combine octahedral tilting and different ordering of Ca/Nb ions in *B*-site. The polymorphs include two

high temperature phases which exhibit disordered or 1:1 ordering and two low temperature phases which has 1:2 ordering of Ca/Nb ions in the octahedral site.

Because of the interesting structural properties, recently Bendersky *et al.*[35] studied the phase equilibria and microstructure of xCaTiO$_3$ - (1- x)Ca$_4$Nb$_2$O$_9$ ceramics and found that all the phases participating in equilibrium are solid solutions of the binary end members. Since both the end members have perovskite based structures, it is expected that the solid solution phases form as Ca$_5$Nb$_2$TiO$_{12}$, which is a novel composition. For the sake of discussion, the material can be represented in the usual complex perovskite form as Ca(Ca$_{1/4}$Nb$_{2/4}$Ti$_{1/4}$)O$_3$, with *A*-site occupied by Ca and *B*-site by Ca, Nb and Ti in 1:2:1 proportion. Bendersky *et al.*[35] suggested that the phase diagram of Ca$_5$Nb$_2$TiO$_{12}$ has four single phase fields (i) cubic disordered (*Pm3m*) (ii) a series of disordered CaTiO$_3$ – type polymorphs (*Pnma*) with different combinations of tilting (iii) a low temperature disordered/tilted (*Pnma*) phase and (iv) 1:1 or 1:2 ordered Ca$_4$Nb$_2$O$_9$ type fields. In addition a metastable transition to the 1:3 ordered phase occurs for a wide range of compositions. Most importantly they found that, the X-ray diffraction patterns of compositions in xCaTiO$_3$ - (1- x)Ca$_4$Nb$_2$O$_9$ with $0 < x < 1$ were indexable by an orthorhombic lattice with parameters close to those of CaTiO$_3$. The same result was consolidated employing Transmission Electron Microscopic (TEM) techniques by observing different [110] – type Selected Area Electron Diffraction (SAED) patterns, and also supported the *Pnma* symmetry.

Consequent to the ~~invention~~ discovery of novel Ca$_5$Nb$_2$TiO$_{12}$, in 1999, Cava *et al.*[21] reported the 1 MHz dielectric properties of Ca$_5$Nb$_2$TiO$_{12}$ and Ca$_5$Ta$_2$TiO$_{12}$ materials. The authors studied the dielectric properties at different processing temperatures of the specimens and reported that in the vicinity of ambient temperature, the dielectric constants are approximately 35 and 23 for the Nb and Ta-based ceramics respectively, and dielectric losses of the order of 0.0002 and temperature variation of dielectric constant, $\tau_\varepsilon < 5$ ppm/°C. The distribution of Ca, Nb/Ta and Ti atoms on the *B*-site was often found to be dependent on temperature, as order–disorder transitions are expected due to the competition between size or charge driven ordering and the disorder induced by maximizing entropy. At low temperatures, for example, the different *B*-site atoms may be fully or partially ordered in crystallographically inequivalent *B*-sites, and at high temperatures there may be more extensive disorder of atoms

among the possible sites due to the influence of entropy. Cava *et al.*[21] observed a highly unusual behaviour of double zero crossing of τ_ε with firing temperature. The samples fired at a temperature below 1450°C for both $Ca_5Nb_2TiO_{12}$ and $Ca_5Ta_2TiO_{12}$ showed negative τ_ε values. Above this temperature, τ_ε of both the ceramics shifted to positive values and the authors concluded that the positive τ_ε state was due to the formation of an ordered state of the cations on the *B*-sites. This ordered state appears to be short-range in nature, since the conventional powder X-Ray diffraction patterns did not show the appearance of new diffraction peaks in the corresponding temperature interval. When the processing temperature was between 1500 and 1525°C for the niobate and between 1575 and 1600 °C for the tantalate, the negative τ_ε state returned. For both materials, this transition occurred abruptly and independent of firing time, suggesting the presence of a high temperature transition from an ordered *B*-site structure to a disordered *B*-site structure. Again, the conventional powder X-Ray diffraction patterns revealed that the materials remained single-phase perovskites and that there has been no long-range structural rearrangement or discontinuity in lattice parameter. Apparently the diffraction patterns only revealed a gradually decreasing unit-cell volume, with increasing firing temperature, and a continuously decreasing orthorhombic distortion.

Later Cava *et al.*[36] explored the effect of chemical substitutions (Zr for Ti) in the niobium based compound that would enhance the kinetics of the formation of the short range ordered state and resulted in the low τ_ε of $Ca_5Nb_2TiO_{12}$ ceramics. The low temperature coefficient state was at the borderline between ordered and disordered states of the Ca, Nb, and Ti ions in the *B*-sites of the perovskite lattice. The pure Zr analog of this phase, $Ca_5Nb_2ZrO_{12}$, had a positive τ_ε value at all firing temperatures, as opposed to the generally encountered negative τ_ε values for $Ca_5Nb_2TiO_{12}$. Hence intermediate compositions with low τ_ε values were synthesized. However partial substitution of Zr for Ti were found to have a very significant effect on the τ_ε values, suggesting that the added component had a strong effect on the order/disorder on the *B*-site sublattice, rather than having a simple mixing effect. However Zr substitutions at the higher concentrations significantly increased the range of firing temperature of the polycrystalline ceramics.

In 2001, a much more authoritative investigation on the dielectric properties and microstructure of $Ca_5Nb_2TiO_{12}$ and $Ca_5Ta_2TiO_{12}$ ceramics were carried out by Bendersky *et al.*[37] The authors applied transmission electron microscopy (TEM) techniques to probe into the details about the complex structural changes and dielectric behaviour in $Ca_5Nb_2TiO_{12}$ and $Ca_5Ta_2TiO_{12}$ since X-ray powder diffraction method alone does not appear to be a good technique to approach the problem. It was found that different types of ordering between (111) planes, namely 1:1, 1:2 and 1:3, as well as distortions by tilting of octahedra, are involved in the formation of a microstructural state at an ambient temperature. Both the compounds in the as-sintered conditions have a microdomain structure but with a different type of ordering, 1:3 for $Ca_5Nb_2TiO_{12}$ and 1:2 for $Ca_5Ta_2TiO_{12}$. Moreover both the ceramics have a tilting phase transition from the disordered *Pm3m* to distorted *Pnma* (with the $a^-b^+a^-$ tilt of octahedra) structures at temperatures that coincided with the observed second shift of τ_ε towards the negative values in the temperature versus τ_ε plot. The authors found that the structures of $Ca_5Nb_2TiO_{12}$ and $Ca_5Ta_2TiO_{12}$ ceramics sintered at temperatures below 1450°C were different; the disordered *Pnma* structure was found for $Ca_5Ta_2TiO_{12}$, and the 1:1 ordered *Pnma* (monoclinic P21/c= P121/n1) structure was found for $Ca_5Nb_2TiO_{12}$. Because of kinetic reasons, the 1:1 ordering was only weakly developed during continuous cooling for $Ca_5Nb_2TiO_{12}$ sintered at temperatures above 1500°C. The dramatic changes in dielectric properties for materials sintered at temperatures above 1500°C are clearly associated with the formation of the twin structure for both materials. Comparison of the dielectric properties of the two compounds and their type of ordering led to the conclusion that 1:2 ordering of $Ca_5Ta_2TiO_{12}$ results in higher τ_ε and lower ε_r, as compared to the 1:1+1:3 ordering of $Ca_5Nb_2TiO_{12}$. Such an effect of ordering was recently demonstrated for the $Ca(Ca_{1/3}Nb_{2/3})O_3$[13] polymorphs (having similar structure as that studied here) and the $(Sr_{1-x}Ba_x)(Sr_{1/3+y}Ta_{2/3-y})O_3$[38,39] system. The extreme chemical and microstructural complexity of the system, however, indicate that further analysis and characterization would be necessary to unambiguously associate the chemical and microstructural features with the dielectric properties, a correlation which has to date been made with very few members of this complex class of materials.

Investigations on the characterization of $Ca_5Nb_2TiO_{12}$ and $Ca_5Ta_2TiO_{12}$ ceramics at the microwave frequency range has not been tried though the materials were predicted as low loss at 1 MHz frequency[21]. However it is established[40,41] that at microwave frequencies pore eliminated dense specimen devoid of secondary phases yields better results. Keeping this in mind the synthesizing conditions of $Ca_5Nb_2TiO_{12}$ and $Ca_5Ta_2TiO_{12}$ ceramics were optimized for maximum densification and hence better microwave dielectric properties.

3.3 SYNTHESIS, CHARACTERIZATION AND MICROWAVE DIELECTRIC PROPERTIES OF $Ca(Ca_{1/4}B_{2/4}Ti_{1/4})O_3$ (B = Nb, Ta) and $Ca_5Nb_{2-x}Ta_xTiO_{12}$ CERAMICS

3.3.1 Experimental

$Ca(Ca_{1/4}B_{2/4}Ti_{1/4})O_3$ (B = Nb, Ta) and $Ca_5Nb_{2-x}Ta_xTiO_{12}$ ceramics were prepared by conventional solid-state ceramic route as described in Chapter 2 Section 2.1. Stoichiometric amounts of high purity $CaCO_3$, TiO_2 (99.99$^+$ %, Aldrich Chemical Company Inc., Milwaukee WI, USA), and Ta_2O_5/Nb_2O_5 (99.9$^+$ %, Nuclear Fuel Complex, Hyderabad, India) were weighed and ball milled using zirconia balls in distilled water medium for 24 h. The mixture was dried and calcined. The calcinations were carried out at temperatures in the range 1200-1400°C for 4 h. The calcined powders were again ground well for 1h in an agate mortar and then mixed with 5 wt % solution of poly vinyl alcohol (PVA) as the binder. The slurry was dried and ground again and pressed into cylindrical disks of diameter 14mm and height about 7mm under a pressure of 100MPa. The green pellets were preheated at 600°C for 1h to expel the binder and then sintered for 4 hrs at high temperatures in air. $Ca_5Nb_2TiO_{12}$ samples were sintered in the temperature range 1500-1600°C and $Ca_5Ta_2TiO_{12}$ in the range 1575-1650°C (Nabertherm Furnace, Model LHT 02/18, Lilienthal, Germany). The effect of different sintering durations were also studied. The sintered ceramic pucks were polished and their bulk density was measured using Archimedes method. The structure and phase purity was examined by powder X-Ray diffraction (XRD) method using CuKα radiation. The sintered samples were thermally etched at a temperature about 50°C below the sintering temperature of each sample and the surface morphology was investigated using scanning

electron microscopic technique. The microwave dielectric properties such as dielectric constant, unloaded quality factor and temperature variation of resonant frequency was measured by using an HP 8510 C Network analyzer attached with a sweep oscillator and test parameter unit employing resonance method[42, 43, 44] as explained in Section 2.3.2 to 2.3.5 of Chapter 2.

3.3.2 Results and Discussion

Fig. 3.1 shows the X- Ray diffraction patterns of $Ca_5Nb_2TiO_{12}$ and $Ca_5Ta_2TiO_{12}$ powdered ceramics. The patterns are similar for both materials with a slight shift in the position of peaks. Both these materials are having orthorhombic symmetry[21].

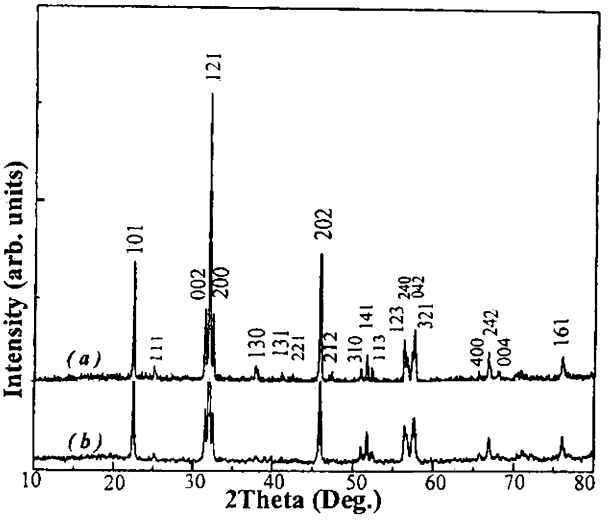

Fig. 3.1 X-Ray diffraction patterns of (a) $Ca_5Nb_2TiO_{12}$ and (b) $Ca_5Ta_2TiO_{12}$ ceramics

The lattice parameters for $Ca_5Nb_2TiO_{12}$ are a = 5.510(4)Å, b = 7.907(9)Å and c = 5.688(0)Å. The theoretical density of $Ca_5Nb_2TiO_{12}$ is calculated to be 4.19g/cm^3. The $Ca_5Ta_2TiO_{12}$ has a = 5.502(2)Å, b = 7.893(1)Å and c = 5.668(5)Å with theoretical density 5.41g/cm^3. The tolerance factor (t)[45] of ABO_3 structured ceramics are given by eqn. 3. 1. In

the case of $Ca_5B_2TiO_{12}$ (B= Nb, Ta) perovskite materials, the equation can be modified with the inclusion of three cations in the complex perovskite as,

$$t = \frac{R_{Ca} + R_O}{\sqrt{2}\{[R_{Ca}/4 + R_{Nb/Ta}/2 + R_{Ti}/4] + R_O\}} \tag{3.2}$$

where R denotes the radii of corresponding cations reported by Shannon[46]. The value was found to be the same for both materials and is equal to 0.8823, which is much less than that for an ideal cubic structure (t = 1). It is established that the microwave dielectric properties of ceramic materials strongly depend on the synthesizing conditions.

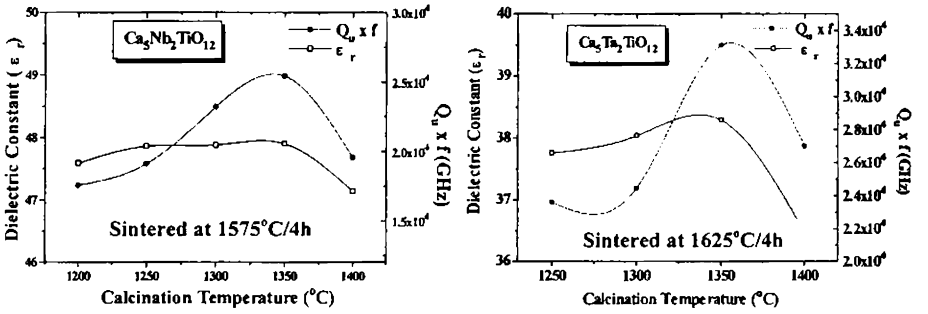

Fig. 3.2 Variation of ε_r and Q_u of $Ca_5B_2TiO_{12}$ (B = Nb, Ta) ceramics with calcination temperature

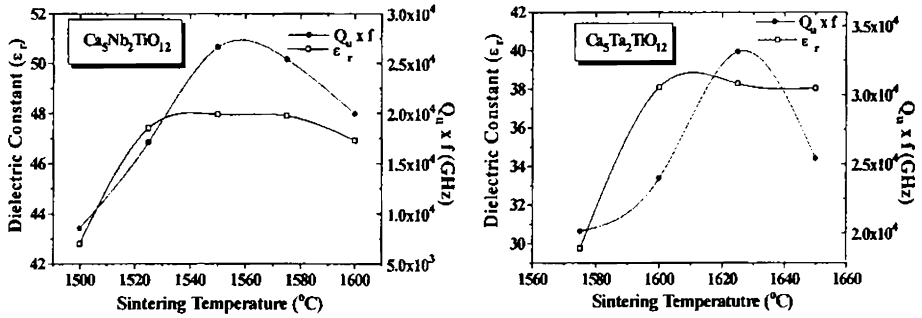

Fig. 3.3 Variation of ε_r and Q_u of $Ca_5B_2TiO_{12}$ (B = Nb, Ta) ceramics with sintering temperature

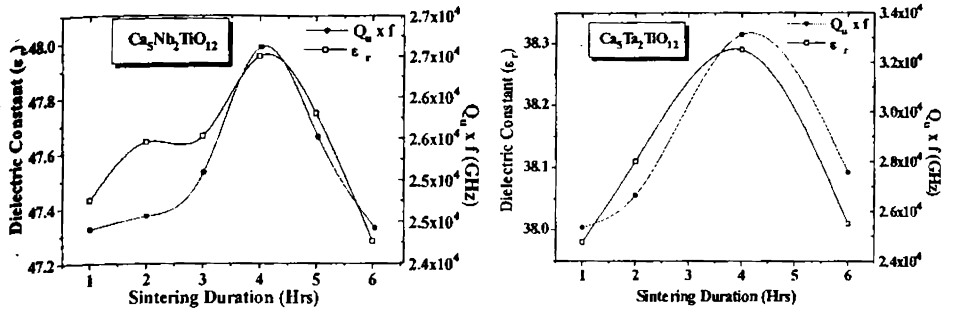

Fig. 3.4 Variation of ε_r and Q_u of $Ca_5B_2TiO_{12}$ (B = Nb, Ta) ceramics with sintering duration

With this view the calcination temperature, sintering temperature and their durations were optimized for $Ca_5Nb_2TiO_{12}$ and $Ca_5Ta_2TiO_{12}$ materials to get maximum density and best dielectric properties. The dependence of dielectric properties on the synthesizing conditions are depicted in the figures 3.2 to 3.4.

It is evident from Figs. 3.2 – 3.4 that the dielectric constant and quality factor increases with calcination and sintering temperature and with sintering duration up to a certain value of the latter and then decreased beyond the critical variable. The best density and dielectric properties of $Ca_5Nb_2TiO_{12}$ ceramics are at a calcination temperature of 1350°C/4h and sintering temperature of 1550°C/4h. In the case of $Ca_5Ta_2TiO_{12}$ ceramics the calcination temperature is the same as that of the niobates but the sintering temperature is 1625°C/4h. The maximum experimental density was obtained at optimum synthesizing conditions and the values were 4.06g/cm^3 and 5.26g/cm^3 for the niobates and tantalates respectively. In the optimized preparation conditions $Ca_5Nb_2TiO_{12}$ has ε_r = 48, $Q_u x f$ > 26000 GHz and τ_f = +40ppm/°C, whereas $Ca_5Ta_2TiO_{12}$ has ε_r = 38, $Q_u x f$ > 33000 GHz and τ_f = +10ppm/°C.

It has been reported that[47,48,49,50] in titanium based ceramics prolonged heating at a temperature slightly less than that of the sintering temperature will improve the density and dielectric properties. Hence we have annealed $Ca_5Nb_2TiO_{12}$ samples at a temperature of 1350°C/10h and followed by annealing at 1150°C for 15 h each. Similarly $Ca_5Ta_2TiO_{12}$ was annealed at 1450°C/10h and 1250°C for 15 h each. In both the cases for both materials no significant improvement in density or dielectric properties were observed. The density,

dielectric constant and Q_u decreased on annealing while τ_f increased slightly. The sintered samples were kept in boiling water for 2 h. There was no change in density, dielectric properties or in XRD pattern indicating excellent chemical and thermal stability of the material. The sintered samples were thermally etched and the microstructures were examined under SEM. No secondary phases can be observed (Fig. 3.6). Uniformly distributed grains of relatively large size up to 10 μm can be seen in figure.

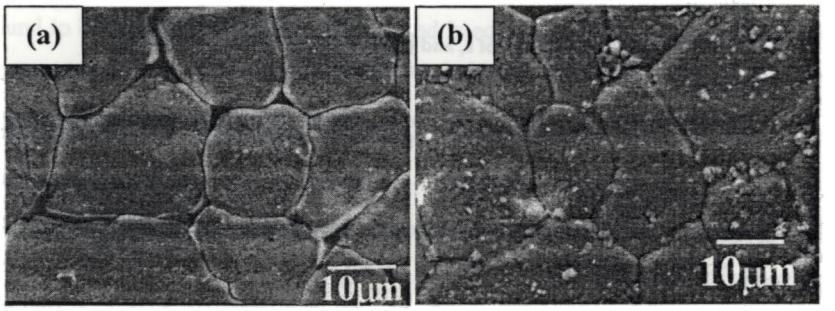

Fig. 3.6 Typical SEM photographs of (a) $Ca_5Nb_2TiO_{12}$ and (b) $Ca_5Ta_2TiO_{12}$ microwave ceramics

3.4 $Ca_5Nb_{2-x}Ta_xTiO_{12}$ [$0 \leq x \leq 2$] CERAMICS

The $Ca_5Nb_{2-x}Ta_xTiO_{12}$ [$0 \leq x \leq 2$] ceramics show intermediate dielectric properties between the end members $Ca_5Nb_2TiO_{12}$ and $Ca_5Ta_2TiO_{12}$ as in the case of perfect solid-solutions[51].

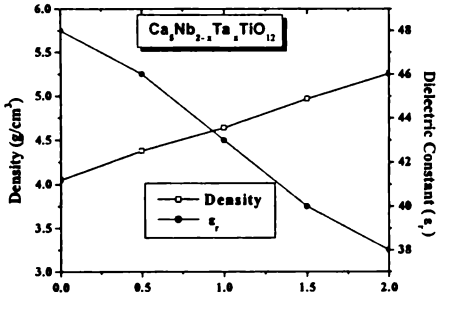

Fig. 3.7 Variation of density and ε_r of $Ca_5Nb_{2-x}Ta_xTiO_{12}$ ceramics with x.

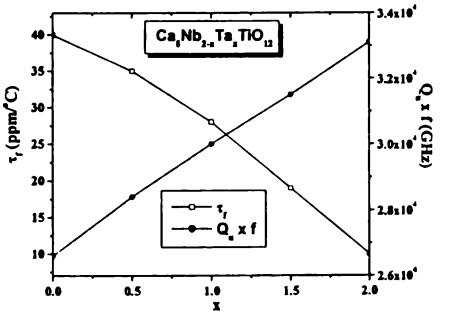

Fig. 3.8 Variation of τ_f and $Q_u \times f$ of $Ca_5Nb_{2-x}Ta_xTiO_{12}$ ceramics with x.

Since the ionic radii[46] and charge are the same for both Nb and Ta ions the $Ca_5Nb_{2-x}Ta_xTiO_{12}$ forms a complete range of solid solution for all values of x with properties changing linearly with x. The crystal symmetry was similar for all compositions with the orthorhombic structure like that of $Ca_5Nb_2TiO_{12}$ and $Ca_5Ta_2TiO_{12}$. Density and microwave dielectric properties are varying linearly between the title compounds for $x = 0$ to $x = 2$. Density increased with the amount of tantalum and can be attributed to the high molecular weight of Ta compared with Nb. Dielectric constant and τ_f was decreasing as x increases and the unloaded quality factor was increasing with the value of x (see Figs. 3.7 & 3.8). This variation can be attributed to the change in ionic polarizability[52] and cell volume.

3.5 EFFECT OF DOPANTS IN $Ca(Ca_{1/4}B_{2/4}Ti_{1/4})O_3$ (B = Nb, Ta) CRERAMICS

3.5.1 Introduction

Commercially available dielectric resonator materials for microwave applications show high Q_u and high ε_r, but need to be sintered at high temperatures for longer duration to attain better densification and thereby improved performance[53,54,55]. As it has been outlined earlier in section 3.4 of this chapter, best microwave dielectric properties of $Ca_5Nb_2TiO_{12}$ and $Ca_5Ta_2TiO_{12}$ ceramics were reported at a processing temperature of 1550°C and 1625°C respectively. The high sintering temperature of the ceramics also put constrain over their immediate use in practical applications. Several methods are proposed and investigated in literature, like (i) chemical synthesis[56,57,58] (ii) using raw materials with smaller particle size[59] and (iii) liquid phase sintering[60] by the addition of glassy materials, to decrease the sintering temperature and improve the dielectric properties of low loss materials. However each technique has got many disadvantages which precludes the industrial production of high quality DRs.[61] Doping of ceramics with suitable dopants[62,63,64,65,66] have been established as an effective tool for tuning the properties of microwave dielectric materials. Hence to explore the possibility of bringing down the sintering temperature and improving the densification and microwave dielectric properties, aliovalent and isovalent dopants were added to calcined $Ca_5Nb_2TiO_{12}$ and $Ca_5Nb_2TiO_{12}$ powders. A comprehensive investigation was made to study

the effect of various dopants of different ionic radii and valency on the densification, sinterability and dielectric properties of $Ca_5B_2TiO_{12}$ (B = Nb, Ta) ceramics.

3.5.2 Experimental

The $Ca_5B_2TiO_{12}$ (B = Nb, Ta) ceramics were prepared through conventional mixed oxide route as described in Section 2.1.2 of Chapter 2. Stoichiometric amount of high purity $CaCO_3$, TiO_2 and Ta_2O_5/Nb_2O_5 were used as the starting materials. The powder mixture was ball milled in distilled water medium using zirconia balls in a plastic container for 24h. The slurry was dried and the reaction mixture thus obtained was calcined at 1350°C/4h and the resultant crispy material was ground into very fine powder. The calcined $Ca_5B_2TiO_{12}$ (B = Nb, Ta) precursor was divided into several batches and different mole % of dopants were added to selected weight of the parent material. The oxides to be doped were categorized based on their high temperature stable valency. Accordingly different mole % of various dopants such as divalent (MgO, $MnCO_3$, ZnO, NiO, CuO & Co_3O_4), trivalent (In_2O_3, Al_2O_3, Cr_2O_3, Y_2O_3, Bi_2O_3, Ga_2O_3 & Dy_2O_3), tetravalent (ZrO_2, SnO_2, HfO_2), pentavalent (Sb_2O_3, V_2O_5) and hexavalent (WO_3 & MoO_3) were added to calcined powders of the parent materials. The resultant mixture was well ground in distilled water medium, dried and mixed with 4 wt. % Ploy Vinyl Alcohol (PVA) as binder, dried again and ground into very fine powder. Cylindrical ceramic pucks of 14 mm diameter and 6 - 7 mm height were formed under a uniaxial pressure of 100 MPa. Doped $Ca_5Nb_2TiO_{12}$ specimens were fired at an optimum temperature of 1550°C/4h, whereas the tantalates were sintered at 1625°C/4h. The sintered samples were well polished and their densities were measured by Archimedes methods. Phase purity of the materials was studied by powder X-Ray diffraction (XRD) analysis using CuKα radiation and microstructural analysis was done using scanning electron microscopic techniques. The dielectric properties Q_u, ε_r and τ_f of the materials were measured[42,43,44] in the microwave frequency range as described in Chapter 2, section 2.3.2 to 2.3.5.

It is to be noted that, dopants such as $MnCO_3$, Y_2O_3, Bi_2O_3, Ga_2O_3, Dy_2O_3, HfO_2, WO_3 & MoO_3 when added in 0 – 2 mole % to the parent $Ca_5B_2TiO_{12}$ (B = Nb, Ta) materials badly affected the densification and severely deteriorated their microwave dielectric

properties and hence the results are not described here. However the quality factor of $Ca_5B_2TiO_{12}$ (B = Nb, Ta) ceramics doped with 1 mole % of the above mentioned dopants are described in Fig. 3.22 to correlate ionic radius of the dopant with quality factor of the ceramics. We found a relationship between ionic radius of the dopant and average radius of the *B*-site ions in the parent complex perovskite material (discussed in a later section in this chapter) and only the dopants satisfying this condition were tried in different concentrations.

3.5.3 Results and Discussion

3.5.3.1 Phase Analysis

Pure $Ca_5Nb_2TiO_{12}$ and $Ca_5Ta_2TiO_{12}$ have an orthorhombic structure and belong to *Pnma* space group similar to $CaTiO_3$ ceramics and the Bragg reflections were indexed accordingly. $Ca_5B_2TiO_{12}$ (B = Nb, Ta) ceramics doped with small (0 to 1 mole %) amount of all dopants form phase pure materials and hardly any additional phases appeared in the XRD spectrum. Moreover a slight shift of maximum intensity peaks towards the higher angle region was observed with di-and tetravalent dopants and shifted to the opposite direction with the doping of pentavalent impurities (figure not shown). It indicates a possible partial substitution of smaller divalent ions[46] like Mg, Zn, Ni, Cu and Co for Ca^{2+}, Sn and Zr for Ti^{4+} and Sb or V in place of Nb/Ta^{5+} in the complex perovskite *B*-site of the material. However, higher (> 1 mole %) amount of doping developed secondary phases in both the materials as is evident from Figs. 3.8(a) and 3.8(b). The additional phases formed, their scan angles in the XRD spectrum and ICDD file numbers are listed in Table 3.1.

3.5.3.2 Densification and Microstructural Analysis

Fig. 3.9 (a) and 3.10 (a) represents the variation of percentage densification of $Ca(Ca_{1/4}B_{2/4}Ti_{1/4})O_3$ (B = Nb, Ta) dielectrics doped with divalent impurities such as MgO, ZnO, NiO, CuO & Co_3O_4. The densification was relatively high with 1 mole % doping of MgO, CuO and Co_3O_4. However these dopants in more than 1 mole % deteriorate the properties and lead to the formation of additional phases.

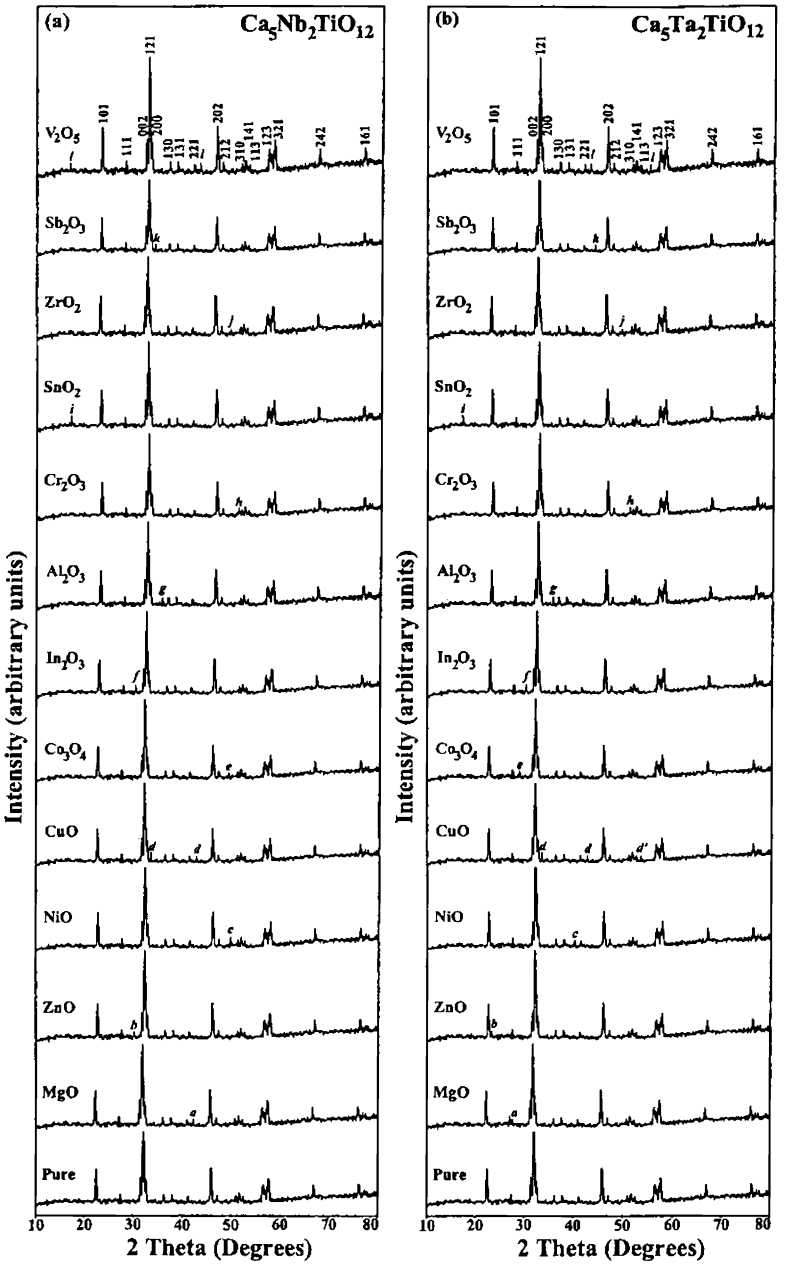

Fig. 3.8 XRD patterns of 2 mole % dopant added (a) $Ca_5Nb_2TiO_{12}$ and (b) $Ca_5Ta_2TiO_{12}$ ceramics (Italic letters denote the additional phases)

Table 3.1 Additional phases formed, their ICDD file numbers and positions when 2 mole % of various dopants were added to $Ca(Ca_{1/4}B_{2/4}Ti_{1/4})O_3$ [B = Nb, Ta] ceramics

Dopant	$Ca_5Nb_2TiO_{12}$			$Ca_5Ta_2TiO_{12}$		
	Additional phases	Scan angle 2θ (Degrees)	ICDD File Number	Additional phases	Scan angle 2θ (Degrees)	ICDD File Number
MgO	$MgNb_2O_{3.67}$	42.21	25 - 525	$MgTa_2O_6$	26.68	32 - 631
ZnO	$ZnNb_2O_6$	30.28	37 - 1371	$ZnTa_2O_6$	23.85	36 - 862
NiO	$NiNb_2O_6$	53.91	31 - 906	Ni_3TiO_5	42.27	30 - 865
CuO	CaCuO2	32.92, 43.49	46 – 54	$CaCuO_2$ $CuTa_2O_6$	32.92, 43.49 60.48	24 - 380
Co_3O_4	$Co_2Nb_5O_{14}$	52.25	42 - 422	Co_2TiO_4	29.95	39 - 1410
In_2O_3	$InNbO_4$	29.87	25 - 384	$InTaO_4$	29.46	33 - 625
Al_2O_3	$Ca_2Al_2O_5$	33	33 - 252	$Ca_2Al_2O_5$	33	33 - 252
Cr_2O_3	$CrNbO_4$	53.57	34 - 366	$CrTaO_4$	35.47	39 - 1428
SnO_2	$CaSnO_3$	17.38	34 - 939	$CaSnO_3$	17.38	34 - 939
ZrO_2	$CaZrO_3$	45.09	35 - 645	$CaZrO_3$	45.09	35 - 645
Sb_2O_3	$CaSb_2O_4$	19.12	29 - 292	$Ca_3Sb_2O_6$	43.49	20 - 209
V_2O_5	$V_2Nb_6O_{20}$	17.95,43.93	33 - 1438	$VTaO_4$	35.2, 52.90	24 - 1261

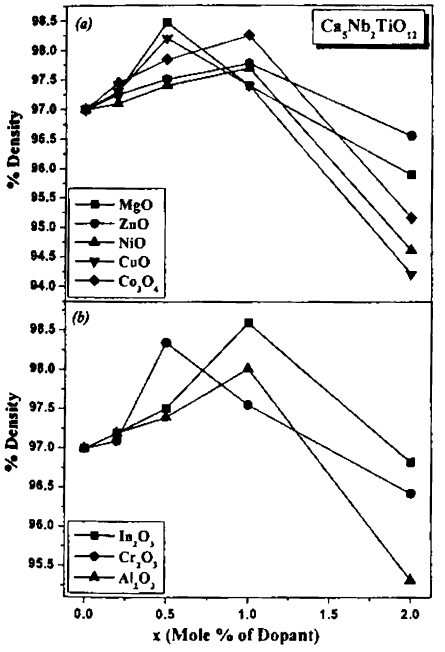

Fig. 3.9 Percentage densification of 0 – 2 mole % (a) divalent and (b) trivalent dopant added $Ca_5Nb_2TiO_{12}$ ceramics

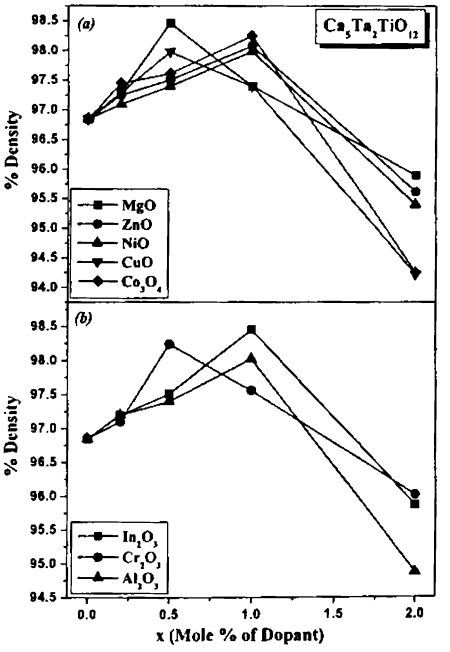

Fig. 3.10 Percentage densification of 0 – 2 mole % (a) divalent and (b) trivalent dopant added $Ca_5Ta_2TiO_{12}$ ceramics

Trivalent dopants like In_2O_3, Al_2O_3 and Cr_2O_3 have slightly improved the densities of $Ca(Ca_{1/4}B_{2/4}Ti_{1/4})O_3$ (B = Nb, Ta) ceramics as seen in Fig. 3.9 (b) and 3.10 (b). It can be seen that the percentage densification is least for Al_2O_3 dopant, which is due to the poor sinterability of the ceramic. Similarly with tetravalent SnO_2 a densification of more than 98% was reached with 1 mole % of the dopant whereas with ZrO_2 a gradual decrease in the density was observed [See Figs. 3.11(a) and 3.12 (a)] and it was obviously due to poor sinterability of the ceramic owing to the very high sintering temperature of ZrO_2-based materials[67]. In the case of 0.2 to 2 mole % of ZrO_2 doping, sintering temperature of the ceramics were increased by 50°C compared with that of the pure material to attain maximum density.

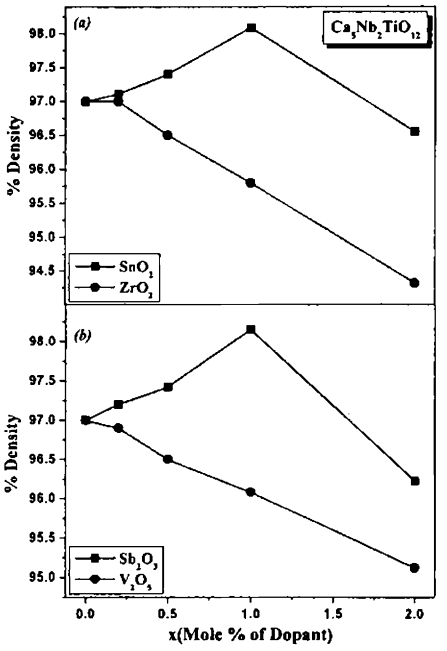

Fig. 3.11 Percentage densification of 0 – 2 mole % (a) tetravalent and (b) pentavalent dopant added $Ca_5Nb_2TiO_{12}$ ceramics

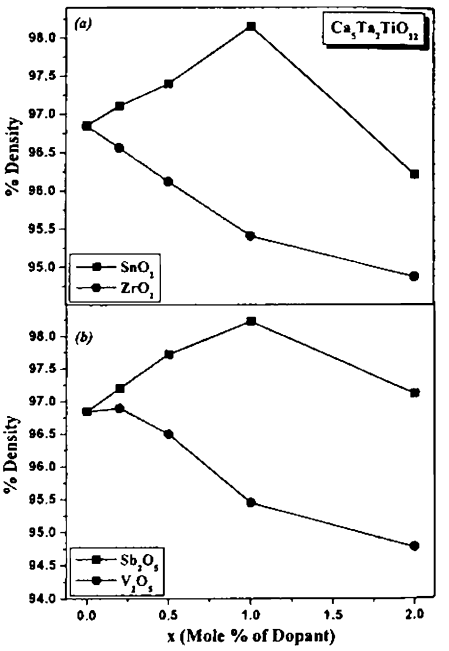

Fig. 3.12 Percentage densification of 0 – 2 mole % (a) tetravalent and (b) pentavalent dopant added $Ca_5Ta_2TiO_{12}$ ceramics

The variation of percentage densification as a function of mole % of the pentavalent dopants (Sb_2O_3 and V_2O_5) are shown in Figs. 3.11 (b) and 3.12 (b). The percentage density of $Ca(Ca_{1/4}B_{2/4}Ti_{1/4})O_3$ [B = Nb, Ta] ceramics reached about 98.5% with 1 mole % doping of Sb_2O_3. It was reported[68] that at high temperatures, Sb_2O_3 provides an ideal wetting medium for vitreous sintering to enhance densification. Recently Huang *et al.* reported[69] an increase in density and improved dielectric properties with V_2O_5 doping on $Ba(Mg_{1/3}Ta_{2/3})O_3$ complex perovskites. But we found that doping of V_2O_5 in $Ca(Ca_{1/4}B_{2/4}Ti_{1/4})O_3$ [B = Nb, Ta] ceramics deteriorate the density and dielectric properties.

The surface morphology of pure $Ca_5Nb_2TiO_{12}$ and $Ca_5Ta_2TiO_{12}$ has described in Section 3.3.2 of this Chapter. Fig. 3.13 shows the microstructural evolution of two typical doped $Ca(Ca_{1/4}B_{2/4}Ti_{1/4})O_3$ (B = Nb, Ta) ceramic samples. It was found that the addition of 0.5 mole % of Cr_2O_3 into the $Ca_5Nb_2TiO_{12}$ material has resulted in better densification characteristics as seen from Fig. 3.13 (a). The grains were up to 5 μm in size. The surface micrograph presented a well packed grain structure with relatively smaller grains.

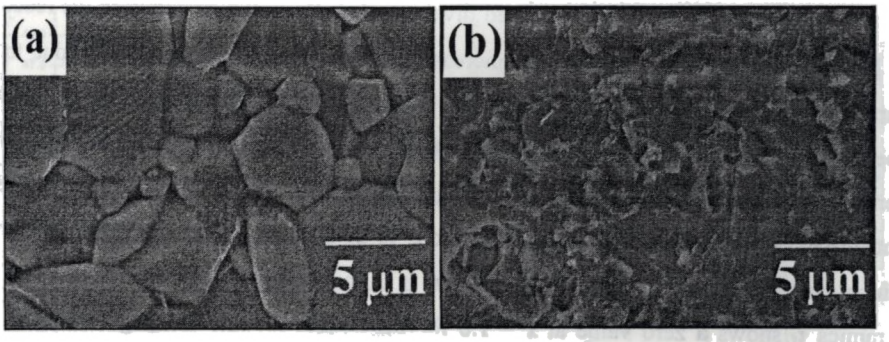

Fig. 3.13 SEM pictures of (a) 0.5 mole % Cr_2O_3 doped $Ca_5Nb_2TiO_{12}$ and (a) 2 mole % ZnO doped $Ca_5Ta_2TiO_{12}$ ceramics

It is due to the dopant action to control the particle coarsening and thereby enhancing densification[70]. Fig. 3.13 (b) represents the surface morphology of $Ca_5Ta_2TiO_{12}$ samples doped with 2 mole % ZnO. Addition of ZnO promoted liquid phase sintering as they melt at a temperature much lower than 1625°C. But due to the insufficient wetting of the matrix, the densification remained poor in this case. More over the ZnO evaporation[71] has left out porosity between the grains which in turn lead to poor dielectric properties.

3.5.3.3 Microwave Dielectric Properties

3.5.3.3.1 Divalent dopants

As described in Section 3.3.2 of this Chapter, $Ca_5Nb_2TiO_{12}$ has ε_r = 48, $Q_u \times f >$ 26000 and τ_f = + 40 ppm/°C, when sintered at 1550°C/4h. The $Ca_5Ta_2TiO_{12}$ has ε_r = 38, $Q_u \times f$ > 33000 and τ_f = +10 ppm/°C at a sintering temperature of 1625°C/4h. Fig. 3.14 & 3.15 shows microwave dielectric properties of $Ca_5Nb_2TiO_{12}$ and $Ca_5Ta_2TiO_{12}$ complex perovskites doped with divalent dopants such as MgO, ZnO, NiO, CuO and Co_3O_4. In both the niobates and tantalate materials, ε_r showed a gradual decrease with dopant concentration. It is known that ionic polarizability[56] is the major factor contributing towards the ε_r of the dielectric material. Accordingly ions with higher polarizability should have high ε_r. Ionic polarizabilities of the dopant cations Mg, Zn, Ni, Cu and Co are 1.32, 2.04, 1.23, 2.11 and 1.652 respectively and which is much less than that of divalent calcium (3.16). The possible substitution of divalent dopant for Ca^{2+} will thus cause a resultant decrease in ionic polarizability[52] and hence a reduction in ε_r.

The decrease in ε_r with increased divalent concentration also supports the reduction in lattice parameter, cell volume and increased X-Ray density which may be due to the partial substitution of smaller dopant ions for bigger Ca^{2+} ions. Variation of the temperature coefficient of resonant frequency in $Ca_5B_2TiO_{12}$ (B = Nb, Ta) ceramics as a function of mole percent of divalent dopants is depicted in Fig. 3.14 & 3.15. As is clear from the figures in both cases, τ_f decreased with increase in mole % of dopants except for CuO addition in which case it behaved in the reverse manner. It is interesting to note that in $Ca_5Ta_2TiO_{12}$ ceramics τ_f shows a zero value at x = 1.6 for Co_3O_4 and x = 1.7 for MgO addition. The variation of quality factor with mole % of divalent dopants in $Ca_5Nb_2TiO_{12}$ and $Ca_5Ta_2TiO_{12}$ ceramics are depicted in Figs. 3.14 and 3.15 respectively.

Consistent with the increased densification, 0.5 mole% MgO and CuO doped $Ca_5Nb_2TiO_{12}$ has a $Q_u \times f$ = 33000 GHz and 30000 GHz, where as doping of 1 mole % each ZnO, NiO and Co_3O_4 increased the $Q_u \times f$ to 28000 GHz, 29000 GHz and 31000 GHz respectively. On the other hand the quality factor of $Ca_5Ta_2TiO_{12}$ reached a maximum of more than 40000 GHz and 38000 GHz with 0.5 mole % doping of MgO and CuO

respectively. The doping of 1 mole % ZnO, NiO and Co_3O_4 increased the Q_u x f of $Ca_5Ta_2TiO_{12}$ ceramics to reach 39000 GHz, 38000 GHz and 38500 GHz respectively. Doping of more than 1 mole % divalent dopants was detrimental to the quality factor of $Ca_5B_2TiO_{12}$ (B = Nb, Ta) ceramics as they form additional phases. Out of the 5 divalent dopants investigated, MgO and Co_3O_4 were found to be more effective because they improved both $Q_u x f$ and τ_f of $Ca_5B_2TiO_{12}$ (B = Nb, Ta) ceramics.

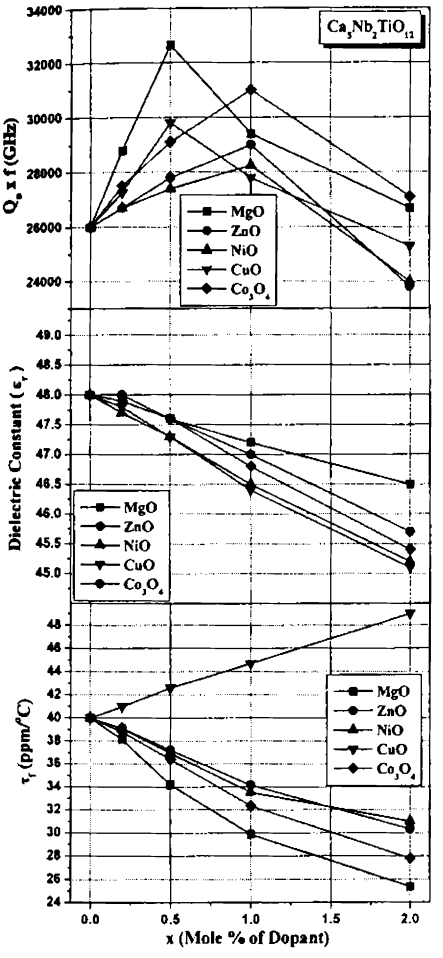

Fig. 3.14 Microwave dielectric properties of 0 – 2 mole % divalent dopant added $Ca_5Nb_2TiO_{12}$ ceramics

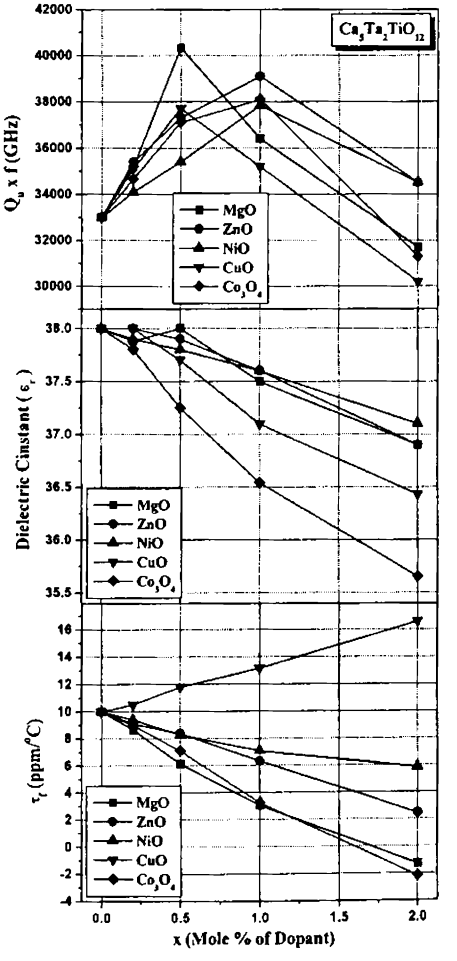

Fig. 3.15 Microwave dielectric properties of 0 – 2 mole % divalent dopant added $Ca_5Ta_2TiO_{12}$ ceramic

3.5.3.3.2 Trivalent dopants

The microwave dielectric properties of $Ca_5Nb_2TiO_{12}$ and $Ca_5Ta_2TiO_{12}$ ceramics with dopants of oxidation state 3 are shown in Fig. 3.16 & 3.17. Doping with 1 mole % of In_2O_3 and Cr_2O_3 increased the ε_r of $Ca_5Nb_2TiO_{12}$ by 2 %. In $Ca_5Ta_2TiO_{12}$ ceramics the same dopants in same quantity increased ε_r from 38 to 39 (2.6 % increase). The quality factor of both the ceramics also showed the same trend as exhibited in ε_r.

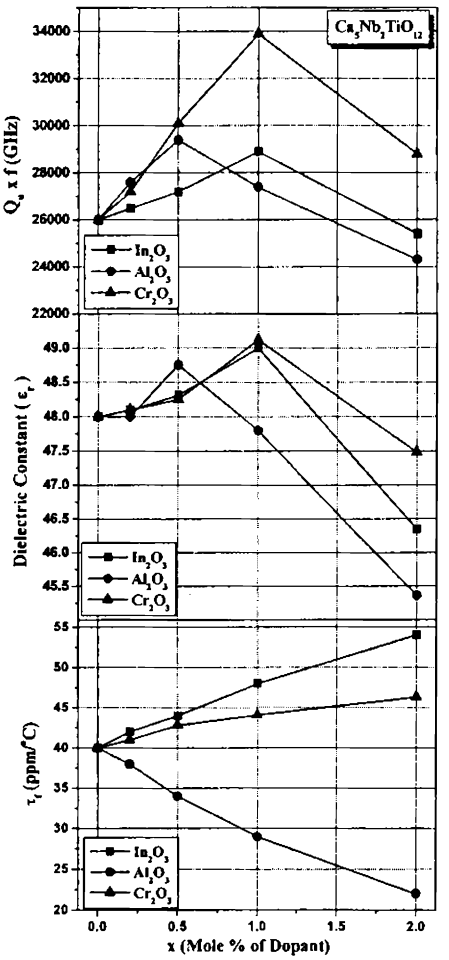

Fig. 3.16 Microwave dielectric properties of 0 – 2 mole % trivalent dopant added $Ca_5Nb_2TiO_{12}$ ceramics

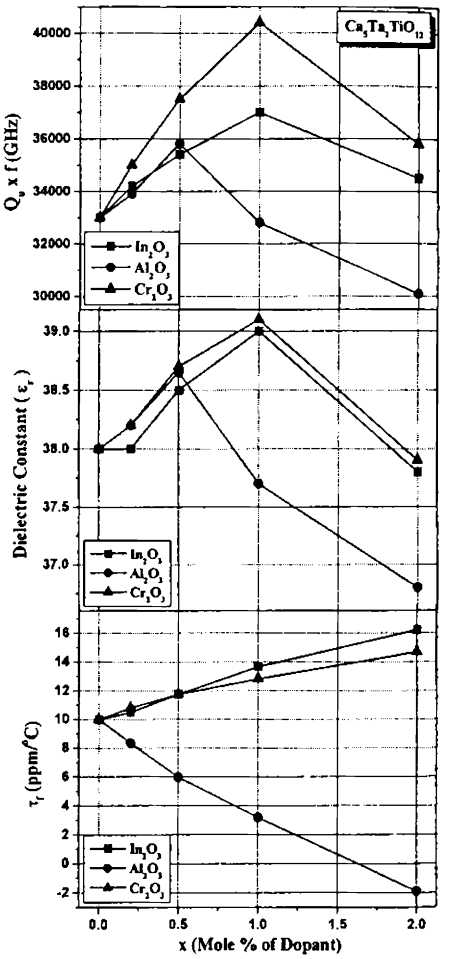

Fig. 3.17 Microwave dielectric properties of 0 – 2 mole % trivalent dopant added $Ca_5Ta_2TiO_{12}$ ceramics

The quality factor of $Ca_5Nb_2TiO_{12}$ ceramics reached as high as 34000 GHz (31 % increase) with 1 mole % doping of Cr_2O_3 whereas with 1 mol % In_2O_3, $Q_u \times f$ = 29000 GHz and the same value was observed with 0.5 % Al_2O_3 doping. $Ca_5Ta_2TiO_{12}$ ceramics doped with 1 mole % each of Cr_2O_3 and In_2O_3 has $Q_u \times f$ = 40500 GHz and 37000 GHz respectively. 0.5 mole % addition of Al_2O_3 could produce 10 % increase in the quality factor of $Ca_5Nb_2TiO_{12}$ and $Ca_5Ta_2TiO_{12}$ ceramics.

The increase observed in the value of ε_r and Q_u of both the ceramics can be attributed to the improvement in densification. With higher concentration of dopant ions, the measured dielectric constant and quality factor decreased which are due to high temperature phenomena like abnormal grain growth and formation of additional phases. The temperature coefficient of resonant frequencies of $Ca_5Nb_2TiO_{12}$ and $Ca_5Ta_2TiO_{12}$ ceramics as a function of mole % of trivalent dopants is given in Figs. 3.16 and 3.17 respectively. Except for Al_2O_3, the τ_f of doped samples shifted towards the high positive values. Since Al_2O_3 being a negative τ_f dielectric resonator[72] the fall in τ_f with this dopant was expected. In $Ca_5Ta_2TiO_{12}$ doping of 1.65 mole % Al_2O_3 tune the $\tau_f \approx 0$ ppm/°C. It is evident that out of the three trivalent dopants studied, Cr_2O_3 increased ε_r and Q_u but deteriorated the τ_f, whereas Al_2O_3 improved τ_f but with relatively less improvement in ε_r and Q_u of $Ca(Ca_{1/4}B_{2/4}Ti_{1/4})O_3$ [B = Nb, Ta] ceramics.

3.5.3.3.3 Tetravalent dopants

Variation of microwave dielectric properties of $Ca(Ca_{1/4}B_{2/4}Ti_{1/4})O_3$ [B = Nb, Ta] ceramics with the doping of different mole % of tetravalent dopants (SnO_2 and ZrO_2) are shown in Figs. 3.18 and 3.19. ε_r of both the ceramics increased with SnO_2 concentration for 0 to 1 mole % and then decreased for higher percentage due to the formation of additional phases. The increase in ε_r with Sn^{4+} having lesser polarizability (2.83) than that of Ti^{4+} (2.93) is contradictory to the relation between polarizability and ε_r. However it is believed that improvement in densification of $Ca(Ca_{1/4}Nb_{2/4}Ti_{1/4})O_3$ and $Ca(Ca_{1/4}Ta_{2/4}Ti_{1/4})O_3$ ceramics with SnO_2 doping contribute more towards the ε_r, which hides the effect of small difference in polarisability[56] between the two ions. An increase in ε_r was expected with Zr^{4+} of ploarizability (3.25) which is higher than that of Ti^{4+}. However ε_r of $Ca(Ca_{1/4}Nb_{2/4}Ti_{1/4})O_3$

and $Ca(Ca_{1/4}Ta_{2/4}Ti_{1/4})O_3$ showed a linear decrease with increase in mole % of Zr^{4+} doping and is assumed to be due to the poor sinterability and densification of the specimens. The investigations revealed that 1 mole % doping of SnO_2 in $Ca(Ca_{1/4}Nb_{2/4}Ti_{1/4})O_3$ and $Ca(Ca_{1/4}Ta_{2/4}Ti_{1/4})O_3$ ceramics showed an improvement of 7 % in $Q_u \, x \, f$ and which is due to increased densification of the samples. With ZrO_2 doping, poor densification of the ceramics lead to a linear decrease in the quality factor with increased dopant concentration.

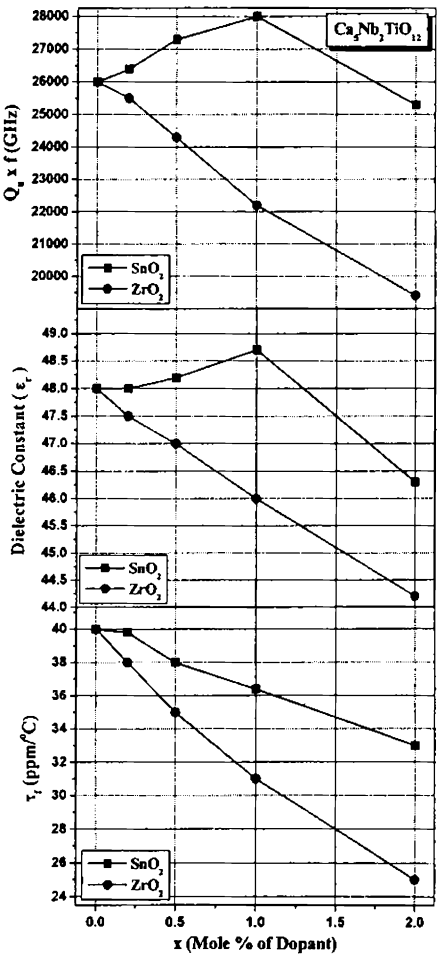

Fig. 3.18 Microwave dielectric properties of 0 – 2 mole % tetravalent dopant added $Ca_5Nb_2TiO_{12}$ ceramics

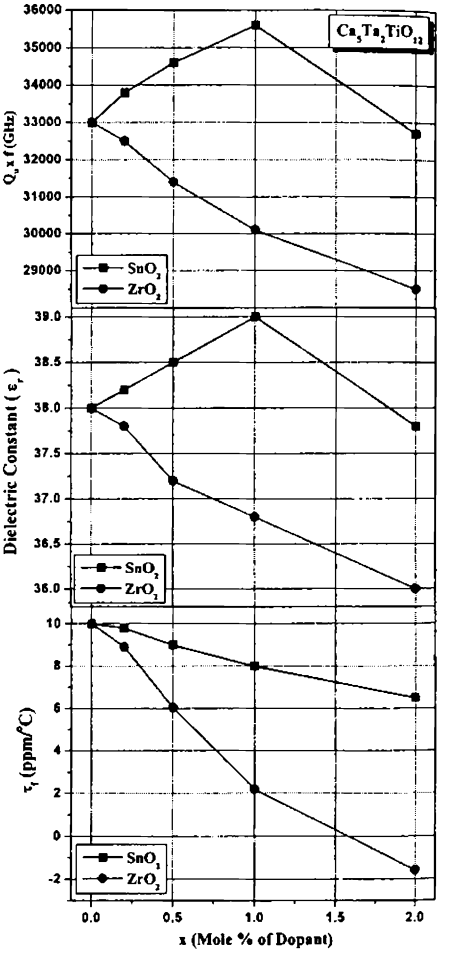

Fig. 3.19 Microwave dielectric properties of 0 – 2 mole % tetravalent dopant added $Ca_5Ta_2TiO_{12}$ ceramics

The τ_f of $Ca(Ca_{1/4}Nb_{2/4}Ti_{1/4})O_3$ specimens decreased from +40 to +33 ppm/°C and that of $Ca(Ca_{1/4}Ta_{2/4}Ti_{1/4})O_3$ ceramics decreased from +10 to + 6ppm/°C with the doping of 0 to 2 mole % SnO_2. This observation is consistent with a previous report of Matsumoto[73] in $Ba(Mg_{1/3}Ta_{2/3})O_3$ ceramics. Doping of ZrO_2 on $Ca(Ca_{1/4}Nb_{2/4}Ti_{1/4})O_3$ specimens in 0 to 2 mole % yielded dielectric resonator materials with τ_f ranging from +40 to +24 ppm/°C, whereas with $Ca(Ca_{1/4}Ta_{2/4}Ti_{1/4})O_3$ the value varied from +10 to -2 ppm/°C. It is worthwhile to note that the doping of 1.6 mole % ZrO_2 in $Ca_5Ta_2TiO_{12}$ lead to temperature stable dielectric resonator. The modification of τ_f in $Ca(Ca_{1/4}B_{2/4}Ti_{1/4})O_3$ [B = Nb, Ta] ceramics with doping of SnO_2 and ZrO_2 was believed to be due to the possible partial substitution of the dopant for tetravalent Ti^{4+} ions.

3.5.3.3.4 Pentavalent dopants

The microwave dielectric properties of $Ca(Ca_{1/4}Nb_{2/4}Ti_{1/4})O_3$ and $Ca(Ca_{1/4}Ta_{2/4}Ti_{1/4})O_3$ ceramics with 0 to 2 mole % pentavalent dopants (Sb_2O_3 and V_2O_5) are depicted in Fig. 3.20 and 3.21 respectively. It is evident from the figures that the doping of 0 to 1 mole % of Sb_2O_3 increased the ε_r to reach a maximum of 49 for the niobates and 39 for the tantalate material and then decreased for 2 mole % of the dopant. The substitution of Sb^{5+} with higher polarizability (4.27) than niobium (3.97) and increased density of the ceramic has contributed to the enhanced dielectric constant. On the other hand substitution of Sb^{5+} with lesser polarizability than Ta^{5+} (4.73), still increased the ε_r of Sb_2O_3 doped $Ca(Ca_{1/4}Ta_{2/4}Ti_{1/4})O_3$ samples. Improved experimental density (more than 98%) of the specimens was assumed to be the reason behind this effect. The measured dielectric constant showed a decrease with increase in V_2O_5 concentration. This is due to the substitution of a less polarizable V^{5+} ion (polarizability = 2.92) at the Nb/Ta site with higher polarizability. Moreover the percentage densification of $Ca(Ca_{1/4}Nb_{2/4}Ti_{1/4})O_3$ and $Ca(Ca_{1/4}Ta_{2/4}Ti_{1/4})O_3$ ceramics with V_2O_5 doping was very poor which also reduced ε_r of the samples. The quality factor of $Ca_5Nb_2TiO_{12}$ and $Ca_5Ta_2TiO_{12}$ ceramics showed 20 % and 14 % increase respectively with 1 mole % doping of Sb_2O_3 and the values decreased with 2 mole % of the dopant due to the existence of additional phases in the doped materials.

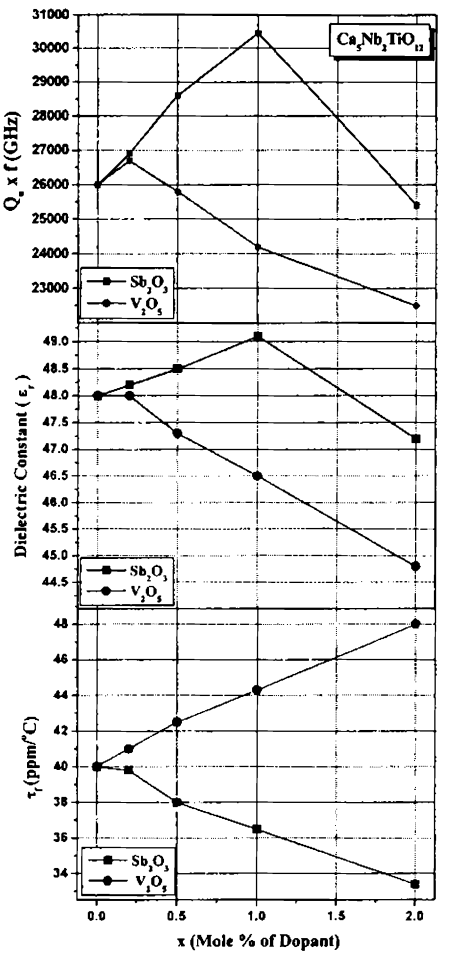

Fig. 3.20 Microwave dielectric properties of 0 – 2 mole % pentavalent dopant added $Ca_5Nb_2TiO_{12}$ ceramics

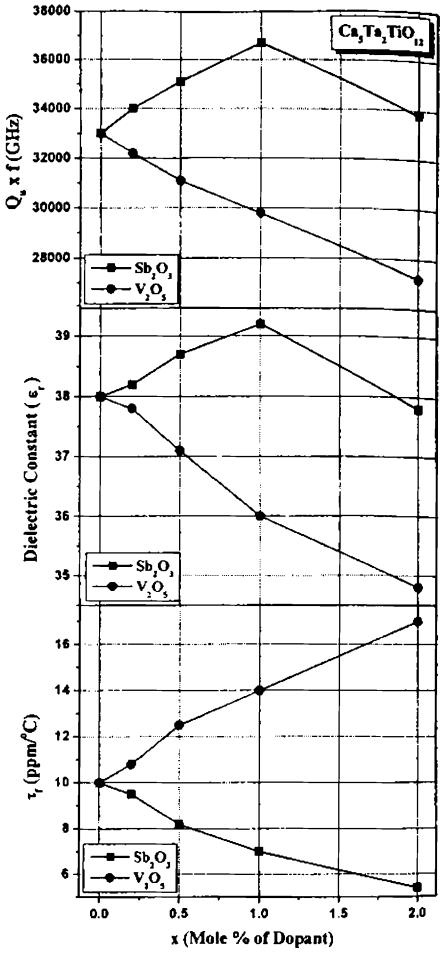

Fig. 3.21 Microwave dielectric properties of 0 – 2 mole % pentavalent dopant added $Ca_5Ta_2TiO_{12}$ ceramics

The quality factor of 0 to 2 mole % V_2O_5 doped ceramics showed an inverse relation with dopant concentration and is due to the poor sinterability and densification of the matrix with this dopant. The τ_f increased monotonously with increase in the V_2O_5 content in $Ca_5Nb_2TiO_{12}$ and $Ca_5Ta_2TiO_{12}$ ceramics. This coincides with a recent observation[62] that, temperature coefficient of resonant frequency increases with V_2O_5 doping. On the other hand τ_f of Sb_2O_3 doped $Ca_5Nb_2TiO_{12}$ and $Ca_5Ta_2TiO_{12}$ specimens decreases with mole % of the

dopant. Accordingly the τ_f of $Ca_5Nb_2TiO_{12}$ decreased from +40 to +33ppm/°C and that of $Ca_5Ta_2TiO_{12}$ specimens varied from +10 to +5 ppm/°C.

Fig. 3.22 shows the variation of quality factor of $Ca_5Nb_2TiO_{12}$ and $Ca_5Ta_2TiO_{12}$ ceramics doped with 1 mole % of different dopants as a function of ionic radii of the dopants. The average *B*-site ionic radius of $Ca(Ca_{1/4}Nb_{2/4}Ti_{1/4})O_3$ and $Ca(Ca_{1/4}Ta_{2/4}Ti_{1/4})O_3$ are the same and is equal to 0.7213 Å. The ionic radius of the dopants at a coordination number of 6 is taken since the investigated dopants (di-, tri-, tetra- and pentavalent dopants can possibly get substituted in the *B*-site of $Ca(Ca_{1/4}B_{2/4}Ti_{1/4})O_3$ [B = Nb, Ta] complex perovskites. In general when the ionic radii of the dopants are between 0.65 to 0.75 Å (i.e. close to the average ionic radii of the *B*-site ion in $Ca(Ca_{1/4}B_{2/4}Ti_{1/4})O_3$ [B = Nb, Ta] ceramics, the quality factor reached maximum values. However Mn^{2+}, Hf^{4+} and Zr^{4+} doping (0 to 2 mole %) has lowered the $Q_u \times f$, even though ionic radius of the dopants were comparable to that of the average *B*-site ionic radius of the parent materials.

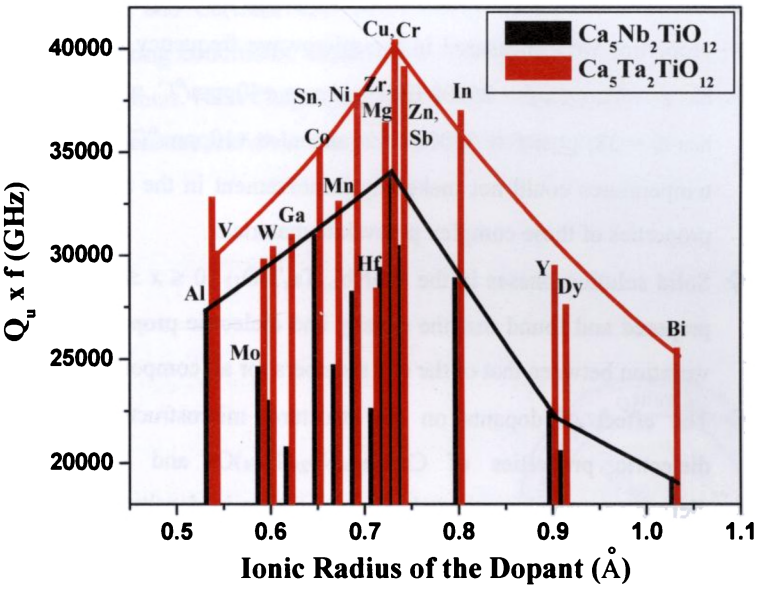

Fig. 3.22 Plot of ionic radius of dopant versus quality factor of 1 mole % doped $Ca_5Nb_2TiO_{12}$ and $Ca_5Ta_2TiO_{12}$ ceramics.

At the same time doping of Al^{3+} and In^{3+} improved the quality factor, though their ionic radius markably deviate from the average *B*-site ionic radius of $Ca(Ca_{1/4}B_{2/4}Ti_{1/4})O_3$ [B = Nb, Ta] ceramics. A similar observation was recently reported[65,74] in $Ba(Zn_{1/3}Ta_{2/3})O_3$ and $Ba(Mg_{1/3}Ta_{2/3})O_3$ ceramics and the $Q_u x f$ improved when the ionic radius of the dopant was close to the average *B*-site ionic radius of the complex perovskite material.

3.6 CONCLUSIONS

- $Ca_5Nb_2TiO_{12}$ and $Ca_5Ta_2TiO_{12}$ ceramics were prepared as single phase materials by conventional solid state ceramic route. The complex perovskite materials with an unusual occupancy of three cations in the *B*-site have orthorhombic symmetry and belong to *Pnma* space group. To the best of our knowledge these are the only dielectric resonator materials reported in literature with the mixing of three cations in the complex perovskite *B*-site.
- The synthesizing conditions of the ceramics were optimized and dielectric properties were measured in the microwave frequency range. $Ca_5Nb_2TiO_{12}$ has $\varepsilon_r = 48$, $Q_u x f > 26000$ GHz and $\tau_f = +40$ppm/°C, whereas $Ca_5Ta_2TiO_{12}$ has $\varepsilon_r = 38$, $Q_u x f > 33000$ GHz and $\tau_f = +10$ppm/°C. Annealing at lower temperatures could not make any improvement in the microwave dielectric properties of these complex perovskite materials.
- Solid solution phases in the $Ca_5Nb_{2-x}Ta_xTiO_{12}$ ($0 \leq x \leq 2$) system has been prepared and found that the density and dielectric properties shows a linear variation between that of the end members for all compositions.
- The effect of dopants on the structure, microstructure and microwave dielectric properties of $Ca(Ca_{1/4}Nb_{2/4}Ti_{1/4})O_3$ and $Ca(Ca_{1/4}Ta_{2/4}Ti_{1/4})O_3$ dielectrics were investigated. Slight increase in density was found with the addition of MgO, ZnO, NiO, CuO, Co_3O_4, Cr_2O_3, In_2O_3, SnO_2 and Sb_2O_3. Divalent dopants in general, trivalent Cr_2O_3, In_2O_3 and pentavalent Sb_2O_3 were identified as the efficient candidates for improving the microwave dielectric properties of $Ca(Ca_{1/4}Nb_{2/4}Ti_{1/4})O_3$ and $Ca(Ca_{1/4}Ta_{2/4}Ti_{1/4})O_3$ ceramics.

- ❖ Increase in ε_r and $Q_u \times f$ of $Ca(Ca_{1/4}B_{2/4}Ti_{1/4})O_3$ [B = Nb, Ta] dielectrics were attained with up to 1 mole % addition of these dopants. All the dopants mentioned above except CuO and Cr_2O_3 reduced the τ_f of both the parent materials. Temperature stable dielectric resonators were obtained with the addition of about 1.6 mole % each of MgO, Co_3O_4, Al_2O_3 and ZrO_2 to $Ca(Ca_{1/4}Ta_{2/4}Ti_{1/4})O_3$ material.
- ❖ A correlation between the radius of the dopant ion and quality factor of the parent materials were established. It was found that dopants with ionic radii comparable to that of the average *B*-site radius of the perovskite structure became more efficient in improving the microwave dielectric properties of $Ca(Ca_{1/4}Nb_{2/4}Ti_{1/4})O_3$ and $Ca(Ca_{1/4}Ta_{2/4}Ti_{1/4})O_3$ ceramics.

In this Chapter we have introduced two novel microwave dielectrics in $Ca(Ca_{1/4}Nb_{2/4}Ti_{1/4})O_3$ and $Ca(Ca_{1/4}Ta_{2/4}Ti_{1/4})O_3$ compositions and described the effect of factors like synthesizing conditions, dopants etc. which controls the microwave dielectric properties of the ceramics. Next Chapter will throw light into the influence of glass additives on the sintering temperature and dielectric properties of the reported ceramics.

3.7 REFERENCES

[1] W. Wong-Ng, T. Holesinger, G. Riley, and R. Guo (Eds), *Perovskite Oxides for Electronic Energy Conversion, and Energy Efficiency Applications*, Ceramic Transactions, 104, American Ceramic Society, Westerville, USA (2000).

[2] M.J. Rosseinsky, Materials Network on Perovskite Oxides, http://www.ssci.liv.ac.uk/~perox/ perovskiteintro.html

[3] C. N. R. Rao, J. Gopalakrishnan, K.Vidyasagar, *Indian J. Chem. Sect.* **A 23A** (1984) 265.

[4] D. M. Smyth, *Annu. Rev. Mater. Sci.* **15** (1985) 329.

[5] D. M. Smyth, *Properties and Applications of Perovskite-Type* Oxides; L. G. Tejuca, J. L. G. Fierro, Marcel Dekker: New York, 1993; p. 47.

[6] V. M. Goldschmidt, *Skr. Nor. Viedenk.-Akad., Kl. I: Mater.- Naturvidensk.* Kl. No. 8. (1926).

[7] H. D. Megaw, *Proc. Phys. Soc.* **58** (1946)133.

[8] F. S. Galasso, *Structure, properties and preparation of perovskite type compounds,* Pergamon press, Oxford, London, 1969.

[9] C. P. Khattak, F. F. Y. Wang, *Handbook of the Physics and Chemistry of Rare Earths*; Eds.; K. A. Gschneider Jr.and L.Eyring, North-Holland Publisher: Amsterdam, 1979; p 525.

[10] J. B. Goodenough and J. M. Longo, *Landolt-Bronstein New Series*; Hellwege, K. H., Helwege, A. M., Eds.; Springer-Verlag: Berlin;Vol. 4, part A, p. 126.

[11] J. B. Goodenough, *Solid State Chemistry;* Ed. C. N. R. Rao, Marcel Dekker: New York, 1974; p 215. **55** (1982) 394

[12] R. Roy, *J. Am. Ceram. Soc.* **37** (1954) 581-84.

[13] F.S. Galasso, J. R. Barrante and Lewis Katz, *J. Am. Chem. Soc.* **83** (1961) 2830-32.

[14] F. S. Galaso, W. Darby, *J. Phys. Chem.* **67** (1962) 1451.

[15] F. S. Galaso, L. Katz, R. Ward, *J. Amer. Ceram. Soc.* **81**(1959) 820.

[16] F. S. Galaso, J. Pyle, *J. Phys. Chem.* **67** (1963) 1561.

[17] J. A. Alonso, E. Mzayek and I. Rasines, *Mater. Res. Bull.* **22** (1987) 69.

[18] I. S. Kim, T. Nakamura, M. Itoh and Y. Inaguma, *Mater. Res. Bull.* **28** (1993) 1029.

[19] Y. Ozaki, M. Ghedira, J. Chenavas, J. C. Joubert and M. Marezio, *Acta. Cryst.* **B33** (1977) 3613.

[20] B. Bochu, M. N. Deschizeaux, J. C. Joubert, A. Collomb, J. Chenavas amd M. Marzeio, *J. Sol. State Chem.* **29** (1979) 291.

[21] R. J. Cava, J. J. Krajewski and R. S. Roth, *Mater. Res. Bull.* **34** (1999) 355.

[22] Internet data, URL: http://www.lsbu.ac.uk/dielectric-materials

[23] S. Kucheiko and D-H Yeo, *J. Am. Ceram. Soc.* **85** (2002) 1327.

[24] S. Kucheiko, J-W Choi, H-J Kim and H-J Jung, *J. Am. Ceram. Soc.* **79** (1996) 2739.

[25] D. H. Yeo, J. B. Kim, J. H. Moon, S. J. Yoon and H. J. Kim, *Jpn. J. Appl. Phys.* **35** (1996) 663.

[26] C-L. Huang, H-L. Chen, C-C. Wu, *Mater. Res. Bull.* **36** (2001)1645.

[27] P. Liu, E. S. Kim, S. G. Kang, H. S. Jang, *Mater. Chem. Phys.* **79** (2003) 270.

[28] B. J. Kennedy, C. J. Howard, and B. C. Chakoumakos, *J. Phys. Condens. Matter.* **11** (1999) 1479.

[29] A. M. Glazer, *Acta Crystallogr.* **B 28** (1972) 3384.

[30] X. Liu and R. C. Liebermann, *Phys. Chem. Miner.* **20** (1993) 171.

[31] Y. Wang and R. C. Liebermann, *Phys. Chem. Miner.* **20** (1993) 147.

[32] H. Kagata and J. Kato, *Jpn. J. Appl. Phys.* **35** (1994) 5463.

[33] M. Hervieu, F. Studer and B. Raveu, *J. Sol. State Chem.* **22** (1997) 273.

[34] I. Levin, L. A. Bendersky, J. P. Cline, R. S. Roth, and T. A. Vanderah, *J. Solid State Chem.* **150** (2000) 43.

[35] L. A. Bendersky, I. Levin, R. S. Roth, and A. J. Shapiro, *J. Solid State Chem.* **160** (2001) 257.

[36] R. J. Cava, J. J. Krakewsky and R. S. Roth, *Mater. Res. Bull.* **34** (1999) 1817.

[37] L. A. Bendersky, J.J. Krajewski, and R. J. Cava, *J. Eur. Ceram. Soc.* **21** (2001) 2653.

[38] T. A.Vanderah, W. Febo, J. Y. Chan, R. S. Roth, J. M. Loezos, L. D. Rotter, R. G. Geyer, and D. B. Minor, *Int. J. Inorg. Mater.* (in press).

[39] J. Takahashi, T. Fuji, S. Shimada and K. Kodaira, *J. Eur. Ceram. Soc.* **19** (1999)1089.

[40] W. D. Kingery, *J. Am. Ceram. Soc.* **37** (1954) 42.

[41] K. Fukuda, R. Kitoh and I. Awai, *J. Mater. Sci.* **30** (1995) 1209.

[42] B. W. Hakki and P. D. Coleman, *IRE Trans. on Microwave Theory Tech.* **MTT-8** (1960) 402.

[43] W. E. Courtney, *IEEE Trans. on Microwave Theory Tech.* **MTT-18** (1970) 476.

[44] J. Krupka, K. Derzakowski, B. Riddle and J. B.-Jarvis, *Meas. Sci. Technol.* **9** (1998)1751.

[45] R. S. Roth, *J. Res. Natl. Bur. Stand.* **58** (1957) 75.

[46] R. D. Shannon, *Acta Cryst.* **A32** (1976) 751.

[47] M. Menneraye, J. Seridat and C. Jourwersma, *Glass Technol.* **9** (1968) 70.

[48] H. Ikawa, A. Iwai, K. Hiruta, H. Shimojima, K. Urabe and S. Udagawa, *J. Am. Ceram. Soc.* **71** (1988) 120.

[49] Y. Zhang and P. K. Davies, *J. Am. Ceram. Soc.* **77** (1994) 743.

[50] D. Houivet, J. E. Fallah, B. Lamagnere and J-M. Haussone, *J. Eur. Ceram. Soc.* **21** (2001) 1727.

[51] C. C. You and C-L Huang, *Jpn. J. Appl. Phys.* **34** (1995)1911.

[52] R. D. Shannon, *J Appl. Phys.* **73** (1993) 384.

[53] S. Nomura, K. Toyama and K. Kaneta, *Jpn. J. Appl. Phys.* **21** (1982) 624.

[54] Y. Kawashima, N. Nishida, I. Ueda and H. Ouchi, *J. Am. Ceram. Soc.* **66** (1983) 421.

[55] M. P. Seabra, M. Avdeev, V. M. Ferreira, R. C. Pullar and N. McN. Alford, *J. Eur. Ceram. Soc.* **23** (2003) 2403.

[56] I. Maclaren and C. B. Ponton, *J. Mater. Sci.* **33** (1998)17.

[57] O. Renoult, J-P. Boilot, F. Chaput, R. Papiernik, L. G. Hubert-Pfalzgraf and M. Lejeune, *J. Am. Ceram. Soc.* **75** (1992) 3337.

[58] C-H. Lu, and C-C. Tsai, *Mater. Sci. Eng.* **B 55** (1998) 95.

[59] M-H. Liang, S-Y. Wu, C-T. Hu and I-N. Li, *Mater. Chem. Phys.* **79** (2003) 276.

[60] H. M. Shirey, "*Low temperature synthesis of the microwave dielectric material Barium Magnesium Tantalate (BMT)*", M. S. Thesis, University of Pittsburg (2002).

[61] S. Katayama, I. Yoshinaga, N. Yamada and T. Nagai, *J. Am. Ceram. Soc.* **79** (1996) 2059.

[62] Q. Wang, H. Rushan and Z. Z. Gan, *J. Am. Ceram. Soc.* **75** (1992) 2881.

[63] G. Rong, N. Newman, B. Shaw and D. Cronin, *J. Mater.Res.* **14** (1999) 4011.

[64] X. M. Chen and Y. J. Wu, *J. Mater. Sci. Mater. Electron.* 7 (1996) 369.

[65] M. R. Varma, R. Reghunandan and M. T. Sebastian, *Jpn. J. Appl. Phys.* **44** (2005) 298.

[66] S-Y Chen and Y-J Lin, *Jpn. J. Appl. Phys.* **40** (2001) 3305.

[67] P. K. Davies, T. Jong, T. Negas, *J. Am. Ceram. Soc.* **80** (1997)1727.

[68] J. H. Lee, Y. I. Jang, H. J. Youn, J. W. Jang and B. K. Kim, *J. Mater. Sci.* **34** (1999) 625.

[69] C-L Huang, K-H Chiang and S-C Chuang, *Mater. Res. Bull.* **39** (2004) 629.

[70] M. F. Yan, *Solid State Sintering, Advances in Ceramics, Ceramic Powder Science*, (American Ceramic Society, Westerville, Ohio 21, 1987) p. 635.

[71] S. Kawashima, *Am. Ceram. Soc. Bull.* **72** (1993) 120.

[72] N. McN. Alford, J. Breeze, S. J. Penn and M. Poole, *IEE. Proc. Meas. Sci. Technol.* **147** (2000) 296.

[73] H. Matsumoto, H.Tamura, and K. Wakino, *Jpn. J. Appl. Phys.* **30** (1991) 2347.

[74] K. P. Surendran, M. Jacob, P. Mohanan and M. T. Sebastian, *J. Appl. Phys.* (in press).

CHAPTER 4

INFLUENCE OF GLASS ADDITION IN $Ca(Ca_{1/4}B_{2/4}Ti_{1/4})O_3$ [B = Nb, Ta] CERAMICS

Microwave dielectric properties of polycrystalline $Ca_5B_2TiO_{12}$ (B = Nb, Ta) ceramics have been tailored using different glass additives such as B_2O_3, SiO_2, B_2O_3-SiO_2, ZnO-B_2O_3, Al_2O_3-SiO_2, Al_2O_3-B_2O_3-SiO_2, BaO-B_2O_3-SiO_2, MgO-B_2O_3-SiO_2, ZnO-B_2O_3-SiO_2, PbO-B_2O_3-SiO_2, and $2MgO$-Al_2O_3-$5SiO_2$. The intentions of the investigation were (a) to study the effect of glass fluxing on the structure and density of $Ca_5B_2TiO_{12}$ (B = Nb, Ta) ceramics (b) to explore the possibility of low temperature sintering and hence to reduce the cost of production of the dielectrics (c) to improve the microwave dielectric properties of $Ca_5B_2TiO_{12}$ (B = Nb, Ta) ceramics. The influence of the above mentioned glasses on the phase purity, structure, microstructure, densification, sintering temperature and microwave dielectric properties of $Ca_5Nb_2TiO_{12}$ and $Ca_5Ta_2TiO_{12}$ ceramics are discussed. The results of this research established low temperature synthesis of $Ca_5B_2TiO_{12}$ (B = Nb, Ta) ceramics with improved microwave dielectric properties for dielectric resonator and possible Low Temperature Co-fired Ceramics (LTCC) applications.

4.1 INTRODUCTION

The rapid advance in wireless communication in the past decade was because of the revolutionary progress in the discovery and development of increasingly sophisticated materials. The use of these materials in the circuitry of wireless devices, microelectronic technology and in monolithic microwave integrated circuits (MMIC)[1,2] have led to dramatic decrease in the size and weight of devices such as cellular phones in recent years. Non integrated bulk ceramics designed to be working as dielectric resonators (DRs), resonating at the frequency of the carrier wave and their efficiency to allow miniaturization and improved performance of microwave circuits have been the subject for discussion in the previous chapters. The excellent performance of the circuit is mainly controlled by the properties like dielectric constant (ε_r), unloaded quality factor (Q_u) and temperature variation of resonant frequency (τ_f) of the material used. These stringent requirements prevent the use of all available DRs for practical applications and keep the development of advanced materials for wireless communication[3,4] as a challenging area of research. The active work now in this field is the search for new materials[5,6,7] and tailoring the properties of existing materials by solid solution formation,[8,9] doping[10,11] etc. In producing miniaturized devices, ceramic multilayer structures with low sintering temperature are needed because they can be co-fired with high conductivity metals such as silver, copper and their alloys.[12] In this point of view low temperature co-fired ceramics (LTCC) has gained much attention because of their design and functional benefits over conventional techniques. LTCC materials will contribute much to the integration of electronic materials.[13] Commercially available dielectric resonator materials for microwave application show high Q_u and high ε_r, but need to be sintered at high temperatures for longer duration to attain better densification and thereby improved performance.[14,15,16]

Complex perovskite [$A(B'_{1/3}, B''_{2/3})O_3$] materials are an important structural base for dielectric resonator applications and have excellent properties at microwave frequencies as explained in Chapter 3, Section 3.1.3. Ba based complex perovskites like $Ba(Mg_{1/3}Ta_{2/3})O_3$ and $Ba(Zn_{1/3}Ta_{2/3})O_3$ are reported[17] to have good dielectric properties from the application point of view. The microwave dielectric properties of calcium based

complex perovskites[18,19,20] are also reported in literature. As explained in Section 3.3.1 – 3.3.2 of Chapter 3, $Ca_5Nb_2TiO_{12}$ and $Ca_5Ta_2TiO_{12}$ ceramics posses reasonably good dielectric properties at microwave frequencies. $Ca_5Nb_2TiO_{12}$ has $\varepsilon_r = 48$, $Q_u \times f > 26\,000$ GHz and $\tau_f = +40$ ppm/°C when sintered at 1550°C/4h. $Ca_5Ta_2TiO_{12}$ has $\varepsilon_r = 38$, $Q_u \times f > 33\,000$ GHz at 5GHz and $\tau_f = +10$ ppm/°C, when sintered at 1625°C for 4 hours. Efforts have been made to tailor the microwave dielectric properties of these ceramics by doping and solid solution formation (See Chapters 3, 5 and 6). More recently, these materials were found (See Chapters 7 and 8) to be suited for the bandwidth enhancement of DR loaded microstrip patch antenna and for the fabrication of wide band dielectric resonator antennas. However the relatively high sintering temperature of these ceramics put constraint over their use for practical purposes. Further, the demands for mass production of the resonators require reliable, reproducible and cost effective processing of ceramics. Several methods are reported in literature to reduce the sintering temperature of low loss dielectric materials such as by (i) chemical synthesis[21,22,23] (ii) using raw materials with smaller particle size[24] and (iii) liquid phase sintering[25] by the addition of glassy materials. The complex procedures involved, high cost of the chemicals and poor microwave dielectric properties precludes the use of chemical synthesis for the industrial production of DRs.[26] Recent researches suggest that the addition of glassy materials as sintering aids are most effective and simple method available to reduce the sintering temperature. Efforts have been made to lower the sintering temperature of low loss dielectric resonator materials like (Zr, Sn)TiO_4[27], $Ba_2Ti_9O_{20}$[28,29,30], $BaTi_4O_9$[31,32,33], $(Mg_{0.5}Ca_{0.5})TiO_3$[34,35,36], $BiNbO_4$[37] and $Ba(Mg_{1/3}Ta_{2/3})O_3$[38,39,40] with glass fluxing. The microwave dielectric properties of DRs were affected by the liquid phase sintering due to the development of microstructure at low firing temperature or the reaction between the host material and additives. However for most of the systems with higher amount of glass, the reduction of sintering temperature is usually accompanied by an abrupt decrease of physical and dielectric properties of the matrix material due to the formation of secondary phases.[41] Only in a few cases could the sintering temperature be reduced without degradation of dielectric properties due to the enhancement of density or the elimination of oxygen vacancies[42] in the material.

With this point of view we have carried out investigations on the liquid phase sintering effect of $Ca_5B_2TiO_{12}$ (B = Nb, Ta) ceramics using several glasses like B_2O_3 (abbreviated as B), SiO_2 (S), B_2O_3 - SiO_2 (BS), ZnO - B_2O_3 (ZB), Al_2O_3 - SiO_2 (AS), Al_2O_3 – B_2O_3 – SiO_2 (ABS), BaO - B_2O_3 - SiO_2 (BBS), MgO - B_2O_3 - SiO_2 (MBS), ZnO - B_2O_3 - SiO_2 (ZBS), PbO - B_2O_3 - SiO_2 (PBS), and 2MgO - Al_2O_3 - $5SiO_2$ (MAS). The goal of the present study is to find out an ideal glass system which promotes the vitreous phase sintering without deteriorating the microwave dielectric properties of $Ca_5B_2TiO_{12}$ (B = Nb, Ta) ceramics. Effort has also been made to understand the effect of concentration of glass additives on the sintering temperature, density, structure and microstructure of the host materials.

4.2 EXPERIMENTAL

The glass powders used in this investigation were classified into three categories. (i) Primary glasses like B_2O_3, SiO_2 (ii) Binary glasses such as B_2O_3 – SiO_2, ZnO – B_2O_3, Al_2O_3 –SiO_2 and (iii) Ternary glasses like Al_2O_3 – B_2O_3 – SiO_2, BaO – B_2O_3 – SiO_2, MgO – B_2O_3 – SiO_2, ZnO – B_2O_3 – SiO_2, PbO – B_2O_3 – SiO_2 and 2MgO – Al_2O_3 – $5SiO_2$. Recently Surendran *et al.*[40] reported the thermal characteristics and dielectric properties of these glasses. High purity (99.9 %) oxides or carbonates were used as the raw materials for the synthesis of glass powder. The oxides were weighed in their appropriate stoichiometric compositional molar ratios and mixed in an agate mortar for 2h in distilled water medium. It was then melted in a platinum crucible above their softening temperature[40] quenched and made into fine powder form.

$Ca_5B_2TiO_{12}$ (B = Nb, Ta) materials were prepared by conventional solid-state ceramic route as explained in Section 2.1.2 of Chapter 2. Different weight percentage of the glasses were added to $Ca_5B_2TiO_{12}$ (B = Nb, Ta) materials calcined at 1350°C/4h. The prepared glass additives were well mixed with the matrix in distilled water medium in an agate mortar. The green pellets were preheated at 800°C for 1h to expel the binder and then fired in their optimum temperature in a high temperature furnace to get maximum densification and thereby best microwave dielectric properties. Very slow cooling (75°C/h) was given to the sintered samples to avoid the possibility of cracking due to

rapid thermal variations. The sintered ceramic pucks were polished and their bulk density was measured using Archimedes method. The structure and phase purity was examined by powder X-Ray diffraction (XRD) method using CuKα radiation and the surface morphology was investigated using scanning electron microscopic techniques.

The dielectric properties ε_r, Q_u and τ_f of the materials were measured in the microwave frequency range using resonance technique[43, 44, 45] as described in Chapter 2, sections 2.3.2 to 2.3.5.

4.3 RESULTS AND DISCUSSION

4.3.1 Phase Analysis

As it is described in Section 3.3.2 of Chapter 3, $Ca_5B_2TiO_{12}$ (B = Nb, Ta) has orthorhombic symmetry with a cell volume involving multiple simple perovskite subcells. At low temperatures, the different *B*-site atoms may be fully or partially ordered in crystallographically inequivalent *B*-sites and at high temperatures there may be more extensive disorder of atoms among the possible sites due to the influence of entropy. However, prolonged heating at a temperature below the sintering temperature of $Ca_5B_2TiO_{12}$ (B = Nb, Ta) ceramics could not make any significant change in its structure, density or microwave dielectric properties. Hence it could be concluded that no such ordering was observed in these ceramics by annealing. XRD study was made on $Ca_5B_2TiO_{12}$ (B= Nb, Ta) ceramics fluxed with various glasses in different weight percentages (0 -2 wt. %). Addition of all glasses up to 1wt. % form single phase $Ca_5B_2TiO_{12}$ (B = Nb, Ta) ceramics except for B_2O_3, ZnO - B_2O_3 and ZnO - B_2O_3 - SiO_2, which form traces of borate based secondary phases from 0.2wt % onwards. The strong intensity peaks in the XRD pattern of $Ca_5B_2TiO_{12}$ (B = Nb, Ta) ceramics added with 0.1 wt. % SiO_2, Al_2O_3-SiO_2, Al_2O_3–B_2O_3–SiO_2, MgO-B_2O_3-SiO_2 and 2MgO-Al_2O_3-5SiO_2 were found to be shifted to the higher angle region, indicating a decrease in lattice parameters and a resultant reduction in cell volume (not shown here). In the case of 0 to 2 wt. % of B_2O_3, B_2O_3-SiO_2, ZnO-B_2O_3, ZnO-B_2O_3-SiO_2, BaO-B_2O_3-SiO_2 and PbO-B_2O_3-SiO_2 glass added ceramics, the intensity peaks of the XRD profile were shifted to

the low angle region indicating an increase in *a*, *b*, *c* values and a corresponding increase in unit cell volume.

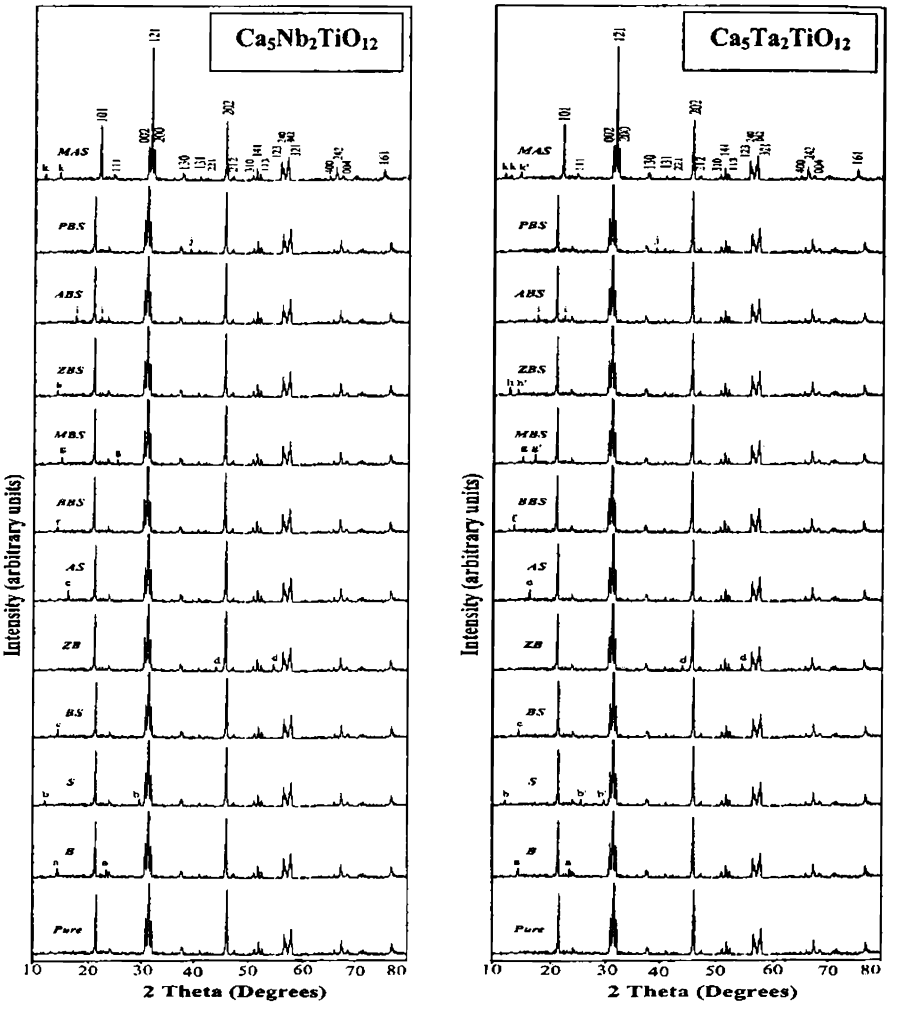

Fig. 4.1 XRD pattern of 2 wt % of various glass added $Ca_5B_2TiO_{12}$ (B = Nb, Ta) ceramics
$B \rightarrow B_2O_3$, $S \rightarrow SiO_2$, $BS \rightarrow B_2O_3 - SiO_2$, $ZB \rightarrow ZnO - B_2O_3$, $AS \rightarrow Al_2O_3 - SiO_2$,
$ABS \rightarrow Al_2O_3 - B_2O_3 - SiO_2$, $BBS \rightarrow BaO - B_2O_3 - SiO_2$, $MBS \rightarrow MgO - B_2O_3 - SiO_2$,
$ZBS \rightarrow ZnO - B_2O_3 - SiO_2$, $PBS \rightarrow PbO - B_2O_3 - SiO_2$ and $MAS \rightarrow 2MgO - Al_2O_3 - 5SiO_2$
($a \rightarrow Ca_3B_2O_6$, $b \rightarrow Ca_2SiO_4$, $b' \rightarrow Ca_2Ti_5O_{12}$, $c \rightarrow Ca_2B_2SiO_7$, $d \rightarrow \beta$ - $Zn_5B_4O_{11}$,
$e \rightarrow CaAl_2Si_2O_8$, $f \rightarrow CaBa_2(B_3O_6)$, $g \rightarrow Ca_2MgSi_2O_7$, $g' \rightarrow Mg_2B_2O_5$,
$h \rightarrow Ca_2B_2O_5$, $h' \rightarrow Ca_2ZnSi_2O_7$, $i \rightarrow CaAlB_2O_7$, $j \rightarrow PbB_4O_7$
$k \rightarrow Ca_2SiO_4$, $k' \rightarrow Ca_3MgAl_4O_{10}$ additional phases respectively)

The XRD pattern recorded from $Ca_5Nb_2TiO_{12}$ and $Ca_5Ta_2TiO_{12}$ ceramics fluxed with 2 wt % of various glasses are shown in Fig. 4.1. Addition of 2 wt % B_2O_3 promotes the formation of $Ca_3B_2O_6$ (JCPDS File Card No. 26 - 347) and SiO_2 addition causes the appearance of Ca_2SiO_4 (JCPDS File Card No.31 – 302). Intensity peaks corresponding to $Ca_2B_2SiO_7$ (JCPDS File Card No. 29 – 303), β - $Zn_5B_4O_{11}$ (JCPDS File Card No. 9 – 153) and $CaAl_2Si_2O_8$were found in the XRD pattern of $Ca_5B_2TiO_{12}$ (B = Nb, Ta) ceramics when 2 wt % of binary glasses like B_2O_3 - SiO_2, ZnO - B_2O_3 and Al_2O_3 - SiO_2 were added respectively to the host materials. The addition of even 1 wt % each of ternary glasses to $Ca_5B_2TiO_{12}$ (B = Nb, Ta) ceramics form additional phases as is evident in the XRD profile. This is because of the easier decomposition of the glasses at high temperatures to yield its components to react with the matrix. Impurity phases of $CaBa_2(B_3O_6)_2$ (JCPDS File Card No. 39 – 230) are seen with the addition of BaO - B_2O_3 - SiO_2 and peaks corresponding to $Mg_3(BO_3)_2$ (JCPDS File Card No. 33 – 858) and $Ca_2MgSi_2O_7$ (JCPDS File Card No. 43 – 1491) appeared with the doping of MgO-B_2O_3-SiO_2 glass to $Ca_5Nb_2TiO_{12}$ powders. Whereas secondary phases of Ba_2SiO_4 (JCPDS File Card No. 26 – 1403) were found with the addition of BaO - B_2O_3 - SiO_2 and peaks representing $CaMgSiO_4$ (JCPDS File Card No. 35 – 590) were detected when $Ca_5Ta_2TiO_{12}$ powders were fluxed with 2 wt % MgO - B_2O_3 - SiO_2 glasses. The addition of even a small percentage of ZnO-B_2O_3-SiO_2 will promote the formation of $Ca_2B_2O_5$ (JCPDS File Card No. 18 - 279) and $Ca_2ZnSi_2O_7$ (JCPDS File Card No. 35 – 745) and this may be detrimental to the density and microwave dielectric properties. Traces of $CaAlB_3O_7$ (JCPDS File Card No. 29 – 280) and PbB_4O_7 (JCPDS File Card No. 15 – 278) were appeared in the XRD profile of $Ca_5Nb_2TiO_{12}$ ceramics fluxed with 2 wt % of Al_2O_3 – B_2O_3 – SiO_2 and PbO - B_2O_3 - SiO_2 glasses respectively. The density and microwave dielectric properties of 2 wt % of ZnO - B_2O_3 - SiO_2 and PbO - B_2O_3 - SiO_2 glass added calcium tantalum titanates were much deteriorated due to the presence of satellite phases like $Ca_2ZnSi_2O_7$ (JCPDS File Card No. 35 – 745) and PbB_4O_7 (JCPDS File Card No. 15 – 278) respectively. Sintering of $Ca_5Ta_2TiO_{12}$ (B= Nb, Ta) ceramics with 2 wt % Al_2O_3–B_2O_3–SiO_2 glass also forms traces of $CaAlB_3O_7$ (JCPDS File Card No. 29 - 280) as their niobium analogue as is evident from the XRD profile. 2MgO-Al_2O_3-5SiO_2 was found to

be the most effective fluxing agent in $Ca_5Nb_2TiO_{12}$ ceramics also form secondary phases when excess glass is added as is visible in the XRD profile. Peaks corresponding to Ca_2SiO_4 (JCPDS File Card No. 31 – 302) and formation of polyphases such as $Ca_3MgAl_4O_{10}$ (JCPDS File Card No. 17 – 737) were detected in the XRD pattern as shown in Fig. 4.1. The density and microwave dielectric properties of $Ca_5Ta_2TiO_{12}$ ceramics were also least affected by the addition of $2MgO - Al_2O_3 - 5SiO_2$ glass addition. Traces of impurity peaks corresponding to $Ca_3MgAl_4O_{10}$ (JCPDS File Card No. 17 – 737) were found with 2 wt % addition of $2MgO - Al_2O_3 - 5SiO_2$ glasses to the matrix $Ca_5Ta_2TiO_{12}$ ceramics. It is possible that at temperatures above 1250°C, the multicomponent glasses decomposed and these components may remain in the grain boundary or react with the matrix material to form glass based additional phases and were detected in the XRD profile. Significant reduction in mechanical strength and crystalline nature of $Ca_5B_2TiO_{12}$ (B = Nb, Ta) ceramics were observed with the addition of 2 wt % of various glasses and the same was supported by decrease in the relative intensity of XRD peaks. This effect was more prominent with boron oxide based glasses and also more satellite phases were detected with these glasses.

4.3.2 Sintering and Densification

It is observed that glass fluxing facilitates vitreous sintering by forming low melting phases and hence reduces the sintering temperature of the ceramics. The variation of sintering temperature with wt% of glasses in $Ca_5B_2TiO_{12}$ (B= Nb, Ta) ceramics is depicted in Fig. 4.2 and 4.3. It is established earlier[46] that boron based glasses are more effective in lowering the sintering temperature. This may be due to the low softening temperature of B_2O_3[46]. It is evident from Fig. 4.2 and 4.3 that by the addition of 2 wt% B_2O_3, sintering temperature of $Ca_5Nb_2TiO_{12}$ and $Ca_5Ta_2TiO_{12}$ ceramics decreased significantly. 2 wt% addition of $2MgO – Al_2O_3 – 5SiO_2$ glass has lowered the sintering temperature even up to 1320°C in the case of niobates and to 1350°C for the tantalates. However higher weight percentage of glass addition is needed to lower the firing temperature of the ceramics up to 950°C for the immediate use of these materials for LTCC applications, but it may considerably deteriorate the dielectric properties.

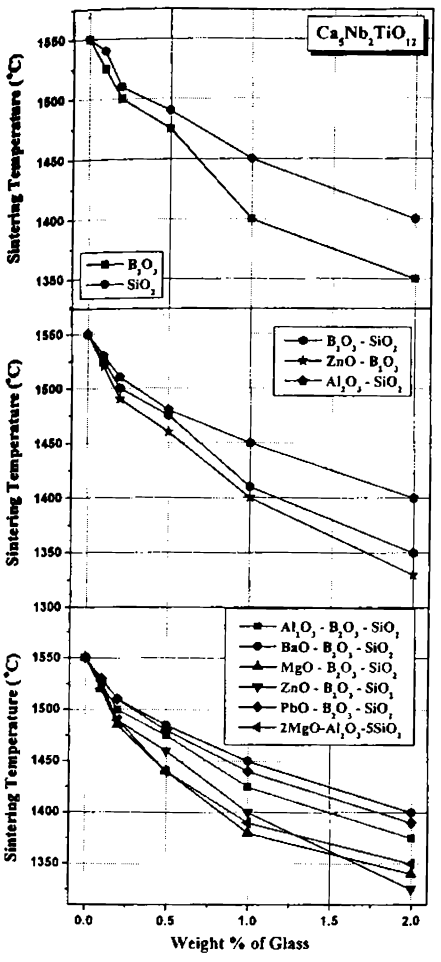

Fig. 4.2 Variation of sintering temperature with weight % of glasses in $Ca_5Nb_2TiO_{12}$ ceramics

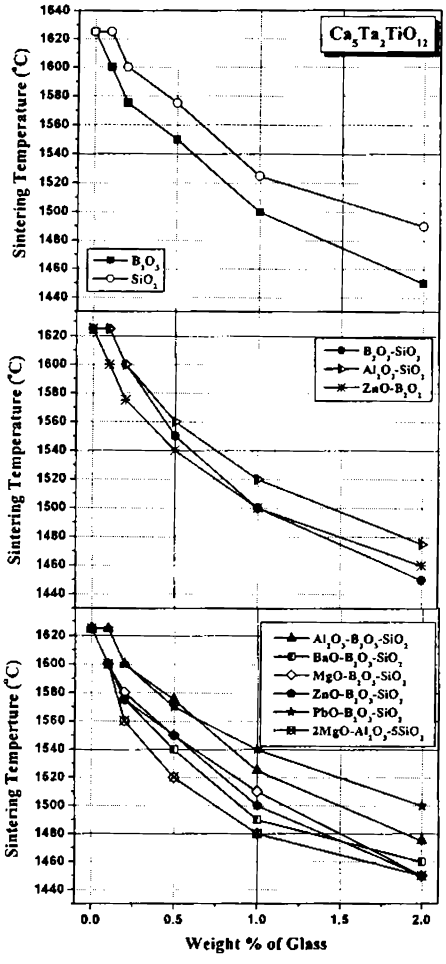

Fig. 4.3 Variation of sintering temperature with weight % of glasses in $Ca_5Ta_2TiO_{12}$ ceramics

In liquid phase sintering, grain to grain material transport will be enhanced only if the additive can wet the grain of the matrix material. In such cases the transient glassy phase formed at a lower temperature can wet the ceramic and hence reduce the viscosity and enhances pore elimination resulting in densification. On the other hand, if the glass is not soluble in the ceramic, the wetting effect will be poor. Fig. 4.4 and 4.5 indicate the

densification characteristics of $Ca_5Nb_2TiO_{12}$ and $Ca_5Ta_2TiO_{12}$ ceramics doped with various glasses in different weight percentage

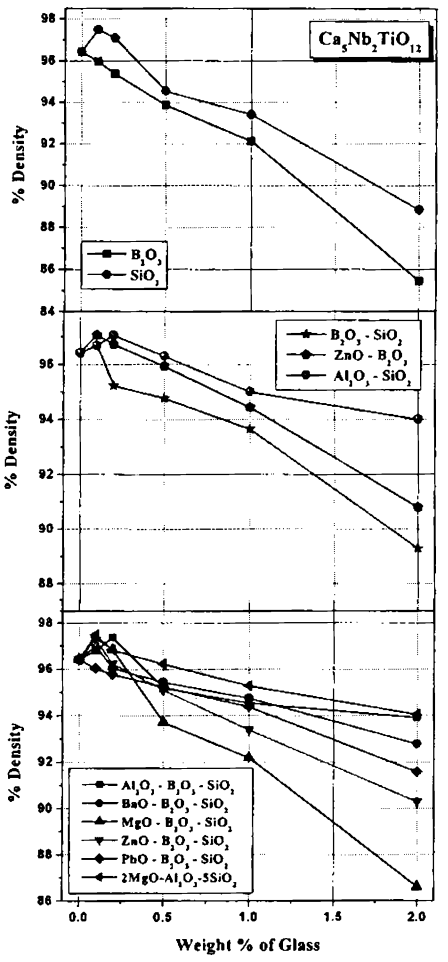

Fig. 4.4 Variation of percentage densification with weight % of glasses in $Ca_5Nb_2TiO_{12}$ ceramics

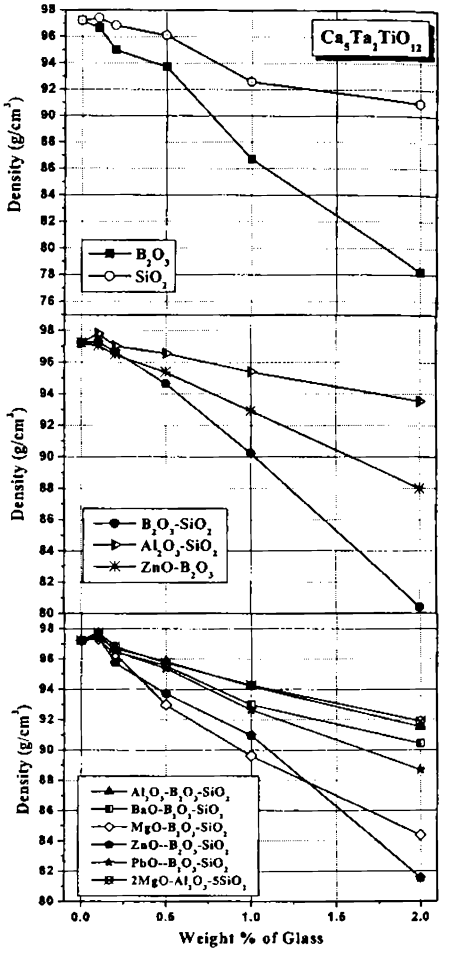

Fig. 4.5 Variation of percentage densification with weight % of glasses in $Ca_5Ta_2TiO_{12}$ ceramics

Out of the two primary glasses added to $Ca_5B_2TiO_{12}$ (B = Nb, Ta) ceramics, 0.1 wt. % of SiO_2 enhanced the bulk density, while B_2O_3 addition continuously decreased the density of the ceramic. Slight increase in percentage density was observed with the

addition of small amount of Al_2O_3 - SiO_2, MgO – B_2O_3 – SiO_2, ZnO – B_2O_3 – SiO_2 and 2MgO - Al_2O_3-SiO_2. The percentage experimental density of $Ca_5B_2TiO_{12}$ (B = Nb, Ta) ceramics was found to be adversely affected by the addition of 0 – 2 wt. % of B_2O_3, B_2O_3 – SiO_2, ZnO - B_2O_3 and PbO – B_2O_3 – SiO_2.

The addition of more than 0.5 wt. % of all glasses decreased the percentage density of $Ca_5B_2TiO_{12}$ (B= Nb, Ta) ceramics. The excess quantity of glass doping leaves out more amount of decomposed glassy components in the matrix material. The trapped porosity associated with grain growth, evaporation of glass component and chemical reaction between glass and matrix material to form traces of secondary phases are the reasons for reduction in density with higher concentration of glass addition. Good densification was found for by Si, Al and Mg based glass additives. Dopants with smaller ionic radii[47] than Ca^{2+} results in the decrease of unit cell volume and hence increase in density. However excess addition of the same glasses was detrimental to density and is attributed to the formation of glass based secondary phases like $CaAl_2Si_2O_8$ and $Ca_3MgAl_4O_{10}$.

4.3.3 Microstructural Analysis

Scanning electron micrographs of a few typical glass added $Ca_5B_2TiO_{12}$ (B = Nb, Ta) specimens are shown in Fig. 4.6. Pure $Ca_5Nb_2TiO_{12}$ and $Ca_5Ta_2TiO_{12}$ ceramics were sintered at 1550°C/4h and 1625 °C/4h respectively and their surface morphology is shown in Chapter 3, section 3.3.2. The grains are relatively large in size up to 10μm and clearly separated grain boundaries were visible in the micrograph. By the addition of 0.1 wt. % of 2MgO – Al_2O_3 – $5SiO_2$ in $Ca_5Nb_2TiO_{12}$ and $Ca_5Ta_2TiO_{12}$ ceramics, the number of voids decreased considerably as shown in Fig. 4.6(a) and 4.6(b) respectively. The microstructure of 2MgO – Al_2O_3 – $5SiO_2$ glass added $Ca_5B_2TiO_{12}$ (B = Nb, Ta) sintered specimens show uniformly sized grains of average size less than 10μm. This improvement in densification is in good agreement with a previous report[48] that, liquid phase sintering can produce smaller grains than that formed by solid state process. The grain growth rate also found to be decreased by glass addition. Hence it can be concluded that the effect of glass addition was demonstrated not only by the decrease of the

sintering temperature, but also by densification of $Ca_5B_2TiO_{12}$ (B = Nb, Ta) ceramics. Fig. 4.6(c) gives the surface morphology of 1 wt. % MgO – B_2O_3 – SiO_2 added $Ca_5Nb_2TiO_{12}$ ceramics and 4.6(d) represents the SEM picture of 1 wt % Al_2O_3 – B_2O_3 – SiO_2 glass fluxed $Ca_5Ta_2TiO_{12}$ ceramics.

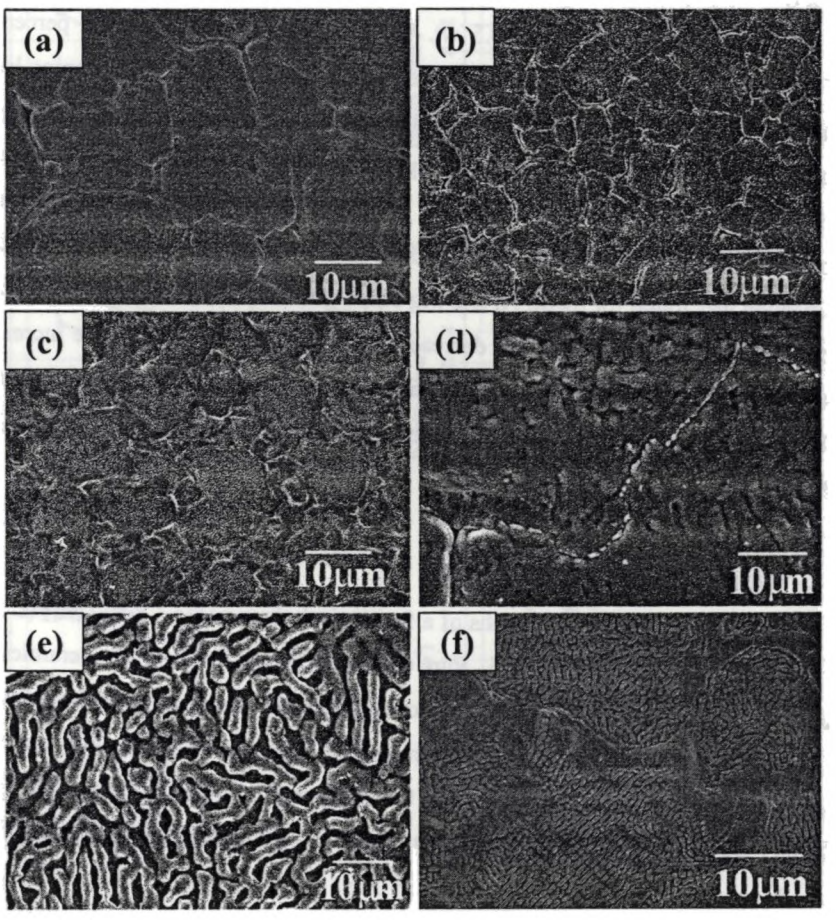

Fig. 4.6 SEM pictures of some typical glass added $Ca_5B_2TiO_{12}$ (B= Nb, Ta) ceramics (a) $Ca_5Nb_2TiO_{12}$ + 0.1 wt % 2MgO – Al_2O_3 – 5SiO_2 (b) $Ca_5Ta_2TiO_{12}$ + 0.1 wt % 2MgO – Al_2O_3 – 5SiO_2 (c) $Ca_5Nb_2TiO_{12}$ + 1 wt % MgO – B_2O_3 – SiO_2 (d) $Ca_5Nb_2TiO_{12}$ + 1 wt % Al_2O_3–B_2O_3–SiO_2 (e) $Ca_5Nb_2TiO_{12}$ + 2 wt % ZnO – B_2O_3 and (f) $Ca_5Ta_2TiO_{12}$ + 2 wt % ZnO – B_2O_3

It is evident from the figures that, the glassy material coated the grains of the matrix and reacted with the host material to form a glass based low melting phase. It increases the porosity of the host material. Distinct cracks with the segregation of secondary phases can be seen in the SEM micrograph and the density falls to even less than 90% of its theoretical value. Microstructural examination of sintered $Ca_5Nb_2TiO_{12}$ and $Ca_5Ta_2TiO_{12}$ ceramics added with 2 wt. % ZnO – B_2O_3 glass shows a large extent of porosity as is evident from Fig. 4.6 (e) and 4.6(f) respectively. Addition of 2 wt. % ZnO – B_2O_3 to $Ca_5B_2TiO_{12}$ (B = Nb, Ta) ceramics causes the formation of porous melt of glass, which further reduces the density of the host materials. However no additional phases are visible in the scanning electron micrograph though it appeared in the XRD spectra for higher weight percentage addition of glasses.

4.3.4 Microwave dielectric Properties

The microwave dielectric properties of glass doped ceramics depend on their density and presence of secondary phases.[40,47] Generally, the addition of excess glass dopants to a ceramic lowers the sintering temperature accompanied by significant deterioration in the microwave dielectric properties.[48,49] This happens when the decomposed glass remains in the host material, or due to the formation of glass based secondary phases because of the chemical reaction between glass and matrix. But it is noteworthy that, small amount of glass addition increases the density and microwave dielectric properties of the host material, because the liquid forming composition enables better pore elimination by enhancing the material transport. Hence the sintering of ceramics with glass may or may not improve the microwave dielectric properties depending upon the mode of reaction executed in the matrix with glass.

4.3.4.1 Primary Glasses

The variation of microwave dielectric properties of $Ca_5Nb_2TiO_{12}$ and $Ca_5Ta_2TiO_{12}$ ceramics with the addition of primary glasses like B_2O_3 and SiO_2 in different concentration (0 to 2 wt %) are depicted in Fig. 4.7 and 4.8 respectively. Pure $Ca_5Nb_2TiO_{12}$ has ε_r = 48, $Q_u \times f$ > 26000 GHz and τ_f = +40 ppm/°C when sintered at

1550°C/4h (See Section 3.3.2 of Chapter 3). It can be seen from the Fig. 4.7 that the addition of any amount of B_2O_3 to $Ca_5Nb_2TiO_{12}$ deteriorated the dielectric properties except the decrease in τ_f.

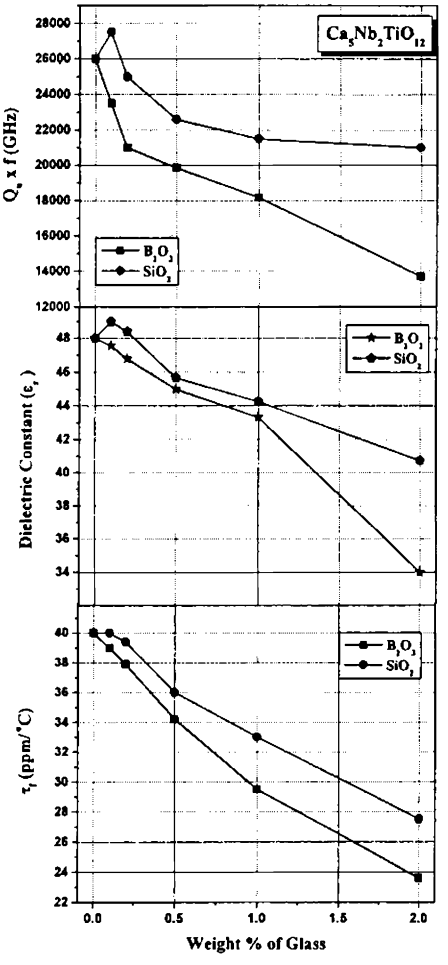

Fig. 4.7 Microwave dielectric properties of 0 – 2 weight % primary glass added $Ca_5Nb_2TiO_{12}$ ceramics

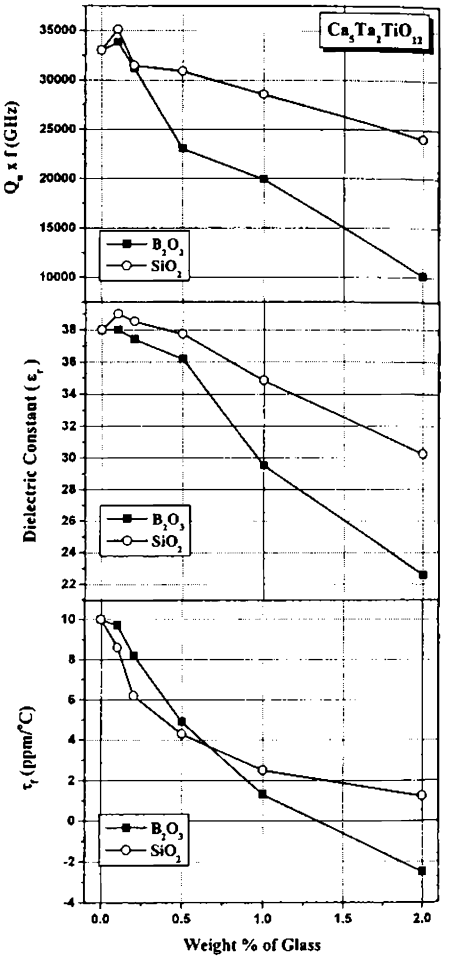

Fig. 4.8 Microwave dielectric properties of 0 – 2 weight % primary glass added $Ca_5Ta_2TiO_{12}$ ceramics

On the other hand 0.1 wt % of SiO_2 doping increased the quality factor and dielectric constant with a slight reduction in τ_f, which is desired. In this case the $Q_u \times f$ increased to

27500 GHz and ε_r increased to 49. Higher amount of SiO_2 (> 0.1%) deteriorated the quality factor and dielectric constant with considerable decrease in τ_f.

The microwave dielectric properties of pure $Ca_5Ta_2TiO_{12}$ ceramics sintered at 1625°C/4h are ε_r = 38, $Q_u \times f$ > 33000 GHz and τ_f = +10 ppm/°C (See Section 3.3.2 of Chapter 3). With the addition of B_2O_3 from 0 to 2 wt %, the dielectric constant decreases from 38 to 23, τ_f changes from 10 ppm/°C to -3 ppm/°C and $Q_u \times f$ reduces to 10000 GHz (See Fig. 4.8). It is quite interesting to note the zero crossing of temperature variation of resonant frequency of $Ca_5Ta_2TiO_{12}$ ceramics with an addition of about 1.3 wt % of B_2O_3. The formation of secondary phases like $Ca_3B_2O_6$ and poor densification are supposed to be the reason for poor dielectric properties with large amount of B_2O_3 addition. The addition of 0.1 wt. % SiO_2 to $Ca_5Ta_2TiO_{12}$ ceramics enhances its ε_r and quality factor. ε_r increases to 39 and $Q_u \times f$ reaches 35000 GHz for 0.1 wt. % addition of silica. Higher weight percentage addition of SiO_2 adversely affected the values of ε_r and Q_u but improved τ_f of the matrix material.

4.3.4.2 Binary Glasses

The microwave dielectric properties of binary glass added $Ca_5Nb_2TiO_{12}$ ceramics are plotted in Fig. 4.9 as a function of weight percentage of glass. The doping of 0.2 wt. % Al_2O_3 – SiO_2 glass to the host $Ca_5Nb_2TiO_{12}$ ceramics increased its Q_u and ε_r values by 12 and 3 percentages respectively. Above 0.2 wt. % of Al_2O_3 – SiO_2 addition a gradual decrease in dielectric properties of $Ca_5Nb_2TiO_{12}$ was observed. This can be attributed to the formation of $CaAl_2Si_2O_8$ secondary phase. B_2O_3 – SiO_2 and ZnO – B_2O_3 glass addition to $Ca_5Nb_2TiO_{12}$ ceramics seriously deteriorated their quality factor and dielectric constant. It is obvious from Fig. 9 that, monotonous decrease in τ_f was observed by the addition of all binary glasses we experimented. 2 wt. % addition of Al_2O_3 – SiO_2 to $Ca_5Nb_2TiO_{12}$ gives ε_r = 42, $Q_u \times f$ > 17000 GHz and τ_f = +13ppm/°C. Out of the three binary glasses investigated Al_2O_3 – SiO_2 was found to be most effective for improving the microwave dielectric properties of $Ca_5Nb_2TiO_{12}$ ceramics. Addition of 0.1 wt. % of Al_2O_3 - SiO_2 to $Ca_5Ta_2TiO_{12}$ enhanced the ε_r and Q_u of the host material as is evident from Fig. 4.10. In this case ε_r = 39.5 and $Q_u \times f$ > 36000 GHz and τ_f = 9 ppm/°C. Further

addition of the same glass deteriorated ε_r and Q_u whereas the τ_f value reduced to 2 ppm/°C for 2 wt. % of Al_2O_3-SiO_2 glass addition.

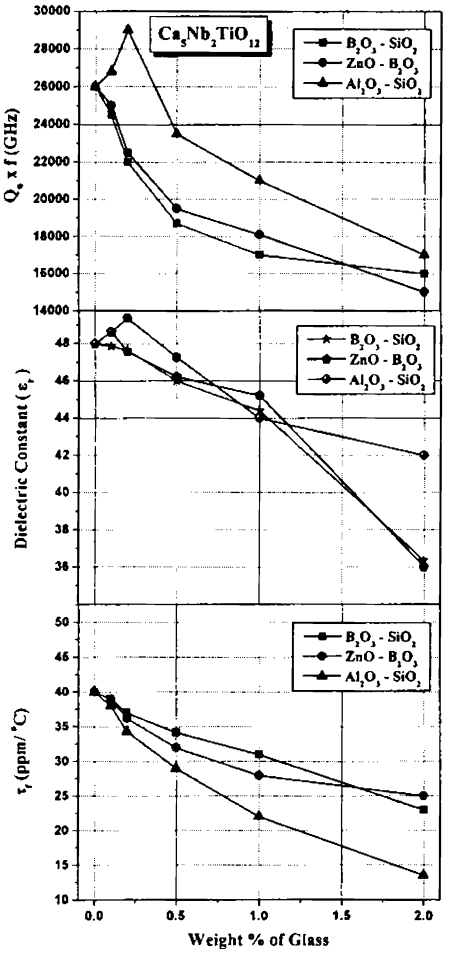

Fig. 4.9 Microwave dielectric properties of 0 – 2 weight % binary glass added $Ca_5Nb_2TiO_{12}$ ceramics

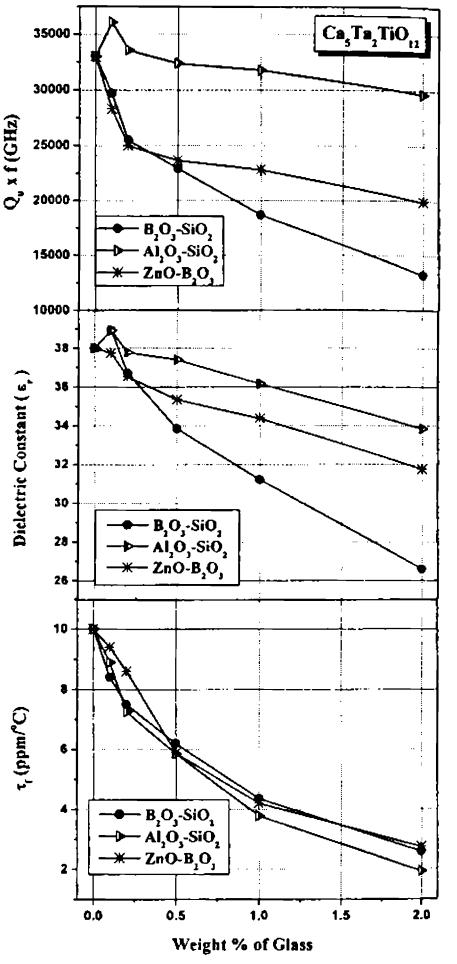

Fig. 4.10 Microwave dielectric properties of 0 – 2 weight % binary glass added $Ca_5Ta_2TiO_{12}$ ceramics

When $Ca_5Ta_2TiO_{12}$ ceramics were added with different wt. % of B_2O_3-SiO_2 glasses, monotonous decrease in dielectric properties were observed. The τ_f decreased from 10 to 2 ppm/°C, ε_r varied from 38 to 27 and quality factor decreased to 13000 GHz

from the initial value of 33000 GHz. The dielectric properties of ZnO-B_2O_3 added $Ca_5Ta_2TiO_{12}$ ceramics showed a continuous deterioration with the weight percentage of glass added as shown in Fig. 4.10 In this case poor densification and hence the deterioration of microwave dielectric properties occurred due to the formation of β - $Zn_5B_4O_{11}$ secondary phase. Out of the three binary glasses B_2O_3-SiO_2, ZnO-B_2O_3 and Al_2O_3-SiO_2 added with $Ca_5Nb_2TiO_{12}$ and $Ca_5Ta_2TiO_{12}$ ceramics, 0.2 wt % of Al_2O_3-SiO_2 addition could only improve the microwave properties of the dielectric materials.

4.3.4.2 Ternary Glasses

The best and most well known liquid phase sintering agents are oxides of boron and copper. But it is reported[50] that multicomponent glasses are more effective than single component glasses to reduce sintering temperature and to enhance density and dielectric properties. This is due to the fact that multicomponent glasses with SiO_4 and BO_3 configurations joined to form (Si – O – B – O) linkages with continuous atomic structures, which will have high electrical resistance and low dielectric loss.

The effect of addition of ternary glasses such as $Al_2O_3 – B_2O_3 – SiO_2$, BaO - B_2O_3 - SiO_2, MgO - B_2O_3 - SiO_2, ZnO - B_2O_3 - SiO_2, PbO - B_2O_3 - SiO_2 and $2MgO$ - Al_2O_3 - $5SiO_2$ on the microwave dielectric properties of $Ca_5Nb_2TiO_{12}$ ceramics are shown in Fig. 4.11. Marginal increase in quality factor was observed with 0.1 wt. % addition of $2MgO – Al_2O_3 – 5SiO_2$ and $MgO – B_2O_3 – SiO_2$ glasses, whereas the same increase was observed with 0.2 wt. % addition of $Al_2O_3 – B_2O_3 – SiO_2$ glass. Higher weight percentage doping of these glasses decreased the quality factor of $Ca_5Nb_2TiO_{12}$ ceramics and is due to the formation of glass based secondary phase. The same trend was observed in the variation of dielectric constant when $Ca_5Nb_2TiO_{12}$ was fluxed with these glasses. Addition of up to 0.2 wt % of $Al_2O_3 – B_2O_3 – SiO_2$, $MgO – B_2O_3 – SiO_2$ and $2MgO – Al_2O_3 – 5SiO_2$ increased ε_r of the host material from 48 to 50 and $Q_u \times f$ from 26000 GHz to 30000 GHz. Liquid phase sintering of $Ca_5Nb_2TiO_{12}$ ceramics with ternary glasses like $BaO – B_2O_3 – SiO_2$, $ZnO – B_2O_3 – SiO_2$ and $PbO – B_2O_3 – SiO_2$ deteriorated the microwave dielectric properties for 0 to 2 wt % of glass concentration.

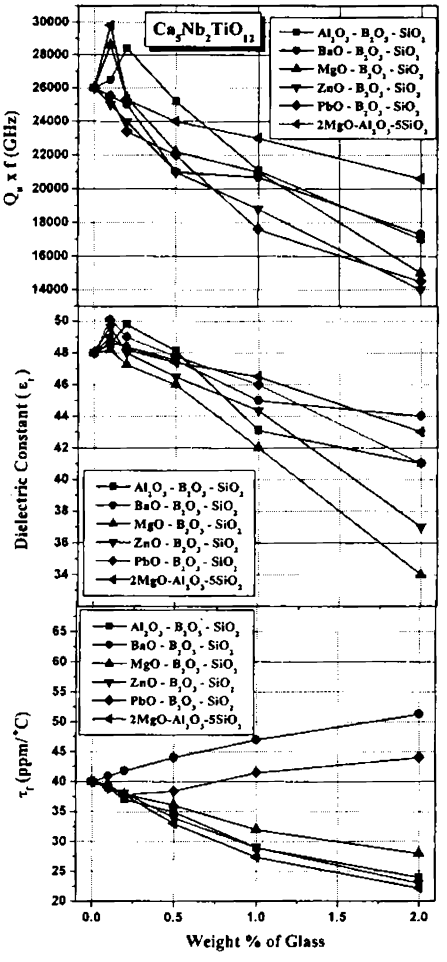

Fig. 4.11 Microwave dielectric properties of 0 – 2 weight % of ternary glass added $Ca_5Nb_2TiO_{12}$ ceramics

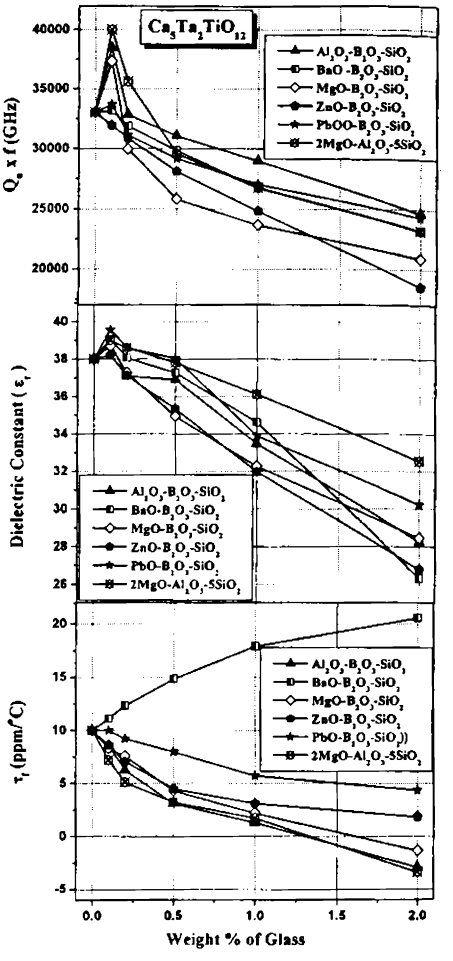

Fig. 4.12 Microwave dielectric properties of 0 – 2 weight % of ternary glass added $Ca_5Ta_2TiO_{12}$ ceramics

However it is interesting to note that 0.1wt % addition of PbO – B_2O_3 – SiO_2 to $Ca_5Nb_2TiO_{12}$ made more than 4% increase in the dielectric constant. It may due to the formation of PbB_4O_7 second phase (even with 0.1 wt % addition of the glass) due to chemical reaction between decomposed lead based glass and the matrix. Higher wt % of all ternary glasses decreased the Q_u and ε_r of $Ca_5Nb_2TiO_{12}$ ceramics, may be due to the

formation of additional phases. It is worth to note the variation of τ_f with wt % of ternary glasses added in $Ca_5Nb_2TiO_{12}$ ceramics. The addition of $Al_2O_3 - B_2O_3 - SiO_2$, $MgO - B_2O_3 - SiO_2$, $ZnO - B_2O_3 - SiO_2$ and $2MgO - Al_2O_3 - 5SiO_2$ decreased the τ_f of the host material. It is quite expected as most of the glass compositions have negative τ_f values.[51] On the other hand $BaO - B_2O_3 - SiO_2$ and $PbO - B_2O_3 - SiO_2$ glass fluxing resulted in an increase in the τ_f of $Ca_5Nb_2TiO_{12}$ ceramics with the wt. % of glass added. A linear increase was observed in the case of $BaO - B_2O_3 - SiO_2$ addition, while $PbO - B_2O_3 - SiO_2$ fluxing showed an initial decrease (up to 0.2 wt. %) and a later increase for higher concentration of glass. Considerable increase in dielectric constant and quality factor was observed with 0.1 wt. % addition of $Al_2O_3 - B_2O_3 - SiO_2$, $MgO - B_2O_3 - SiO_2$ and $2MgO - Al_2O_3 - 5SiO_2$ glass addition. Fluxing of $Ca_5Ta_2TiO_{12}$ ceramics with 0.1 wt. % $2MgO - Al_2O_3 - 5SiO_2$ glass increased its ε_r to 39, $Q_u \times f$ to 40000 (at 5 GHz) and lowered the τ_f to 8 ppm/°C. The τ_f reached negative values with 2 wt. % addition of $Al_2O_3 - B_2O_3 - SiO_2$, $MgO - B_2O_3 - SiO_2$ and $2MgO - Al_2O_3 - 5SiO_2$ glasses. The addition of different wt. % of $BaO - B_2O_3 - SiO_2$, $ZnO - B_2O_3 - SiO_2$ and $PbO - B_2O_3 - SiO_2$ glasses continuously deteriorated the microwave dielectric properties of $Ca_5Ta_2TiO_{12}$ ceramics. In the case of $BaO - B_2O_3 - SiO_2$ glass fluxing τ_f of $Ca_5Ta_2TiO_{12}$ ceramics showed an increase unlike other glasses which showed a decrease.

In low temperature sintering, the microwave dielectric properties depends[52] on the density and secondary phases formed due to the reaction between decomposed glass component and host material. For small percentage of glass doping no secondary phase was detected (except for B_2O_3, $ZnO - B_2O_3$ and $ZnO - B_2O_3 - SiO_2$) and hence the dielectric properties of $Ca_5B_2TiO_{12}$ (B = Nb, Ta) ceramics were largely depend on density. The variation of ε_r and Q_u showed the same trend as that observed with density. The detailed investigation held on the glass addition of $Ca_5B_2TiO_{12}$ (B = Nb, Ta) ceramics revealed that, ternary glasses were more effective compared with primary and binary glasses to improve the dielectric properties. Decrease in τ_f of the host materials with concentration of glass was quite expected as most of the glasses were reported[53] to have negative τ_f. However the increase in τ_f of $Ca_5B_2TiO_{12}$ (B = Nb, Ta) ceramics with $BaO - B_2O_3 - SiO_2$ glass addition is quite surprising since it is reported[53] to have a

negative τ_f. It is observed that borate glasses were more effective in lowering the sintering temperature of matrix materials while dielectric properties witnessed more improvement with silica based glasses. SiO_2, Al_2O_3 - SiO_2, $Al_2O_3 - B_2O_3 - SiO_2$, MgO - B_2O_3 - SiO_2 and 2MgO - Al_2O_3 - $5SiO_2$ enhanced the density and microwave dielectric properties of $Ca_5B_2TiO_{12}$ (B = Nb, Ta) ceramics. Off these, small amount of (about 0.1 wt. %) alumina and silica based glasses were found to be best suited for the effective vitreous phase sintering in $Ca_5B_2TiO_{12}$ (B = Nb, Ta) dielectrics, because of the improved microwave dielectric properties with the addition of these glasses. A ceramic material can be co-fired with internal copper or silver electrode only if the temperature reaches below the melting point of the electrode material (961°C for Ag and 1083°C for Cu). 2 wt. % glass additions on $Ca_5B_2TiO_{12}$ (B= Nb, Ta) ceramics could lower its sintering temperature only down to about 1320°C. Hence addition of a large amount of glass to $Ca_5B_2TiO_{12}$ (B = Nb, Ta) is needed for LTCC applications, which will further deteriorate the microwave dielectric properties.

4.4 CONCLUSIONS

- Effect of glass addition on the structure, density and microwave dielectric properties of $Ca_5B_2TiO_{12}$ (B = Nb, Ta) ceramics have been investigated.
- The structure of $Ca_5B_2TiO_{12}$ (B = Nb, Ta) ceramics were unaffected by the addition of small amount of primary, binary and ternary glasses. However glass based additional phases appeared in the XRD patterns for higher concentration of all glasses.
- Glasses like B_2O_3, $B_2O_3 - SiO_2$, $ZnO - B_2O_3$, and $ZnO - B_2O_3 - SiO_2$ deteriorate densification and microwave dielectric properties of $Ca_5B_2TiO_{12}$ (B = Nb, Ta) ceramics. Boron oxide based glasses were found to be more effective in lowering the sintering temperature. 2 wt. % additions of glasses lowered the firing temperature of $Ca_5Nb_2TiO_{12}$ ceramics even down to 1320°C from 1550°C whereas the sintering temperature of $Ca_5Ta_2TiO_{12}$ was brought down to 1450°C from 1625°C.

- Microstructural analysis showed that small amount of glass additives like SiO_2, $Al_2O_3 - SiO_2$, $Al_2O_3 - B_2O_3 - SiO_2$, $MgO - B_2O_3 - SiO_2$ and $2MgO - Al_2O_3 - 5SiO_2$ improved vitreous phase sintering and uniform grain growth along with increased densification. Higher amount of glass fluxing resulted in the formation of porosity and hence significant reduction in density.
- It was observed that small amount of SiO_2, $MgO - B_2O_3 - SiO_2$, $Al_2O_3 - SiO_2$ and $Al_2O_3 - B_2O_3 - SiO_2$ and $2MgO - Al_2O_3 - 5SiO_2$ increased the density and improved the microwave dielectric properties of $Ca_5B_2TiO_{12}$ (B = Nb, Ta) ceramics. $Ca_5B_2TiO_{12}$ (B = Nb, Ta) ceramics mixed with small amount of Al_2O_3 and SiO_2 based glass compositions exhibited good microwave dielectric properties. The improvement of microwave dielectric properties were more pronounced with ternary glasses than that with primary and binary glasses.
- Marginal increase of 2 % density, 14 % quality factor and 4 % dielectric constant was attained when $Ca_5Nb_2TiO_{12}$ ceramics was doped with small amount of SiO_2, $Al_2O_3 - SiO_2$, $Al_2O_3 - B_2O_3 - SiO_2$, $MgO - B_2O_3 - SiO_2$ and $2MgO - Al_2O_3 - 5SiO_2$. 0.1 wt % $2MgO - Al_2O_3 - 5SiO_2$ glass added $Ca_5Nb_2TiO_{12}$ ceramics sintered at 1520°C/4h has $\varepsilon_r = 50$, $Q_u x f > 30000$ GHz and $\tau_f = +38$ ppm/°C.
- 0.1 wt % addition of Al_2O_3-SiO_2, MgO-B_2O_3-SiO_2 and $2MgO$-Al_2O_3-$5SiO_2$ to $Ca_5Ta_2TiO_{12}$, produced an enhancement of 4 % in ε_r and 22 % in $Q_u x f$ values.
- Addition of B_2O_3, Al_2O_3–B_2O_3–SiO_2, MgO-B_2O_3-SiO_2 and $2MgO$-Al_2O_3-$5SiO_2$ glasses to $Ca_5Ta_2TiO_{12}$ shifted the τ_f of the ceramics from positive to negative values forming temperature stable compositions. Alumina based glasses were more effective in improving the temperature variation of resonant frequency.

The effect of glass additives on the sintering temperature and microwave dielectric properties of $Ca_5Nb_2TiO_{12}$ and $Ca_5Ta_2TiO_{12}$ ceramics were investigated in this Chapter. The forthcoming Chapter describes the method of cationic substitutions to tailor the microwave dielectric properties of $Ca(Ca_{1/4}Nb_{2/4}Ti_{1/4})O_3$ complex perovskites material.

4.5 REFERENCES

[1] W. Wersing, *Electronic ceramics*, edited by B. C. H. Steele (Elsevier, Amsterdam, 1991) p. 67.

[2] S. J. Fiedziuszko, I. C. Hunter, T. Itoh, Y. Kobayashi, T. Nishikawa, S. N. Stitzer and K. Wakino, *IEEE Trans. Microwave Theory Tech.* **MTT 50** (2002) 706 - 720.

[3] P. K. Davies, *Materials and Processes for Wireless communication*, edited by T. Negas and H. Ling (Ceramic Transactions, American Ceramic Society, Westerville, OH, 53, 1995) p. 137.

[4] R. J. Cava, *J. Mater. Chem.* **11** (2001) 54.

[5] K. P. Surendran, Manoj R. Varma, M. T. Sebastian and P. Mohanan, *J. Mater. Res.* **17** (2002) 2561.

[6] P. V. Bijumon, S. Solomon, P. Mohanan and M. T. Sebastian, *J. Mater. Sci. Mater. Electron.* **14** (2003) 5.

[7] M.T. Sebastian, N. Santha, P. V. Bijumon, Anna Axelsson and Neil Mc Alford, *J. Eur. Ceram. Soc.* **24** (2004) 2583.

[8] K. P. Surendran, Manoj R. Varma, M. T. Sebastian and P. Mohanan, *J. Am. Ceram. Soc.* **86** (2003) 1695.

[9] K. P. Surendran, P. Mohanan and M. T. Sebastian, *J. Eur. Ceram. Soc.* **23** (2003) 2489 - 2495.

[10] C – L Huang and Y – C Chen, *J. Eur. Ceram. Soc.* **23** (2003) 167.

[11] S. K. Kucheiko, D – H. Yeo, J-W. Choi, S-J. Yoon and H-J. Kim, *J. Am. Ceram. Soc.* **85** (2002) 1327.

[12] T. Takada, S. F.Wang, Y. Yoshikawa, S. J. Jang and R. E. Newnham, *J. Am. Ceram. Soc.* **77** (1994) 2485.

[13] N. Setter, and R. Waser, *Acta. Mater.* **48** (2000) 151.

[14] S. Nomura, K. Toyama and K. Kaneta, *Jpn. J. Appl. Phys.* **21** (1982) 624.

[15] Y. Kawashima, N. Nishida, I. Ueda and H. Ouchi, *J. Am. Ceram. Soc.* **66** (1983) 421.

[16] M. P. Seabra, M. Avdeev, V. M. Ferreira, R. C. Pullar and N. McN. Alford,

J. Eur. Ceram. Soc. **23** (2003) 2403.

[17] W. Wersing, *Current opinion in solid state and material science* **1** (1996) 715.

[18] S. Nomura, *Ferroelectrics* **49** (1983) 61.

[19] H. Kagata and J. Kato, *Jpn. J. Appl. Phys.* **33** (1994) 5463.

[20] S. Kucheiko, J. W. Choi, H. J. Kim and H – J Jung, *J. Am. Ceram. Soc.* **79** (1996) 2739.

[21] I. Maclaren and C. B. Ponton, *J. Mater. Sci.* **33** (1998) 17.

[22] O. Renoult, J-P. Boilot, F. Chaput, R. Papiernik, L. G. Hubert-Pfalzgraf and M. Lejeune, *J. Am. Ceram. Soc,* **75** (1992) 3337.

[23] C-H. Lu, and C-C. Tsai, *Mater. Sci. Eng.* **B 55** (1998) 95.

[24] M-H. Liang, S-Y. Wu, C-T. Hu and I-N. Li, *Mater. Chem. Phys.* **79** (2003) 276.

[25] H. M. Shirey, "*Low temperature synthesis of the microwave dielectric material Barium Magnesium Tantalate (BMT)*", M. S. Thesis, University of Pittsburg (2002).

[26] S. Katayama, I. Yoshinaga, N. Yamada and T. Nagai, *J. Am. Ceram. Soc.* **79** (1996) 2059.

[27] G. Huang, D. Zhou, J. Xu, X. Chen, D. Zhang, W. Lu and B. Li, *Mater. Sci. Eng.* **B99** (2003) 416.

[28] C. L. Huang, M., H. Weng, C. T. Lion and C. C. Wu, *Mater. Res. Bull.* **35** (2000) 2445.

[29] Y. C. Lee, W. H. Lee and F. S. Shieu, *Jpn. J. Appl. Phys.* **419** (2002) 6049.

[30] S. F. Wang, C. C Chiang, C., H. Wang and J. P. Chu, *J. Mater. Res.* **18** (2003) 201.

[31] C-M. Cheng, C-F.Yang, S-H. Lo and T-Y. Tseng, *J. Eur. Ceram. Soc.* **20** (2000) 1061.

[32] D. W. Kim, D. G. Lee and K. S. Hong, *Mater. Res. Bull.* **36** (2001) 585.

[33] S. G. Lu, K. W. Kwok, H. L. W. Chen and C. L.Choy, *Mater. Sci. Engg.* **B99** (2003) 491.

[34] H. Jantunen, R. Rautioaho, A. Uusimaki and S. Leppavuri, *J. Eur. Ceram. Soc.* **20** (2000) 2331.

[35] H. Jantunen, R. Rautioaho, A. Uusimaki and S. Leppavuori, *J. Am. Ceram. Soc.* **85** (2002) 697.

[36] C-S. Chen, C-C. Chou, C-S. Chen and I-N. Lin, *J. Eur. Ceram. Soc.* **24** (2004) 1795.

[37] H. Kagata, T. Inoue, J. Kato and I. Kameyama, *Jpn. J. Appl. Phys.* **31** (1992) 3152.

[38] C-M. Cheng, Y-T. Hsieh and C-F. Yang, *Ceram. Inter.* **28** (2002) 255.

[39] C.-M. Cheng, Y-T. Hsieh and C-F. Yang, *Mater. Lett.* **57** (2003) 1471.

[40] K. P. Surendran, P. Mohanan and M. T. Sebastian, *J. Solid State Chem.* **177** (2004) 4031.

[41] J. H. Jeon and S. C. Lin, *J. Amer. Ceram. Soc.* **83** (2000) 1417.

[42] K. H. Yoon, S. J. Yoo, W. S. Kim, J. B. Kim and E. S. Kim, *Jpn. J. Appl. Phys.* **38** (1999) 5616.

[43] B. W. Hakki and P. D. Coleman, *IRE Trans. on Microwave Theory Tech.* **MTT-8** (1960) 402.

[44] W. E. Courtney, IEEE Trans. on Microwave Theory Tech. **MTT-18** (1970) 476.

[45] J. Krupka, K. Derzakowski, B. Riddle and J. B.-Jarvis, *Meas. Sci. Technol.* **9** (1998) 1751.

[46] P. Liu, E. S. Kim and K. H. Yoon, *Jpn. J. Appl. Phys.* **40** (2001) 5769.

[47] R. D. Shannon, *Acta Cryst.* **A32** (1976) 751.

[48] D. L. Corker, R. W. Whatmore, E. Ringgaand and W. W. Wolny, *J. Eur. Ceram. Soc.* **20** (2000) 2039.

[49] D-W. Kim, K. S. Hong, C. S. Yoon and C. K. Kim, *J. Eur. Ceram. Soc.* **23** (2003) 2597.

[50] H. Jantunen, "*A Novel Low Temperature Co-firing Ceramics (LTCC) material for telecommunication devices*", Ph.D Thesis, University of Oulu, Finland (2001).

[51] J-M. Wu and H-L. Huang, *J. Non. Cryst. Sol.* **260** (1999) 116.

[52] P. Liu, E. S. Kim and K. H.Yoon, *Jpn. J. Appl. Phys.* **40** (2001) 5769.

[53] J-M. Wu and H-L. Huang, *J. Non. Cryst. Sol.* **260** (1999) 116.

CHAPTER 5

TAILORING THE PROPERTIES OF $Ca(Ca_{1/4}Nb_{2/4}Ti_{1/4})O_3$ CERAMICS BY CATIONIC SUBSTITUTIONS

The effect of cationic substitutions on the structure, microstructure and microwave dielectric properties of $Ca_5Nb_2TiO_{12}$ ceramics are discussed in this chapter. Microwave dielectrics in the $Ca_{5-x}A_xNb_2TiO_{12}$ (A = Ba, Sr), $Ca_{5-x}A'_xNb_2TiO_{12}$ (A' = Mg, Zn, Ni & Co) and $Ca_5Nb_2Ti_{1-x}C_xO_{12}$ (C = Zr, Hf) ceramics have been prepared. The structural transformation in $Ca_{5-x}A_xNb_2TiO_{12}$ (A = Ba, Sr) ceramics are investigated by Raman and FTIR spectroscopic methods. Transmission mode resonance spectra of $Ca_{5-x}A'_xNb_2TiO_{12}$ (A' = Mg, Zn, Ni & Co) dielectric resonator materials are simulated employing 3D TLM methods and hence the microwave dielectric properties were calculated. The results present excellent agreement between experiment and simulation. $Ca_{5-x}A'_xNb_2TiO_{12}$ (A' = Mg, Zn, Ni & Co) and $Ca_5Nb_2Ti_{1-x}C_xO_{12}$ (C = Zr, Hf) ceramics form temperature stable dielectric resonator materials for $0 \leq x \leq 1$ and are potential candidates for applications in wireless communication devices.

5.1 INTRODUCTION

The progress in wireless communication technology necessitated the development of microwave dielectric resonator (DR)[1,2] materials with improved properties to enable cost effective and more efficient application in devices[3,4,5] comprising them. However, because of the difficulty in controlling all the dielectric properties at microwave frequencies, intense work is going on in search of new materials with high ε_r, high Q_u and low τ_f. Complex perovskite oxide (ABO_3) materials[6,7,8,9] form a major class of dielectric resonator family and have been extensively investigated because of their excellent microwave dielectric properties (See Section 3.1.3 of Chapter 3). Most of them have high quality factor and posses ε_r in the range 20 - 35. Materials having still high dielectric constant are preferable since they can further aid size reduction of the microwave circuit. Calcium and strontium based complex perovskites[10,11] are of special interest since they feature moderate dielectric constant and τ_f. Presently active work is being carried out in search of new materials[12,13] with improved properties as well as tailoring the properties of existing materials by doping[14,15] glass addition[16,17] and solid solution formations.[18,19,20,21]

Solid solution is simply the act of dissolving one ionic material into another. When other elements are dissolved into the lattice of a crystal, they help to impede the movement of dislocations and lattice defects. This in turn affects the physical, mechanical, chemical and electrical properties of the material. There are two types of solid solutions. The first is a substitutional solution. In this case atoms of the solute material replace atoms of the solvent material in the crystal lattice. The second type is called an interstitial solid solution formation. In this case, solute atoms are small enough to fit into spaces (interstices) between the solvent atoms in the crystal lattice. There are some fundamental criteria to be obeyed for ionic material solid solution to occur; which include (i) The ionic radii of the solute element should be comparable with that of the solvent ion which is to be replaced (ii) the valence charge of the replacing ion has to be identical to the charge of the replaced ion and (iii) the solute and solvent ion to be get replaced should have similar chemical affinity with other ions in the case of solid solution formation in polycrystalline materials. In most of the practical cases, while forming solid solutions in polycrystalline ceramics, the above mentioned ideal conditions will not be maintained. The slight difference in ionic radius,

polarizability etc. of the substituted ion brings out significant changes in the properties of the host material. Hence this method has been extensively used for tailoring the microwave dielectric properties of dielectric resonator materials.

As described in Section 3.3.2 of Chapter 3, complex perovskite type material, $Ca_5Nb_2TiO_{12}$ is a promising dielectric resonator with reasonably good dielectric properties. The ceramics has ε_r = 48, $Q_u \times f >$ 26000 GHz and τ_f = +40 ppm/°C at microwave frequencies. Efforts have also been made to tailor the microwave dielectric properties of the materials by doping and glass addition (See Chapters 3 and 4). Cationic substitution in the complex perovskite structure has been reported in literature[18 - 21] as an efficient method to tune the dielectric properties of ceramics, especially to attain the temperature compensation of their resonant frequency. Hence in this chapter the effect of cationic substitutions in the perovskite *A* and *B*-sites of $Ca_5Nb_2TiO_{12}$ ceramics are discussed. Solid solutions of ceramic systems in (i) $Ca_{5-x}A_xNb_2TiO_{12}$ (*A* = Ba, Sr), (ii) $Ca_{5-x}A'_xNb_2TiO_{12}$ (*A'* = Mg, Zn, Ni & Co) and (iii) $Ca_5Nb_2Ti_{1-x}C_xO_{12}$ (C = Zr, Hf) have been synthesized and their structure, microstructure and microwave dielectric properties were investigated.

Calcium-barium and calcium-strontium solid solution formation[22,23,24] in the perovskite *A*-site of dielectric resonator material has attracted much attention because of their interesting structural and dielectric properties. The extreme chemical and structural complexity of $Ca_5Nb_2TiO_{12}$ system indicates that additional studies must be carried out for an improved understanding of structure-property relationship. Also, the introduction of other isovalent metal ions in the system, like barium/strontium, could modify the structural and dielectric properties of these materials. In this respect, Raman and Fourier-transform infrared spectroscopies were employed, to investigate the vibrational properties originated from the gradual substitution of Ba/Sr on the perovskite *A*-site in place of Ca, as well as its effects on the metal-oxygen stretching/bending vibrations in $Ca_{5-x}A_xNb_2TiO_{12}$ (A = Ba, Sr) dielectric resonator materials.

$Ca_5Nb_2TiO_{12}$ material is preferable for use in miniaturized devices because of its high dielectric constant along with reasonably good quality factor. But the relatively high τ_f value precludes their immediate use in practical circuits. For microwave dielectrics the tuning ability of τ_f is required for stability of the circuit with an accuracy of ± 0.5 ppm/°C[25]. The

compensation of resonant frequency with temperature can be achieved either by combining two comparable compounds with opposite τ_f[26,27,28] or by modifying the unit cell volume with the partial substitution of suitable ions.[21,29,30] With this in mind the microwave dielectric properties of $Ca_{5-x}A'_xNb_2TiO_{12}$ (A' = Mg, Zn, Ni & Co) and $Ca_5Nb_2Ti_{1-x}C_xO_{12}$ (C = Zr, Hf) ceramics as a function of x have been investigated. The effect of substitution reactions on the phase purity, structure, microstructure and densification of the ceramics were also been investigated.

5.2 $Ca_{5-x}A_xNb_2TiO_{12}$ (A = Ba, Sr) CERAMICS

5.2.1 Experimental

$Ca_{5-x}Ba_xNb_2TiO_{12}$ and $Ca_{5-x}Sr_xNb_2TiO_{12}$ ceramics were prepared by conventional solid-state route as described in Chapter 2, Section 2.1.2. Stoichiometrically weighed and ball milled oxide mixtures were calcined in the temperature range 1200 – 1350°C for 4 hours in platinum crucibles. The synthesized ceramic pucks were sintered in the temperature range 1470-1550°C, for 4 hours with an intermediate firing at 800°C to expel the organic binder. The sintered samples were well polished and their bulk densities were calculated by Archimedes method. Structural phases were identified by powder X-Ray diffraction (XRD) technique using CuKα radiation. Scanning electron micrographs were recorded from the surface of sintered thermally etched samples to analyze the microstructure of the ceramics. The microwave dielectric properties were measured employing resonance method[31,32,33] as described in Chapter 2, Sections 2.3.2 to 2.3.5.

Micro-Raman scattering spectra were recorded using a Horiba/Jobin-Yvon LABRAM-HR spectrometer, equipped with a 1800 grooves/mm diffraction grating, a liquid-N_2-cooled CCD detector and a confocal microscope (100 × objective). The experimental resolution was better than 1 cm^{-1}. After fitting, the ultimate resolution was 0.2 cm^{-1}. The measurements were carried out in back-scattering geometry at room temperature, using the 632.8 nm line of a helium-neon ion laser (power 12.5 mW) as excitation source. A holographic notch filter was used to stray-light rejection (Rayleigh scattered light). The

sample surfaces of the sintered materials were previously polished to an optical grade in order to improve the ratio of inelastic to elastic scattered light.

Infrared reflectance spectra were recorded in a Fourier-transform spectrometer (Bomem DA8-02) equipped with a fixed-angle specular reflectance accessory (external incidence angle of 11.5°). The far-infrared range (50-500 cm^{-1}) was studied by using a mercury-arc lamp, a 6 μm coated Mylar hypersplitter,® and LHe-cooled Si-bolometer. In the mid-infrared region (500-4000 cm^{-1}) we used a globar source (SiC), a Ge-coated KBr beam splitter and a LN_2-cooled HgCdTe detector. One of the ceramic faces received a thin gold coating and was used as a "rough" mirror for the reference spectra. This procedure allowed us to improve the reflectivity spectra, since the mirror surface mimics the sample one, which compensates the effects of diffuse reflection at the sample surface. The measurements were performed under low vacuum (10^{-3} bar) with a typical resolution of 2 cm^{-1}.

5.2.2 Results and Discussion

5.2.2.1 Structural Characterization

XRD pattern of $Ca_{5-x}Ba_xNb_2TiO_{12}$ and $Ca_{5-x}Sr_xNb_2TiO_{12}$ ceramics are shown in Figs. 5.1 and 5.2 respectively. The patterns are different for both Ba and Sr based ceramics. It is known that[34] in a perovskite material bigger cation will occupy *A*-site of the perovskite structure and hence in the present case, the compositions can be possibly represented as $Ca(Ca_{1/4}Nb_{2/4}Ti_{1/4})O_3$, $Ca_{3/4}A_{1/4}(Ca_{1/4}Nb_{2/4}Ti_{1/4})O_3$, $Ca_{2/4}A_{2/4}(Ca_{1/4}Nb_{2/4}Ti_{1/4})O_3$, $Ca_{1/4}A_{3/4}(Ca_{1/4}Nb_{2/4}Ti_{1/4})O_3$, and $A(Ca_{1/4}Nb_{2/4}Ti_{1/4})O_3$ [A = Ba, Sr] for x = 0, 1, 2, 3 and 4, respectively owing to the onset of higher ionic radius[35] of A^{2+} compared with that of Ca^{2+}. $Ca_5Nb_2Ti_1O_{12}$ has orthorhombic structure with four formula units in the primitive cell and regular alternation of *B*-site ions along *a, b, c* axes. Hence, the XRD patterns in Figs. 5.1 and 5.2 for the compositions with x = 0 have been indexed based on the orthorhombic *Pnma* symmetry.

With the substitution of one Ba^{2+} ion for Ca^{2+}, a multiphase ceramic was formed instead of single phase $Ca_4BaNb_2TiO_{12}$ as evidenced by the XRD profile shown in Fig. 5.1 (b). The phases were identified as $Ca_4Nb_2O_9$ (ICDD File Card Nos. 49 – 911) and $BaTiO_3$ (ICDD File Card No. 34 – 129) and were indexed accordingly. In the compositions with x =

2, 3 and 4 the materials have cubic double perovskite structure with an occupancy of two cations in the *A*-site (Ca, Ba) for $x = 2$ and 3 and only one cation (Ba) for $x = 4$. In order to obtain their structural parameters, their main reflections were indexed comparing with the XRD profile of $Ba(Zn_{1/3}Nb_{2/3})O_3$ (ICDD File 17–182) having cubic symmetry.

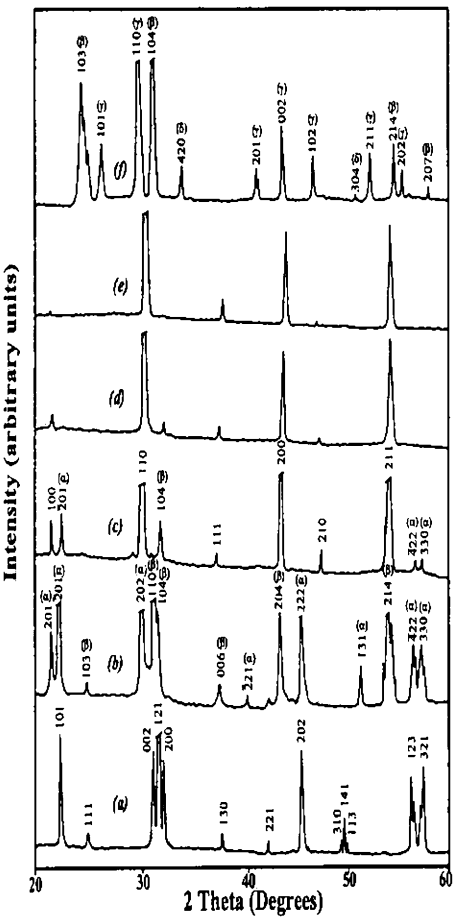

Fig. 5.1 X-Ray diffraction pattern of (a) $Ca_5Nb_2TiO_{12}$ (b) $Ca_4Nb_2O_9 - BaTiO_3$ mixture (c) $Ca_3Ba_2Nb_2TiO_{12}$ (d) $Ca_2Ba_3Nb_2TiO_{12}$ (e) $CaBa_4Nb_2TiO_{12}$ and (f) $Ba_4Nb_2O_9 - BaTiO_3$ mixture ($\alpha \rightarrow Ca_4Nb_2O_9$, $\beta \rightarrow BaTiO_3$, $\gamma \rightarrow Ba_4Nb_2O_9$ and $\delta \rightarrow BaNb_2O_6$ diffraction peaks)

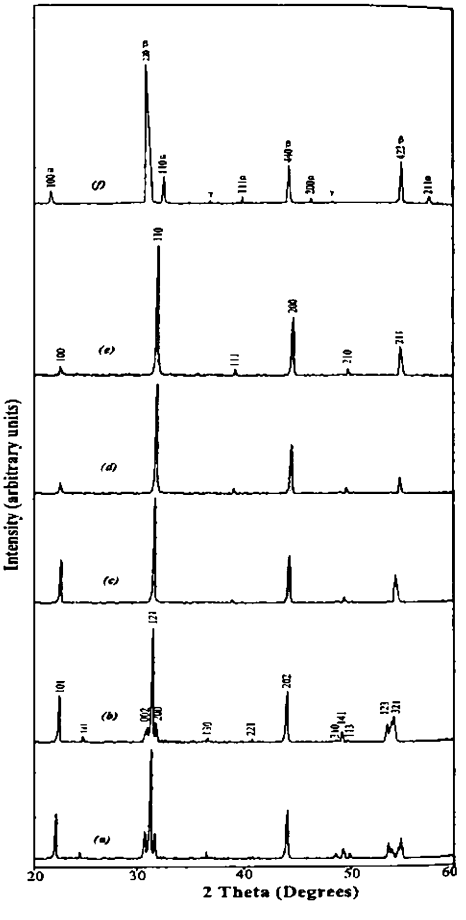

Fig. 5.2 X-Ray diffraction pattern of (a) $Ca_5Nb_2TiO_{12}$, (b) $Ca_4SrNb_2TiO_{12}$, (c) $Ca_3Sr_2Nb_2TiO_{12}$, (d) $Ca_2Sr_3Nb_2TiO_{12}$, (e) $CaSr_4Nb_2TiO_{12}$, and (f) $Sr_4Nb_2O_9$ - $SrTiO_3$ ceramics ($\alpha \rightarrow SrTiO_3$, $\beta \rightarrow Sr_4Nb_2O_9$ and $\gamma \rightarrow$ unidentified peaks).

With x = 2 and 3, traces of secondary phases corresponding to $Ca_4Nb_2O_9$ and $BaTiO_3$ were also detected in the XRD pattern. For x = 4, phase pure $Ba(Ca_{1/4}Nb_{2/4}Ti_{1/4})O_3$ was formed as shown in Fig. 5.1 (e) with cubic symmetry. With x = 5, a mixture of $Ba_4Nb_2O_9$ - $BaTiO_3$ and a few peaks corresponding to $BaNb_2O_6$ (ICDD File Card No. 32 – 77) was formed.

In the case of strontium substitution, the compositions with x = 0 and 1, have been indexed based on the orthorhombic *Pnma* symmetry (See Section 3.3.2 of Chapter 3) as shown in Fig. 5.2 (a) and 5.2 (b). The compositions with x = 2 to 4, Figs. 5.2 (c), 5.2 (d) and 5.2 (e) presented an averaged cubic double-perovskite[36] structure as that occurred with Ba substitution. With x = 5, a mixture of $Sr_4Nb_2O_9$ (ICDD File 48–558) and $SrTiO_3$ (ICDD File 35–734) is formed as it is evident from Fig. 5.2 (f).

In the case of both Ba and Sr-substitution, for x = 2 to 4, the XRD profiles consist of strong peaks characteristic of the primitive *Pm3m* cubic perovskite together with extra lines arising from superlattice reflections. However, XRD analysis are not accurate enough to assure that a structural phase transition from *Pnma* to *Pm3m* takes place when x varies from 1 to 2 in both $Ca_{5-x}Ba_xNb_2TiO_{12}$ and $Ca_{5-x}Sr_xNb_2TiO_{12}$ ceramics. Indeed, as we can observe in Figs. 5.1 (c) and 5.2 (c) (both for x = 2), the (123) and (321) orthorhombic peaks are still present in the diffractograms. A similar effect can be observed for the orthorhombic (200) and (002) peaks that merge with the (121) peak into the experimental resolution. For higher x values (x = 3 and 4), X-Ray diffractometry is no longer able to distinguish between a true cubic structure and a pseudo-cubic one, where the orthorhombic ferroelastic distortion became too small. This difficulty could be overcome by the study of the local symmetries by spectroscopic techniques, as it will be shown in the corresponding sections below. With the introduction of larger $(Ba/Sr)^{2+}$ ions, the anisotropic cell expansion decreases the differences between the lattice parameters and the structure evolves from a clear orthorhombic to a pseudo-cubic structure, but the space group remains *Pnma*. The effect of radius of the substituted cation is still more important for x = 5. Indeed, $(Ba/Sr)^{2+}$ ion is too large to enter into the *B*-site of the perovskite structure, so that this structure is not formed.

The synthesizing conditions, cell volume, density and tolerance factor of $Ca_{5-x}Ba_xNb_2TiO_{12}$ and $Ca_{5-x}Sr_xNb_2TiO_{12}$ are given in Table 5.1 and 5.2 respectively. It is evident from the tables that, the sintering temperature varies from 1550 – 1470°C/4h with variation

of x from 0 to 4 in $Ca_{5-x}Ba_xNb_2TiO_{12}$ whereas, only slight change in sintering temperature was observed in the Sr-substituted system with compositional variations. In the Ba-based system, with $x = 5$, the ceramics were not able to sinter in compact form as they crumbled to powder after firing. Efforts were made to sinter these materials by adding different wt. % of low melting CuO, but did not succeed. It is evident from Tables 5.1 and 5.2 that, the substitution of Ba/Sr for Ca in the perovskite *A*-site increases the cell volume. The enhancement in cell volume observed with compositional variations is due to the substitution of bigger barium/strontium ion in place of comparatively smaller calcium ion. It should be remembered that, for $x = 2$, 3 and 4 the superstructure volumes were calculated based on cubic perovskite framework, for which the atomicity is $Z = 1$, whereas for the orthorhombic group $Z = 4$. Hence, to make in line with the cell volume of orthorhombic structures the unit cell volumes of the pseudo-cubic structures were multiplied by 4 in both Ba and Sr substituted systems. In $Ca_{5-x}Ba_xNb_2TiO_{12}$ ceramics the theoretical density varies from 4.19 to 5.84 g/cm^3 whereas, in $Ca_{5-x}Sr_xNb_2TiO_{12}$ ceramics the theoretical density varies from 4.19 to 5.13 g/cm^3. In both the cases the percentage density increased with orthorhombic to cubic transformation and reached more than 98 % of the theoretical value.

Table 5.1 Synthesizing conditions, structure, cell volume, density and tolerance factor of $Ca_{5-x}Ba_xNb_2TiO_{12}$ ($0 \leq x \leq 5$) ceramics

x	Calcination Temperature (°C)	Sintering Temperature (°C)	Structure of the unit cell	Lattice Parameters (Å)			Cell Volume (Å^3)	Theoretical Density (g/cm^3)	% Density	Tolerance factor (t)
				a	b	c				
0	1350	1550	Orthorhombic	5.510(4)	7.907(9)	5.688(0)	247.858	4.19	96.4	0.9189
1	1300	1490	Mixture	#	#	#	#	#	#	#
2	1275	1475	Cubic	4.115(6)	--	--	278.849	4.99	97.0	0.9585
3	1240	1500	Cubic	4.137(9)	--	--	283.410	5.42	97.4	0.9810
4	1210	1470	Cubic	4.162(7)	--	--	288.522	5.76	98.3	1.0035
5	1200	*	Mixture				#	#	#	#

* Could not be sintered

Formed as mixture phase

Secondary phase observed

The increase in density with x is quite expected, as the molecular weight of Ba/Sr is higher than that of Ca. The tolerance factor (t)[37], which is a measure of the symmetry of the perovskite structure is calculated for the investigated ceramic systems using the relation,

$$t = \frac{R_O + R_{Ca}(4-x)/4 + R_A(x)/4}{\sqrt{2}\ \left[R_O + \left(0.25R_{Ca} + 0.50R_{Nb} + 0.25R_{Ti}\right)\right]} \qquad (5.1)$$

where R denotes the radius of corresponding cations occupying the appropriate perovskite sites.

Table 5.2 Synthesizing conditions, lattice parameters, cell volume, density and tolerance factor of $Ca_{5-x}Sr_xNb_2TiO_{12}$ ($0 \le x \le 5$) ceramics

x	Calcination Temp. (°C)	Sintering Temp. (°C)	Structure of the unit cell	Lattice parameters (Å)			Cell Volume (Å^3)	Theoretical Density (g/cm^3)	% Density	Tolerance factor (t)
				a	b	c				
0	1350	1550	Orthorhombic	5.510(4)	7.907(9)	5.688(0)	247.858	4.19	96.42	0.9189
1	1300	1550	Orthorhombic	5.533(5)	7.906(9)	5.696(2)	249.225	4.29	96.41	0.9273
2	1275	1540	Pseudo-Cubic	3.974(1)	-	-	251.051	4.77	96.70	0.9357
3	1275	1530	Pseudo-Cubic	4.024(0)	-	-	260.641	4.91	96.21	0.9441
4	1260	1530	Pseudo-Cubic	4.043(6)	-	-	264.115	5.13	98.66	0.9525
5	1240	1550	Mixture ($Sr_4Ta_2O_9$ – $SrTiO_3$	b	b	b	b	b	b	b

[b] Could not be calculated because of the mixed-phase nature.

In both the systems, the tolerance factor was found to be increased and approaches unity which can be attributed to the increase in average A-site ionic radius due to the substitution of bigger Ba/Sr ions for Ca. This is in line with the fact that as the tolerance factor tends to unity, the symmetry changes to cubic perovskite form. From Tables 5.1 and 5.2, it is clear that, with the increase of barium/strontium content the tolerance factor increases and approaches unity.

5.2.2.2 Microstructural Analysis

The microstructure of few typical $Ca_{5-x}A_xNb_2TiO_{12}$ (A = Ba, Sr) ceramics for different x values recorded using Scanning Electron Microscopic method are shown in Fig. 5.3. Microstructure of $Ca_5Nb_2TiO_{12}$ has been described earlier with uniform distribution of large grains of about 10 μm size (See Chapter 3, Section 3.3.2).

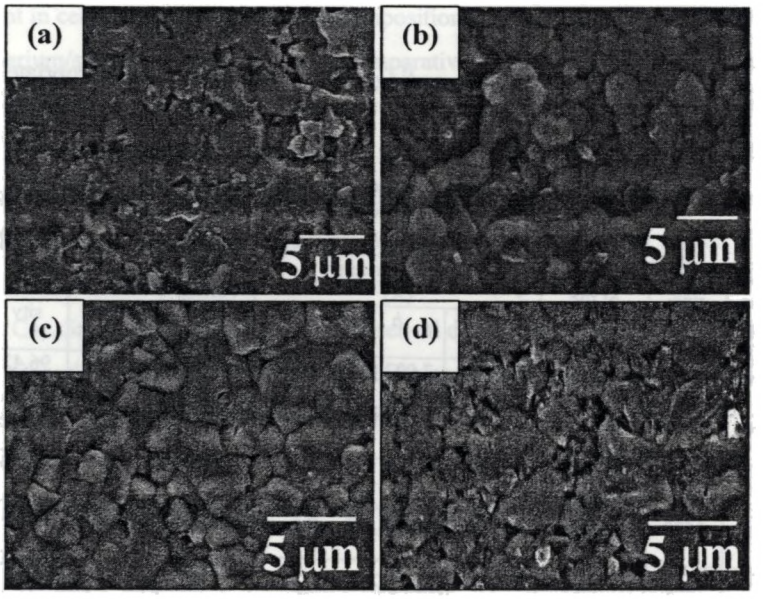

Fig. 5.3 SEM pictures of (a) $Ca_4Nb_2O_9$ – $BaTiO_3$ mixture (b) $Ca_3Ba_2Nb_2TiO_{12}$ (c) $CaSr_4Nb_2TiO_{12}$ and (d) $Sr_4Nb_2O_9$ - $SrTiO_3$ mixture

Fig. 5.3 (a) shows the surface morphology of $Ca_4Nb_2O_9$ - $BaTiO_3$ mixture phase formed in $Ca_{5-x}Ba_xNb_2TiO_{12}$ system for x = 1. Two different types of grains are clearly visible with an additional indication of liquid phase formation. The surface morphology of $Ca_2Ba_3Nb_2TiO_{12}$ ceramics are shown in Fig. 5.3 (b). The grain distribution become more uniform in this specimen compared with its previous x composition. A gradual change in grain shape is visible indicating the structural transformation with composition. The microstructure of $CaSr_4Nb_2TiO_{12}$ are shown in Fig. 5.3 (c). It is evident from the figures that their average grain size is about 2 μm, which is much less than that of $Ca_5Nb_2TiO_{12}$ ceramics described in Chapter 3, Section 3.3.2. Moreover the grains are thickly packed leaving less porosity in the

specimen. This implies that the substitution of Sr^{2+} with Ca^{2+} improves the sinterability and enhances densification (see Tables 5.1 and 5.2). The surface morphology of $Sr_4Nb_2O_9$-$SrTiO_3$ specimen is depicted in Fig. 5.3 (d). The complete substitution of Sr^{2+} in place of Ca^{2+} ions resulted in the formation of a mixture phase as is evident from the presence of two distinct types of grains. A pronounced difference in microstructure is observed between samples shown in Fig. 5.3 (a) & 5.3 (d) and that appeared in Fig. 5.3 (b) & 5.3 (c). In Fig. 5.3 (a) and 5.3 (d) mixture phases can be observed in the specimen as that confirmed by XRD analysis whereas Figs. 5.3 (b) and 5.3 (c) show uniform microstructural distribution with well defined grain boundaries indicating the formation of single phase materials in the solid solution compositions.

5.2.2.3 Microwave Dielectric Properties

The microwave dielectric properties of $Ca_{5-x}Ba_xNb_2TiO_{12}$ ($0 \leq x \leq 4$) ceramics are shown in Fig. 5.4. The $Q_u \times f$ shows an abrupt decrease when x is varied from 0 to 1 and thereafter decreases gradually. This can be attributed to the lack of phase purity of the specimen for $x = 1$. The quality factor of $Ca_{5-x}Sr_xNb_2TiO_{12}$ ceramics with different mole fraction of strontium content also shows the same trend as that exhibited by the barium analogue (See Fig. 5.5). In this case the quality factor varies from 26000 GHz to 6000 GHz, when x changes from 0 to 3 and the $Q_u \times f$ increases abruptly to 11000 GHz, for $x = 4$. In $Ca_{5-x}Sr_xNb_2TiO_{12}$ ceramics, when $x = 0$ and $x = 4$ the perovskite A-site is completely occupied by either Ca (for $x = 0$) or Sr (for $x = 4$) ions and has higher $Q_u \times f$ compared to other compositions from $x = 1$ to 3, where combined occupancy of Ca and Sr ions takes place in the perovskite A-site. Moreover, it is evident from Fig. 5.5 that, the quality factor is higher for $x = 0$ than that of $x = 4$. The replacement of larger Ba/Sr ion with comparatively smaller Ca ions in the perovskite A-site leads to distortions in the unit cell and hence structural phase transition occurs, which causes the reduction of quality factor in $Ca_{5-x}Ba_xNb_2TiO_{12}$ and $Ca_{5-x}Sr_xNb_2TiO_{12}$ ceramics with increasing x. For $x = 5$ the multiphase compound which is a mixture of $Ba_4Nb_2O_9/Sr_4Nb_2O_9$ and $BaTiO_3/SrTiO_3$ was formed and it did not resonate in the

case of strontium based ceramics, whereas in the barium analogue the sample crumbled into powder and failed to form a pellet.

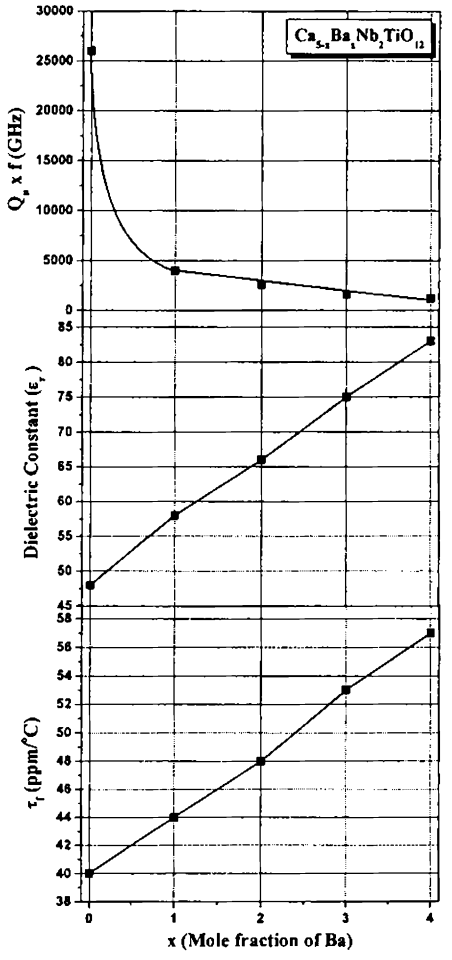

Fig. 5.4 Microwave dielectric properties of $Ca_{5-x}Ba_xNb_2TiO_{12}$ $(0 \leq x \leq 4)$ ceramics

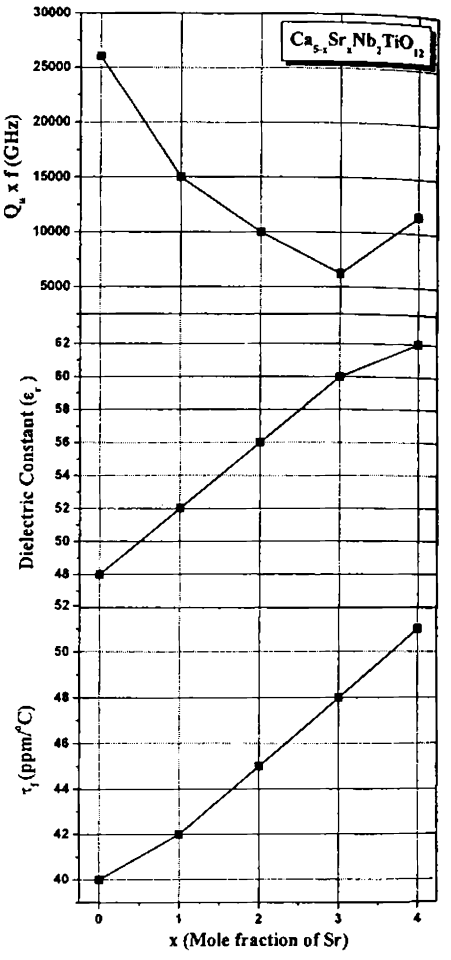

Fig. 5.5 Microwave dielectric properties of $Ca_{5-x}Sr_xNb_2TiO_{12}$ $(0 \leq x \leq 4)$ ceramics

In both the ceramics, the ε_r and τ_f shows a linear increase with increase in x (See Fig. 5.4 and 5.5). The dielectric constant and τ_f of $Ca_{5-x}A_xNb_2TiO_{12}$ (A = Ba, Sr) increases with A^{2+}content. It is quite expected as the dielectric polarisability of A^{2+} ions is higher than that

of Ca^{38}. The τ_f of both the ceramics shifted to higher positive values with A^{2+} concentration and it is attributed to the high positive τ_f of $BaTiO_3/SrTiO_3$[11]. The microwave dielectric properties in $Ca_{5-x}Ba_xNb_2TiO_{12}$ ceramics were believed to affected by the presence of secondary phase of lossy $BaTiO_3$[39] with high ε_r and high positive τ_ε.

5.2.2.4 Raman Spectroscopic Studies

Figs. 5.6 and 5.7 show the Raman spectra for $Ca_{5-x}Ba_xNb_2TiO_{12}$ and $Ca_{5-x}Sr_xNb_2TiO_{12}$ ($0 \leq x \leq 5$) microwave ceramics respectively. For $x = 0$ ($Ca_5Nb_2TiO_{12}$), characteristic bands of *A*-site occupied by Ca (117-123 cm^{-1}) and a complex set of bands related to *B*-site, which present an average $Ca_{1/4}Nb_{2/4}Ti_{1/4}$ occupancy appears in the spectrum. The broad band observed at 640 cm^{-1} can be assigned to the *B*-O symmetric stretching vibration.[40,41,42] The bands at 450-455 and 475-485 cm^{-1} are assigned to B-O_3 torsional (bending or internal vibration of oxygen cage) modes, although the frequencies verified in similar perovskites were higher.[49,50,51] This behaviour can be understood as an effect caused by the more distorted coordination environment of *B*-sites due to the presence of Ca, Nb and Ti in the solid solutions. The bands in the region 235-370 cm^{-1} are related to the modes associated with rotations of oxygen cage and *B*-site ordering.[51] The bands at 530-600 and 750-800 cm^{-1} correspond to oxygen motion (A_{1g} mode), which can be represented as symmetric and asymmetric "breathing" of the BO_6 octahedra, respectively. Concerning ordering, it is clear that the bands in the regions 300-400 and 750-800 cm^{-1} are related to 1:1 ordering, similar to the results of Raman spectroscopic studies carried out by Levin *et al.*[43] and Zheng *et al.*[46] in $Ca(Ca_{1/3}Nb_{2/3})O_3$ and $CaTiO_3$-based ceramics, respectively. According to the group-theory analysis for 1:1 superstructures with $Fm3m$ and 1:2 ordered perovskites with $P\bar{3}m1$ space group, A_{1g} and F_{2g} modes become Raman active due to *B*-site ordering.[44,45]

The Raman spectra of $Ca_{5-x}Ba_xNb_2TiO_{12}$ ceramics shows the same number of features for $x = 0$ and $x = 1$. The only noticeable change is the shifting of the spectra to lower frequencies as Ba is introduced in the system. On the other hand, microwave dielectric properties varied significantly by changing Ca by Ba, as it can be seen in Fig. 5.4 that, the introduction of only one Ba atom in the structure led to sudden decrease in $Q_u \times f$, from

26000 to 4000 GHz. The increase in the Ba content led to the reduction of the amount of $Ca_4Nb_2O_9$ phase at $x = 2$ and $x = 3$ (See Fig. 5.1). This result produced more significant changes in the Raman spectra. Bands at around 260 and 360 cm^{-1} appeared, increasing their intensity and became more narrow for increasing x.

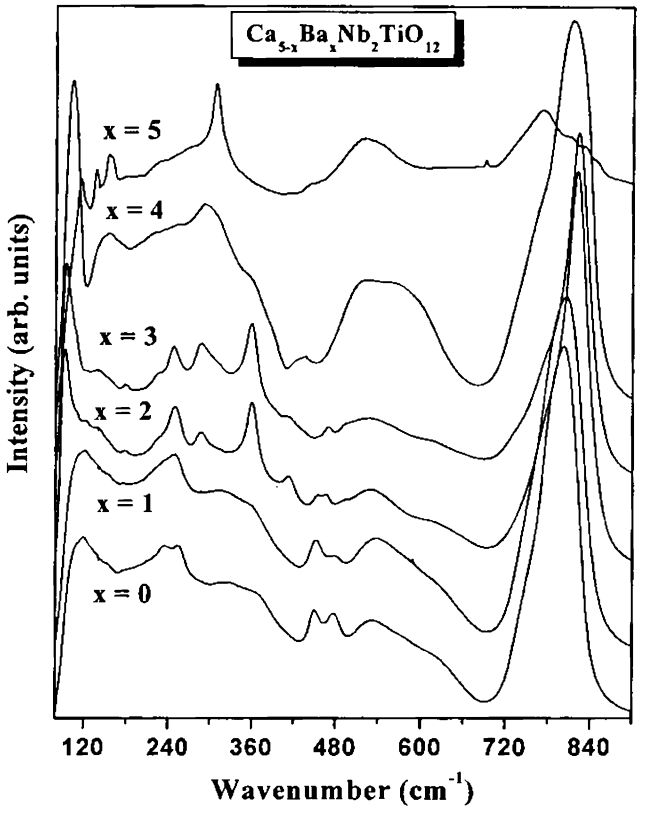

Fig. 5.6 Raman spectra of $Ca_{5-x}Ba_xNb_2TiO_{12}$ ceramics

Also, the bands at 120 and 800 cm^{-1} shifted to 100 cm^{-1} (redshift) and to 820 cm^{-1} ($A_{1g}(O)$ mode, which blue shifted). The $A_{1g}(O)$ mode shifted to higher frequencies for increasing Ba content is the result of volume change rather than mass. The strongest band around 800 cm^{-1} is related to the "breathing" mode of the NbO_6 octahedra and more pronounced shoulders are visible on both sides of this band. Levin *et al.*[43] observed these shoulders on the Raman

spectra of $Ca_4Nb_2O_9$ and attributed them to the presence of metastable superstructures. A similar result was observed by Zheng *et al.*[46] in $CaTiO_3$-$Sr(Mg_{1/3}Nb_{2/3})O_3$ ceramics and could be associated with short-range ordering.

The observed changes in the Raman bands at around 100 and 820 cm^{-1} for $x = 4$, in relation to lower values of x (at $x = 2$ and $x = 3$) announce the presence of a single-phase material. The first band of the spectra reflects the *A*-site environment, as well as probable rotations of the oxygen cage.[44] In this composition, the remained peaks of $BaTiO_3$ present in the X-Ray diffraction data at $x = 3$ (See Fig. 5.1) disappeared completely and a solid solution could be obtained with the nominal stoichiometry $Ba(Ca_{1/4}Nb_{2/4}Ti_{1/4})O_3$. Here, all Ba ions are now in the *A*-site and no more distortions observed at lower values of x (Ca ion in the *A*-site) can be visualized or detected. The broad bands showed that the *B*-site long-range ordering is already poor. With $x = 5$, the material represent, as a first approximation, a solid solution between $BaTiO_3$ and $Ba_4Nb_2O_9$, with titanium incorporation on the *B*-site of the perovskite-like structure. However, as verified by X-Ray diffraction (Fig. 5.1), the ceramics presented multiple phases ($Ba_4Nb_2O_9$, $BaTiO_3$ and $BaNb_2O_6$) and could not be sintered. At least 22 bands can be seen in the spectra as a result of the superposition of different combination modes of all the crystalline phases. The appearance of different phases led to the development of multiple bands within the broad Raman peaks, which difficult the assignment in these materials.

With Sr substitution, we note first that the spectra for $x = 0$ to 4 show all the same number of features. This is compatible with the interpretation that, although the structure evolves to pseudo-cubic for higher x values, it remains orthorhombic for lower x values ($x = 0$ and 1). The band centered at 98 cm^{-1} shifted to lower frequencies with the introduction of Sr for x up to 4. Also, the peaks at 265 cm^{-1} decreased their intensity and became broader at higher frequencies for increasing x. It is evident from Fig. 5.7 that, the band at 117–123 cm^{-1} is shifted to higher frequencies with increase in x. As explained earlier, this region of the spectra reflects the *A*-site environment, as well as probable rotations of the oxygen cage. These results are also in line with the structural characterization that, the substitution of strontium by calcium occurs in the perovskite *A*-site, which cause strong effects in the band at 117–123 cm^{-1}. These effects results from the more pronounced distortions in the oxygen

octahedra due to the size difference between the isovalent cations Ca and Sr. Increasing amount of strontium atoms ($1 \leq x \leq 4$), now in *A*-sites, led to higher distortions, shifting the bands continuously to lower frequencies. This behaviour is related to the increased global mass in *A*-site due to the substitution of heaviour Sr^{2+} ions in the mixed complex ceramics. On the other hand, the $A_{1g}(O)$ mode shifted to higher frequencies for increasing Sr content as a result of the volume change as observed with Ba-substitution. When $x = 4$, the presence of only one calcium in *B*-site and complete substitution of Ca with Sr in the perovskite *A*- site lead to a maximum distortion, which activated forbidden Raman modes at 140-160 cm^{-1} in $Ca_{5-x}Sr_xNb_2TiO_{12}$ ceramics. In this case, the microwave properties showed interesting results for $x = 4$ (Fig. 5.5), with a sudden increase in Q_u probably associated to the distortions in the octahedra verified by Raman spectroscopy.

The most important variations were observed in the band centered at 455-482 cm^{-1}. The variations are assigned to BO_3 torsional modes, which shifted continuously to lower values for $x = 0$ to 4, together with a decreasing of the second band. Similarly, the bands in the region 540-660 cm^{-1} presented the same behaviour, and also increased their intensities with Sr introduction. On the contrary, the "breathing" modes centered at around 800 cm^{-1} shifted to higher frequencies with Sr substitution by more than 20 cm^{-1} when $x = 4$. But with $x = 5$, the same mode returns to lower frequency and appears at 795 cm^{-1} The mixture phase formation of $Ca_{5-x}Sr_xNb_2TiO_{12}$ with $x = 5$ is verified in the Raman spectroscopy by the unusual behaviour of shifting and disappearance of certain modes. The bands at 140-160cm^{-1} and 455-482 cm^{-1} disappeared and a final shift to higher frequencies occurred for the band at around 95 cm^{-1}, which moved to 118 cm^{-1} and the spectra looked different from that of all other compositions. It is in agreement with the XRD pattern that with $x = 5$, $Sr_5Nb_2TiO_{12}$ does not form but it is a mixture of $SrTiO_3$ and $Sr_4Nb_2O_9$.

The $A_{1g}(O)$ mode represents a qualitative indication of the degree of *B*-site ordering and, obviously, differences in charge or ionic sizes will influence the distribution of ions on any given site. Ca and Ba/Sr atoms present significant differences in their ionic sizes[35] and larger the difference, greater the influence on the vibrational modes, particularly those related to ordering. Zheng *et al.*[46] considered the possibility that the width and frequency of $A_{1g}(O)$ mode band may be affected by the size distribution of the *A*-site cations.

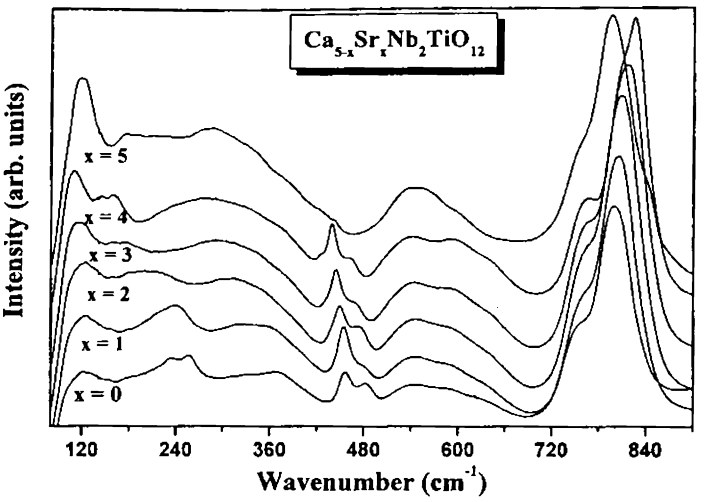

Fig. 5.7 Raman spectra of $Ca_{5-x}Sr_xNb_2TiO_{12}$ ceramics

Their conclusions are that the *A*-site ionic distribution influences the degree of short-range order on the *B*-site or, also, the size differences in *A*-site could constrict in some manner the octahedra "breathing" mode to occur in a given range of frequencies. In our case, it is believed that the $A_{1g}(O)$ mode is a function of the volume cage, which presents the maximum variation for $x = 4$ (complete replacement of Ca with Ba/Sr in *A*-site). Finally, correlating this result to the microwave properties, the decrease in Q_u with Ba/Sr introduction (See Figs. 5.4 and 5.5) could be expected, since its presence alters *A*-site distribution and probably increases the degree of short-range order. This increase is detrimental to Q_u because it induces anharmonicity and increases phonon damping. Zheng *et al.*[46] and Webb *et al.*[47] reported that the values of Q_u must increase only when the order changes from short to long-range. In this respect, it is interesting to observe the increase in Q_u for $x = 4$, with complete introduction of Sr in the perovskite *A*–site which probably leading to a long-range order at this composition. But no such effect was observed with Ba substitution where the quality factor decreased linearly with increasing Ba content. The mode at 240 cm^{-1} almost disappears for $x = 1$, 2 and 3, but reappears for $x = 4$ in both the systems. This is in agreement with the assumption that with $x = 0$ and $x = 4$ the perovskite *A*-site is occupied by single ions. When x

= 0, Ca^{2+} ions and with x = 4, $(Ba/Sr)^{2+}$ ions occupy the perovskite A-site. But the difference in ionic radius between the two makes lattice distortion and resultant structural changes, which was verified in XRD as well as Raman spectroscopic studies.

5.2.2.5 FTIR Analysis

Fig. 5.8 and 5.9 shows the infrared-reflectivity spectra between 50 – 700cm^{-1} for $Ca_{5-x}Nb_2TiO_{12}$ and $Ca_{5-x}Nb_2TiO_{12}$ microwave ceramics. FTIR results agree well with Raman-spectroscopic data, both concerning the conclusions on the structural evolution and on the dependence of vibrational features with cation substitutions.

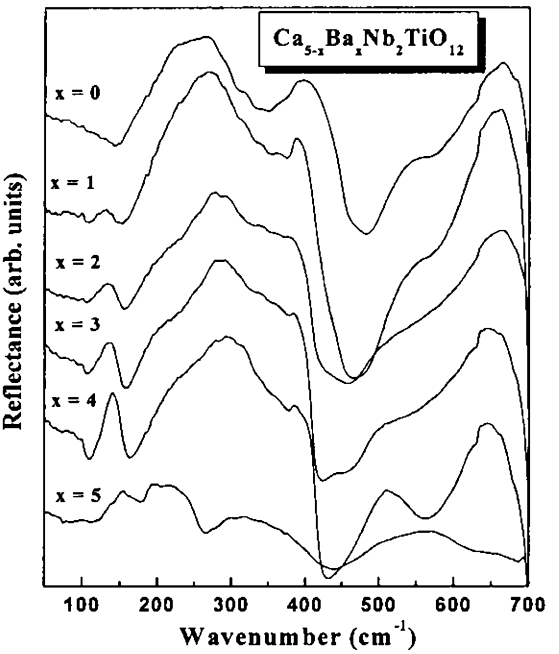

Fig. 5. 8 FTIR spectra of $Ca_{5-x}Ba_xNb_2TiO_{12}$ ceramics

In the FTIR spectra, bands below 100 cm^{-1} and above 600 cm^{-1} are difficult to assign due to instabilities in the measurements with consequent poor quality. Compounds with x = 0 ($Ca_5Nb_2TiO_{12}$), include a defined set of bands at 220, 265, 318, 370, 396, 470, 540, 570 and

370 cm^{-1}. The frequency region below 150 cm^{-1} can be attributed to the *A*-BO_3 external mode, while the O-*B*-O bending modes appear[48] between 170 and 500 cm^{-1}. The highest wavenumber range, 500-700 cm^{-1}, is due to the oxygen octahedra-elongation mode, that is, BO_6 stretching.

Barium substitution lead to a better definition of the bands at around 130 cm^{-1} with a maximum at $x = 4$. Also, a continuous shift occurred especially in the dip which centered at a region 490 cm^{-1} to 460 cm^{-1} with the addition of one Ba atom. The increase of the band at 520 cm^{-1} can be seen, which represents the oxygen octahedral elongation mode. Stronger bands at 130 and 180-260 cm^{-1} are a result of perturbations in the O-metal-O bending modes (inner mode vibrations) on *B*-sites, as well as in the band at around 320 cm^{-1}. The maximum broadening occurred at $x = 4$ in the spectral range 150-370 cm^{-1} and coincides with the formation of solid solutions in the composition $Ba(Ca_{1/4}Nb_{2/4}Ti_{1/4})O_3$. This frequency range can be considered as specific for ordered structures and their strength can be used as a relative measure of this ordering.[55,48] The frequency shifts observed from 440 to 420 cm^{-1} and from 550 to 520 cm^{-1} could be related to BO_3 torsional (ν_2) and *B*O stretching (ν_1) modes, and confirm our hypothesis that the Ba introduction occurs in the *A*-site of $Ca(Ca_{1/4}Nb_{2/4}Ti_{1/4})O_3$ perovskites. For $x = 5$, the spectra consist of four sets of broad bands because of the multiple-phase nature of these samples. The first of these bands is located below 180 cm^{-1}, the second one at 180-260 cm^{-1}, the third one at 260-440 cm^{-1} and the fourth one between 440 and 700 cm^{-1}. Other features, abundantly observed in the spectra, must be due to the additional polar modes activated by the multiple phases present.

Strontium substitution lead to the appearance of bands at around 150 cm^{-1} and in the range 220-320 cm^{-1} with a maximum at $x = 4$. Also, lattice distortions caused by changing of Ca by Sr broadened the band at 350-360 cm^{-1}. As in the case of Ba-substituted systems, shifts occurred especially in the dip centered at 490 cm^{-1} for $Ca_{5-x}Sr_xNb_2TiO_{12}$ ceramics. Also, it is interesting to note the increase of band at 550 cm^{-1}, which is related to the oxygen octahedral-elongation modes. In this case stronger bands at 150 and 220-320 cm^{-1} represent the perturbations in the O-metal-O bending modes on *B*-sites, as well as in the band at around 350 cm^{-1}. The maximum distortions at $x = 4$ coincides with the sudden increase observed in Q_u, and verified with the particular features formed in Raman spectra.

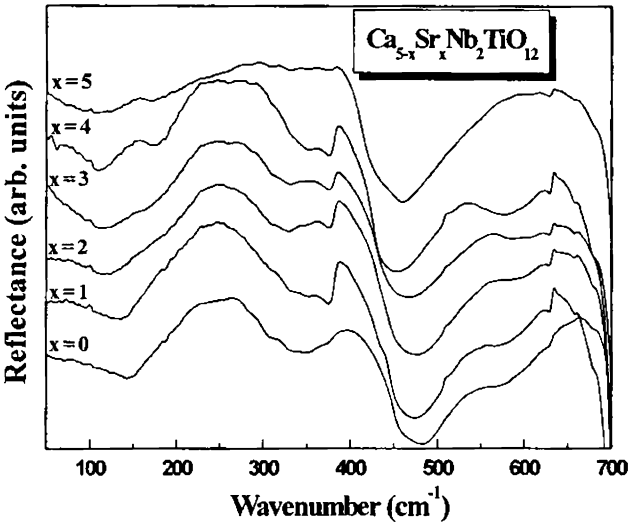

Fig. 5. 9 FTIR spectra of $Ca_{5-x}Sr_xNb_2TiO_{12}$ ceramics

In $Ca_{5-x}Sr_xNb_2TiO_{12}$ ceramics, the frequency shifts observed around 480 and 550 cm^{-1} in the FTIR spectra can be related to BO_3 torsional (ν_2) and BO stretching (ν_1) modes. It confirms the hypothesis that the Sr substitution occurs on the *A*-site of the complex perovskite material as observed with Ba substitution. At the same time with x = 5, the spectra looks different from that of all other cases, where the material form as a mixture.

5.3 $Ca_{5-x}A'_xNb_2TiO_{12}$ (A' = Mg, Zn, Ni & Co) CERAMICS

5.3.1 Experimental

5.3.1.1 Ceramic synthesis and characterization

The solid-state reaction route as described in Section 2.1.2 of Chapter 2 is used for synthesis of $Ca_{5-x}A'_xNb_2TiO_{12}$ (A' = Mg, Zn, Ni & Co) dielectrics. High purity (> 99.9%) oxides of $CaCO_3$, $(MgCO_3)_4$. $Mg(OH)_2$. $5H_2O$, ZnO, NiO, Co_3O_4, TiO_2 (Aldrich Chemicals, Milwaukee WI, USA), and Nb_2O_5 (Nuclear Fuel Complex, Hyderabad, India) were used as the starting raw materials. Stoichiometric amounts of the oxides were weighed according to

their corresponding chemical formulae $Ca_{5-x}Mg_xNb_2TiO_{12}$, $Ca_{5-x}Zn_xNb_2TiO_{12}$, $Ca_{5-x}Ni_xNb_2TiO_{12}$ and $Ca_{5-x}Co_xNb_2TiO_{12}$ for x = 0, 0.2, 0.4, 0.6, 0.8, 1, 2, 3, 4 and 5 separately. The dried mixtures were calcined in the range 850 –1350°C for 4 hours depending upon the compositional variations. The ceramics were sintered in the temperature range 1010 – 1550°C, for different values of x to get maximum densification. The experimental density of well polished samples were measured using Archimedes method. Structure and phase purity of powdered specimens were analyzed employing X-Ray diffraction technique using CuKα radiation. Microstructural analysis was held using scanning electron microscopic techniques. The materials were characterized in the microwave frequency range employing resonance technique as explained in Chapter 2, Section 2.3.2 to 2.3.5.

5.3.1.2 Simulation procedure

The geometric structure for simulation was made using solid modeler based on ASCIs Kernel plotting software. To simulate the structure for quality factor measurement, a hollow cylindrical copper metallic cavity with inner diameter 40 mm and depth 24 mm was drawn as described in Fig. 5.10.

The cavity was filled with air (ε_r = 1). A quartz spacer of height 8 mm and diameter 7 mm was fixed at the inner bottom surface of the cavity over which cylindrical dielectric resonator of height L = 6.89 mm and diameter D = 12.02 mm, whose resonant frequency has to be measured was placed. The properties of relevant materials were assigned to the geometry. Material properties like conductivity, relative permittivity and dielectric loss (tan δ) were assigned. In the case of DR, the experimentally observed ε_r and tan δ (tan $\delta = 1/Q_u$) were given as the reference values. The boundary conditions for each surface were assigned accordingly and mesh size and duration can be assigned or automized. Co-axial probe excitation was assigned to the transmission and reception ports and the desired result was assigned as S_{21}. The time domain TLM solves for Maxwell's equations in each node and yields the S_{21} resonance spectrum. From the spectrum, the $TE_{01\delta}$ mode was identified and its resonant frequency (f) and 3dB bandwidth (Δf) were noted and hence Q_u was calculated.

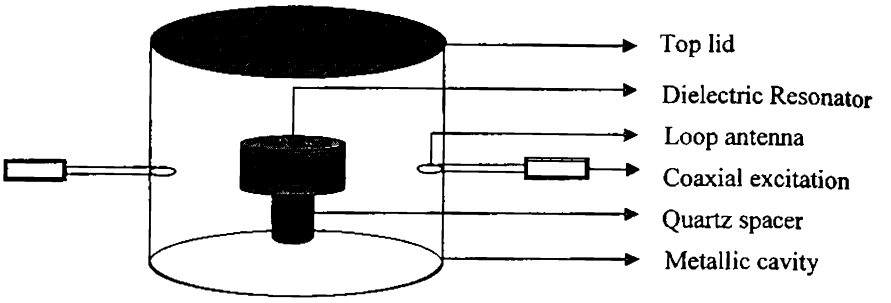

Fig. 5. 10 Geometry of cavity shielded DR (to simulate Q_u)

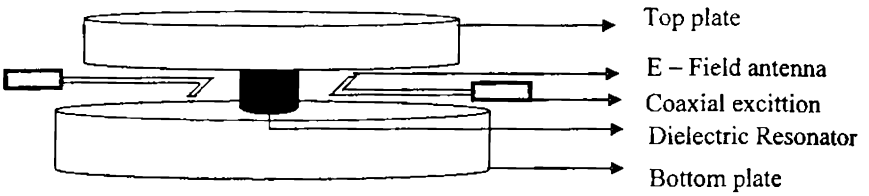

Fig. 5.11 Geometry of end shorted DR (to simulate ε_r)

The Hakki-Colemann rod resonator method for the determination of ε_r of the DR sample was simulated as shown in Fig. 5.11. The circular disc of material (with the dimensions specified above) was inserted between two perfectly conducting plates (80 mm diameter for top plate and 1200 mm for the bottom plate with a thickness of 5 mm). Boundary conditions and excitation are assigned in accordance with the structure. The resonant frequency of TE_{011} mode is measured from the transmission mode spectrum. The ε_r was calculated from the simulated value of resonant frequency and geometrical dimensions of DR using Hakki-Colemann program[31].

5.3.2 Results and Discussion

5.3.2.1 XRD Analysis

Fig. 5.12 shows the powder X-Ray diffraction (XRD) patterns of $Ca_{5-x}Mg_xNb_2TiO_{12}$ samples for various values of x. In this figure two critical phase regions were observed with increasing amount of Mg^{2+} ions. The solid solution based on $Ca_{5-x}Mg_xNb_2TiO_{12}$ was observed only for x up to 1. Hence for $0 \leq x \leq 1$, the diffraction peaks can be indexed on the basis of $Ca_5Nb_2TiO_{12}$ with orthorhombic symmetry (See Chapter 3, Section 3.3.2).

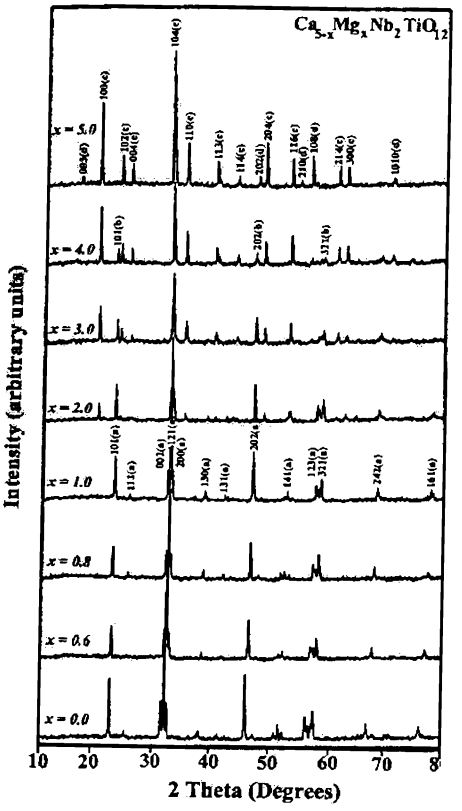

Fig. 5.12 X-Ray diffraction patterns of $Ca_{5-x}Mg_xNb_2TiO_{12}$ ceramics
a → $Ca_5Nb_2TiO_{12}$, b → $CaTiO_3$,
c → $Mg_4Nb_2O_9$ and d → $MgTiO_3$

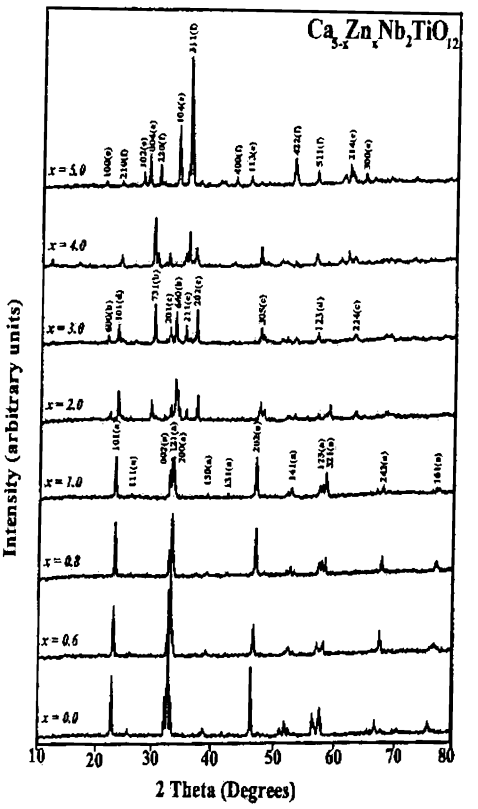

Fig. 5.13 X-Ray diffraction patterns of $Ca_{5-x}Zn_xNb_2TiO_{12}$ ceramics
a → $Ca_5Nb_2TiO_{12}$, b → $Ca_3Nb_2O_8$,
c → Zn_2TiO_4, d → $CaTiO_3$, e → $Zn_4Nb_2O_9$
and f → $ZnTiO_3$

However as Mg^{2+} concentration increased ($x \geq 2$), mixture phases were formed as is evident from the XRD profile. For $2 \leq x \leq 4$, $Mg_4Nb_2O_9$ (ICDD File 38 - 1459) and $CaTiO_3$ (ICDD File 39 – 145) phases were identified in the XRD pattern and the $Mg_4Nb_2O_9$ phase became more prominent with the increase of Mg^{2+} concentration. With $x = 5$, the ceramic was found to be a mixture of $Mg_4Nb_2O_9$ – $MgTiO_3$ (ICDD File 6 - 494), with $Mg_4Nb_2O_9$ as the major phase.

Fig. 5.13 shows the XRD pattern recorded from the powdered specimens of $Ca_{5-x}Zn_xNb_2TiO_{12}$ with $0 \leq x \leq 5$. As in the case of Mg^{2+} substitution, $Ca_{5-x}Zn_xNb_2TiO_{12}$ also formed a solid solution for $0 \leq x \leq 1$. However higher concentrations of Zn^{2+} ($2 \leq x \leq 5$) has resulted in the formation of mixture phases as seen from Fig. 5.13. For $x = 2$, 3 and 4, phases corresponding to $Ca_3Nb_2O_8$ (ICDD File 15 – 156), $CaTiO_3$, $ZnTiO_3$ (ICDD File 39 – 190) and $Zn_4Nb_2O_9$ were identified in the XRD profile. As is evident from the figure, the concentration of the latter two phases ($Zn_4Nb_2O_9$ and $ZnTiO_3$) became more prominent and the presence of $Ca_3Nb_2O_8$ and $CaTiO_3$ were diminished with increase in Zn^{2+} substitution. With $x = 5$, the ceramic was identified as a mixture of $Zn_4Nb_2O_9$ - $ZnTiO_3$ phases.

XRD patterns of $Ca_{5-x}Ni_xNb_2TiO_{12}$ with $0 \leq x \leq 5$ are depicted in Fig. 5.14. In this case no mixture phase was detected up to $x = 1$ and was indexed comparing with the parent $Ca_5Nb_2TiO_{12}$ material. On the other hand from $x = 2$ to $x = 5$, $Ca_{5-x}Ni_xNb_2TiO_{12}$ form as a mixture of few compounds. Phases corresponding to Ni_3TiO_5 (ICDD File 30 – 865), $CaTiO_3$ and $NiTiO_3$ (ICDD File 33 – 960) were identified in the XRD patterns with $x = 2$ and 3, whereas for $x = 4$, a mixture of $Ni_4Nb_2O_9$ (ICDD File 46 – 525) and $CaTiO_3$ was formed. The composition with $x = 5$ was identified as a mixture of $Ni_4Nb_2O_9$ and $NiTiO_3$ and the diffraction peaks were indexed accordingly.

Fig. 5.15 shows the XRD spectra of powdered samples of $Ca_{5-x}Co_xNb_2TiO_{12}$ with $0 \leq x \leq 5$. There was no evidence of any second phase in the XRD pattern, implying that $Ca_{5-x}Co_xNb_2TiO_{12}$ form a complete solid solution in the range $0 \leq x \leq 1$. Similar to the case of Mg, Zn and Ni substitution, mixture phases were formed for Co^{2+} in the range $x \geq 2$. XRD peaks corresponding to $CoNb_2O_6$ (ICDD File 32 – 304), Co_2TiO_4 (ICDD File 39 – 1410), $CoTiO_3$ (ICDD File 29 – 516) and $CaTiO_3$ were identified with $2 \leq x \leq 4$, whereas $x = 5$ composition formed as a mixture of $Co_4Nb_2O_9$ - $CoTiO_3$ phases.

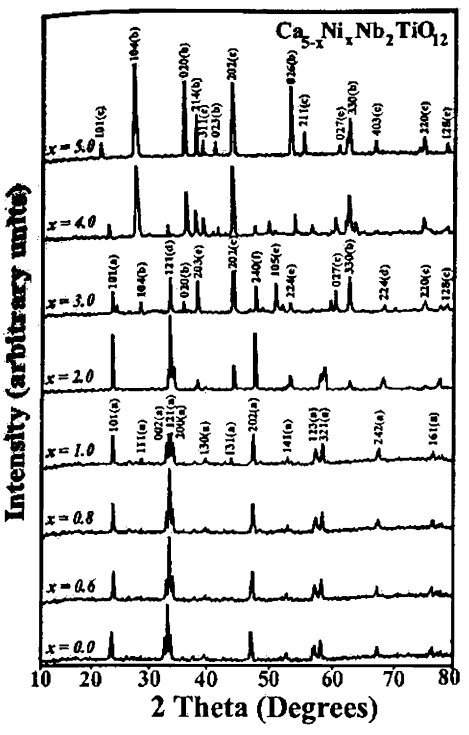

Fig. 5.14 X-Ray diffraction patterns of $Ca_{5-x}Ni_xNb_2TiO_{12}$ ceramics a → $Ca_5Nb_2TiO_{12}$, b → $Ni_4Nb_2O_9$, c → $NiTiO_3$, d → $CaTiO_3$, e → Ni_3TiO_5 and f → $CaNb_2O_6$

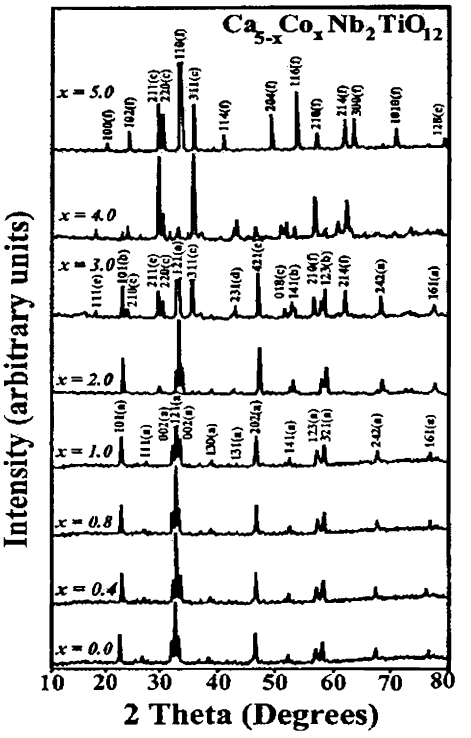

Fig. 5.15 X-Ray diffraction patterns of $Ca_{5-x}Co_xNb_2TiO_{12}$ ceramics a → $Ca_5Nb_2TiO_{12}$, b → $CaTiO_3$, c → $CoTiO_3$, d → $CoNb_2O_6$, e → Co_2TiO_4 and f → $Co_4Nb_2O_9$

In all the XRD patterns indicating the substitution reactions mentioned above, the structure remained the same for $0 \leq x \leq 1$. It is known that[34], normally smaller cations occupy the *B*-site of perovskite structure. In Figs. 5.12 to 5.15, for $0 \leq x \leq 1$, the main Bragg reflections were shifted towards the higher angle region with increase in x, suggesting a possible substitution. It is consistent with the decrease in unit cell volume and an equivalent increase in experimental and X-Ray density with x (See Table 5.3), because of the possible substitution of Mg^{2+}, Zn^{2+}, Ni^{2+} and Co^{2+} ions in place of Ca^{2+} in the perovskite *B*-site. With $x \geq 1$, more than one Mg, Zn Ni or Co ions are to be substituted in the $Ca(Ca_{1/4}Nb_{2/4}Ti_{1/4})O_3$ perovskite, where simultaneous partial replacement of Ca^{2+} ions from the perovskite *A* and

B-sites may take place, resulting in the formation of mixture phases as is evidenced by XRD studies.

5.3.2.2 Densification and Microstructural Analysis

The lattice parameters, cell volume, density and tolerance factor of $Ca_{5-x}A'_xNb_2TiO_{12}$ (A' = Mg, Zn, Ni and Co) ceramics for $0 \leq x \leq 1$ are tabulated in Table 5.3. It is evident from the table that, the unit cell parameters and cell volume decreased linearly with A'^{2+} ion concentration.

Table 5.3The lattice parameters, unit cell volume, density and tolerance factor of $Ca_{5-x}A'_xNb_2TiO_{12}$ (A' = Mg, Zn, Ni & Co) ceramics for $0 \leq x \leq 1$

Material	x	Lattice parameters			Cell Volume ($Å^3$)	X-Ray density (g/cm^3)	% Density	Tolerance factor (t)
		a (Å)	b (Å)	c (Å)				
$Ca_5Nb_2TiO_{12}$	0.0	5.510(4)	7.907(9)	5.688(0)	247.844	4.19	96.89	0.9189
$Ca_{5-x}Mg_xNb_2TiO_{12}$	0.2	5.481(2)	7.859(2)	5.661(4)	243.849	4.24	97.01	0.9240
	0.4	5.453(1)	7.814(3)	5.632(2)	239.398	4.29	97.20	0.9290
	0.6	5.437(3)	7.786(1)	5.620(5)	237.908	4.31	97.65	0.9342
	0.8	5.405(5)	7.752(4)	5.607(0)	234.930	4.33	98.07	0.9394
	1.0	5.382(4)	7.739(7)	5.591(0)	232.872	4.35	98.38	0.9447
$Ca_{5-x}Zn_xNb_2TiO_{12}$	0.2	5.479(0)	7.860(2)	5.666(4)	244.006	4.29	96.86	0.9235
	0.4	5.441(3)	7.829(3)	5.651(2)	240.719	4.38	96.78	0.9282
	0.6	5.427(6)	7.789(9)	5.623(3)	237.694	4.47	97.54	0.9329
	0.8	5.398(5)	7.755(8)	5.593(6)	234.131	4.58	97.62	0.9376
	1.0	5.379(2)	7.738(4)	5.573(1)	231.960	4.66	96.35	0.9424
$Ca_{5-x}Ni_xNb_2TiO_{12}$	0.2	5.468(3)	7.864(0)	5.652(2)	243.038	4.30	96.97	0.9255
	0.4	5.443(0)	7.838(5)	5.607(4)	239.207	4.39	97.23	0.9322
	0.6	5.420(5)	7.795(0)	5.590(7)	236.171	4.47	97.45	0.9390
	0.8	5.405(4)	7.771(4)	5.565(6)	233.742	4.55	96.94	0.9458
	1.0	5.385(6)	7.754(3)	5.538(4)	231.240	4.63	96.91	0.9528
$Ca_{5-x}Co_xNb_2TiO_{12}$	0.2	5.471(2)	7.870(3)	5.634(2)	242.581	4.31	96.95	0.9246
	0.4	5.457(4)	7.844(7)	5.582(1)	238.936	4.40	97.21	0.9304
	0.6	5.421(1)	7.817(2)	5.666(4)	235.864	4.48	97.60	0.9362
	0.8	5.405(8)	7.777(5)	5.553(8)	233.418	4.56	97.52	0.9421
	1.0	5.373(9)	7.762(4)	5.524(0)	230.377	4.64	96.15	0.9481

It can be attributed to the substitution of A'^{2+} with lower ionic radius[35] than Ca^{2+} in the *B*-site of complex perovskite materials. Increase in concentration of A'^{2+} ions was also associated with an increase in X-Ray density and a slight improvement in percentage density of Ca_{5-x}

$A'_xNb_2TiO_{12}$ (A' = Mg, Zn, Ni and Co) ceramics as is clear from Table 5.3. In complex perovskite type materials, the dielectric properties especially τ_f largely depends on the tolerance factor (t)[37] and tilting of oxygen octahedra. Hence the tolerance factor of $Ca_{5-x}A'_xNb_2TiO_{12}$ (A' = Mg, Zn, Ni and Co) dielectrics [$Ca(A'_{1/4}Nb_{2/4}Ti_{1/4})O_3$], in perovskite form] were calculated using the equation,

$$t = \frac{R_{Ca} + R_O}{\sqrt{2}\{[(1-x)R_{Ca} + xR_{A'}]/4 + R_{Nb}/2 + R_{Ti}/4 + R_O\}} \qquad (5.2)$$

for x = 0.0, 0.2, 0.4, 0.6, 0.8 and 1.0 and is listed in Table 5.3. The substitution of smaller ions[35] like Mg^{2+}, Zn^{2+}, Ni^{2+} and Co^{2+} in the complex perovskite B-site in place of bigger Ca^{2+} ions resulted in the increase of tolerance factor with x. The calculations were made only for $0 \leq x \leq 1$ because for $x \geq 2$, the materials form mixture phases.

Microstructure of $Ca_5Nb_2TiO_{12}$ has been described earlier with uniform distribution of large grains of about 10 μm size (See Chapter 3, Section 3.3.2). Fig. 5.16 shows a few typical SEM photographs recorded from the surface of sintered and thermally etched $Ca_{5-x}A'_xNb_2TiO_{12}$ (A' = Mg, Zn, Ni and Co) specimens for $1 \leq x \leq 5$. The surface morphology of $Ca_4ZnNb_2TiO_{12}$ is depicted in Fig. 5.16 (a), which shows uniformly distributed, homogeneous grains of average size about 5 μm. The grains are well separated by distinct grain boundaries as is evident from the figure. No secondary phases were observed confirming the formation of complete solid solution in the complex perovskite material up to x = 1. Fig. 5.16 (b) shows the SEM image of $2CaO - Co_3O_4 - Nb_2O_5 - TiO_2$ (ie. x = 3) ceramics. It has a grain size distribution of about 2 μm with a few percent porosity. Rich phases corresponding to needle like structure and occasional rectangular grains are visible in the microstructure. Indication of the occurrence of liquid phase sintering can be found in the grain boundaries of the specimen and the presence of the same may be responsible for grain growth. The formation of liquid phase may be due to the evaporation of Co_3O_4 similar to the Zn vapourization in $Ba(Zn_{1/3}Ta_{2/3})O_3$ ceramics[49].

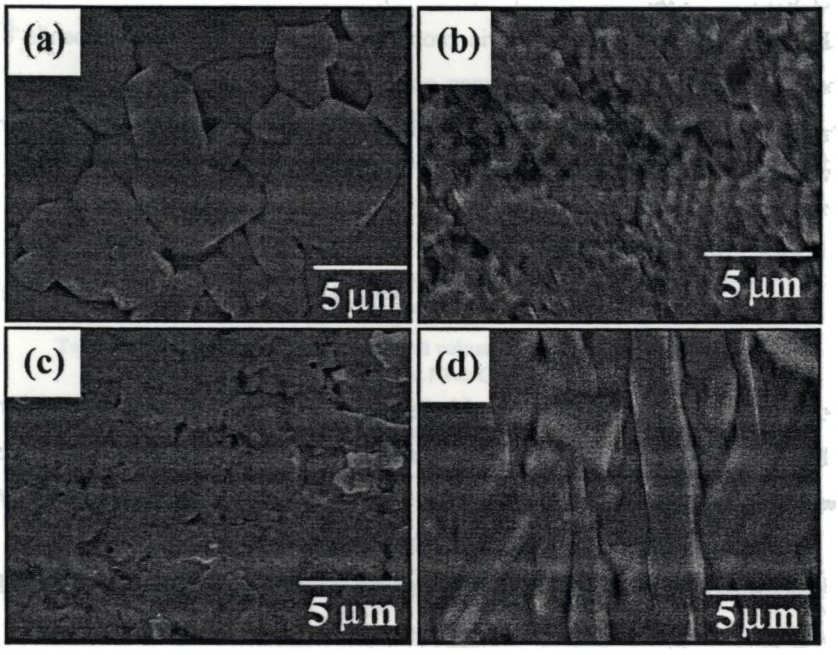

Fig. 5.16 Scanning electron micrographs of (a) $Ca_4ZnNb_2TiO_{12}$ (b) $2CaO - Co_3O_4 - Nb_2O_5 - TiO_2$ (c) $CaO - 4NiO - Nb_2O_5 - TiO_2$ (d) $5MgO - Nb_2O_5 - TiO_2$ ceramics

Non-uniformity in the size and shape of grains indicates the formation of mixture phases as confirmed from XRD analysis. The surface morphology of $CaO - 4NiO - Nb_2O_5 - TiO_2$ (ie. $x = 4$) ceramics is shown in Fig. 5.16 (c). The average grain size is about 2 – 3 μm. In this case also the presence of liquid phase at the grain boundaries can be seen and is due to the evaporation of low melting NiO. Fig. 5.16 (d) features the microstructural evolution of $5MgO-Nb_2O_5-TiO_2$ ($x = 5$) ceramics. Neither the liquid phase nor grain growth can be observed by the microstructure characterization of the specimen. Pore eliminated grain distribution with needle like structure and occasional small laths up to 2 μm in size was detected which confirmed the formation of $Mg_4Nb_2O_9$ and $MgTiO_3$ phases in the sample.

5.3.2.3 Simulation Results

The build module of micro-stripes divides the model (structure plotted) and the total occupied work space into a large number of spatial elements on a Cartesian mesh. The build chooses the default cell-size to be $1/10^{th}$ of the free space wave length at the assigned upper frequency of operation. The auto-mesh facilitates the reduction of cell-size within the dielectric bodies to account for special material properties and the build sets sensible default duration. The build monitor the response after every multigriding analysis and yield a graph of time domain response at the end of the simulation process. To plot the frequency response curve with S_{21}, the TLM transfers the time domain response into frequency domain employing Fourier transformation equations.

Fig. 5.17(a) and 5.17(b) illustrates the variation of electric and magnetic fields inside $Ca_5Nb_2TiO_{12}$ dielectric resonator kept inside a copper cavity[33]. It can be seen that, the electric field makes concentric circles around the DR, while the magnetic flux lines form loops in a direction parallel to the height of the DR, which is in agreement with earlier reports[1] regarding field distribution of $TE_{01\delta}$ mode in a cylindrical dielectric resonator (Also See Section 1.1.4 of Chapter 1). The magnitude of current density distribution on the surface of dielectric resonator is shown in Fig. 5.18, which is also consistent with that of the identified $TE_{01\delta}$ mode.

Fig. 5.19 shows the transmission mode resonance spectrum of $Ca_5Nb_2TiO_{12}$ dielectric material kept in a shielded cavity exactly matching with the experimental conditions. Excellent agreement between experimental and simulated resonant frequencies and quality factor was obtained. In experiment the $Q_u \times f = 26000$ (at 3.6813 GHz) and the simulated value was 26670 (at 3.6801 GHz). The error in $Q_u \times f$ was about 2.5 %, which usually occurs in high frequency measurements. Fig. 5.20 shows the TE_{011} mode excitation of $Ca_5Nb_2TiO_{12}$ ceramics in Hakki and Coleman[31] end-shorted method. As in the case of cavity resonance, here also excellent agreement between experiment and simulation was obtained. The experimental resonant frequency was $f = 4.6742$ GHz and the dielectric constant, $\varepsilon_r = 47.46$. The simulation yielded a resonance at $f = 4.6726$ GHz and a resultant $\varepsilon_r = 47.79$ with a tolerance of less than 1.0 %.

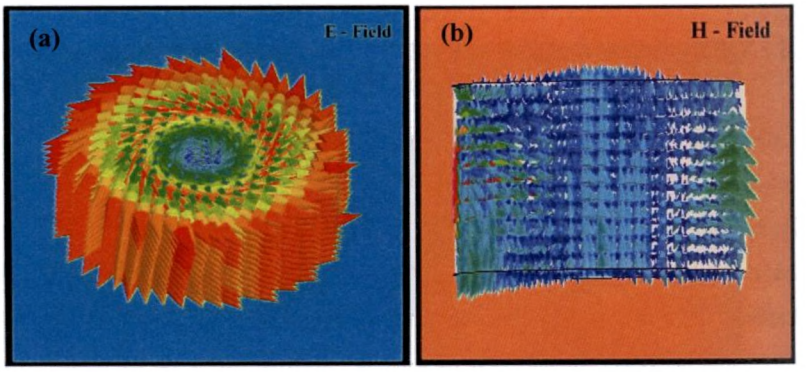

Fig. 5.17 Variation of (a) Electric and (b) Magnetic field of $TE_{01\delta}$ resonance mode of a DR

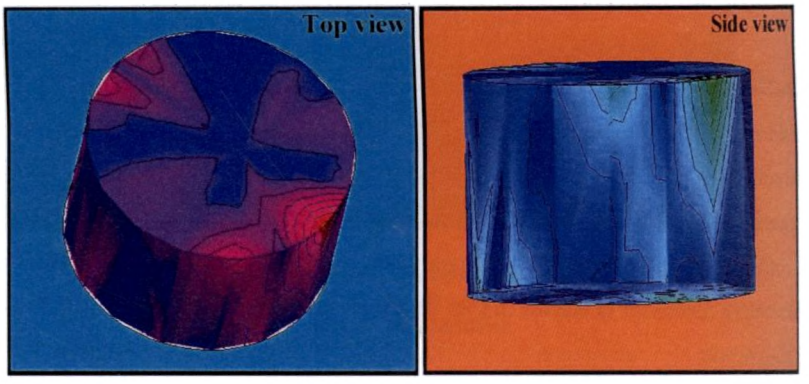

Fig. 5.18 Variation of magnitude of surface current density (J) along the surface of DR

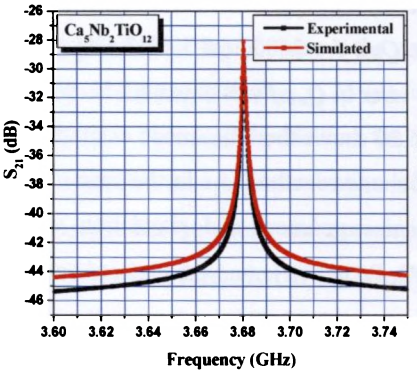

Fig. 5.19. $TE_{01\delta}$ transmission mode resonance spectrum of cavity shielded DR

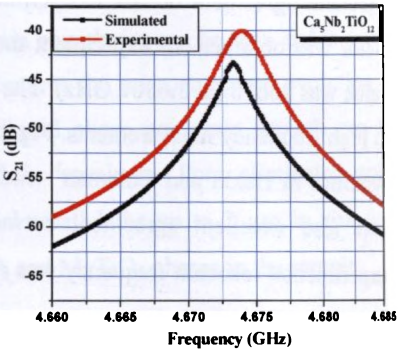

Fig. 5.20. TE_{011} transmission mode resonance spectrum of end shorted DR

The resonant frequency obtained by simulation for calculating Q_u and ε_r was lower than that yielded through experiment. It can be attributed to the surface irregularities of DR, which come into play during the experimental procedure (inaccuracy in dimensional measurements), which in turn creates a thin air layer between the DR and end-shorted plates in the case of ε_r measurements. The presence of air layer reduced the effective ε_r and a resultant shift of resonant frequency to the higher value region was observed. Hence experimental ε_r was lower than that obtained by simulation. In the case of experimental measurement of Q_u, in addition to the limitation in the measurement of dimensions, the conduction and radiation loss of the DR can not be neglected even with the presence of quartz spacer and finely polished metallic cavity. Whereas the conditions remains ideal in simulation process and hence the losses can be minimized. Due to this reason simulation yields an accurate unloaded quality factor of the DR material, which will be normally higher than that obtained by experiment. DRs with different dimensions and dielectric properties were simulated (see Figs. 5.21 – 5.24 and Table 5.4) using TLM technique and the experimental values were well validated using simulation.

5.3.2.4 Microwave dielectric properties

The variation of microwave dielectric properties of $Ca_{5-x}Mg_xNb_2TiO_{12}$, $Ca_{5-x}Zn_xNb_2TiO_{12}$, $Ca_{5-x}Ni_xNb_2TiO_{12}$ and $Ca_{5-x}Co_xNb_2TiO_{12}$ ceramics are shown in Fig. 5.21, 5.22, 5.23 and 5.24 respectively. In all the cases, $Q_u \times f$ increased and ε_r decreased as x is varied from 0 to 1. In general the Q_u is affected by extrinsic factors such as secondary phases, density and oxygen vacancies at microwave frequencies[50]. The effects of secondary phases were neglected because there was no secondary phase in the solid solution range ($0 \leq x \leq 1$) as is evident from Figs. 5.12 – 5.15.

However, with $0 \leq x \leq 1$, the experimental density showed a linear increase whereas the percentage density increased from 96.6 to 98% (See Table 5.3) with the concentration of substituted A'^{2+} ions in all the four systems investigated. Therefore the increased $Q_u \times f$ in these systems is related to improved densification, supported by the substitution of ions with lower ionic radii[35] than Ca^{2+} in the perovskite structure as explained earlier.

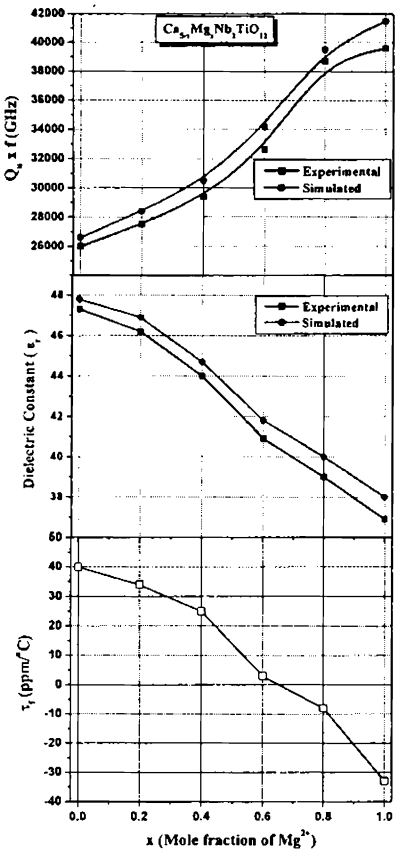

Fig. 5.21 Experimental and simulated microwave dielectric properties of $Ca_{5-x}Mg_xNb_2TiO_{12}$ ceramics for $0 \leq x \leq 1$

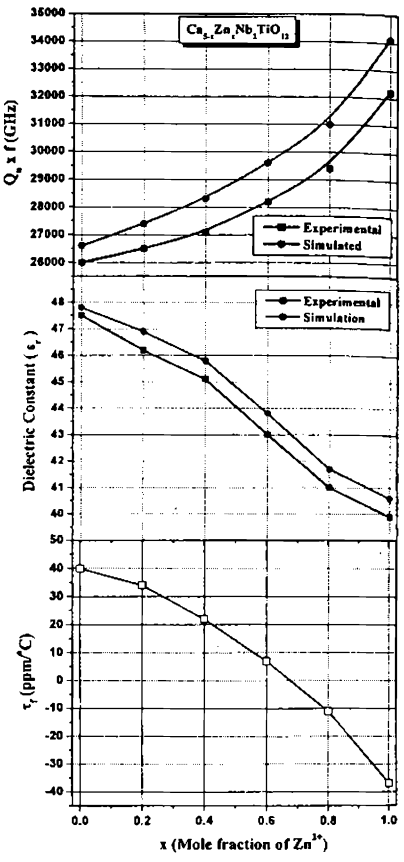

Fig. 5.22 Experimental and simulated microwave dielectric properties of $Ca_{5-x}Zn_xNb_2TiO_{12}$ ceramics for $0 \leq x \leq 1$

Figs. 5.21 – 5.24 shows that, in all the four systems the dielectric constant decreased with increase in A'^{2+} (A' = Mg, Zn, Ni & Co) substitution. Dielectric constant significantly depends on the percentage densification and ionic polarization[38] at microwave frequencies[51]. The percentage densities of $Ca_{5-x}A'_xNb_2TiO_{12}$ (A' = Mg, Zn, Ni & Co) [$0 \leq x \leq 1$] ceramics increased but the dielectric constant decreased with increased A'^{2+} substitution in the solid solution range. Hence it can be concluded that in these systems, the ionic polarization is the

more important factor affecting the dielectric constant. It is noteworthy to mention that, the ionic polarizabilities[38] of substituted A'^{2+} ions are less than that of Ca^{2+} ion and thereby the decrease in ε_r with increase in x within the range $0 \leq x \leq 1$.

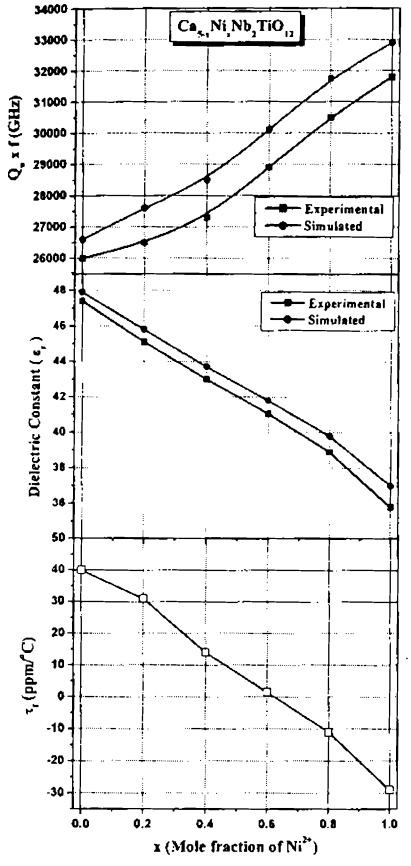

Fig. 5. 23 Experimental and simulated microwave dielectric properties of $Ca_{5-x}Ni_xNb_2TiO_{12}$ ceramics for $0 \leq x \leq 1$

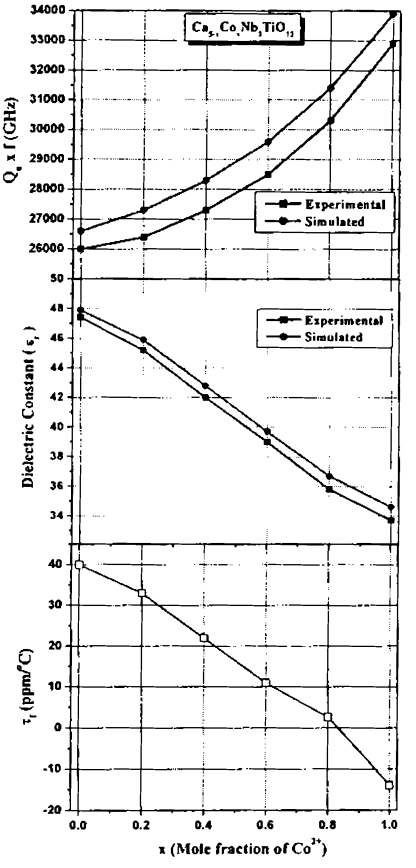

Fig. 5.24 Experimental and simulated microwave dielectric properties of $Ca_{5-x}Co_xNb_2TiO_{12}$ ceramics for $0 \leq x \leq 1$

It can be seen from the figures that the simulated quality factor and dielectric constant matches very well with experimental values in all the four ceramic systems investigated. The tolerance ($\approx$ 2.5 % in Q_u x f and $\approx$1.0 % in ε_r) is well within the experimental error in high

frequency measurements. In $Ca_{5-x}A'_xNb_2TiO_{12}$ (A' = Mg, Zn, Ni & Co) [$0 \le x \le 1$] system, the most interesting phenomena occurred was the shifting of τ_f, which changed from positive to negative values with increase in x (See Figs. 5.21 – 5.24). τ_f is related to temperature variation of dielectric constant (τ_ε) and thermal expansion coefficient (α) as,

$$\tau_f = -[\tau_\varepsilon / 2 + \alpha] \qquad (5.3)$$

It has been showed that[52,53] in perovskite based compounds, the onset of tilt transitions by substitution is the major factor influencing the behaviour of temperature coefficient of dielectric constant (τ_ε) and thereby τ_f. It was reported that[54] τ_ε decreases with increasing tolerance factor (t) accompanied by a lowering in amplitude of tilting. In $Ca_{5-x}Mg_xNb_2TiO_{12}$, $Ca_{5-x}Zn_xNb_2TiO_{12}$, $Ca_{5-x}Ni_xNb_2TiO_{12}$ and $Ca_{5-x}Co_xNb_2TiO_{12}$ ceramics with $0 \le x \le 1$, the tolerance factor (t) increased [See Table 5.3] and hence τ_ε and thereby τ_f decreased with x and approaches zero values.

Further reduction in τ_ε (towards negative values) with increased values of t results in the high negative value of τ_f as is evident from the above equation and the same was verified experimentally and is shown in Figs. 5.21 - 5.24. In $Ca_{5-x}Mg_xNb_2TiO_{12}$ system, the composition $Ca_{4.35}Mg_{0.65}Nb_2TiO_{12}$ has $\varepsilon_r = 41$, $Q_u \times f = 33000$ (at 4.1GHz), and $\tau_f \approx 0$ ppm/°C. In the Zn^{2+} substituted system, the $Ca_{4.36}Zn_{0.64}Nb_2TiO_{12}$ has $\varepsilon_r = 43$, $Q_u \times f = 29000$ (at 4 GHz) and $\tau_f \approx 0$ ppm/°C. Whereas in Ni^{2+} and Co^{2+} substituted systems the compositions $Ca_{4.38}Ni_{0.62}Nb_2TiO_{12}$ with $\varepsilon_r = 42$, $Q_u \times f = 28200$ (at 4.07 GHz) and $Ca_{4.18}Co_{0.82}Nb_2TiO_{12}$ with, $\varepsilon_r = 37$, $Q_u \times f = 30000$ (at 4.31 GHz) are the temperature stable compositions. It is to be noted that all these four compositions are potential candidates for DR applications compared with other current commercially used components.

5.3.2 (5 - x)CaO - xA'O – Nb_2O_5 – TiO_2 ($2 \le x \le 5$) [A' = Mg, Zn, Ni & Co] Ceramics

$Ca_{5-x}A'_xNb_2TiO_{12}$ (A' = Mg, Zn, Ni & Co) ceramics form solid solution with complex perovskite structure for $0 \le x \le 1$. XRD analysis showed that for $2 \le x \le 5$, mixture

phases were formed in all the four different cationic substitutions (See Figs. 5.12 – 5.15). The synthesizing conditions, density and microwave dielectric properties of (5-x)CaO – xA'O – Nb_2O_5 – TiO_2 [A' = Mg, Zn, Ni & Co] ceramics for $2 \leq x \leq 5$ are shown in Table 5.4. As is evident from the table, the calcination and sintering temperature decreased in all the four systems with increase in x value. The variation in density with x can be attributed to the concentration and composition of the mixture phases formed. The dielectric constant showed a linear decrease with increase in x value in all the four ceramic systems investigated. In (5-x)CaO - xMgO - Nb_2O_5 - TiO_2 ceramics, ε_r decreased from 38 to 15, and in (5-x)CaO - xZnO - Nb_2O_5 - TiO_2, the variation of ε_r was from 26 to 18 as x is changed from 2 to 5. The ε_r gradually decreased from 35 to 20, in (5-x)CaO - xNiO - Nb_2O_5 - TiO_2 and 32 to 9 in (5-x)CaO - xCoO - Nb_2O_5 - TiO_2 dielectrics for x = 2 to 5. The lowering of ε_r with increase in x was due to the gradual decrease of high ε_r $CaTiO_3$[11] phase concentration from the mixture as indicated by the XRD analysis (See Figs. 5.12 – 5.15). With increase in x, the ceramics form A'^{2+}-based phases (A' = Mg, Zn, Ni & Co) like $Mg_4Nb_2O_9$, $MgTiO_3$, Zn_2TiO_4, $Zn_4Nb_2O_9$, $ZnTiO_3$, $Ni_4Nb_2O_9$, $NiTiO_3$, $CoNb_2O_6$, Co_2TiO_4, $CoTiO_3$ etc., which all have low dielectric constant compared with $CaTiO_3$.[11] The $Q_u \times f$ values of $Ca_{5-x}A'_xNb_2TiO_{12}$ (A' = Mg, Zn, Ni & Co) ceramics for $2 \leq x \leq 5$ are shown in Table 5.4. It is clear from the table that, beyond the solid solution range ($0 \leq x \leq 1$), the quality factor tends to decrease with increasing value of x. It was reported that[53] presence of mixture and secondary phases in the specimen are more important factor than porosity, to reduce the quality factor of microwave dielectric ceramics. In (5-x)CaO - xMgO - Nb_2O_5 - TiO_2 ceramics, the $Q_u \times f$ increases from 19000 GHz to 59000 GHz with τ_f shifted more towards the negative side. This was due to the formation of low loss, low ε_r and negative τ_f phases such as $Mg_4Nb_2O_9$ and $MgTiO_3$.[11] In (5-x)CaO - xZnO - Nb_2O_5 - TiO_2 system, the gradual decrease in $Q_u \times f$ and shifting of τ_f towards the more negative region with increasing x can be seen. In contrast to the case of Mg^{2+} substitution, here the mixture phases formed such as $Ca_3Nb_2O_8$, Zn_2TiO_4, and $Zn_4Nb_2O_9$ are lossy[11] compared with their Mg-based analogues.

Table 5.4. The synthesizing conditions, experimental density and microwave dielectric properties of (5-x)CaO – xA'O – Nb_2O_5 – TiO_2 (A' = Mg, Zn, Ni & Co) ceramics for $2 \leq x \leq 5$

Material System	x	Calcination Temp. (°C)	Sintering Temp. (°C)	Density (Experimental) (g/cm^3) [SD = ± 0.03]	ε_r (Experimental)	ε_r (Simulation)	$Q_u x f$ (GHz) (Experimental)	$Q_u x f$ (GHz) (Simulation)	τ_f (Experimental) (ppm/°C)
(5-x)CaO-xMgO-Nb_2O_5-TiO_2	2	1225	1340	4.23	38	38.8	19000	19400	-20
	3	1225	1325	4.21	31	31.7	33000	33500	-24
	4	1150	1340	4.20	23	23.6	52000	52800	-30
	5	1150	1325	4.17	15	15.6	59000	60000	-77
(5-x)CaO-xZnO-Nb_2O_5-TiO_2	2	1150	1325	4.30	26	26.5	22000	22400	-25
	3	1000	1140	4.71	23	23.7	15000	15300	-34
	4	950	1125	5.05	20	20.5	9000	9200	-47
	5	925	1050	5.51	18	18.4	6000	6200	-57
(5-x)CaO-xNiO-Nb_2O_5-TiO_2	2	1200	1450	4.37	35	35.8	14000	14300	-39
	3	1050	1275	4.90	30	30.6	7500	7700	-49
	4	950	1185	5.16	26	26.6	4000	4100	-58
	5	850	1125	4.82	20	20.5	8200	8500	-64
(5-x)CaO-xCoO-Nb_2O_5-TiO_2	2	1200	1400	4.02	32	32.7	15000	15300	-18
	3	1050	1175	4.58	29	29.5	18500	18900	-28
	4	950	1100	4.47	12	12.4	28000	28500	-42
	5	850	1010	4.32	9	9.30	41000	41700	-59

In (5-x)CaO - xNiO - Nb_2O_5 - TiO_2 system, the $Q_u x f$ showed a gradual decrease followed by a later increase with x = 5 and in (5-x)CaO - xCoO - Nb_2O_5 - TiO_2 ceramics, the quality factor indicated a linear increase with the variation of x from 2 to 5. In both the systems the τ_f has high negative values with increase in x. It is noteworthy that with x = 5, in Mg and Co based systems, the quality factor reached a maximum value owing to the formation of low loss $A'_4Nb_2O_9$ - $ATiO_3$ (A' = Mg, Co)[11] mixture phases. Investigations for tuning the τ_f of these low dielectric constant, low loss materials would be of great interest as they can find application as potential substrate materials[55] in microelectronic technology. It can be seen from Table 5.4 that, the simulated quality factor and dielectric constant shows very good match with experimental values in all the four ceramic systems investigated. It is noteworthy that the simulation results are in agreement with experimental values for $9 \leq \varepsilon_r \leq 48$ in the investigated ceramic systems.

5.4 $Ca_5Nb_2Ti_{1-x}C_xO_{12}$ (C = Zr, Hf) CERAMICS

5.4.1 Experimental

$Ca_5Nb_2Ti_{1-x}Zr_xO_{12}$ and $Ca_5Nb_2Ti_{1-x}Hf_xO_{12}$ ceramics were prepared from their oxides as explained in Section 2.1.2 of Chapter 2. The stoichiometric mixtures were ball milled and calcined in air in platinum crucibles in the temperature range 1300 – 1400°C for 4h. Polycrystalline pellets of 14mm diameter and 7mm height were pressed under a pressure of 100 MPa using their well ground calcined powder. Each composition was sintered at their optimum temperatures (See Table 5.5 and 5.6). In Zr-based system, the compositions with x = 0.9 and 1 and in the Hf- analogue x = 0.8 and 1 were difficult to sinter even at 1700°C and hence were added with low melting B_2O_3 as sintering aid. The bulk densities of well polished samples were measured by Archimedes method. The structure and phase purity of the samples were examined by X-Ray diffraction and microstructural analysis was held by scanning electron microscopic methods after thermal etching. The microwave dielectric properties such as dielectric constant, unloaded quality factor and the temperature coefficient of the resonant frequency were measured by using a Vector Network Analyzer as explained in Chapter 2, Section 2.3.2 to 2.3.5.

5.4.2 Results and Discussion

5.4.2.1 Phase Analysis

Figs. 5.25 and 5.26 show the X-Ray diffraction patterns of $Ca_5Nb_2Ti_{1-x}Zr_xO_{12}$ and $Ca_5Nb_2Ti_{1-x}Hf_xO_{12}$ for $0 \leq x \leq 1$ respectively. A perovskite single phase with the same structure as that of the parent material $Ca_5Nb_2TiO_{12}$ was obtained throughout the entire compositional range. Hence the diffraction peaks were indexed based on orthorhombic $Ca_5Nb_2TiO_{12}$ phase.

It is evident from Figs. 5.25 & 5.26 that, a solid solution is formed for all values of $(Zr/Hf)^{4+}$ fraction in both the systems. No structural change is found from the XRD except the slight shift in the position of peaks. The maximum intensity peaks [(121), (101) & (202)] were slightly shifted towards the lower angle side, which was later confirmed by an increase in lattice parameters and an associated increase in cell volume. It is due to the partial substitution of Zr/Hf ions for Ti in the perovskite *B*-site. However in the Hf based ceramics,

compositions with x = 0.8 and 1.0 show few additional peaks of $Ca_2B_2O_5$ (ICDD File No. 22 – 139), which was formed when 2 wt % B_2O_3 glass[56] was added as sintering aid, whereas no such stray phases were observed in the zirconium analogue.

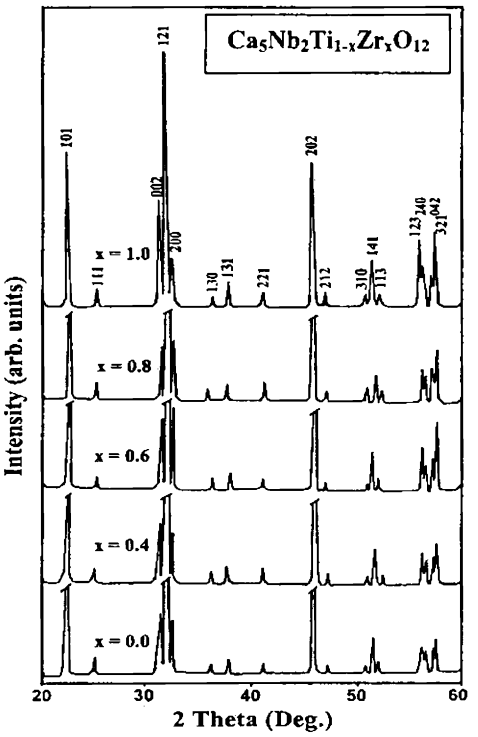

Fig. 5.25 X-Ray diffraction pattern of $Ca_5Nb_2Ti_{1-x}Zr_xO_{12}$ ceramics

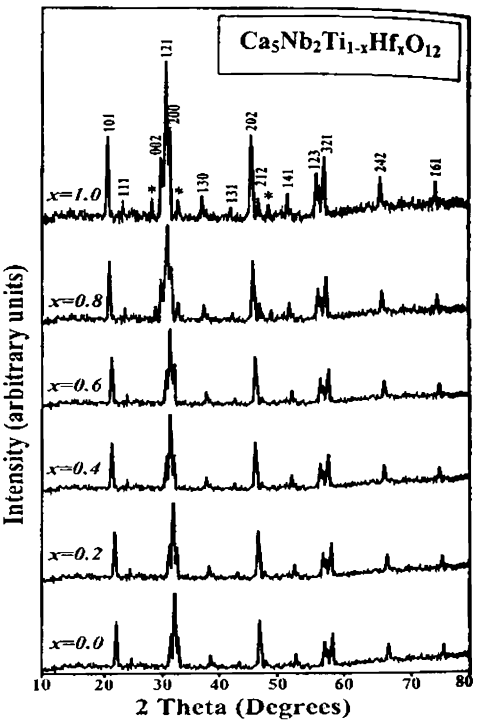

Fig. 5.26 X-Ray diffraction pattern of $Ca_5Nb_2Ti_{1-x}Hf_xO_{12}$ ceramics (* → additional phases)

5.4.2.2 Densification and Microstructural Analysis

The sintering temperatures, lattice parameters, cell volume, density and tolerance factor of $Ca_5Nb_2Ti_{1-x}Zr_xO_{12}$ and $Ca_5Nb_2Ti_{1-x}Hf_xO_{12}$ ceramics are shown in Tables 5.5 and 5.6 respectively. In both Zr/Hf- based materials as x increased from 0 to 1 the sintering temperature shows a linear increase. As described earlier, in both the ceramic systems, the sinterability was very poor for compositions with $x \geq 0.8$ and hence were sintered with low melting B_2O_3 glass additives.

Table 5.5 Sintering temperature, density, lattice parameters, and tolerance factor of $Ca_5Nb_2Ti_{1-x}Zr_xO_{12}$ ceramics

x	Sintering Temperature (°C/4 h)	Lattice parameters			Cell Volume ($Å^3$)	X-Ray density (g/cm^3)	% Density	Tolerance factor (t)
		a (Å)	b (Å)	c (Å)				
0.0	1550	5.510(4)	7.907(9)	5.688(0)	247.8585	4.19	96.63	0.9189
0.1	1550	5.514(2)	7.917(3)	5.677(9)	247.8834	4.23	96.01	0.9176
0.2	1560	5.529(9)	7.929(7)	5.653(4)	247.9435	4.26	95.90	0.9164
0.3	1590	5.538(9)	7.938(1)	5.640(4)	248.0972	4.29	95.89	0.9152
0.4	1610	5.542(4)	7.946(5)	5.635(8)	248.3361	4.31	95.41	0.9139
0.5	1625	5.547(8)	7.953(1)	5.635(4)	248.5463	4.32	95.29	0.9127
0.6	1640	5.548(2)	7.955(2)	5.635(2)	248.7217	4.33	95.24	0.9115
0.7	1650	5.548(7)	7.958(7)	5.634(5)	248.9119	4.35	95.11	0.9102
0.8	1670	5.549(7)	7.968(1)	5.632(4)	249.3358	4.40	94.15	0.9090
0.9	1680*	5.541(2)	7.975(4)	5.631(9)	249.8315	4.42	94.09	0.9078
1.0	1690*	5.552(3)	7.986(2)	5.631(4)	250.0167	4.45	93.79	0.9066

* Sintered with 1 wt % B_2O_3

The variation of unit cell parameters listed in Tables 5.5 and 5.6 show a linear increase with Zr/Hf concentration. It can be attributed to the substitution of $(Zr/Hf)^{4+}$ with higher ionic radius[35] than Ti^{4+} in the *B*-site of complex perovskite materials. Even with reduced cell volume, the X-Ray density showed an increase with x and is due to the increased mass of Zr/Hf^{4+} ions compared with Ti^{4+}. But it should be noted that the percentage density decreased with increase in x and can be attributed to the poor sinterability of ZrO_2/HfO_2 compared with that of TiO_2. The tolerance factor (t)[37] of $Ca_5Nb_2Ti_{1-x}C_xO_{12}$ (C = Zr, Hf) ceramics were calculated for $0 \leq x \leq 1$ and is listed in Tables 5.5 and 5.6 respectively. A gradual decrease in t with increasing x can be seen and is due to the increased average *B*-site ionic radius due to the substitution of bigger Zr/Hf^{4+} in place of Ti^{4+} ions.

Table 5.6. Sintering temperature, unit cell parameters, density and tolerance factor of $Ca_5Nb_2Ti_{1-x}Hf_xO_{12}$ ceramics

x	Sintering Temperature (°C/4 h)	Lattice parameters			Cell Volume ($Å^3$)	X-Ray density (g/cm^3)	% Density	Tolerance factor (t)
		a (Å)	b (Å)	c (Å)				
0.0	1550	5.510(4)	7.908(9)	5.688(0)	247.844	4.19	96.89	0.9189
0.2	1580	5.531(3)	7.930(1)	5.674(1)	248.866	4.35	96.21	0.9166
0.4	1625	5.547(2)	7.955(2)	5.656(4)	249.579	4.51	96.03	0.9144
0.6	1680	5.559(5)	7.969(3)	5.661(2)	250.780	4.64	95.38	0.9121
0.8	1650#	5.565(4)	7.977(2)	5.669(0)	251.658	4.82	94.21	0.9098
1.0	1675#	5.574(2)	7.986(1)	5.671(1)	252.440	4.97	93.35	0.9076

Sintered with 2 wt % B_2O_3

The microstructure of $Ca_5Nb_2TiO_{12}$ ceramics have described in Chapter 3, Section 3.3.2. Well packed grains with an average size of 10 μm were observed. Fig. 5.27 shows the surface morphology of few typical $Ca_5Nb_2Ti_{1-x}Hf_xO_{12}$ ceramics. Fig. 5.27 (a) is the SEM photographs for $Ca_5Nb_2Ti_{0.4}Hf_{0.6}O_{12}$ ceramics, where the dielectrics appeared as temperature stable.

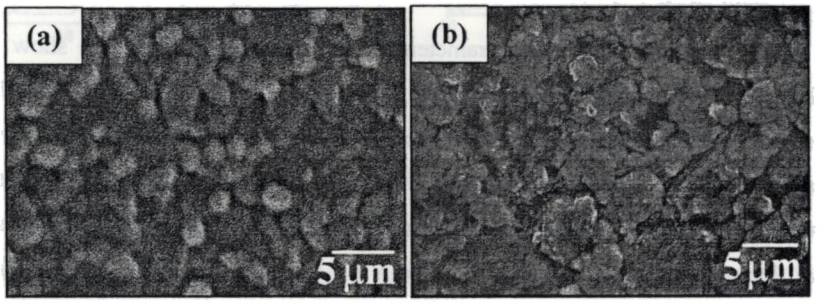

Fig. 5.27 SEM photographs of (a) $Ca_5Nb_2Ti_{0.4}Hf_{0.6}O_{12}$ and (b) $Ca_5Nb_2HfO_{12}$ ceramics

The specimens have a homogeneous microstructure and the average grain size is about 3 μm. It should be noted that the grains are not well packed and leaves porosity confirming the

decreased percentage density with increase in x. It is noteworthy that the grain shape is uniform and is similar to that of the parent $Ca_5Nb_2TiO_{12}$ material shown in Chapter 3, which concludes that the ceramics form solid solution in the $Ca_5Nb_2Ti_{1-x}Hf_xO_{12}$ composition. Fig. 5.27 (b) exhibits the SEM image taken from the thermally etched surfaces of $Ca_5Nb_2HfO_{12}$. A large amount of liquid phase coated over the grains can be seen in the micrograph. The B_2O_3 - based glassy material coated the grains of the matrix and reacted with the host materials to form a glass based low melting phase. It increased the porosity of the matrix material and the density decreased to about 93 % of its theoretical value.

5.4.2.3 Microwave Dielectric Properties

Variation of quality factor, dielectric constant and temperature coefficient of resonant frequency with x in $Ca_5Nb_2Ti_{1-x}Zr_xO_{12}$ and $Ca_5Nb_2Ti_{1-x}Hf_xO_{12}$ ceramics are illustrated in Fig. 5.28 and 5.29 respectively. In $Ca_5Nb_2Ti_{1-x}Zr_xO_{12}$ dielectric resonators, the Q_u x f decreased from 26000 to 23000 whereas in $Ca_5Nb_2Ti_{1-x}Hf_xO_{12}$ ceramics the Q_u x f decreased from 26000 to 16000 GHz. In general, dielectric loss mechanisms can be divided into (i) intrinsic loss by anharmonic interaction which is a measure of ordering and symmetry and (ii) extrinsic loss by porosity and presence of secondary phases. In the present case, the substitution of $(Zr/Hf)^{4+}$ ions for Ti^{4+} has decreased the percentage density of the ceramics and hence contributed towards the extrinsic loss with a resultant decrease in quality factor with increased x.

The ε_r of $Ca_5Nb_2Ti_{1-x}Zr_xO_{12}$ decreased from 48 to 25 and that of $Ca_5Nb_2Ti_{1-x}Hf_xO_{12}$ ceramics decreased from 48 to 22. In both cases the porosity corrected ε_r was calculated[57] using the equation

$$\varepsilon' = \varepsilon_m \left[1 - \frac{3P(\varepsilon_m - 1)}{2\varepsilon_m + 1} \right] \qquad (5.4)$$

where ε' is the experimental dielectric constant of the composite sample which contains a porosity P and ε_m is the porosity corrected dielectric constant of the material. In

$Ca_5Nb_2Ti_{1-x}Zr_xO_{12}$ and $Ca_5Nb_2Ti_{1-x}Hf_xO_{12}$ ceramics, the porosity corrected ε_r decreased from 51 to 29 when x is varied from 0 to 1.

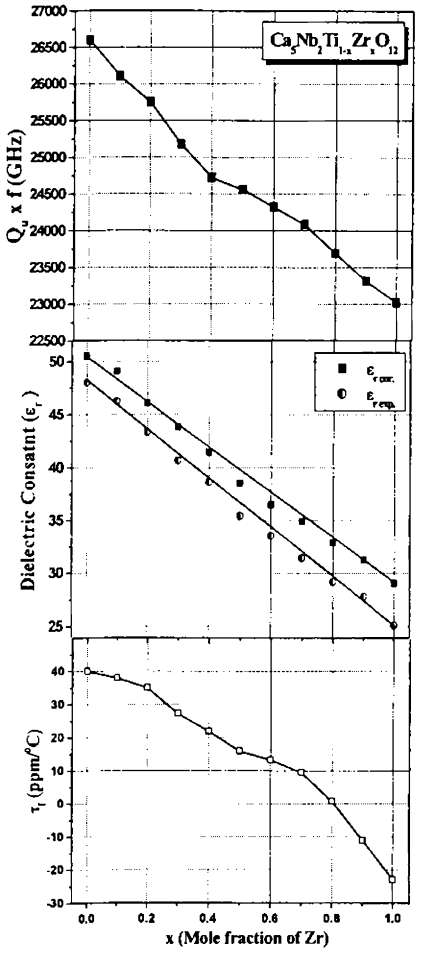

Fig. 5.28 Microwave dielectric properties of $Ca_5Nb_2Ti_{1-x}Zr_xO_{12}$ ceramics

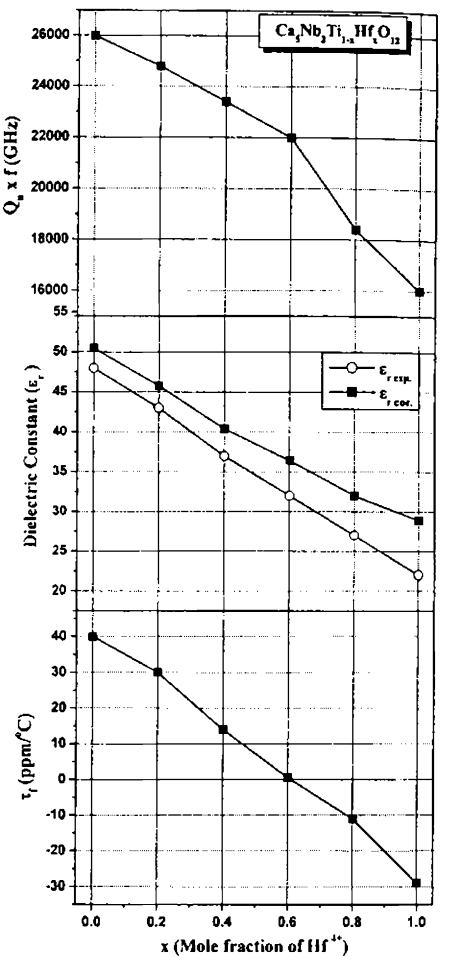

Fig. 5.29 Microwave dielectric properties of $Ca_5Nb_2Ti_{1-x}Hf_xO_{12}$ ceramics

At microwave frequencies[58] dielectric constant of ceramic materials significantly depend on the percentage densification and ionic polarization.[39] ε_r being directly related to ionic polarizability, an increase was expected with $(Zr/Hf)^{4+}$ content since its polarizability is

higher than that of Ti^{4+}. In the present case the porosity increased with $(Zr/Hf)^{4+}$concentration (See Tables 5.5 and 5.6), which resulted in the decrease of ε_r. Moreover the increased radius of substituted ions also increased the bond valence[59,60] between the cationic *B*-site and anions to reduce the rattling effect and hence the polarization induced under the action of electric field decreased and thereby contributed towards the decrease of ε_r.

It has been showed that[61] in perovskite based compounds, the tilt transitions by substitution reactions is the major factor influencing the behaviour of temperature coefficient of dielectric constant (τ_ε) and thereby τ_f. In both the $Ca_5Nb_2Ti_{1-x}Zr_xO_{12}$ and $Ca_5Nb_2Ti_{1-x}Hf_xO_{12}$ systems, τ_f decreased with increase in x. This variation can be attributed to a possible BO_6 octahedral tilting due to the substitution of bigger $(Zr/Hf)^{4+}$ for Ti^{4+} ions. In $Ca_5Nb_2Ti_{1-x}Zr_xO_{12}$ ceramics τ_f decreased from +40 to -19 ppm/°C as x is varied from 0 to 1. The zero crossing of τ_f occurs at $x = 0.8$. In $Ca_5Nb_2Ti_{1-x}Hf_xO_{12}$ ceramics, the τ_f decreased from +40 to -30 ppm/°C with the zero τ_f at $x = 0.6$.

5.5 CONCLUSIONS

- Microwave dielectric ceramics in the $Ca_{5-x}A_xNb_2TiO_{12}$ (A = Ba, Sr), $Ca_{5-x}A'_xNb_2TiO_{12}$ (A' = Mg, Zn, Ni & Co) and $Ca_5Nb_2Ti_{1-x}C_xO_{12}$ (C = Zr, Hf) ceramics have been synthesized and their structure, microstructure and microwave dielectric properties were investigated.
- X-Ray diffraction analysis showed that $Ca_{5-x}A_xNb_2TiO_{12}$ (A = Ba, Sr) ceramics undergo a structural transformation with increasing x. In $Ca_{5-x}Ba_xNb_2TiO_{12}$ ceramics, a complete solid solution was obtained only for the composition $CaBa_4Nb_2TiO_{12}$, which represents all Ba ions in *A*-site and all Ca ions on *B*-site. For all other compositions (x = 1, 2 & 3), traces of additional peaks were identified in the XRD profile. In $Ca_{5-x}Sr_xNb_2TiO_{12}$ dielectrics, for $x = 0$ and 1 the materials exist in a clear perovskite orthorhombic symmetry. Both Ba and Sr substituted systems, for x = 2 to 4, evolves in to pseudo-cubic structure, with a slight difference between lattice parameters but whose orthorhombic true symmetry was revealed by spectroscopic analysis. For x =

5, $Ca_{5-x}A_xNb_2TiO_{12}$ (A = Ba, Sr) ceramics form mixture phases of $(Ba/Sr)_4Nb_2O_9$ – $(Ba/Sr)TiO_3$. The results obtained by XRD analysis was supported by SEM studies.

- The structural evolution was followed by changes in unloaded quality factor of $Ca_{5-x}A_xNb_2TiO_{12}$ (A = Ba, Sr) dielectrics. In Ba-substituted ceramics, Q_u showed a linear decrease with increasing Ba-content, where as in Sr-based system, Q_u showed a gradual decrease for $x = 0$ to 3 (26000 – 6000 GHz) and then increased for $x = 4$ (11500 GHz). The ε_r and τ_f exhibited a linear increase with Ba/Sr content in $Ca_{5-x}A_xNb_2TiO_{12}$ (A = Ba, Sr) ceramics.
- Raman spectra of $Ca_{5-x}A_xNb_2TiO_{12}$ (A = Ba, Sr) showed bands related to *A*-site as well as *B*-site vibrations. The analysis revealed that isovalent Ba/Sr substitution on $Ca_5Nb_2TiO_{12}$ samples led to rotations of oxygen cage that redshifted the bands related to *A*-sites. Maximum distortions occurred at $x = 4$ in the octahedral cages, which represents the complete substitution of Ba/Sr in the complex perovskite *A*-site of $Ca(Ca_{1/4}Nb_{2/4}Ti_{1/4})O_3$ ceramics. FTIR results agree well with Raman data: introduction of barium/strontium in calcium-based ceramics produced perturbations on the polar vibrational modes, especially on the bending modes, which increased their intensities.
- $Ca_{5-x}A'_xNb_2TiO_{12}$ (A' = Mg, Zn, Ni and Co) complex perovskites have been prepared by solid-state ceramic route and their dielectric properties were measured in the microwave frequency range. The ceramics form solid solutions with improved dielectric properties for $0 \leq x \leq 1$. $Ca_{4.35}Mg_{0.65}Nb_2TiO_{12}$ has $\varepsilon_r = 41$, $Q_u \times f = 33000$ (at 4.1GHz), $\tau_f \approx 0$ ppm/°C, $Ca_{4.36}Zn_{0.64}Nb_2TiO_{12}$, has $\varepsilon_r = 43$, $Q_u \times f = 29000$ (at 4 GHz), $\tau_f \approx 0$ ppm/°C, $Ca_{4.38}Ni_{0.62}Nb_2TiO_{12}$ has $\varepsilon_r = 42$, $Q_u \times f = 28200$ (at 4.07 GHz), $\tau_f \approx 0$ ppm/°C and $Ca_{4.18}Co_{0.82}Nb_2TiO_{12}$ has $\varepsilon_r = 37$, $Q_u \times f = 30000$ (at 4.31 GHz) and $\tau_f \approx 0$ ppm/°C. All these low loss, temperature stable compositions are found to be promising materials for applications in wireless technology. In all the four systems with $0 \leq x \leq 1$, an inverse linearity was established between mole fractions of substituted ions and unit cell volume. On the other hand a direct

proportionality between concentrations of A'^{2+} substituted ions with theoretical density and tolerance factor of the ceramics were observed. With $2 \leq x \leq 5$, all the compositions formed mixture phases with high negative τ_f. The resonant frequency, unloaded quality factor and dielectric constant of $Ca_{5-x}A'_xNb_2TiO_{12}$ (A' = Mg, Zn, Ni and Co) ceramic resonators excited in the fundamental transverse electric mode have been computed by means of 3D-Transmission Line Matrix methods. The simulated values of microwave dielectric properties were found to be in excellent agreement with experimental results with a tolerance of $\approx$ 2.5 % in $Q_u \times f$ and 1.0 % in ε_r. Hence the ability of TLM method to compute the resonant frequency and dielectric properties of a cylindrical ceramic resonator shielded by a metallic cavity was established.

- Temperature stable complex perovskite $Ca_5Nb_2Ti_{1-x}Zr_xO_{12}$ and $Ca_5Nb_2Ti_{1-x}Hf_xO_{12}$ ($0 \leq x \leq 1$) ceramics have been prepared through mixed oxide route. The samples were characterized at microwave frequency range. X-Ray diffraction analysis revealed phase purity of the specimens. The density and cell volume were found to be increased with increase in Zr/Hf content. In $Ca_5Nb_2Ti_{1-x}Zr_xO_{12}$ and $Ca_5Nb_2Ti_{1-x}Hf_xO_{12}$ ceramics the ε_r, τ_f and Q_u were found to be decreasing with increase in x. $Ca_5Nb_2Ti_{0.2}Zr_{0.8}O_{12}$ and $Ca_5Nb_2Ti_{0.4}Hf_{0.6}O_{12}$ ceramics were found to have stable resonant frequency with temperature. $Ca_5Nb_2Ti_{0.2}Zr_{0.8}O_{12}$ has $\varepsilon_r = 34$, $Q_u \times f = 24000$ GHz and $\tau_f = 0$ ppm/°C and $Ca_5Nb_2Ti_{0.4}Hf_{0.6}O_{12}$ has $\varepsilon_r = 32$, $Q_u \times f = 22000$ GHz and $\tau_f = 0$ ppm/°C.

In this Chapter we have discussed about the effect of cationic substitutions on the structure and microwave dielectric properties of $Ca_5Nb_2TiO_{12}$ ceramics. The effects of substitutions on the tantalum analogue of the parent material ($Ca_5Ta_2TiO_{12}$) are described in the forthcoming Chapter.

5.6 REFERENCES

[1] D. Kajfez and P. Guillon, *Dielectric Resonators*, (Artech House, Massachusetts 1986).

[2] W. Wersing, *Electronic ceramics*, ed. B. C. H. Steele (Elsevier, Amsterdam, 1991) p. 67.

[3] A. I. Kingon, J. P. Maria and S. K. Streiffer, *Nature* **406** (2000) 1032.

[4] E. K. Hollmann, O. G. Vendic, A. G. Zaitsev and B. T. Melekh, *Superconductor Science and Technol.* **7** (1994) 609.

[5] B. Cheng, M. Cao, R. Rao, .A. Inani, V. P. Voorde, W. M. Greene, J.M.C. Stork, Z. Yu, P. M. Zeitzoff and P. J. C. S. Woo, *IEEE Transactions on Electron Devices* **46** (1999) 1537.

[6] Y. Kawashima, M. Nishida, J. Ueda & H. Ouchi, *J. Amer. Ceram. Soc.* **66** (1983) 421.

[7] S. Kawashima, *Am. Ceram. Soc. Bull.* **75** (1993) 120.

[8] S. B. Desu and H. M. O'Bryan, *J. Am. Ceram. Soc.* **68** (1985) 546.

[9] J-W Choi, J-Y Ha, C-Y Kang, S-J Yoon, H-J Kim and K. H. Yoon, *Jpn. J. Appl. Phys.* **39** (2000) 5923.

[10] I. Levin, T. A. Vanderah and R. Coutts, *J. Mater. Res.* **17** (2002) 1729.

[11] Internet Data, URL : http://www.lsbu.ac.uk/dielectric-materials

[12] N. Santha, M. T. Sebastian, P. Mohanan, N.McN. Alford, K. Sarma, R. C. Pullar, S. Kamba, A. Pashkin, P. Samukhina, and J. Petzelt, *J. Am. Ceram. Soc.* **87** (2004) 1233.

[13] K. P. Surendran, Manoj R. Varma, M. T. Sebastian and P. Mohanan, *J. Mater. Res.* **17** (2002) 2561.

[14] S. K. Kucheiko, D – H. Yeo, J-W. Choi, S-J. Yoon and H-J. Kim, *J. Am. Ceram. Soc.* **85** (2002) 1327.

[15] P. Liu, E. S. Kim, S. G. Kang and H. S. Jang, *Mater. Chem. Phys.* **79** (2003) 270.

[16] G. Huang, D. Zhou, J. Xu, X. Chen, D. Zhang, W. Lu and B. Li, *Mat. Sci.Eng.* **B99** (2003) 416.

[17] H. Jantunen, R. Rautioaho, A. Uusimaki and S. Leppavuri, *J. Eur. Ceram. Soc.* **20** (2000) 2331.

[18] A. Y. Borisevich and P. K. Davies, *J. Am. Ceram. Soc.* **85** (2002) 573.

[19] M-H Kim, S. Nahm, C-H Choi, H-J Lee and H-M Park, *Jpn. J. Appl. Phys.* **41** (2002) 717.

[20] M.T. Sebastian, N. Santha, P. V. Bijumon, Anna Axelsson and Neil Mc Alford, *J. Eur. Ceram. Soc.* **24** (2004) 2583.

[21] K. P. Surendran, Manoj R. Varma, M. T. Sebastian and P. Mohanan, *J. Am. Ceram. Soc.* **86** (2003) 1695.

[22] T. Simada, *J. Eur. Ceram. Soc.* **21** (2001) 2617.

[23] H. Bagshaw, D. Iddles, R. Quimby and I. M. Reaney, *J. Eur. Ceram. Soc.* **23** (2003) 2435.

[24] P. L. Wise, I. M. Reaney, W. E. Lee, T. J. Price, D. M. Iddles, and D. S. Cannell, *J. Eur. Ceram. Soc.* **21** (2001) 1723.

[25] P. L. Wise, I. M. Reaney, W. E. Lee, D. M. Iddles, D. S. cannel and T. J. Price, *J. Mater. Res.* **17** (2002) 2033.

[26] K. P. Surendran, N. Santha, P. Mohanan and M. T. Sebastian, *Eur. Phys. J. B*, **41** (2004) 301.

[27] C-W. Ahn, S. Nahm, S-J. Yoon, H-M. Park, and H-J. Lee, *Jpn. J. Appl. Phys.* **42** (2003) 6964.

[28] M. P. Seabra, M. A. Avdeev, V. M. Ferreira, R. C. Pullar, N. McN. Alford and I. M. Reaney, *J. Am. Ceram. Soc.* **87** (2004) 584.

[29] H. T. Kim and M. T. Lanagan, *J. Am. Ceram. Soc.* **86** (2003) 1874.

[30] H.Ohsato, A. Atsushi, Y.T. Takagi, S. Nishigaki and T. Okuda, *Jpn. J. Appl. Phys.* **39** (2000) 6608.

[31] B. W. Hakki and P. D. Coleman, *IRE Trans. on Microwave Theory Tech.* **MTT-8** (1960) 402.

[32] W. E. Courtney, *IEEE Trans. on Microwave Theory Tech.* **MTT-18** (1970) 476.

[33] J. Krupka, K. Derzakowski, B. Riddle and J. Baker-Jarvis, *Meas. Sci. Technol.* **9** (1998) 1751.

[34] A. M. Glazer, *Acta. Cryst.* **B28** (1972) 3384.

[35] R. D. Shannon, *Acta. Cryst.* **A32** (1976) 751.

[36] M. A. Akbas and P. K. Davies, *J. Am. Ceram. Soc.* **81** (1998) 2205.

[37] R. S. Roth, *J. Res. Natl. Bur. Stand.* **58** (1957) 75.

[38] R. D. Shannon, *J. Appl. Phys.* **73** (1993) 348.

[39] F. Weill, J. L. Rehspringer and J. C. Benrnier, *Mater. Sci. Eng.* **A109** (1989) 193.

[40] T. Hirata, K. Ishioka, and M. Kitasima, *J. Solid State Chem.* **124** (1996) 353.

[41] U. Balachnadran, and N. G. Eror, *Sol. State Comm.* **44** (1982) 815.

[42] H. Zheng, G. D. C.Csete de Gyorgyfalva, R. Quimby, H. Bagshaw, R. Ubic, I. M. Reaney, and J. Yarwood, *J. Eur. Ceram. Soc.* **23** (2003) 2653.

[43] I. Levin, J. Y. Chan, R. G. Geyer, J. E. Maslar, and T. A. Vanderah, *J. Solid State Chem.* **156** (2001) 122.

[44] I. G. Siny, R. Tao, R. S. Katiyar, R. Guo, and A. S. Bhalla, *J. Phys. Chem. Solids* **59** (1998) 181.

[45] H. Zheng, I. M. Reaney, G. D. C. Csete de Gyorgyfalva, R. Ubic, J. Yarwood, M. P. Seabra, and V. M. Ferreira, *J. Mater. Res.* **19** (2004) 488.

[46] H. Zheng, H. bagshaw, G. D. C. Csete de Gyorgyfalva, I. M. Reaney, R. Ubic and J. Yarwood, *J. Appl. Phys.* **94** (2003) 2948.

[47] S. J. Webb, J. Breeze, R. I. Scott, D. S. Cannell, D. M. Iddles, and N. McN Alford, *J. Am. Ceram. Soc.* **85** (2002) 1753.

[48] A. Dias, and R. L. Moreira, *J. Appl. Phys.* **94** (2003) 3414.

[49] C-W. Ahn, H-J. Jang, S . Nahm, H-M. Park, H-J. Lee, *J. Eur. Ceram. Soc.* **23** (2003) 2473.

[50] D. M. Iddles, A. J. Bell, A. J. Moulson, *J. Mater. Sci.* **27** (1992) 6303.

[51] S. Hirano, T. Hayashi, A. Hattori. *J. Am. Ceram. Soc.* **74** (1991) 1320.

[52] E. L. Colla, I. M. Reaney, N. Setter, *Ferroelectrics* **154** (1994) 1173.

[53] I. M. Reaney, E. L. Colla, N. Setter, *Jpn. J. Appl. Phys.* **33** (1994) 3984.

[54] J. Petzelt, S. Pacesova, J. Fousek, S. Kamba, V. Zelezny, V. Koukal, J. Schwarzbach, B. P. Gorshunov, G. V. Kozolov and A. A. Volkov, *Ferroelectrics* **93** (1998) 77.

[55] A. Roosen, *A. Ceram. Trans.* **106** (2000) 479.

[56] H. M. Shirey, *Low temperature synthesis of the microwave dielectric material Barium Magnesium Tantalate (BMT),* M. S. Thesis, University of Pittsburg (2002).

[57] S. J. Penn, N. McN. Alford, A. Templeton, X. Wang, M. Xu, M. Reece and K. Schrapel, *J. Am. Ceram. Soc.* **80** (1997) 1885.

[58] S. Hirano, T. Hayashi, A. Hattori, *J. Am. Ceram. Soc.* **74** (1991)1320.

[59] N. E. Brese and M. O'Keefe, *Acta Cryst.* **B47** (1991) 192.

[60] H. S. Park, K. H. Yoon and E. S. Kim, *Mater. Chem. Phys.* **79** (2003) 181.

CHAPTER 6

CATIONIC SUBSTITUTIONS IN $Ca(Ca_{1/4}Ta_{2/4}Ti_{1/4})O_3$ CERAMICS

This chapter discusses about tailoring the microwave dielectric properties of $Ca_5Ta_2TiO_{12}$ ceramics by cationic substitutions in the A and B-sites of complex perovskites. Ceramic compositions in the $Ca_{5-x}A_xTa_2TiO_{12}$ (A = Ba, Sr), $Ca_{5-x}A'_xTa_2TiO_{12}$ (A' = Mg, Zn, Ni & Co) and $Ca_5Ta_2Ti_{1-x}C_xO_{12}$ (C = Zr, Hf) systems have been prepared. Orthorhombic to pseudo-cubic structural transformation was observed in $Ca_{5-x}A_xTa_2TiO_{12}$ (A = Ba, Sr) dielectrics which was studied employing Raman and FTIR spectroscopic methods. Microwave dielectric properties of $Ca_{5-x}A'_xTa_2TiO_{12}$ (A' = Mg, Zn, Ni & Co) ceramics are investigated experimentally and the results were verified by simulating the transmission mode resonance spectra of the dielectric resonators using 3D TLM methods. Excellent agreement between simulated and experimental results are presented. Temperature stable dielectric resonator materials were identified in $Ca_{5-x}A'_xTa_2TiO_{12}$ (A' = Mg, Zn, Ni & Co) and $Ca_5Ta_2Ti_{1-x}C_xO_{12}$ (C = Zr, Hf) ceramics for $0 \leq x \leq 1$ which are suitable for applications in telecommunication devices.

6.1 INTRODUCTION

In Chapter 3, we have seen that $Ca_5Nb_2TiO_{12}$ and $Ca_5Ta_2TiO_{12}$ ceramics are potential dielectric resonator materials for use in wireless communication devices. The interesting dielectric properties of these ceramics led to further investigations to tailor their microwave dielectric properties by doping and glass addition as described in Chapters 3 and 4. Solid solutions between different types of ceramic materials are of special interest, including complex titanium and niobium/tantalum-based oxides with perovskite-like structure[1,2]. Moreover it is well established that, the most common and accepted practice for tuning temperature coefficient of resonant frequency of microwave ceramics through zero value is by mixing two compounds with opposite τ_f. This can result in the formation of a mixture phase material with zero τ_f[3,4,5] or a single phase material with the modification of unit cell volume with the partial substitution[6,7,8] of suitable ions provided that a solid solution is formed.

In Chapter 5, the effect of cationic substitution in $Ca_5Nb_2TiO_{12}$ ceramics is described. $Ca_5Ta_2TiO_{12}$ has high Q_u and low τ_f compared with their niobium analogue and are practically more suitable for DR applications, though their ε_r is slightly less than that of $Ca_5Nb_2TiO_{12}$ dielectrics. In this chapter the effect of cationic substitutions in the perovskite *A* and *B*-site of $Ca_5Ta_2TiO_{12}$ ceramics are discussed. Accordingly, solid solutions of (i) $Ca_{5-x}A_xTa_2TiO_{12}$ (*A* = Ba, Sr), (ii) $Ca_{5-x}A'_xTa_2TiO_{12}$ (*A'* = Mg, Zn, Ni & Co) and (iii) $Ca_5Ta_2Ti_{1-x}C_xO_{12}$ (C = Zr, Hf) ceramics have been synthesized and their structure, microstructure and microwave dielectric properties were investigated. In addition, the general state of art of 3D Transmission Line Matrix (TLM)[9,10,11,12,13] modeling for the simulation of transmission mode resonance spectra of cavity backed and end-shorted $Ca_{5-x}A'_xTa_2TiO_{12}$ (A' = Mg, Zn, Ni & Co) DRs were made using a commercially available computer aided design (CAD) package Microstripes 6.5[14] (See Chapter 2, Section 2.6.2). The simulated resonant frequencies were used along with sample dimensions to compute Q_u and ε_r of the materials and the dielectric properties thus obtained were compared with experimental results. Investigations were also made on the structure and microwave dielectric properties of $Ca_5Ta_2Ti_{1-x}C_xO_{12}$ (C = Zr, Hf) ceramics.

6.2 $Ca_{5-x}A_xTa_2TiO_{12}$ (A = Ba, Sr) CERAMICS

6.2.1 Experimental

$Ca_{5-x}A_xTa_2TiO_{12}$ (A = Ba, Sr) complex perovskite dielectrics were prepared by conventional solid-state ceramic route as described in Chapter 2, Section 2.1.2. The reaction mixture was calcined in the temperature range 1200 – 1350°C for 4 hours in platinum crucibles. The powder was ground well and mixed with 4 wt. % solution of poly vinyl alcohol (PVA) as the binder. The ceramic pellets were sintered in the temperature range 1500–1625°C (See Tables 6.1 and 6.2) for 4 hours with an intermediate firing at 800°C to expel the organic binder in a high temperature furnace. The sintered ceramic pucks were polished and characterized using XRD and SEM methods. The dielectric properties were measured in the microwave frequency range (2 - 5 GHz) using resonance technique[15, 16, 17] as described Chapter 2, Sections 2.3.2 to 2.3.5. Micro-Raman scattering spectra and Infrared reflectance spectra were recorded as illustrated in Section 5.2.1 of Chapter 5.

6.2.2 Results and Discussion

6.2.2.1 Structural Characterization

In previous works, complex perovskite type $Ca_5Ta_2TiO_{12}$ was studied (See Chapter 3, Section 3.3.2) and the structural analysis confirmed its orthorhombic symmetry, with four molecular formula per unit cell. In Chapter 5, the ceramic systems $Ca_{5-x}Ba_xNb_2TiO_{12}$ and $Ca_{5-x}Sr_xNb_2TiO_{12}$ were investigated and the results showed that these materials also form orthorhombic solid solutions for small values of x ($0 \leq x \leq 1$). In this chapter, the structure and microwave dielectric properties of $Ca_{5-x}Ba_xTa_2TiO_{12}$ and $Ca_{5-x}Sr_xTa_2TiO_{12}$ ceramic systems are studied. The X-Ray diffraction patterns obtained for $Ca_{5-x}Ba_xTa_2TiO_{12}$ and $Ca_{5-x}Sr_xTa_2TiO_{12}$ ($0 \leq x \leq 5$) are shown in Fig. 6.1 and 6.2 respectively. Ba/Sr being bigger ion[18] compared with Ca^{2+}, occupies the perovskite *A*-site of the ceramics. Hence in complex perovskite form, the ceramics can be represented as $Ca(Ca_{1/4}Ta_{2/4}Ti_{1/4})O_3$, $Ca_{3/4}A_{1/4}(Ca_{1/4}Ta_{2/4}Ti_{1/4})O_3$, $Ca_{2/4}A_{2/4}(Ca_{1/4}Ta_{2/4}Ti_{1/4})O_3$, $Ca_{1/4}A_{3/4}(Ca_{1/4}Ta_{2/4}Ti_{1/4})O_3$, and $A(Ca_{1/4}Ta_{2/4}Ti_{1/4})O_3$ [A = Ba, Sr] for x = 0, 1, 2, 3 and 4 respectively.

The substitution of one Ca^{2+} ion by Ba^{2+} in $Ca_{5-x}Ba_xTa_2TiO_{12}$ resulted in the formation of a multiphase ceramic instead of a single phase $Ca_4BaTa_2TiO_{12}$ [See Fig. 6.1

(b)]. These phases were identified as $Ca_4Ta_2O_9$ (ICDD File No. 31-308) and $BaTiO_3$ (ICDD File No. 34–129). For compositions with x = 2, 3 and 4 the materials presented cubic double perovskite structure[19] [See Figs. 6.1 (c), 6.1 (d) and 6.1 (e)]. The diffraction peaks were labeled by comparison with those of $Ba(Zn_{1/3}Nb_{2/3})O_3$ (ICDD File 17–182) with cubic symmetry.

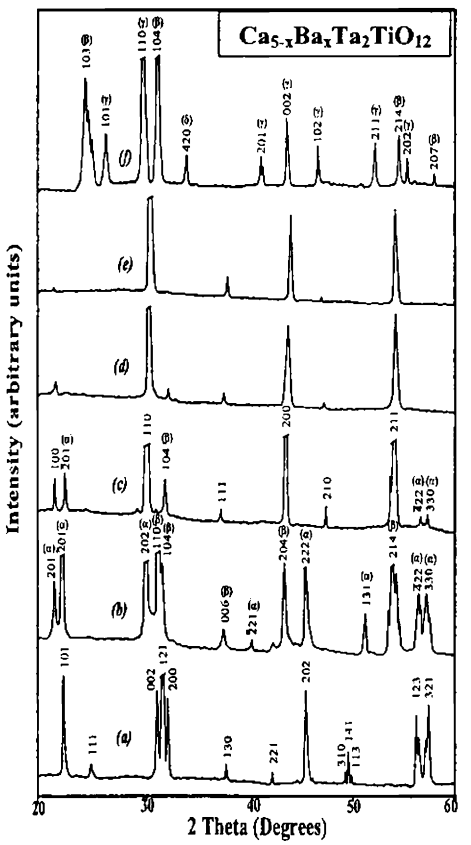

Fig. 6.1 X-Ray diffraction pattern of (a) $Ca_5Ta_2TiO_{12}$ (b) $Ca_4Ta_2O_9 - BaTiO_3$ mixture (c) $Ca_3Ba_2Ta_2TiO_{12}$ (d) $Ca_2Ba_3Ta_2TiO_{12}$ (e) $CaBa_4Ta_2TiO_{12}$ and (f) $Ba_4Ta_2O_9 - BaTiO_3$ mixture ($\alpha \rightarrow Ca_4Ta_2O_9$, $\beta \rightarrow BaTiO_3$, $\gamma \rightarrow Ba_4Ta_2O_9$ and $\delta \rightarrow BaTa_2O_6$ diffraction peaks)

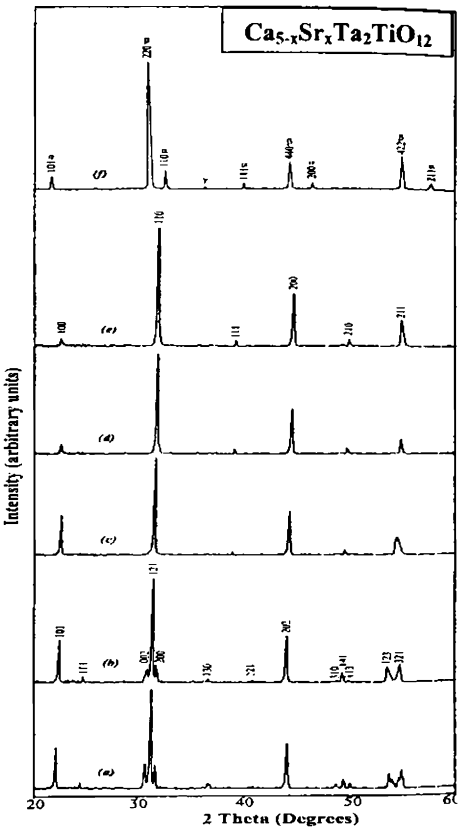

Fig. 6.2 X-Ray diffraction pattern of (a) $Ca_5Ta_2TiO_{12}$, (b) $Ca_4SrTa_2TiO_{12}$, (c) $Ca_3Sr_2Ta_2TiO_{12}$, (d) $Ca_2Sr_3Ta_2TiO_{12}$, (e) $CaSr_4Ta_2TiO_{12}$, and (f) $Sr_4Ta_2O_9$ - $SrTiO_3$ ceramics ($\alpha \rightarrow SrTiO_3$, $\beta \rightarrow Sr_4Ta_2O_9$ and $\gamma \rightarrow$ unidentified peaks).

impurity peaks are very weak and one not marked

For x = 2 and 3, traces of secondary phases corresponding to $Ca_4Ta_2O_9$ and $BaTiO_3$ were detected by X-Ray diffraction. However, for x = 4, phase pure $Ba(Ca_{1/4}Ta_{2/4}Ti_{1/4})O_3$ was formed as shown in Figs. 6.1 (e). For x = 5, a mixture of $Ba_4Ta_2O_9$ - $BaTiO_3$ and a few peaks corresponding to $BaTa_2O_6$ can be seen [Fig. 6.1(f)]. XRD profile of $Ca_{5-x}Sr_xTa_2TiO_{12}$ system was indexed based on complex perovskite structure for x up to 4. Hence, the XRD patterns in Figs. 6.2 (a) and 6.2 (b) for the compositions with x = 0 and 1, have been indexed based on the orthorhombic *Pnma* symmetry. The compositions with x = 2 to 4, Figs. 6.2 (c), 6.2 (d) and 6.2(e) present an averaged cubic double-perovskite structure similar to their barium analogue and were indexed in the same manner.

In $Ca_{5-x}Ba_xTa_2TiO_{12}$ and $Ca_{5-x}Sr_xTa_2TiO_{12}$ systems for x = 2 to 4, XRD profiles consist of strong peaks characteristics of the primitive *Pm3m* cubic perovskite together with extra lines arising from superlattice reflections. It can be seen from Figs. 6.1 and 6.2 that (for x = 2), the (123) and (321) orthorhombic peaks are still present in the diffractograms. A similar effect can be observed for the orthorhombic (200) and (002) peaks that merge with the (121) peak into the experimental resolution. As described in Chapter 5, for the niobium based solid solutions, in this case also for higher x values (x = 3 and 4), it was difficult to distinguish between a true cubic structure and a pseudo-cubic one, where the orthorhombic ferroelastic distortion became too small. Hence spectroscopic methods were adopted to reveal the true crystal structure in both Ba and Sr substituted systems. With the introduction of larger $(Ba/Sr)^{2+}$ ions, the anisotropic cell expansion decreases the differences between the lattice parameters and the structure transforms from a clear orthorhombic to a pseudo-cubic structure, but the space group remains *Pnma*. For x = 5, $(Ba/Sr)^{2+}$ ions are too large to enter into the *B*-site of the perovskite structure, so that this structure is not formed. Instead, a mixture of $(Ba/Sr)_4Ta_2O_9$ and $(Ba/Sr)TiO_3$ is formed as seen from Figs. 6.1(f) and 6.2 (f).

The synthesizing conditions and a summary of lattice parameters, structure, cell volume, density and tolerance factor of $Ca_{5-x}Ba_xTa_2TiO_{12}$ and $Ca_{5-x}Sr_xTa_2TiO_{12}$ ceramics for ($0 \leq x \leq 5$) are given in Tables 6.1 and 6.2 respectively. It is evident from Tables 6.1 and 6.2 that, in $Ca_{5-x}Ba_xTa_2TiO_{12}$ and $Ca_{5-x}Sr_xTa_2TiO_{12}$ system the calcination and sintering temperatures decrease with increase in Ba/Sr concentration.

Table 6.1 Synthesizing conditions, structure, cell volume, density, tolerance factor and microwave dielectric properties of $Ca_{5-x}Ba_xTa_2TiO_{12}$ ($0 \leq x \leq 5$) ceramics

x	Calcination Temp. (°C)	Sintering Temp. (°C)	Structure of the unit cell	Lattice parameters (Å)			Cell Volume (Å^3)	Theoretical Density (g/cm^3)	% Density	Tolerance factor (t)
				a	b	c				
0	1350	1625	Ortho rhombic	5.502(2)	7.893(1)	5.668(5)	246.18	5.41	97.2	0.9189
1	1300	1575	Mixture	#	#	#	#		#	#
2	1275	1540	Cubic	4.109(9)	-	-	277.50	5.98	96.9	0.9585
3	1240	1525	Cubic	4.135(1)	-	-	282.82	6.51	97.2	0.9810
4	1210	1500	Cubic	4.159(8)	-	-	287.92	6.73	98.0	1.0035
5	1200	*	Mixture	#	#	#	#	#	#	#

= Form as a mixture.

* = Could not be sintered (powder sample).

Second phases observed

In Ba-substituted system, the calcination temperature decreases from 1350 to 1200°C and sintering temperature varies from 1625°C to 1500°C for $0 \leq x \leq 5$. At $x = 5$, the ceramics were not able to sinter in compact form as they crumbled to powder after firing. Efforts were made to sinter these materials by adding different amounts of low melting CuO, but could not succeed. In $Ca_{5-x}Sr_xTa_2TiO_{12}$ ceramics, the calcination and sintering temperatures varied from 1350 – 1275 and 1625 – 1560°C, when x shifted from 0 to 5. The materials exist in single phase orthorhombic and cubic symmetries as well as in mixture phases depending on the composition. In both the systems, for $x = 2$, 3 and 4 the superstructure volumes were calculated based on cubic perovskite framework, for which the atomicity is $Z = 1$, whereas for the orthorhombic group $Z = 4$. Hence, to make in line with the cell volume of orthorhombic structure, the unit cell volumes of the pseudo-cubic structures were multiplied by 4. The enhancement in cell volume observed in both systems with compositional variation is due to the substitution of bigger barium/strontium ion in place of comparatively smaller[18] calcium ion. The theoretical density of $Ca_{5-x}Ba_xTa_2TiO_{12}$ ceramics varied from 5.41 to 6.73 g/cm^3 and that of $Ca_{5-x}Sr_xTa_2TiO_{12}$ dielectrics varied from 5.41 to 6.23 g/cm^3. In both the cases the experimental density was found to be more than 98 % of the theoretical value. The

tolerance factor (t)[20], which is a measure of the symmetry of the perovskite structure, is calculated for the investigated ceramic systems using the relation,

$$t = \frac{R_O + R_{Ca}(4-x)/4 + R_{Ba/Sr}(x)/4}{\sqrt{2}\ \left[R_O + \left(0.25R_{Ca} + 0.50R_{Ta} + 0.25R_{Ti}\right)\right]} \qquad (6.1)$$

where R denotes the radius[18] of corresponding cations occupying the appropriate perovskite sites. The increase in average A-site ionic radius is associated with enhancement in tolerance factor and the symmetry approaches cubic when $t \rightarrow 1$ (theoretically).The tolerance factor of $Ca_{5-x}A_xTa_2TiO_{12}$ (A = Ba, Sr) ceramics increased and approached unity with increasing x, which can be attributed to the increase in average A-site ionic radius[18] due to the substitution of Ba/Sr ions in place of Ca. This is in agreement with the fact that as the tolerance factor tends to unity, the symmetry changes to cubic perovskite form.

Table 6.2 Synthesizing conditions, lattice parameters, cell volume, density and tolerance factor of $Ca_{5-x}Sr_xTa_2TiO_{12}$ ($0 \le x \le 5$) ceramics

x	Calcination Temp. (°C)	Sintering Temp. (°C)	Structure of the unit cell	Lattice parameters (Å)			Cell Volume (Å^3)	Theoretical Density (g/cm^3)	% Density	Tolerance factor (t)
				a	b	c				
0	1350	1625	Orthorhombic	5.502(2)	7.893(1)	5.668(5)	246.18	5.41	97.22	0.9189
1	1300	1625	Orthorhombic	5.588(9)	7.957(7)	5.668(8)	252.12	5.60	97.39	0.9273
2	1300	1600	Pseudo-Cubic	3.990(6)	-	-	254.20	5.86	96.76	0.9357
3	1250	1575	Pseudo-Cubic	4.014(6)	-	-	258.82	6.06	96.53	0.9441
4	1250	1550	Pseudo-Cubic	4.044(9)	-	-	264.72	6.23	98.59	0.9525
5	1275	1560	Mixture ($Sr_4Ta_2O_9$ – $SrTiO_3$	b	b	b	b	b	b	b

[b] Could not be calculated because of the mixed-phase nature.

6.2.2.2 Microstructural Analysis

SEM micrographs of polished and thermally etched surfaces of the sintered $Ca_{5-x}A_xTa_2TiO_{12}$ (A = Ba, Sr) samples are shown in Fig. 6.3. Microstructure of $Ca_5Ta_2TiO_{12}$ ceramics has been described earlier (See Chapter 3, Section 3.3.2) with uniform distribution of large grains of about 10 μm in size.

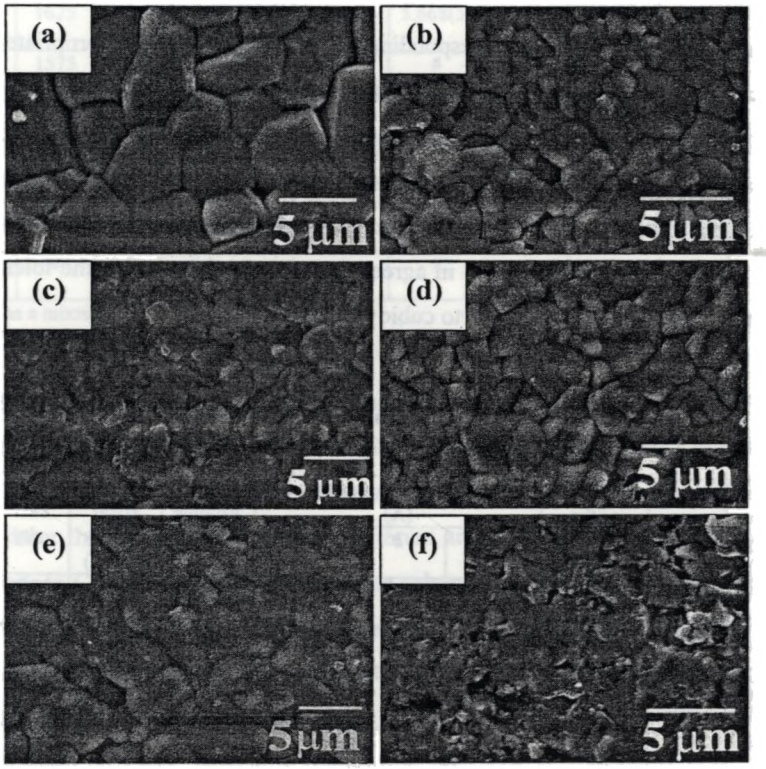

Fig. 6.3 SEM pictures of (a) $Ca_4SrTa_2O_9$ (b) $Ca_3Sr_2Ta_2TiO_{12}$ (c) $Ca_3Ba_2Ta_2TiO_{12}$ (d) $CaSr_4Ta_2TiO_{12}$ (e) $CaBa_4Ta_2TiO_{12}$ and (f) $Sr_4Ta_2O_9$ - $SrTiO_3$ mixture

In Fig. 6.3 (a) surface morphology of $Ca_4SrTa_2TiO_{12}$ ceramics sintered at 1625°C is shown, which has an average grain size of 6 – 7 μm. Figs. 6.3 (b) and 6.3 (d), depict the microstructure of $Ca_3Sr_2Ta_2TiO_{12}$ and $CaSr_4Ta_2TiO_{12}$ ceramics respectively. It is evident from the figures that their average grain size is about 2 μm, which is much less than that of

$Ca_5Ta_2TiO_{12}$ ceramics. A pronounced difference in microstructure is not observed between samples shown in Fig. 6.3 (a), 6.3(b) and 6.3(d) and that of $Ca_5Ta_2TiO_{12}$ ceramics (See Fig. 3.6(b) in Chapter 3, Section 3.3.2). Moreover in Figs. 6.3 (a), 6.3(b) and 6.3(d), no secondary phases can be observed in any specimen and complete solid solution of the complex perovskite phase was confirmed for $x = 0$ to 4. The secondary electron images from the surface of $Ca_3Ba_2Ta_2TiO_{12}$ is shown in Fig. 6.3 (c). The grain distribution is not uniform compared with that in Figs. 6.3 (a) and 6.3 (b), and presents some stray phases corresponding to $BaTiO_3$. Fig. 6.3 (e) shows the microstructure of $CaBa_4Ta_2TiO_{12}$ ceramics. The SEM picture resembles that of parent $Ca_5Ta_2TiO_{12}$ ceramics and is also similar to that of Sr-substituted composition [Fig. 6.3 (d)]. The slight variation in grain shape is evident between that appeared in Fig. 6.3 (a) [orthorhombic phase] and that of 6.3 (b), 6.3(d) and 6.3(e) [pseudo-cubic structure]. No secondary phases were observed for this composition indicating phase pure formation of pseudo-cubic $Ca(Ba/Sr)_4Ta_2TiO_{12}$ material. The grain size of Ba/Sr substituted single-phase compositions is smaller than that of $Ca_5Ta_2TiO_{12}$ (See Chapter 3, Section 3.3.2) and are thickly packed to leave less porosity in the sample, which implies that the substitution of Ca^{2+} by $(Ba/Sr)^{2+}$ improved the sinterability and enhanced the densification. [See Tables 6.1 and 6.2]. Fig. 6.3 (f) shows nonuniform microstructure with pores in the grain boundaries. The complete substitution of Sr^{2+} in place of Ca^{2+} ions in $Ca_5Ta_2TiO_{12}$ results in the formation of a mixture phase as is evident from the presence of two distinct types of grains [$Sr_4Ta_2O_9$ and $SrTiO_3$] in Fig. 6.3 (f).

6.2.2.3 Microwave Dielectric Properties

The microwave dielectric properties of $Ca_{5-x}Ba_xTa_2TiO_{12}$ ($0 \leq x \leq 4$) ceramics are shown in Fig. 6.4. $Q_u\ x\ f$ shows an abrupt decrease when x is varied from 0 to 1 and thereafter decreases gradually [$Q_u\ x\ f$ varied from 33000GHz to 1400 GHz]. ε_r and τ_f shows a linear increase with increasing x. ε_r changed from 38 to 64 and τ_f increased from +10 to +24 ppm/°C when x was altered from 0 to 4 in $Ca_{5-x}Ba_xTa_2TiO_{12}$ ceramics. Microwave dielectric properties of the ceramics were affected by the presence of the $BaTiO_3$ secondary phases.

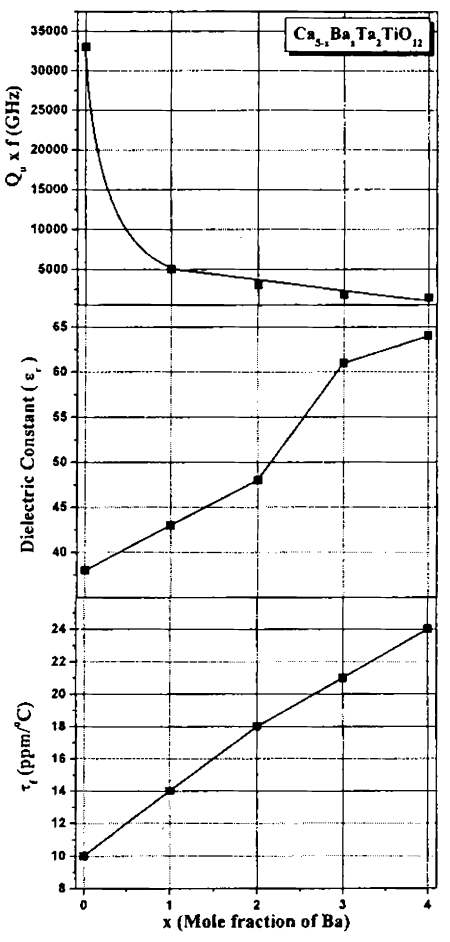

Fig. 6.4 Microwave dielectric properties of $Ca_{5-x}Ba_xTa_2TiO_{12}$ ($0 \leq x \leq 4$) ceramics

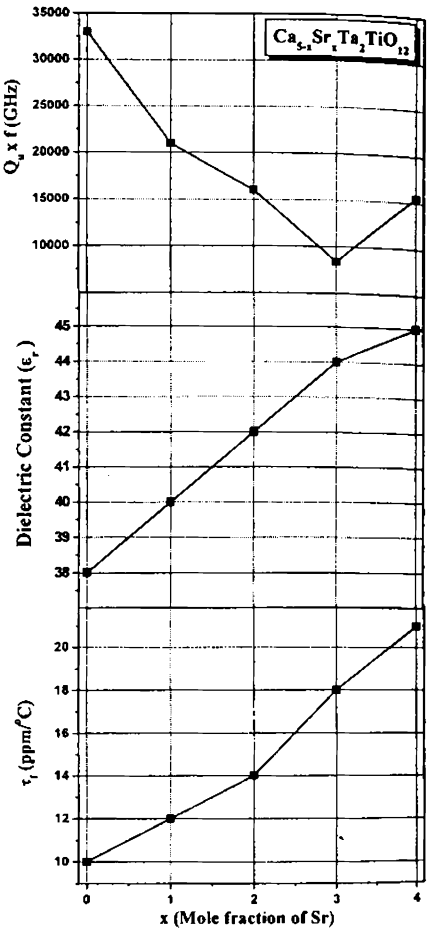

Fig. 6.5 Microwave dielectric properties of $Ca_{5-x}Sr_xTa_2TiO_{12}$ ($0 \leq x \leq 4$) ceramics

The microwave dielectric properties of $Ca_{5-x}Sr_xTa_2TiO_{12}$ ceramics with different mole fraction of strontium content are given in Fig. 6.5. The quality factor gradually decreases from 33000 to 8500 for $x = 0$ to $x = 3$ and then increases to 16000 GHz for $x = 4$. In $Ca_{5-x}Sr_xTa_2TiO_{12}$ ceramics, when $x = 0$ and $x = 4$ the perovskite *A*-site is completely occupied by either Ca (for $x = 0$) or Sr (for $x = 4$) ions and has higher $Q_u \times f$ compared to

other compositions from $x = 1$ to 3, where partial occupancy of Ca and Sr ions takes place in the perovskite *A*-site (double perovskite structure). The behaviour is similar to that exhibited by their niobium analogue (See Chapter 5, Section 5.2.2.3). Moreover, it is evident from Fig. 6.5 that, the quality factor is higher for $x = 0$ than that of $x = 4$. The replacement of smaller Ca ion with comparatively larger Sr ions in the perovskite *A*-site leads to distortions in the unit cell and hence structural phase transition occurs, which causes the reduction of quality factor for $Sr(Ca_{1/4}Ta_{2/4}T_{1/4})O_3$ ceramics compared with $Ca(Ca_{1/4}Ta_{2/4}T_{1/4})O_3$. For $x = 5$ the multiphase compound which is a mixture of $Sr_4Ta_2O_9$ and $SrTiO_3$ was formed and it did not resonate. The dielectric constant and τ_f of $Ca_{5-x}Sr_xTa_2TiO_{12}$ ceramics increases with strontium content. The ε_r varies from 38 to 45 as x changes from 0 to 4 and τ_f shifts to the more positive side and reaches 21 ppm/°C for $x = 4$. The increase in ε_r in both Ba and Sr substituted systems can be attributed to their increased polarizability[21] compared with Ca. Moreover the expansion of the unit cell with the substitution of bigger Ba/Sr ions for Ca in turn increases the ease of polarizability of the unit cell and hence increases ε_r of the system. The shift of τ_f towards the more positive side with Ba/Sr substitution was also quite expected as $(Ba/Sr)TiO_3$ materials posses high positive τ_f.

6.2.2.4 Raman Spectroscopic Studies

The Raman spectra of $Ca_{5-x}Ba_xTa_2TiO_{12}$ ($0 \leq x \leq 5$) microwave ceramics are depicted in Fig. 6.6. The Raman spectra of $Ca_{5-x}A_xTa_2TiO_{12}$ (A = Ba, Sr) ceramics are similar to that of $Ca_{5-x}A_xNb_2TiO_{12}$ (A = Ba, Sr) [See Chapter 5, Section 5.2.2.4]. However the substitution of Nb by Ta produced a faint shift to lower frequencies (redshift), as expected and an exception have occurred at 798-803 cm^{-1}, corresponding to the $A_{1g}(O)$ mode, which blueshifted for the ceramic with tantalum. This behaviour can be explained by the increasing of the force constant or the stiffness of the oxygen octahedra cage, as also verified by Siny *et al.* in $Ba(Mg_{1/3}Ta_{2/3})O_3$ ceramics.[22]

For the parent $Ca_5Ta_2TiO_{12}$ material, the characteristic bands of *A*-site occupied by Ca (120 cm^{-1}) together with a set of bands related to *B*-sites. Also bands at 640 cm^{-1} which related to the *B*-O symmetric stretching vibration,[23,24] and bands at 450-455 & 475-485 cm^{-1} assigned to *B*-O_3 torsional modes[23,25] can be observed in the spectrum. The bands appeared

in the region 235-370 cm^{-1} are related to the modes associated with rotations of oxygen cage and *B*-site ordering,[24] while the bands at 530-600 and 750-800 cm^{-1} correspond to oxygen motion. It is clear from Fig. 6.6 that, the bands in the regions 300-400 and 720-800 cm^{-1} are related to 1:1 ordering, similar to the results of Raman spectroscopic studies carried out by Zheng *et al.*[25] and Levin *et al.*[26] in $Ca(Ca_{1/3}Nb_{2/3})O_3$ and $CaTiO_3$-based ceramics. Moreover, according to the group theory analysis A_{1g} and F_{2g} modes in the spectra become Raman active due to *B*-site ordering,[27] which points towards the possibility of such an effect in the investigated ceramic systems.

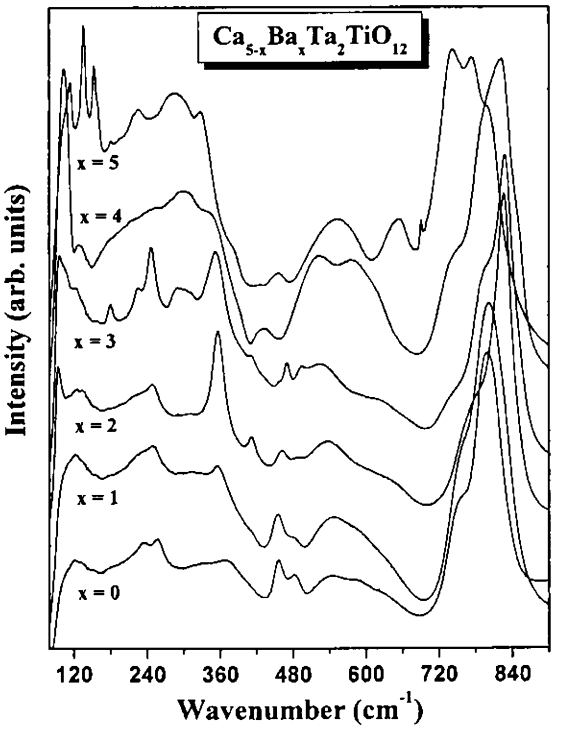

Fig. 6.6 Raman spectra of $Ca_{5-x}Ba_xTa_2TiO_{12}$ ceramics

From the Raman spectra of $Ca_{5-x}Ba_xTa_2TiO_{12}$ ceramics shown in Fig. 6.6 it can be noted that, the spectra for $x = 0$ and $x = 1$ are similar. With the introduction of Ba, the modes

are shifted towards lower frequencies. At $x = 2$ and 3 more significant changes in the Raman spectra was observed. Bands at around 260 and 360 cm^{-1} appeared, increasing their intensity and became more narrow. Also, the bands at 120 and 800 cm-1 shifted to 100 cm^{-1} (redshift) and to 820 cm^{-1} ($A_{1g}(O)$ mode, which blueshifted). The strongest band around 800 cm^{-1} is related to the "breathing" mode of the TaO_6 octahedra and shoulders are visible on both sides of this band. Levin *et al.*[26] observed these shoulders on the Raman spectra of $Ca_4Ta_2O_9$ and attributed them to the presence of metastable superstructures. The $A_{1g}(O)$ mode shifted to higher frequencies for increasing Ba content as a result of the volume change. This result was also verified in $Ca_5Nb_2TiO_{12}$ materials and could be associated with short-range ordering (See Section 5.2.2.4 of Chapter 5).

The Raman spectrum for $x = 4$ looks different from that for lower values of x ($1 \leq x \leq 3$) and hence announces the presence of a single-phase material. In this composition all Ba ions are in the *A*-site and no more distortions could be observed. The broad bands indicate the poor *B*-site long-range ordering. The $A_{1g}(O)$ mode represents a qualitative indication of the degree of *B*-site ordering and, obviously, differences in charge or ionic sizes will influence the distribution of ions on any given site. Ca and Ba atoms present significant differences in their ionic radii and the larger the difference the greater the influence on the vibrational modes, particularly those related to ordering. Zheng *et al.*[27] considered the possibility that the width and frequency of $A_{1g}(O)$ band may be affected by the size distribution of the *A*-site cations. Their conclusions are that the *A*-site distribution influences the degree of short-range order on the *B*-site or, also, the size differences in *A*-site could constrict in some manner the octahedra "breathing" mode to occur in a given range of frequencies. In this case, it is believed that the $A_{1g}(O)$ mode is a function of the volume cage, which presents the maximum variation for $x = 4$. Finally, correlating this result to the microwave properties, the decrease in Q_u with Ba introduction (See Fig. 6.4) could be an expected result, since its presence alters the *A*-site distribution and probably increases the degree of short-range order. This increase is detrimental to Q_u because it induces anharmonicity and increases phonon damping. As verified by Zheng *et al.*[26, 28] and Webb *et al.*[29] only when the order changes from short to long-range the values of Q_u must increase. With $x = 5$, X-Ray diffraction of the ceramics presented multiple phases ($Ba_4Ta_2O_9$, $BaTiO_3$

and $BaTa_2O_6$ phases) and could not be sintered. At least 22 bands can be seen in the spectra as a result of the superposition of different combination modes of all the crystalline phases observed. The appearance of different phases leads to the development of multiple bands within the broad Raman peaks.

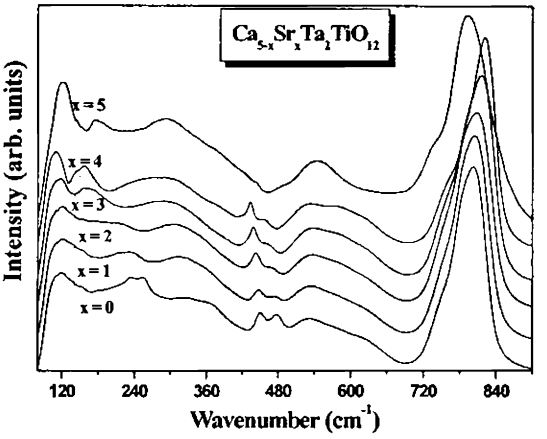

Fig. 6.7 Raman spectra of $Ca_{5-x}Sr_xTa_2TiO_{12}$ ceramics

Fig. 6.7 illustrates the Raman spectra for $Ca_{5-x}Sr_xTa_2TiO_{12}$ ($0 \leq x \leq 5$) microwave ceramics with isovalent cation substitution on *A*-site. Here the characteristic bands are identified in a similar way as that in $Ca_{5-x}Ba_xTa_2TiO_{12}$ ceramics. With compositional variations in Sr substitution, the spectra for x = 0 to 4 exhibits similar features except with the shifting of certain bands. This is compatible with the structural interpretation that, although the structure evolves to pseudo-cubic for higher x values, it remains orthorhombic. With Sr substitution, the bands centered at 93 cm^{-1} (Ta) shifted to lower frequencies for x up to 4. Also, the peaks at 255 cm^{-1} decreased their intensity and became broader at higher frequencies for increasing x. When x = 4, bands appeared at 135-155 cm^{-1}, as a result of a highly distorted structure.

From Fig. 6.7 it is evident that, the band at 117–123 cm^{-1} is shifted to higher frequencies with increase in x. Since this region of the spectra reflects the *A*-site environment, as well as probable rotations of the oxygen cage, it is assumed that the

substitution of strontium by calcium occurs in the perovskite *A*-site. Increasing amount of strontium atoms ($1 \leq x \leq 4$), now in *A*-sites, led to higher distortions, shifting the bands continuously to lower frequencies. This behaviour is related to the increased global mass in *A*-site due to the substitution of heaviour Sr^{2+} ions in the mixed complex ceramics as that observed in the niobium based materials (See Section 5.2.2.4 of Chapter 5). Microwave properties showed interesting results for $x = 4$ (Fig. 6.5), with a sudden increase in Q_u probably associated to the distortions in the octahedra verified by Raman spectroscopy. The mixture phase formation of $Ca_{5-x}Sr_xTa_2TiO_{12}$ with $x = 5$ is verified in the Raman spectroscopy by the unusual behaviour of shifting and disappearance of certain modes. For $x = 5$, certain bands in the range 135 – 155 cm^{-1} disappeared and a final shift to higher frequencies occurred for the band at around 95 cm^{-1}, which moved to 115 cm^{-1} and the spectra looked different from that of all other compositions. It is in agreement with the XRD pattern that with $x = 5$, $Sr_5Ta_2TiO_{12}$ does not form but it is a mixture of $SrTiO_3$ and $Sr_4Ta_2O_9$.

6.2.2.5 FTIR Analysis

Figs. 6.8 and 6.9 show the infrared-reflectivity spectra for $Ca_{5-x}Ba_xTa_2TiO_{12}$ and $Ca_{5-x}Sr_xTa_2TiO_{12}$ microwave ceramics. The results of far-infrared agree with those obtained from Raman analyses. As it can be seen from Fig. 6.8 that, with $x = 0$, $Ca_5Ta_2TiO_{12}$ samples shows defined set of bands at 370, 470 and 540 cm^{-1}. The frequency region below 150 cm^{-1} can be attributed to the *A*-BO_3 external mode, while the O-*B*-O bending modes appear between 170 and 500 cm^{-1}. The highest wave number range, 500-700 cm^{-1}, is due to the oxygen octahedra-elongation mode, that is, BO_6 stretching. In $Ca_5Ta_2TiO_{12}$ materials the shifting of FTIR modes to lower frequencies and increase in the intensities of the bands are observed as expected, compared with Nb-based materials (See chapter 5, Section 5.2.2.4). This behaviour can be associated to the stiffness of the oxygen octahedra with Ta.

Figs. 6.8 present the results of the far-infrared analyses for $Ca_{5-x}Ba_xTa_2TiO_{12}$ microwave ceramics. Barium substitution lead to a better definition of the bands at around 130 cm^{-1} with a maximum at $x = 4$. Also, a continuous shift of bands occurred with the addition of Ba atom. The maximum broadening of bands occurred at $x = 4$ in the spectral range 150-370 cm^{-1} and coincides with the formation of $Ba(Ca_{1/4}Ta_{2/4}Ti_{1/4})O_3$ solid solutions.

With x = 5, the spectra consisted of four sets of broad bands because of the multiple-phase nature of these samples.

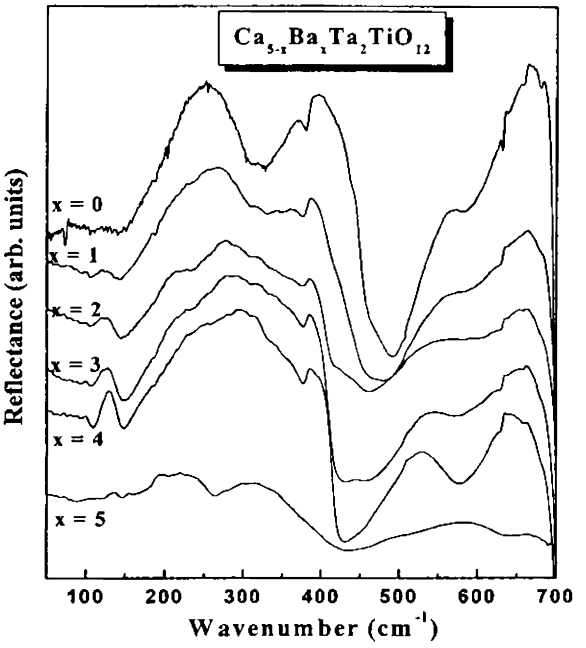

Fig. 6.8 FTIR spectra of $Ca_{5-x}Ba_xTa_2TiO_{12}$ ceramics

Significant changes were observed in the FTIR spectra of $Ca_{5-x}Sr_xTa_2TiO_{12}$ with increasing x. The substitution of Ca by Sr led to lattice distortions to increase the band at 350-360 cm^{-1}. Shifts occurred especially in the dip centered at 480 cm^{-1}. Also, it is interesting to note the increase of band at 550 cm^{-1}, which is related to the oxygen octahedral-elongation modes. As is evident from Fig. 6.9, for x = 4 the bands at around 150 cm^{-1} and in the range 220-320 cm^{-1} are more defined. It is noteworthy that maximum distortion of the spectra occurs at this concentration of the substituted Sr ions.

The maximum distortions at x = 4 coincides with the sudden increase observed in Q_w and verified with the particular features formed in Raman spectra. This frequency range can be considered as specific for ordered structures and their strength can be used as a relative

measure of this ordering.[27] It can be noted from Fig. 6.9 that with x = 5, the spectra appears different from that of all other compositions where the material was formed as a mixture.

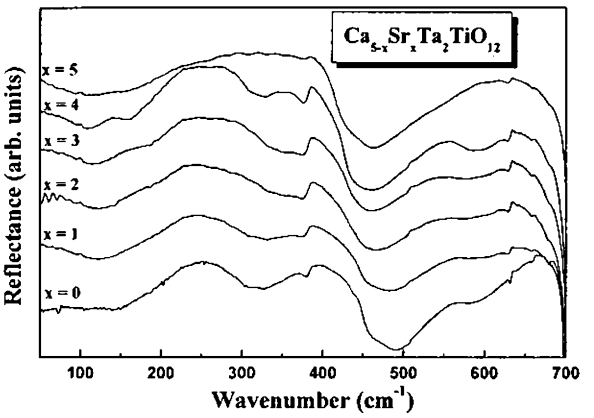

Fig. 6.9 FTIR spectra of $Ca_{5-x}Sr_xTa_2TiO_{12}$ ceramics

6.3 $Ca_{5-x}A'_xTa_2TiO_{12}$ (A' = Mg, Zn, Ni & Co) CERAMICS

6.3.1 Experimental Procedure

The ceramics were processed using conventional mixed oxide route so as to form compounds in the $Ca_{5-x}Mg_xTa_2TiO_{12}$, $Ca_{5-x}Zn_xTa_2TiO_{12}$, $Ca_{5-x}Ni_xTa_2TiO_{12}$ and $Ca_{5-x}Co_xTa_2TiO_{12}$ series with x = 0, 0.2, 0.4, 0.6, 0.8, 1, 2, 3, 4 and 5 as described in Chapter 2, Section 2.1.2. Starting mixtures were wet milled for 24 h, calcined in the temperature range 1350 – 850°C/4h, in air and the resultant reacted powder was hand mixed in distilled water medium. Cylindrical ceramic pellets were sintered at temperatures between 1625 – 1150°C, depending on the compositional variations, until the highest density was achieved. The experimental density, XRD of powdered specimens and surface morphology was analyzed. Microwave characterizations of the ceramics were performed using resonance method as described in Chapter 2, section 2.2.2 to 2.2.5. The computer modeling of cavity shielded and end-shorted DRs for Q_u and ε_r measurements have discussed in Chapter 5, Section 5.3.1.2, using 3D TLM based CAD of Microstripes – 6.5[14].

6.3.2 Results and Discussions

6.3.2.1 Phase Analysis

Fig. 6.10 shows the XRD spectra of $Ca_{5-x}Mg_xTa_2TiO_{12}$ ceramics for $0 \leq x \leq 5$. It is evident from the figure that, the solid solution based on $Ca_{5-x}Mg_xTa_2TiO_{12}$ was formed only for x up to 1. For $0 \leq x \leq 1$, the XRD reflections were indexed based on the single phase orthorhombic structure of $Ca_5Ta_2TiO_{12}$ complex perovskite material.

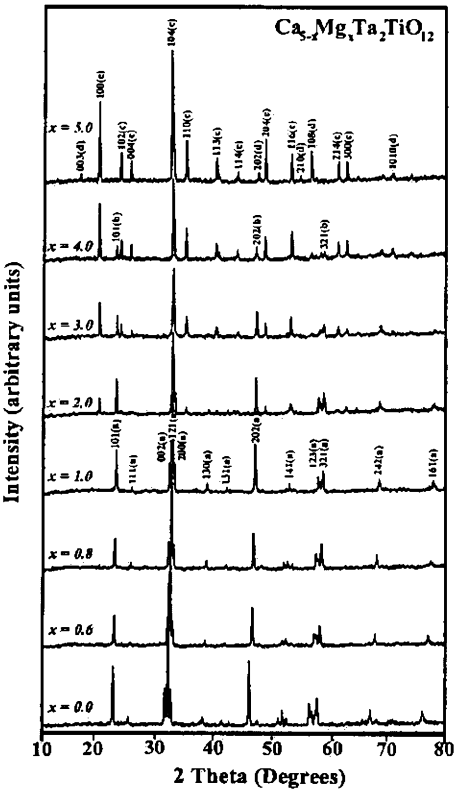

Fig. 6.10 X-Ray diffraction patterns of $Ca_{5-x}Mg_xTa_2TiO_{12}$ ceramics a → $Ca_5Ta_2TiO_{12}$, b → $CaTiO_3$, c → $Mg_4Ta_2O_9$ and d → $MgTiO_3$

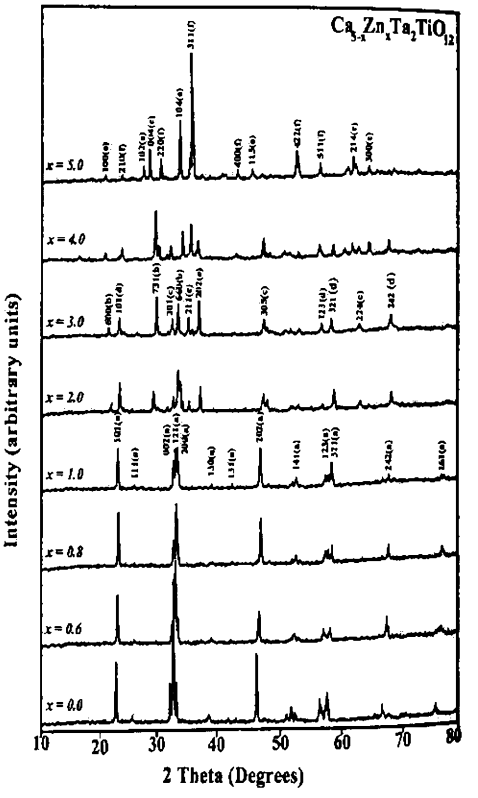

Fig. 6.11 X-Ray diffraction patterns of $Ca_{5-x}Zn_xTa_2TiO_{12}$ ceramics a → $Ca_5Ta_2TiO_{12}$, b → $Ca_3Ta_2O_8$, c → Zn_2TiO_4, d → $CaTiO_3$,e → $Zn_4Ta_2O_9$ and f → $ZnTiO_3$

However for $x > 1$, the XRD patterns exist as a mixture of two distinct phases as shown in Fig. 6.10. These phases were identified as $Mg_4Ta_2O_9$ and $CaTiO_3$ for $2 \leq x \leq 4$. It was observed that with the increase of x from 2 to 4, $CaTiO_3$ concentration gradually decreased with the promotion of $Mg_4Ta_2O_9$. However with $x = 5$, the XRD pattern was found to be a mixture of $Mg_4Ta_2O_9$ - $MgTiO_3$ phases.

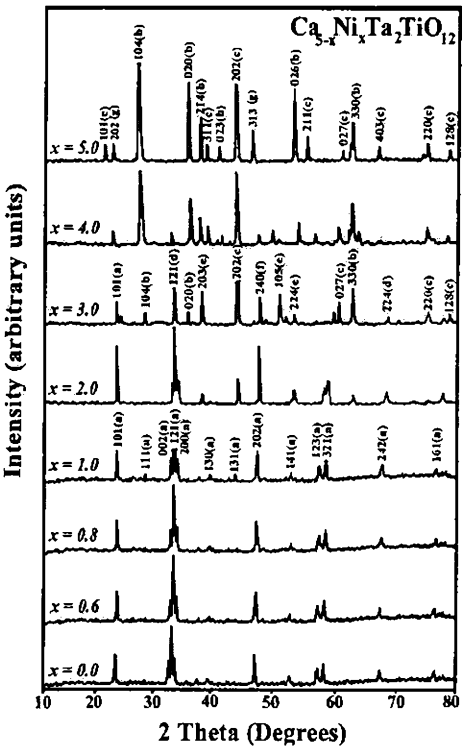

Fig. 6.12 X-Ray diffraction patterns of $Ca_{5-x}Ni_xTa_2TiO_{12}$ ceramics a → $Ca_5Ta_2TiO_{12}$, b → $Ni_4Ta_2O_9$, c → $NiTiO_3$, d → $CaTiO_3$, e → Ni_3TiO_5 and f → $CaTa_2O_6$

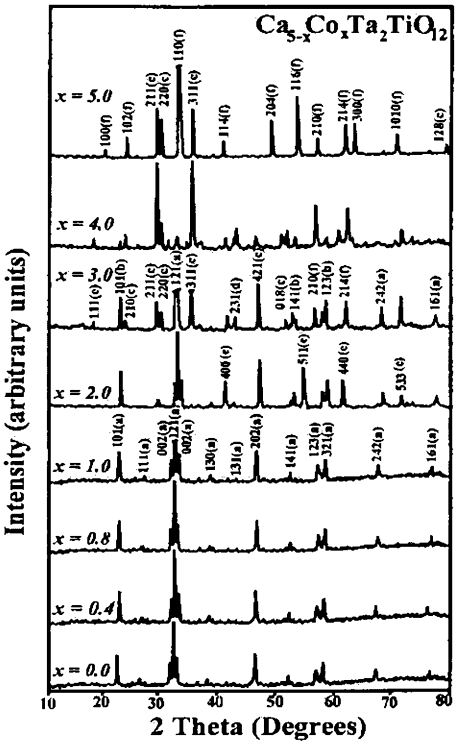

Fig. 6.13 X-Ray diffraction patterns of $Ca_{5-x}Co_xTa_2TiO_{12}$ ceramics a → $Ca_5Ta_2TiO_{12}$, b → $CaTiO_3$, c → $CoTiO_3$, d → $CoTa_2O_6$, e → Co_2TiO_4 and f → $Co_4Ta_2O_9$

XRD patterns of $Ca_{5-x}Zn_xTa_2TiO_{12}$ ceramics for $0 \leq x \leq 5$ are depicted in Fig. 6.11. As in the case of Mg^{2+} substitution, $Ca_{5-x}Zn_xNb_2TiO_{12}$ dielectrics also form solid solution phases only up to $x = 1$. Compositions with higher values of Zn^{2+} substitution formed mixture

phases as is evident from Fig. 6.11. Phases corresponding to $Ca_3Ta_2O_8$, $CaTiO_3$, $ZnTiO_3$ and $Zn_4Ta_2O_9$ were identified in the XRD profile with x = 2, 3 and 4. With x = 5, $Ca_{5-x}Zn_xTa_2TiO_{12}$ ceramics were identified as a mixture of $Zn_4Ta_2O_9$ - $ZnTiO_3$ phases.

Fig. 6.12 shows the XRD pattern recorded from the powdered specimens of $Ca_{5-x}Ni_xTa_2TiO_{12}$ for $0 \leq x \leq 5$. In this case also single phase materials with slight shift of diffraction peaks towards the higher 2θ values was observed for $0 \leq x \leq 1$, in a way similar to that in the case of Mg and Zn substituted materials. The XRD patterns were indexed comparing with that of the parent $Ca_5Ta_2TiO_{12}$ material. For $2 \leq x \leq 5$, the ceramics form mixture phases as evidenced in XRD analysis. With x = 2, 3 and 4, the ceramics were found to be a mixture of $Ni_4Ta_2O_9$, $NiTiO_3$, $CaTiO_3$, Ni_3TiO_5 and $CaTa_2O_6$ depending on the composition. With x = 5, $Ni_4Ta_2O_9$ - $NiTiO_3$ phases were only present in the mixture.

The XRD patterns recorded from the powdered specimens of $Ca_{5-x}Co_xTa_2TiO_{12}$ ceramics are given in Fig. 6.13. As in the case of Mg, Zn and Ni substituted systems, Co based ceramics also form phase pure compositions for $0 \leq x \leq 1$ implying that they form a complete solid solution in this range. With $2 \leq x \leq 4$, the ceramics were formed as a mixture of $CoTa_2O_6$, Co_2TiO_4, $CoTiO_3$ and $CaTiO_3$ whereas for x = 5, the composition was formed as a mixture of $Co_4Ta_2O_9$ - $CoTiO_3$ phases.

In $Ca_{5-x}A'_xTa_2TiO_{12}$ (A' = Mg, Zn, Ni & Co) system, for $0 \leq x \leq 1$ the ceramics form as single phase materials. However the maximum intensity Bragg reflections [(121), (101), and (202)] were shifted towards the higher angle side indicating the modification in the unit cell volume (See Table 6.3). The divalent A'^{2+} cation can be substituted in the perovskite A or B-site. But it is known that[30] in a perovskite structure bigger cation will occupy A-site of the perovskite structure and hence in the present case, the compositions can be possibly represented as $Ca[Ca_{(1-x)/4}A'_{x/4}Ta_{2/4}Ti_{1/4}]O_3$ (A' = Mg, Zn, Ni & Co) for $0 \leq x \leq 1$ owing to the onset of lower ionic radius[18] of A'^{2+} compared with that of Ca^{2+}. With $x \geq 1$, substitution of Mg, Zn, Ni or Co ions obviously do not take place in $Ca(Ca_{1/4}Ta_{2/4}Ti_{1/4})O_3$ complex perovskites to form a solid solution and lead to the formation of mixture phases as is evidenced by XRD studies.

6.3.2.2 Densification and Microstructural Analysis

The lattice parameters, unit cell volume, X-Ray density and tolerance factors of $Ca[Ca_{(1-x)/4}A'_{x/4}Ta_{2/4}Ti_{1/4}]O_3$ (A' = Mg, Zn, Ni & Co) dielectrics for $0 \leq x \leq 1$ are given in Table 6.3. It is evident from the table that, the lattice parameters and cell volume decreased linearly with x, associated with a corresponding increase in X-Ray density. The decrease in cell volume with increase in x was due to the substitution of A'^{2+} ions with lower radii[18] than Ca^{2+}. In $Ca_{5-x}Mg_xTa_2TiO_{12}$ ceramics, the density varied from 97 to 98.5% of the theoretical values, whereas in Zn, Ni & Co substituted systems only a slight increase in percentage density was observed.

Table 6.3. Unit cell parameters, density and tolerance factor of $Ca_{5-x}A'_xTa_2TiO_{12}$ (A' = Mg, Zn, Ni & Co) ceramics for $0 \leq x \leq 1$

Material	x	Lattice parameters (Å)			Cell Volume (Å^3)	X-Ray density (g/cm^3)	% Density	Tolerance factor (t)
		a	b	c				
$Ca_5Ta_2TiO_{12}$	0.0	5.502(2)	7.893(1)	5.668(5)	246.180	5.41	97.19	0.9189
$Ca_{5-x}Mg_xTa_2TiO_{12}$	0.2	5.479(2)	7.854(1)	5.663(4)	243.690	5.44	97.31	0.9240
	0.4	5.455(3)	7.813(3)	5.632(1)	240.035	5.50	97.55	0.9290
	0.6	5.440(0)	7.789(4)	5.621(0)	238.174	5.52	97.81	0.9342
	0.8	5.407(4)	7.755(1)	5.609(8)	235.193	5.58	98.10	0.9394
	1.0	5.380(2)	7.738(0)	5.587(5)	232.589	5.61	98.42	0.9447
$Ca_{5-x}Zn_xTa_2TiO_{12}$	0.2	5.477(5)	7.861(2)	5.664(1)	243.861	5.49	97.26	0.9235
	0.4	5.443(1)	7.827(1)	5.648(4)	240.618	5.60	97.38	0.9282
	0.6	5.425(7)	7.786(0)	5.625(2)	237.595	5.71	97.54	0.9329
	0.8	5.395(6)	7.757(1)	5.590(2)	233.936	5.84	97.72	0.9376
	1.0	5.374(4)	7.734(2)	5.570(3)	231.503	5.93	96.67	0.9424
$Ca_{5-x}Ni_xTa_2TiO_{12}$	0.2	5.465(2)	7.860(4)	5.653(6)	242.824	5.51	97.27	0.9255
	0.4	5.440(5)	7.834(1)	5.609(4)	239.038	5.62	97.36	0.9322
	0.6	5.421(8)	7.799(2)	5.592(2)	236.421	5.71	97.55	0.9390
	0.8	5.400(9)	7.773(4)	5.560(4)	233.376	5.81	96.95	0.9458
	1.0	5.380(6)	7.751(2)	5.532(1)	230.685	5.90	96.99	0.9528
$Ca_{5-x}Co_xTa_2TiO_{12}$	0.2	5.473(4)	7.865(4)	5.631(2)	242.387	5.52	97.42	0.9246
	0.4	5.453(0)	7.842(2)	5.580(5)	238.614	5.63	97.59	0.9304
	0.6	5.420(2)	7.815(5)	5.561(6)	235.548	5.73	97.65	0.9362
	0.8	5.401(1)	7.774(6)	5.555(4)	233.239	5.81	97.34	0.9421
	1.0	5.375(0)	7.764(4)	5.521(7)	230.399	5.91	96.43	0.9481

It was established[31] that the tailoring of dielectric properties of microwave ceramics by substitution reactions are always associated with tilting of oxygen octahedra due to the

difference in ionic radii[18] of two cations being involved in the process. Hence the variation of tolerance factor[20] which is a measure of the symmetry of the perovskite structure was calculated as a function of substituted A'^{2+} ions in $Ca[Ca_{(1-x)/4}A'_{x/4}Ta_{2/4}Ti_{1/4}]O_3$ [A' = Mg, Zn, Ni & Co] ceramics for $0 \leq x \leq 1$. It is clear from the table that the substitution of smaller ions like Mg^{2+}, Zn^{2+}, Ni^{2+} and Co^{2+} in the complex perovskite *B*-site in place of bigger Ca^{2+} ions has resulted in the increase of tolerance factor with x indicating that the system approached to more symmetry which also has validated the improvement in dielectric properties.

The surface morphology of pure sintered $Ca_5Ta_2TiO_{12}$ materials have been described in Section 3.3.2 of Chapter 3. Fig. 6.14 depicts the microstructural evolution of $Ca_{5-x}A'_xTa_2TiO_{12}$ (A' = Mg, Zn, Ni and Co) specimens for $1 \leq x \leq 5$. The SEM photograph recorded from the surface of $Ca_4NiTa_2TiO_{12}$ ceramic is shown in Fig. 6.14 (a). It can be seen that all the grains are of uniform size and packed reasonably well ensuring good densification of the ceramic.

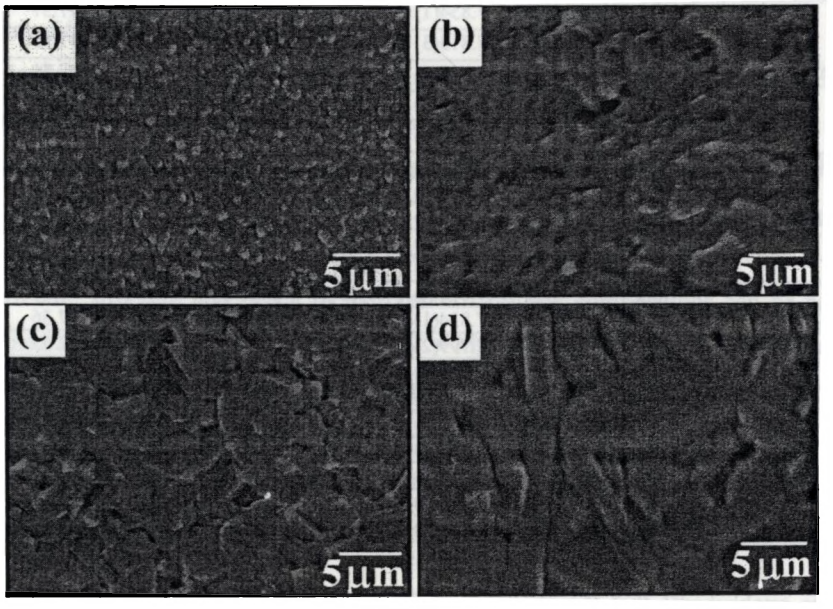

Fig. 6.14 Scanning electron micrographs of (a) $Ca_4NiTa_2TiO_{12}$ (b) $2CaO - Co_3O_4 - Ta_2O_5 - TiO_2$ (c) $CaO - 4ZnO - Ta_2O_5 - TiO_2$ (d) $5MgO - Ta_2O_5 - TiO_2$ ceramics

No secondary phases were observed supporting the conclusion that the formation of complete solid solution in the complex perovskite material has occurred up to $x = 1$. It is to be noted that the substitution of Ni^{2+} for Ca^{2+} has decreased the grain size ($\approx$ 1 μm) of the ceramic. The SEM image of $2CaO - Co_3O_4 - Ta_2O_5 - TiO_2$ (ie. $x = 3$) ceramics are shown in Fig. 6.14 (b). A large amount of liquid phase can be found in the grain boundaries of the specimen. Moreover the grains are of nonuniform size (2 – 4 μm) and shape indicating the formation of mixture phases as confirmed by XRD analysis. Fig. 6.14 (c) illustrates the morphology of $CaO - 4ZnO - Ta_2O_5 - TiO_2$ (ie. $x = 4$) recorded from the surface of sintered specimen. Nonuniformly distributed grains of 3 – 5 μm in size can be seen. The formation of liquid phase found in Figs. 6.14 (b) and 6.14 (c) are assumed to be due to the vaporization of Co_3O_4 and ZnO as that occurred in $Ba(Zn_{1/3}Ta_{2/3})O_3$ ceramics[32] as a result of the evaporation of ZnO. The SEM picture of $5MgO\text{-}Ta_2O_5\text{-}TiO_2$ ceramics are shown in Fig. 6.14 (d). Two distinct phases with an average grain size of 2 μm can be seen in the SEM photograph. Neither the liquid phase nor grain growth can be observed in the microstructure of the specimen. The main grains were needle shaped while occasional small laths were also found indicating the formation of $Mg_4Ta_2O_9$ and $MgTiO_3$ phases in the sample.

6.3.2.3 Microwave dielectric properties

The microwave dielectric properties of $Ca_{5-x}Mg_xTa_2TiO_{12}$, $Ca_{5-x}Zn_xTa_2TiO_{12}$, $Ca_{5-x}Ni_xTa_2TiO_{12}$ and $Ca_{5-x}Co_xTa_2TiO_{12}$ ceramics are shown in Figs. 6.15, 6.16, 6.17 and 6.18 respectively for $0 \leq x \leq 1$. Densification and phase assemblage are believed to be the main factors that determine the dielectric loss[33] and had been seen in several microwave dielectric ceramics. It is evident from Table 6.3 that, the density of $Ca_{5-x}Mg_xTa_2TiO_{12}$, $Ca_{5-x}Zn_xTa_2TiO_{12}$, $Ca_{5-x}Ni_xTa_2TiO_{12}$ and $Ca_{5-x}Co_xTa_2TiO_{12}$ ceramics increased linearly with x, whereas the percentage density exhibited a slight increase. The phase purity and increase in density for $0 \leq x \leq 1$ was followed by an enhancement in Q_u as is evident from the Figs. 6.15 – 6.18. It is reported[34,35] that $Ca(Ca_{1/4}Ta_{2/4}Ti_{1/4})O_3$ ceramics exist in highly disordered state due to the huge difference in ionic radii[18] of *B*-site cations. Hence the substitution of smaller[18] Mg^{2+}, Zn^{2+}, Ni^{2+} or Co^{2+} ions for comparatively bigger Ca^{2+} assumes better ordering. Though XRD analysis could not detect any evidence for ordering, it is established

that[36] ordering of *B*-site cations can suppress the anharmonic interaction between lattice phonons and electromagnetic energy and thereby increases the quality factor of microwave dielectrics. Hence the improvement in quality factor of $Ca_{5-x}A'_xTa_2TiO_{12}$ (A' = Mg, Zn, Ni & Co) complex perovskites for $0 \leq x \leq 1$ could be attributed to the densification, phase purity and improved ordering of *B*-site cations.

The variation of ε_r with x in $Ca_{5-x}Mg_xTa_2TiO_{12}$, $Ca_{5-x}Zn_xTa_2TiO_{12}$, $Ca_{5-x}Ni_xTa_2TiO_{12}$ and $Ca_{5-x}Co_xTa_2TiO_{12}$ ceramics are also depicted in Figs. 6.15 - 6.18, respectively for $0 \leq x \leq 1$, where the materials form solid solutions.

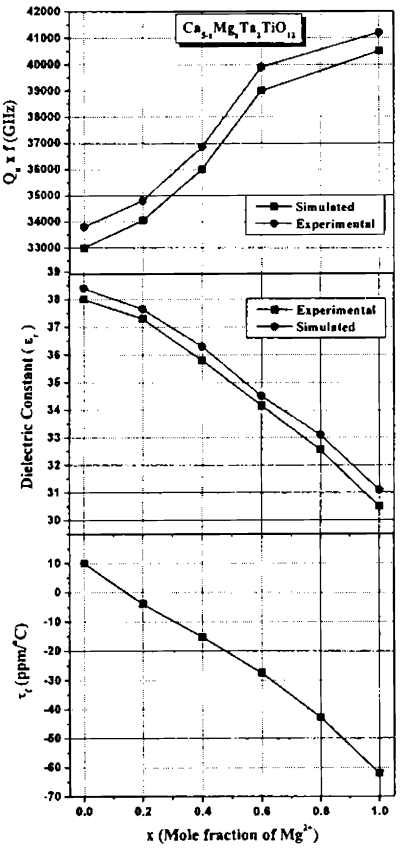

Fig. 6.15 Experimental and simulated microwave dielectric properties of $Ca_{5-x}Mg_xTa_2TiO_{12}$ ceramics for $0 \leq x \leq 1$

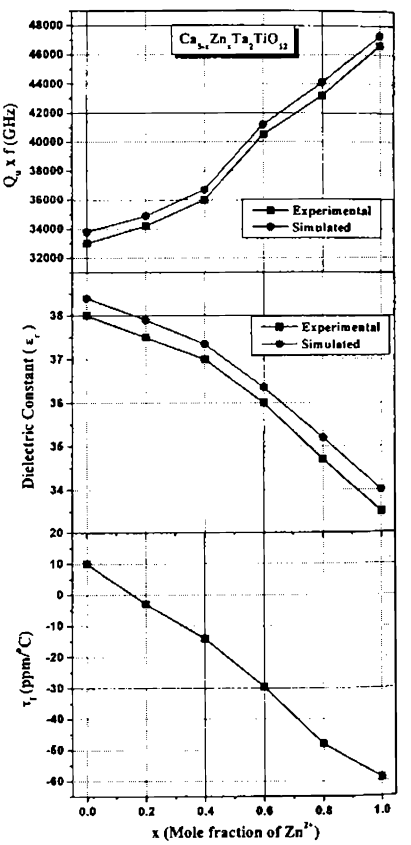

Fig. 6.16 Experimental and simulated microwave dielectric properties of $Ca_{5-x}Zn_xTa_2TiO_{12}$ ceramics for $0 \leq x \leq 1$

It is known that[37] in a phase pure dielectric, ε_r normally depends on percentage densification and the average polarizability[21] of ions comprising the same. It is noteworthy that in $Ca_{5-x}A'_xTa_2TiO_{12}$ (A' = Mg, Zn, Ni & Co) dielectrics, ε_r decreased even with slight increase in percentage density. Hence the decrease in ε_r could be attributed to the substitution of A'^{2+} ions with lesser polarizability than Ca^{2+} and thereby reduced the average polarizability[21] and ε_r of the system with increasing x.

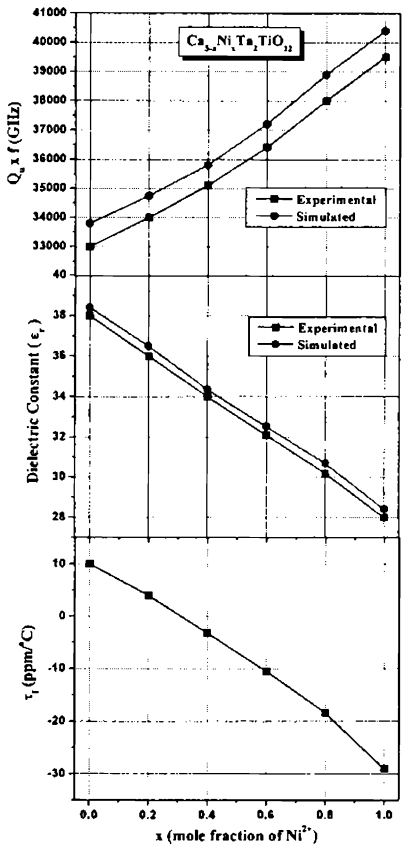

Fig. 6.17 Experimental and simulated microwave dielectric properties of $Ca_{5-x}Ni_xTa_2TiO_{12}$ ceramics for $0 \le x \le 1$

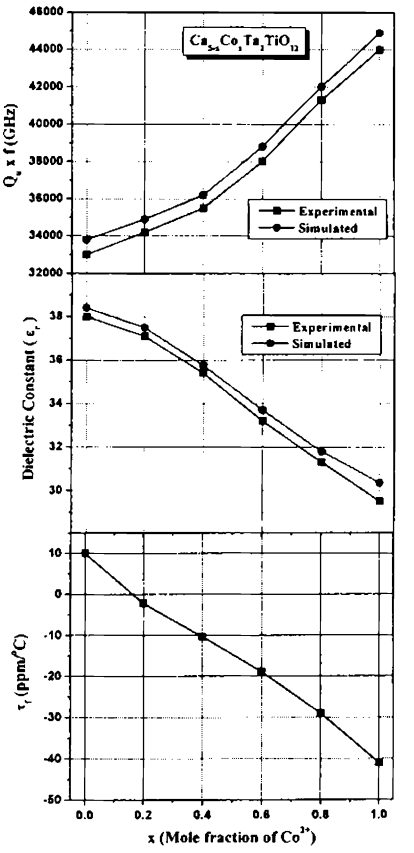

Fig. 6.18 Experimental and simulated microwave dielectric properties of $Ca_{5-x}Co_xTa_2TiO_{12}$ ceramics for $0 \le x \le 1$

The temperature coefficient of resonant frequency of $Ca_{5-x}A'_xTa_2TiO_{12}$ (A' = Mg, Zn, Ni & Co) ceramics shifted from positive to negative values with compositional variations as

illustrated in Figs. 6.15 – 6.18.The relationship between octahedral tilting and tunability of τ_f was demonstrated for complex perovskites by Colla *at al.*[38] and Reaney *et al.*[39] They reported that for solid solutions formed, the modification of unit cell parameters and cell volume is associated with tilting of oxygen octahedra, which in turn controls the temperature variation of dielectric constant (τ_ε) and hence τ_f. It has also been reported that,[31] τ_ε decreases with increasing tolerance factor (t) accompanied by a lowering in amplitude of tilting and reduces τ_f. In $Ca_{5-x}Mg_xTa_2TiO_{12}$, $Ca_{5-x}Zn_xTa_2TiO_{12}$, $Ca_{5-x}Ni_xTa_2TiO_{12}$ and $Ca_{5-x}Co_xTa_2TiO_{12}$ ceramics with $0 \leq x \leq 1$, the tolerance factor increased (See Table 6.3) and hence τ_f decreased with x and approached zero values. Further increase in t still decreased τ_f towards more negative values as is evident from Table 6.3 and Figs. 6.15 – 6.18. Four potential temperature stable dielectric resonator materials were identified in $Ca_{5-x}A'_xTa_2TiO_{12}$ (A' = Mg, Zn, Ni & Co) ceramic systems. In $Ca_{5-x}Mg_xTa_2TiO_{12}$ ceramics, the composition $Ca_{4.82}Mg_{0.18}Ta_2TiO_{12}$ has $\varepsilon_r = 37$, $Q_u \times f = 36000$ (at 4.35 GHz), and $\tau_f \approx 0$ ppm/°C. In the Zn substituted system, $Ca_{4.85}Zn_{0.15}Ta_2TiO_{12}$ has $\varepsilon_r = 37$, $Q_u \times f = 35000$ (at 4.15 GHz) and $\tau_f \approx 0$ ppm/°C. Whereas in Ni and Co substituted systems the compositions $Ca_{4.75}Ni_{0.25}Ta_2TiO_{12}$ with $\varepsilon_r = 35$, $Q_u \times f = 34000$ (at 4.49 GHz) and $Ca_{4.88}Co_{0.12}Ta_2TiO_{12}$ with, $\varepsilon_r = 36$, $Q_u \times f = 35000$ (at 4.48 GHz) are the compositions with temperature compensated resonant frequency.

6.3.2.4 Simulation Results

Fig. 6.19 shows the transmission mode (S_{21}) resonance spectrum of cavity backed[40] $Ca_5Ta_2TiO_{12}$ dielectric resonator. The TE_{018} mode was identified as described in Chapter 5, Section 5.3.2.3. Simulated value of resonant frequency showed excellent agreement with experimental value. The experimentally observed $Q_u \times f = 33000$ (at 4.1816 GHz) which is in good agreement with the simulated $Q_u \times f$ of 33700 (at 4.1801 GHz). The error was less than 2 %, which is well within the permitted range in high frequency measurements.

Fig. 6.20 depicts the transmission mode resonance spectrum (TE_{011} excitation) of $Ca_5Ta_2TiO_{12}$ dielectric resonator kept in the end-shorted position. As in the case of cavity resonance, here also excellent agreement between experimental and simulated resonant frequencies was found. The ε_r of the material was calculated using the simulated value of

resonant frequency and geometric dimensions of the specimen employing Hakki-Colemann program[15]. The unloaded quality factor of the DR material was calculated using the resonant frequency (f) and 3 dB bandwidth (Δf) of the resonant peak from the center maximum. The experimental value of ε_r iss 38 and that obtained using simulated resonant frequency is 38.5. Again very good matching with an error of less than 1 % was obtained between the experimental and simulated values of ε_r. DRs with different quality factor and ε_r in $Ca_{5-x}A'_xTa_2TiO_{12}$ (A' = Mg, Zn, Ni & Co) ceramic systems were simulated using TLM technique for various compositions and the experimental values were compared with simulated results as shown in Figs. 6.15 – 6.18 and Table 6.4.

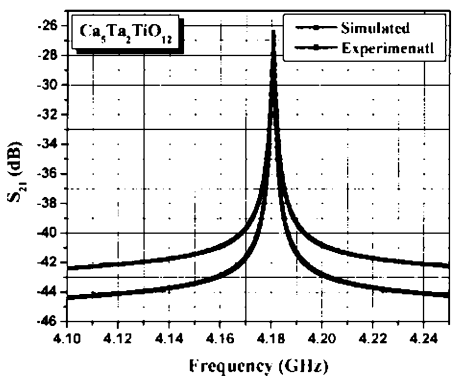

Fig. 6.19 TE_{010} transmission mode resonance spectrum of cavity shielded $Ca_5Ta_2TiO_{12}$ DR

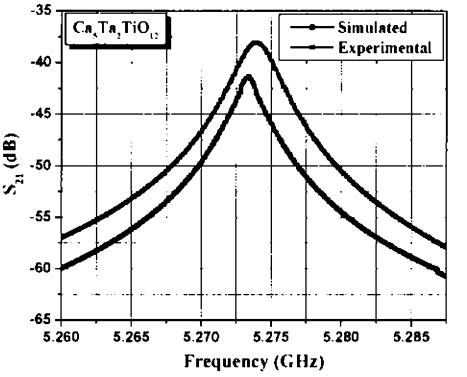

Fig. 6.20 TE_{011} transmission mode resonance spectrum of end shorted $Ca_5Ta_2TiO_{12}$ DR

As the figures and table describes, very good agreement between experiment and simulation was obtained for $8500 \leq Q_u x f \leq 114000$ GHz and $9 \leq \varepsilon_r \leq 38$. The lower values of Q_u and ε_r observed by experiment may be attributed to the presence of thin air layer and unaccountable surface irregularity of the specimen. The presence of air layer reduced the effective ε_r and as a result, the resonant frequency was shifted towards higher values as seen from Figs. 6.19 and 6.20. Hence experimental ε_r is lower than that obtained by simulation. In the case of measurement of Q_u, the DR located at the center of the cavity was assumed to be isolated to minimize the conduction and radiation loss. However under practical experimental situations,

this condition can not be ensured while ideal conditions can be attained during simulation and this difference accounts for the lower Q_u values obtained by experiment.

6.3.3 (5 - *x*)CaO - *x*A'O – Ta_2O_5 – TiO_2 ($2 \leq x \leq 5$) [A' = Mg, Zn, Ni & Co] Ceramics

XRD analysis of $Ca_{5-x}A'_xTa_2TiO_{12}$ (A' = Mg, Zn, Ni & Co) ceramics for $0 \leq x \leq 5$ revealed that they exist in single phase materials only for $0 \leq x \leq 1$ and beyond that mixture phases were formed (See Figs. 6.10- 6.13). The synthesizing conditions, density and microwave dielectric properties of (5 - *x*)CaO - *x*A'O - Ta_2O_5 - TiO_2 [A' = Mg, Zn, Ni & Co] ceramics for ($2 \leq x \leq 5$) are shown in Table 6.4. The processing temperatures decreased with increase in amount of Mg, Zn, Ni & Co as expected since these are all low melting compared with Ca-based materials[40]. The density showed a linear increase with concentration of A'^{2+} (Mg, Zn, Ni & Co) ions substituted. The concentration and composition of the mixture phases formed in each composition controls the density and dielectric properties for each value of *x*. The microwave dielectric properties also showed some relationship with the extent of Ca^{2+} replacement with A'^{2+} [A' = Mg, Zn, Ni & Co] cations. The dielectric constant decreased linearly with increase in *x* in all the four systems. In $Ca_{5-x}Mg_xTa_2TiO_{12}$ ceramics ε_r decreased from 30 to 18, whereas the value varied from 17 to 9 in $Ca_{5-x}Zn_xTa_2TiO_{12}$ for $2 \leq x \leq 5$. A similar effect was observed in $Ca_{5-x}Ni_xTa_2TiO_{12}$ and $Ca_{5-x}Co_xTa_2TiO_{12}$ where ε_r shifted from 29 to 20 and 28 to 14 respectively. The decrease in ε_r with increase in *x* can be attributed to the decrease in concentration of $CaTiO_3$ (See Figs. 6.10 – 6.13) and a proportionate increase in A'^{2+} (*A'* = Mg, Zn, Ni & Co)-based mixture phases like $Mg_4Ta_2O_9$, $MgTiO_3$, Zn_2TiO_4, $Zn_4Ta_2O_9$, $ZnTiO_3$, $Ni_4Ta_2O_9$, $NiTiO_3$, $CoTa_2O_6$, Co_2TiO_4, $CoTiO_3$ etc., because the latter group of ceramics have low dielectric constant compared with $CaTiO_3$.[40] The quality factors of $Ca_{5-x}A'_xTa_2TiO_{12}$ (A' = Mg, Zn, Ni & Co) ceramics decreased beyond the solid solution range $0 \leq x \leq 1$.

It is known[4] that presence of mixture and secondary phases in the specimen increases the dielectric loss of a material at microwave frequencies. In (5 - *x*)CaO - *x*MgO - Ta_2O_5 - TiO_2 ceramics, the $Q_u \times f$ increased from 18500 (at 4.74 GHz) to 114000 (at 6.61 GHz) for $2 \leq x \leq 5$. The increase in quality factor was due to the increased concentration of low loss

$Mg_4Ta_2O_9$ and $MgTiO_3$[40] phases with x. A similar phenomena was observed with Co^{2+} substitution, where the $Q_u x f$ increased from 19500 (at 4.67 GHz) to 48000 (at 6.53 GHz) for $2 \leq x \leq 5$. In Ni and Zn substituted systems the quality factors were low compared with that in Mg and Co based systems and the values are tabulated in Table 6.4. In all the four systems τ_f shifted to high negative values with increase in x and is due to the formation A'^{2+} based phases with negative τ_f[40].

Table 6.4. Synthesizing conditions, experimental density and microwave dielectric properties of (5-x)CaO – xA'O – Ta_2O_5 – TiO_2 (A' = Mg, Zn, Ni & Co) ceramics for $2 \leq x \leq 5$

Material System	x	Calci-nation Temp. (°C)	Sintering Temp. (°C)	Density (Experi-mental) (g/cm^3) [SD = ± 0.03]	ε_r (Experi-mental)	ε_r (Simu-lation)	$Q_u x f$ (GHz) (Experi-mental)	$Q_u x f$ (GHz) (Simu-lation)	τ_f (Experi-mental) (ppm/°C)
(5-x)CaO-xMgO-Ta_2O_5-TiO_2	2	1240	1550	5.17	30	30.5	18500	19000	-24
	3	1240	1450	5.32	26	26.6	30000	30500	-28
	4	1180	1360	5.40	20	20.4	50000	50800	-33
	5	1180	1325	5.49	18	15.5	114000	115000	-47
(5-x)CaO-xZnO-Ta_2O_5-TiO_2	2	1200	1400	5.69	17	17.3	30000	31000	-47
	3	1150	1300	5.92	13	13.3	20000	20800	-54
	4	1100	1225	6.25	10	10.3	15000	15750	-60
	5	1050	1150	6.45	9.0	9.2	9000	9700	-45
(5-x)CaO-xNiO-Ta_2O_5-TiO_2	2	1100	1500	5.51	29	29.5	18000	18800	-33
	3	1050	1410	5.87	26	26.4	11000	11600	-41
	4	950	1340	6.36	23	23.5	8500	8700	-48
	5	850	1300	6.88	20	20.5	14000	14600	-53
(5-x)CaO-xCoO-Ta_2O_5-TiO_2	2	1100	1400	5.75	28	28.4	19500	20200	-14
	3	1050	1260	5.96	24	24.6	13500	14200	-19
	4	950	1210	6.07	20	20.3	26000	27000	-30
	5	850	1150	6.15	14	14.4	48000	48700	-43

It is quite interesting to note that for x = 5, Mg and Co based ceramic systems form very low loss, low ε_r dielectric materials. Efforts to tune the τ_f of these materials would be of great interest as they can be used as potential substrate materials[41] in microelectronic applications. The simulated values of dielectric constant and quality factors are also tabulated in the table, which shows very good agreement with experimental results. It should be mentioned that TLM simulation methods yielded excellent results for the microwave dielectric properties of (5 - x)CaO - xA'O - Ta_2O_5 - TiO_2 (A' = Mg, Zn, Ni & Co) dielectric resonator materials.

6.4 $Ca_5Ta_2Ti_{1-x}C_xO_{12}$ (C = Zr, Hf) CERAMICS

6.4.1 Experimental

$Ca_5Ta_2Ti_{1-x}Zr_xO_{12}$ and $Ca_5Ta_2Ti_{1-x}Hf_xO_{12}$ powder compositions were synthesized using the conventional solid-state reaction method as described in Chapter 2, Section 2.1.2. Stoichiometric compositions of the oxides were mixed for 24h with yttria stabilized ZrO_2 ball media in distilled water, then dried and calcined at 1350°C/4h. The calcined powders were well ground in an agate mortar with pestle and mixed with 4 wt. % poly vinyl alcohol (PVA) as binder and dried again. It was well ground to form fine powder and shaped into cylindrical compacts of about 14 mm diameter and 7 mm height under a pressure of about 100MPa. Each composition was sintered at their optimum temperatures (See Tables 6.5 and 6.6). Compositions rich in Zr/Hf were difficult to sinter even at 1700°C and hence were sintered with the addition of small amount of B_2O_3. The bulk densities of sintered, well polished samples were measured and characterized by XRD, SEM and microwave measurements as described in Chapter 2.

6.4.2 Results and Discussion

6.4.2.1 Phase Analysis

Fig. 6.21 and 6.22 shows the X-Ray diffraction patterns of $Ca_5Ta_2Ti_{1-x}Zr_xO_{12}$ and $Ca_5Ta_2Ti_{1-x}Hf_xO_{12}$ for $0 \leq x \leq 1$ respectively. A perovskite single phase with the same structure as that of the parent material was obtained throughout the entire compositional range. Hence the diffraction peaks were indexed based on orthorhombic $Ca_5Ta_2TiO_{12}$ phase. However, in Hf based systems, compositions with $x \geq 0.8$ show few additional peaks of $Ca_2B_2O_5$ (ICDD File No. 22 – 139), due to the addition of 2 wt % B_2O_3 as sintering aid. A slight shift in the position of maximum intensity peaks [(121), (101) & (202)] towards the lower angle side was observed in both Zr and Hf based systems, which was later confirmed by an increase in lattice parameters and an associated increase in cell volume. It is due to the partial substitution of Zr/Hf ions for Ti in the perovskite *B*-site.

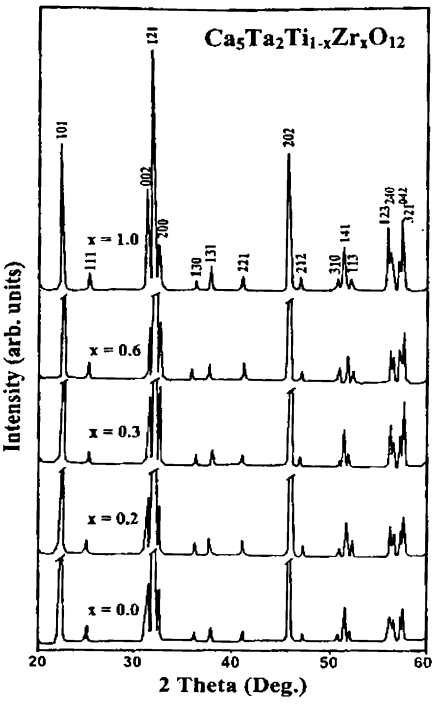

Fig. 6.21 X-Ray diffraction pattern of $Ca_5Ta_2Ti_{1-x}Zr_xO_{12}$ ceramics

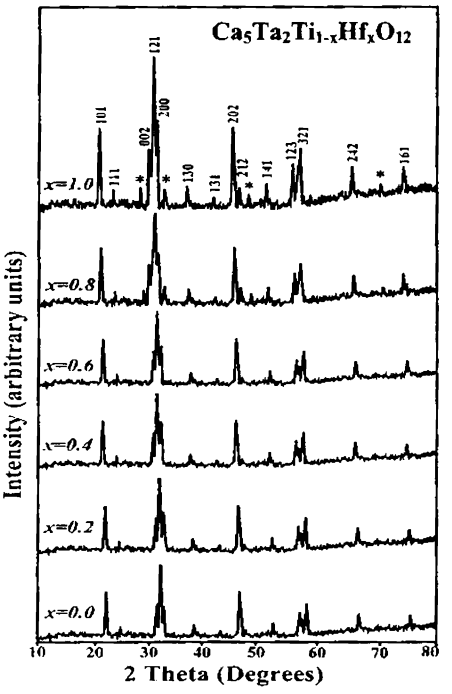

Fig. 6.22 X-Ray diffraction pattern of $Ca_5Ta_2Ti_{1-x}Hf_xO_{12}$ ceramics (* → additional phases)

6.4.2.2 Densification and Microstructural Analysis

The sintering temperatures, lattice parameters, cell volume, density and tolerance factor of $Ca_5Ta_2Ti_{1-x}Zr_xO_{12}$ and $Ca_5Ta_2Ti_{1-x}Hf_xO_{12}$ ceramics are shown in Tables 6.5 and 6.6 respectively. As x is increased from 0 to 1, the sintering temperature of $Ca_5Ta_2Ti_{1-x}Zr_xO_{12}$ ceramics varies from 1625 to 1680°C/4h. The two compositions with x = 0.9 and 1 were difficult to sinter even at 1700°C and hence these samples were sintered by adding 1 wt. % of low melting B_2O_3. It is known that effective low temperature sintering can be achieved by fluxing a ceramic material with a suitable glass in the proper concentration.[42] This glass addition was not found to be adversely affecting any of the material properties. The theoretical density in $Ca_5Ta_2Ti_{1-x}Zr_xO_{12}$ increases from 5.41 to 5.61g/cm^3. Corresponding changes also occurred in the cell volume of these ceramics. The percentage density decreased

from 97 to 95% as the Zr content increased from 0 to 1. The tolerance factor also decreases with increase in Zr content in $Ca_5Ta_2Ti_{1-x}Zr_xO_{12}$ ceramics.

Table 6.5 Sintering temperature, density, lattice parameters, and tolerance factor of $Ca_5Ta_2Ti_{1-x}Zr_xO_{12}$ ceramics

x	Sintering Temperature (°C/4 h)	Lattice parameters (Å)			Cell Volume (Å^3)	X-Ray density (g/cm^3)	% Density	Tolerance factor (t)
		a	b	c				
0.0	1625	5.502(2)	7.893(1)	5.668(5)	246.180	5.41	97.19	0.9189
0.1	1625	5.111(9)	7.899(5)	5.661(9)	246.328	5.42	97.02	0.9176
0.2	1640	5.523(4)	7.912(7)	5.644(8)	246.709	4.44	96.82	0.9164
0.3	1650	5.531(1)	7.931(2)	5.630(5)	246.999	5.51	95.89	0.9152
0.4	1660	5.535(6)	7.946(7)	5.617(4)	247.308	5.52	95.81	0.9139
0.5	1670	5.538(8)	7.954(6)	5.622(9)	247.698	5.53	95.72	0.9127
0.6	1675	5.540(9)	7.960(9)	5.619(9)	248.001	5.54	95.65	0.9115
0.7	1690	5.544(7)	7.969(8)	5.618(7)	248.731	5.56	95.41	0.9102
0.8	1700	5.549(8)	7.979(1)	5.616(9)	249.353	5.58	95.16	0.9090
0.9	1670*	5.553(6)	7.984(3)	5.616(0)	249.790	5.59	95.08	0.9078
1.0	1680*	5.559(2)	7.991(3)	5.613(3)	250.261	5.61	94.90	0.9066

* Sintered with 1 wt % B_2O_3

In $Ca_5Ta_2Ti_{1-x}Hf_xO_{12}$ systems, the sinterability was very poor for compositions with x = 0.8 and 1.0 and hence were sintered with 2 wt % low melting B_2O_3 glass additives. The variation of unit cell parameters listed in Table 6.6 shows a linear increase with HfO_2 concentration. It can be attributed to the substitution of Hf^{4+} with higher ionic radius[18] than Ti^{4+} in the *B*-site of complex perovskite materials. Even with reduced cell volume, the X-Ray density showed an increase with x and is due to the increased mass of Hf^{4+} ions compared with Ti^{4+}. But it should be noted that the percentage density decreased with increase in x and can be attributed to the poor sinterability of HfO_2 compared with that of TiO_2. The tolerance

factor (t)[20] of $Ca_5Ta_2Ti_{1-x}Hf_xO_{12}$ ceramics were calculated for x = 0.0, 0.2, 0.4, 0.6, 0.8 and 1.0 and is listed in Table 6.6. A gradual decrease in t with increasing x can be seen and is due to the increased average *B*-site ionic radius caused by the substitution of bigger Hf^{4+} in place of Ti^{4+} ions.

Table 6. 6 Sintering temperature, unit cell parameters, density and tolerance factor of $Ca_5Ta_2Ti_{1-x}Hf_xO_{12}$ ceramics

x	Sintering Temperature (°C/4 h)	Lattice parameters (Å)			Cell Volume (Å^3)	X-Ray density (g/cm^3)	% Density	Tolerance factor (t)
		a	b	c				
0.0	1625	5.502(2)	7.893(1)	5.668(5)	246.180	5.41	97.19	0.9189
0.2	1650	5.521(1)	7.909(0)	5.671(1)	247.627	5.55	96.82	0.9166
0.4	1680	5.534(2)	7.917(1)	5.679(2)	248.812	5.70	96.22	0.9144
0.6	1650	5.550(0)	7.926(1)	5.675(4)	249.639	5.86	95.11	0.9121
0.8	1675#	5.563(1)	7.941(2)	5.667(2)	250.344	6.01	94.00	0.9098
1.0	1675#	5.571(3)	7.952(1)	5.675(5)	251.406	6.16	92.57	0.9076

Sintered with 1 wt % B_2O_3

The microstructure of $Ca_5Ta_2TiO_{12}$ ceramics have described in Chapter 3, Section 3.3.2. The specimens were observed with an average grain size of 10 μm. Fig. 6.23 shows the surface morphology of few typical $Ca_5Ta_2Ti_{1-x}Hf_xO_{12}$ ceramics.

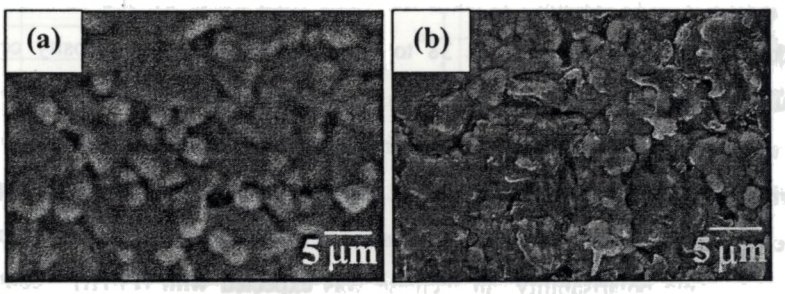

Fig. 6.23 SEM photographs of (a) $Ca_5Ta_2Ti_{0.6}Hf_{0.4}O_{12}$ and (b) $Ca_5Ta_2HfO_{12}$ ceramics

Fig. 6.23 (a) is the SEM photographs for $Ca_5Ta_2Ti_{0.6}Hf_{0.4}O_{12}$ ceramics, where the dielectrics appeared as temperature stable. The specimens have a homogeneous microstructure and the average grain size is about 3 μm. It should be noted that the grains are not well packed and has few porosity confirming the decreased percentage density with increase in x. It is worth to mention that, the grain shape is uniform and is similar to that of the parent material ($Ca_5Ta_2TiO_{12}$), which shows that the ceramics form solid solution in the $Ca_5Ta_2Ti_{1-x}Hf_xO_{12}$ composition. Fig. 6.23 (b) exhibits the SEM image of $Ca_5Ta_2HfO_{12}$ dielectrics. A large amount of liquid phase coated over the grains can be seen because of the low temperature reaction of B_2O_3 glass with the matrix material. The glass coated over the grains increased the porosity of the host materials and the experimental density decreased to even 92 % of the theoretical value.

6.4.2.3 Microwave Dielectric Properties

The variation of microwave dielectric properties of $Ca_5Ta_2Ti_{1-x}Zr_xO_{12}$ and $Ca_5Ta_2Ti_{1-x}Hf_xO_{12}$ are illustrated in Figs. 6.24 and 6.25 respectively. In both the ceramics, the $Q_u \times f$ decreases linearly with x. In $Ca_5Ta_2Ti_{1-x}Zr_xO_{12}$ ($0 \le x \le 1$) ceramics, the quality factor shifts from 33000 to 24500 GHz, whereas in $Ca_5Ta_2Ti_{1-x}Hf_xO_{12}$ the variation was from 33000 to 18000 GHz. The substitution of $(Zr/Hf)^{4+}$ ions for Ti^{4+} has increased the porosity (decreased the percentage density, as is evident from Tables 6.5 and 6.6) of the bulk ceramics and hence contributed towards decreased quality factor with increasing x.

The variation of dielectric constant of $Ca_5Ta_2Ti_{1-x}Zr_xO_{12}$ and $Ca_5Ta_2Ti_{1-x}Hf_xO_{12}$ ceramics with mole fraction of Zr/Hf^{4+} content also shows a linear decrease. In $Ca_5Ta_2Ti_{1-x}Zr_xO_{12}$ ($0 \le x \le 1$) ceramics ε_r takes the value from 38 to 21 and in $Ca_5Ta_2Ti_{1-x}Hf_xO_{12}$ dielectrics, the ε_r decreased from 38 to 17. In both cases, the porosity corrected ε_r is calculated[43] using the equation 5.4 given in Chapter 5. In $Ca_5Ta_2Ti_{1-x}Zr_xO_{12}$ ($0 \le x \le 1$) ceramics, the porosity corrected ε_r varies from 40 to 23 and in $Ca_5Ta_2Ti_{1-x}Hf_xO_{12}$ ($0 \le x \le 1$) ceramics the variation was from 40 to 22. Dielectric constant significantly depends on the percentage densification and ionic polarization at microwave frequencies.[44] ε_r being directly related to ionic polarisability, an increase was expected with $(Zr/Hf)^{4+}$ content since its polarisability is higher than that of Ti^{4+}. In the present case the porosity increased with Zr/Hf

concentration (See Tables 6.5 and 6.6) which resulted in the decrease of ε_r. Moreover the increased ionic radius of Zr/Hf also increased the bond valence[15] between the cationic *B*-site and anions to reduce the rattling effect and hence the polarization induced under the action of electric field decreased and thereby contributes towards the decrease of ε_r.

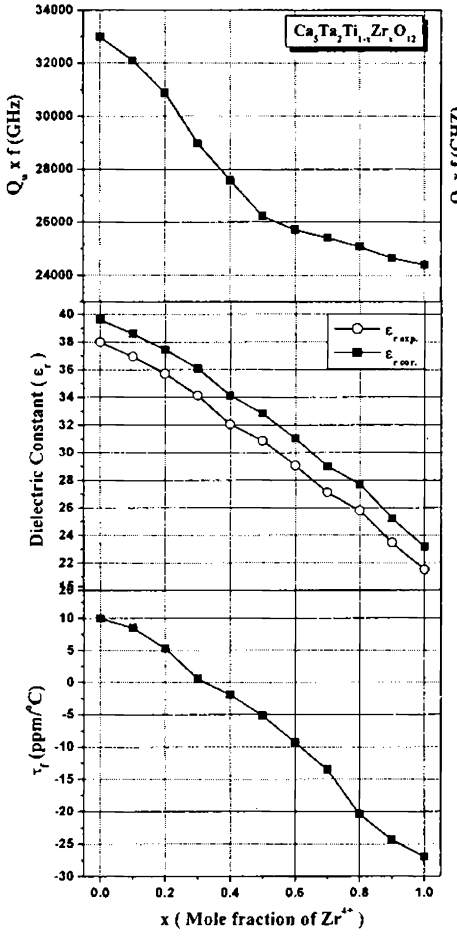

Fig. 6.24 Microwave dielectric properties of $Ca_5Ta_2Ti_{1-x}Zr_xO_{12}$ ceramics

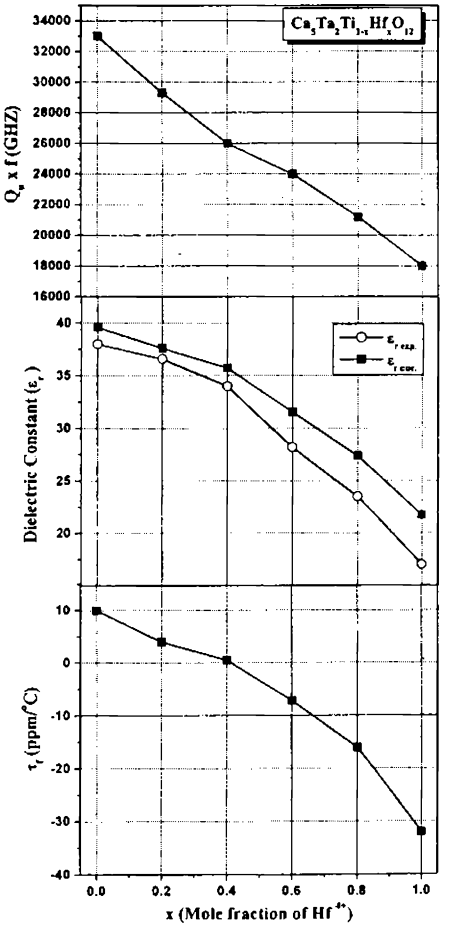

Fig. 6.25 Microwave dielectric properties of $Ca_5Ta_2Ti_{1-x}Hf_xO_{12}$ ceramics

It has been showed that[38,39] in perovskite based compounds, the tilt transitions by substitution reactions is the major factor influencing the behaviour of temperature coefficient of dielectric constant (τ_ε) and thereby τ_f. In both the substituted ceramic systems, τ_f decreases with increase in x. This variation can be attributed to a possible BO_6 octahedral tilting due to the substitution of bigger Zr/Hf for Ti^{4+} ions. In $Ca_5Ta_2Ti_{1-x}Zr_xO_{12}$ ($0 \leq x \leq 1$) ceramics, τ_f changes from +10 to -27ppm/°C and crosses zero at x = 0.3. The $Ca_5Ta_2Ti_{0.7}Zr_{0.3}O_{12}$ was found to be the temperature compensated composition and has ε_r = 36, $Q_u \times f$ = 28,000 GHz and $\tau_f \approx 0$ ppm/°C. In $Ca_5Ta_2Ti_{1-x}Hf_xO_{12}$ ceramics, the τ_f decreased from +10 to -32 ppm/°C with the zero τ_f at x = 0.4. $Ca_5Ta_2Ti_{0.6}Hf_{0.4}O_{12}$ has ε_r = 34, $Q_u \times f$ = 26000 GHz and $\tau_f \approx 0$ ppm/°C.

6.5 CONCLUSIONS

- Effect of cationic substitutions in the *A* and *B*-sites of $Ca_5Ta_2TiO_{12}$ complex perovskites were investigated. Accordingly, solid solution phases in the $Ca_{5-x}A_xTa_2TiO_{12}$ (A = Ba, Sr), $Ca_{5-x}A'_xTa_2TiO_{12}$ (A' = Mg, Zn, Ni & Co) and $Ca_5Ta_2Ti_{1-x}C_xO_{12}$ (C = Zr, Hf) ceramics have been synthesized and their structural aspects and microwave dielectric properties were studied as a function of mole fraction of substituted cations.
- $Ca_{5-x}Ba_xTa_2TiO_{12}$ ceramics form phase pure materials with pseudo-cubic structure only for x = 4. For all other compositions (x = 1, 2 & 3), traces of additional peaks were identified in the XRD profile. $Ca_{5-x}Sr_xTa_2TiO_{12}$ ceramics form single phase materials up to x = 4. For x = 0 and 1 the materials exist in a clear perovskite orthorhombic symmetry and later transforms into a pseudo-cubic structure with increased x values was observed. The structural change in both Ba/Sr substituted systems became more evident for x = 4, where all Ba/Sr ions occupy the *A*-sites and all Ca ions on the *B*-sites of complex perovskite structure. However spectroscopic studies revealed that the ceramics exists in true orthorhombic symmetry itself. For x = 5, $Ca_{5-x}A_xTa_2TiO_{12}$ (A = Ba, Sr) ceramics form mixture phases of $(Ba/Sr)_4Ta_2O_9$ - $(Ba/Sr)TiO_3$.

- The microwave dielectric properties of $Ca_{5-x}A_xTa_2TiO_{12}$ (A = Ba, Sr) ceramics were highly affected by variations in x. In Ba-substituted ceramics, Q_u showed a linear decrease with increasing Ba-content, where as in Sr-based system, Q_u showed a gradual decrease for x = 0 to 3 (33000 – 8500 GHz) and then increased for x = 4 (16000 GHz). The ε_r and τ_f increased with mole fraction of barium/strontium content in $Ca_{5-x}A_xTa_2TiO_{12}$ (A = Ba, Sr) dielectrics.
- Raman spectra of $Ca_{5-x}A_xTa_2TiO_{12}$ (A = Ba, Sr) showed bands related to *A*-sites and the analysis revealed that isovalent Ba/Sr substitution in $Ca_5Ta_2TiO_{12}$ samples led to rotations of oxygen cage that red shifted the bands related to *A*-sites. Maximum distortions occurred at x = 4 in the octahedral cages, which represents the complete substitution of Ba/Sr in the complex perovskite *A*-site of $Ca(Ca_{1/4}Ta_{2/4}Ti_{1/4})O_3$ ceramics. Modes related to ordering varied their intensities and frequencies as a result of the increased short-range order. FTIR results agree well with Raman data. The introduction of barium/strontium in $Ca_5Ta_2TiO_{12}$ ceramics produced perturbations on the polar vibrational modes, especially on the bending modes, which increased their intensities.
- Investigations were made on the microwave dielectric properties of $Ca_{5-x}A'_xTa_2TiO_{12}$ (A' = Mg, Zn, Ni & Co) ceramics. Low loss, temperature stable dielectric resonator materials were identified in all the four systems for $0 \le x \le 1$. $Ca_{4.82}Mg_{0.18}Ta_2TiO_{12}$ has $\varepsilon_r = 37$, $Q_u \times f = 36000$ (at 4.35 GHz) and in the Zn substituted system, the $Ca_{4.85}Zn_{0.15}Ta_2TiO_{12}$ has $\varepsilon_r = 37$, $Q_u \times f = 35000$ (at 4.15 GHz). Whereas in Ni and Co substituted systems, the compositions $Ca_{4.75}Ni_{0.25}Ta_2TiO_{12}$ with $\varepsilon_r = 35$, $Q_u \times f = 34000$ (at 4.49 GHz) and $Ca_{4.88}Co_{0.12}Ta_2TiO_{12}$ with, $\varepsilon_r = 36$, $Q_u \times f = 35000$ (at 4.48 GHz) has stable resonant frequency with temperature.
- With $2 \le x \le 5$, all the compositions in $Ca_{5-x}A'_xTa_2TiO_{12}$ (A' = Mg, Zn, Ni & Co) system form as a mixture of various phases. The ε_r decreased and τ_f varied to high negative values. With x = 5, Mg and Co-based materials have

high quality factor and low dielectric constant which enable them as potential candidates for substrate applications in microelectronic technology.

- The transmission mode resonance spectrum of $Ca_{5-x}A'_xTa_2TiO_{12}$ (A' = Mg, Zn, Ni & Co) ceramics for $0 \leq x \leq 5$ was simulated by means of 3D-Transmission Line Matrix methods. The simulated values of microwave dielectric properties were found to be in excellent agreement with experimental results with less than 2 % error in quality factor and 1 % tolerance in ε_r.
- The microwave dielectric properties of $Ca_5Ta_2Ti_{1-x}Zr_xO_{12}$ and $Ca_5Ta_2Ti_{1-x}Hf_xO_{12}$ ($0 \leq x \leq 1$) ceramics have been investigated. The density and cell volume were found to be increased with increase in Zr/Hf content. In $Ca_5Ta_2Ti_{1-x}Zr_xO_{12}$ and $Ca_5Ta_2Ti_{1-x}Hf_xO_{12}$ ceramics, the ε_r, τ_f and Q_u were found to be decreasing with increase in x. Two potential compositions with temperature compensation of resonant frequency were identified. In the Zr-based system, $Ca_5Ta_2Ti_{0.7}Zr_{0.3}O_{12}$ has $\varepsilon_r = 36$, $Q_u \times f = 28000$ GHz and $\tau_f \approx 0$ ppm/°C, whereas in the Hf substituted composition $Ca_5Ta_2Ti_{0.6}Hf_{0.4}O_{12}$ has $\varepsilon_r = 34$, $Q_u \times f = 26000$ GHz and $\tau_f \approx 0$ ppm/°C.

Chapters 3 to 6 has introduced the structure and microwave dielectric properties of two complex perovskite materials in the $Ca_5B_2TiO_{12}$ (B = Nb, Ta) system and the methods to tailor their dielectric properties by different methods. Dielectric resonators with $9 < \varepsilon_r < 83$, $1500 < Q_u \times f < 1$, 14000 and $+65 < \tau_f < -77$ ppm/°C have been developed. The application of these DR materials in the fabrication of broad band antennas are discussed in the next two chapters.

6.6 REFERENCES

[1] P. K. Davies, T. Jong, T. Negas, *J. Amer Cer Soc.* **80** (1997)17227

[2] H. Tamura, T. Konoike, Y. Sakabe, and K. Wakino, *J. Amer. Cer. Soc.* **67** (1984)59

[3] M.T. Sebastian, N. Santha, P. V. Bijumon, Anna Axelsson and Neil McN Alford, *J. Eur. Ceram. Soc.* **24** (2004) 2583.

[4] M. P. Seabra, M. A. Avdeev, V. M. Ferreira, R. C. Pullar, N. McN. Alford and I. M. Reaney, *J. Am. Ceram. Soc.* **87** (2004) 584.

[5] S. X. Zhang, J. B. Li, J. Cao, H. Z. Zhai and B. Zhang, *J. Eur. Ceram. Soc.* **21** (2001) 2931.

[6] H. T. Kim and M. T. Lanagan, *J. Am. Ceram. Soc.* **86** (2003) 1874.

[7] H.Ohsato, A. Atsushi, Y.T. Takagi, S. Nishigaki and T. Okuda, *Jpn. J. Appl. Phys.* **39** (2000) 6608.

[8] H. Kagata and J. Kato, *Jpn. J. Appl. Phys.* **33** (1994) 5463.

[9] P. B. Johns and R. L. Beurle, *Proc. IEE.* **118** (1971) 1203.

[10] S. Akhtarrzad and P. B. Johns, *IEEE Trans.* **MTT-23** (1975) 990.

[11] J. B.-Jarvis, M. D. Janezic, P. D. Domich and R. G. Geyer, *IEEE Trans. Instrum. Meas.* **43** (1994) 711.

[12] J. Chuma, C. W. Sim and D. Mirshekar-Syahkal, *Electron. Lett.* **35** (1999) 1712.

[13] W. J. R. Hoefer, *IEEE Trans. Microwave Theory Tech.* **MTT-40** (1992) 1517.

[14] Micro-stripes 6.5 reference manual, Flomerics Limited, Surrey, UK.

[15] B. W. Hakki and P. D. Coleman, *IRE Trans. Microwave Theory Tech.* **MTT-8** (1960) 402-10.

[16] W. E. Courtney, *IEEE Trans. Microwave Theory* Tech. **MTT-18** (1970) 476.

[17] J. Krupka, K. Derzakowski, B. Riddle and J. Baker-Jarvis, *Meas. Sci. Technol.* **9** (1998) 1751.

[18] R. D. Shannon, *Acta Cryst.* **A32** (1976) 751.

[19] M. A. Akbas and P. K. Davies, *J. Am. Ceram. Soc.* **81** (1998) 2205.

[20] R. S. Roth, *J. Res. Natl. Bur. Stand.* **58** (1957) 75.

[21] R. D. Shannon, *J. Appl. Phys.* **73** (1993) 348.

[22] I. G. Siny, R. Tao, R. S. Katiyar, R. Guo, and A. S. Bhalla, *J. Phys. Chem. Solids* **59** (1998) 181.

[23] T. Hirata, K. Ishioka, and M. Kitasima, *J. Solid State Chem.* **124** (1996) 353.

[24] U. Balachandran and N. G. Eror, *Sol. State Comm.* **44** (1982) 815.

[25] H. Zheng, G. D. C.Csete de Gyorgyfalva, R. Quimby, H. Bagshaw, R. Ubic, I. M. Reaney, and J. Yarwood, *J. Eur. Ceram. Soc.* **23** (2003) 2653.

[26] I. Levin, J. Y. Chan, R. G. Geyer, J. E. Maslar, and T. A. Vanderah, *J. Solid State Chem.* **156** (2001) 122.

[27] H. Zheng, I. M. Reaney, G. D. C. Csete de Gyorgyfalva, R. Ubic, J. Yarwood, M. P. Seabra, and V. M. Ferreira, *J. Mater. Res.* **19** (2004) 488.

[28] H. Zheng, H. Bagshaw, G. D. C. Csete de Gyorgyfalva, I. M. Reaney, R. Ubic, and J. Yarwood, *J. Appl. Phys.* **94** (2003) 2948.

[29] S. J. Webb, J. Breeze, R. I. Scott, D. S. Cannell, D. M. Iddles, and N. McN Alford, *J. Am. Ceram. Soc.* **85** (2002) 1753.

[30] A. M. Glazer, *Acta. Cryst.* **B28** (1972) 3384.

[31] P. L. Wise, I. M. Reaney, W. E. Lee, D. M. Iddles, D. S. cannel and T. J. Price, *J. Mater. Res.* **17** (2002) 2033.

[32] C-W Ahn, H-J Jang, S. Nahm, H-M. Park and H-J Lee, *J. Eur. Ceram. Soc.* **23** (2003) 2473.

[33] V. L. Gurevich and A. K. Tagantsev, *Adv. Phys.* **40** (1991) 719.

[34] R. J. Cava, J. J. Krajewski, and R. S. Roth, *Mater. Res. Bull.* **34** (1999) 355.

[35] L. A. Bendersky, J.J. Krajewski, and R. J. Cava, *J. Eur. Ceram. Soc.* **21** (2001) 2653.

[36] J. Petzelt, S. Pacesova, J. Fousek, S. Kamba, V. Zelezny, V. Koukal, J. Schwarzbach, B. P. Gorshunov, G. V. Kozolov and A. A. Volkov, *Ferroelectrics* **93** (1989) 77.

[37] D. M. Iddles, A. J. Bell and A. J. Moulson, *J. Mater. Sci.* **27** (1992) 6303.

[38] E. L. Colla, I. M. Reaney and N. Setter, *Ferroelectrics* **154** (1994) 35.

[39] I. M. Reaney, E. L. Colla and N. Setter, *Jpn. J. Appl. Phys.* **33** (1994) 3984.

[40] Internet Data, URL: http://www.lsbu.ac.uk/dielectric-materials

[41] A. Roosen, *Ceram. Trans.* **106** (2000) 479.

[42] H. M. Shirey, Low temperature synthesis of the microwave dielectric material Barium Magnesium Tantalate (BMT), M. S. Thesis, University of Pittsburg (2002).

[43] S. J. Penn, Neil McN. Alford, A. Templeton, X. Wang, M. Xu, M. Reece and K. Schrapel, *J. Am. Ceram. Soc.* **80** (1997) 1885.

[44] S. Hirano, T. Hayashi, A. Hattori, *J. Am. Ceram. Soc.* **74** (1991)1320.

CHAPTER 7

DIELECTRIC RESONATOR LOADED WIDEBAND MICROSTRIP PATCH ANTENNAS

A novel technique for the bandwidth enhancement of conventional rectangular microstrip antenna is proposed in this chapter. When a high permittivity dielectric resonator of suitable resonant frequency was loaded over a radiating patch, the percentage bandwidth of the antenna was increased by more than 5 times without much affecting its gain and other radiation characteristics. A much more improved bandwidth was obtained when the dielectric resonator was placed on the feed line. Experimental study showed a 2:1 VSWR bandwidth of about 14%, excellent cross polarization performance with increased pass band and radiation coverage almost the same as that of rectangular microstrip antenna.

7.1 INTRODUCTION

In the previous chapters we have seen temperature stable, high Q_u DRs with ε_r in the range 9 to 83. This chapter describes the fabrication of broadband DR loaded microstrip patch antennas. We have loaded DRs developed in the previous chapters as well as several other DRs to study the effect of ε_r on the antenna properties.

During recent years, there has been an enormous growth in the wireless communication industry. The development of systems such as cellular telephone networks, wireless local loop networks and wireless local area networks are rapidly evolving worldwide. The field of antenna engineering is of course central to all wireless technologies, and plays a significant role in the successful deployment and optimization of such systems. As such the growing demand for wireless communications has stimulated extensive research in order to find new solutions to problems in antenna engineering. With the advances in wireless communication technologies and associated proliferation of base stations throughout major cities and most of the countryside, demand relatively cheap, low profile, light weight, compact and easy to manufacture antennas. This of course is also applicable for handset antennas where the size of the device is constantly shrinking. Due to the excellent radiation performance and other characteristics that fulfills all the above requirements, microstrip antennas are commonly employed in handsets and Wireless Local Area Network (WLAN) applications.

7.1.1 History of Microstrip Antennas

With the development of Microwave Integrating Circuits (MIC) and high frequency semiconductor devices, microstrip has drawn the maximum attention of the antenna community in recent years. In 1953, Deschamps[1] proposed the concept of microstrip radiators for the first time. The revolutionary progress in material science in the same era has produced a wide variety of dielectric materials with attracting dielectric, thermal and mechanical properties. This triggered the research in microstrip antennas. After intense work on theoretical modeling, the first practical microstrip antenna was developed in early 1970's by Howell[2] and Munson[3], employing photo-etch technique. Since then the immense research in microstrip antennas and microwave substrates gave

birth to a variety of microstrip antenna configurations and arrays and is still one of the most active field in microwave antenna research.

7.1.2 Basic operation of the Microstrip Antenna

In one of its most basic forms, microstrip antenna is comprised of a metallic radiating patch of any shape etched on a low loss microwave substrate with a ground plane. It is usually manufactured by printing the patch on a thin microwave substrate. Ideally the dielectric constant (ε_r) of the substrate should be low ($\varepsilon_r < 5$), so as to enhance the fringe fields which account for the radiation. The patch conductors are normally of copper or gold and can assume virtually any shape but conventional shapes are generally used to simplify the analysis and performance prediction. Because of the unique properties of microstrip antennas, this technology is nowadays often used to manufacture small antennas and arrays.

Radiation from discontinuities in microstrip was first studied by Lewin[4] in 1960. The analysis confirmed that open-circuited microstrip lines radiate more power when fabricated on thick low dielectric constant substrates. Radiation from microstrip antennas occurs from the fringing fields between the edge of the microstrip antenna conductor and the ground plane. The patch is a resonant element and therefore one of its dimensions must be nearly one half of the guided wavelength in the dielectric substrate. Radiation may be ascribed mostly to the open-circuited edges of the patch and hence the fields can be resolved into two components: one normal and the other tangential to the ground plane. The normal components became out of phase as the patch dimension in that direction is $\lambda/2$ long and hence vanishes in the far field. The tangential field components being in phase are added up and results in a radiation normal to the surface of the conductor (along the broadside direction). In addition to the radiation, certain *TM* and *TE* modes, which propagate into the substrate outside the microstrip patch which will excite some surface waves giving rise to endfire radiation and these are to be eliminated or minimized for better radiation performance of the antenna.

There are four fundamental techniques to feed or excite the patch. These include (i) Probe feed[5] (ii) Microstripline feed[6] (iii) Aperture coupled feed [7]and (iv) Proximity

coupled feed[8]. Probe feed is constructed by extending a probe through the ground plane and connecting it to the patch, typically by soldering it. In the case of single element antenna the probe is usually the inner conductor of a coaxial cable of which the outer conductor is soldered to the ground plane. The input impedance is controlled by the feed point location. The microstrip line fed consists of a microstrip feed that is connected to one of the edges of the patch. The position of the connection point is also used to tune the input impedance. In aperture coupled feed mechanism, the microstrip feedline and patch are separated by a ground plane and coupling is achieved via a small slot in the ground plane. In proximity coupling, another microstrip line is printed on a substrate layer between the ground plane and the patch. In this case power from the feedline is electromagnetically coupled to the patch. Each one of the feeding techniques has its own advantages and disadvantages. However microstrip line method is the simplest one which is employed in the present study.

7.1.3 Rectangular Microstrip Antennas

There are virtually an unlimited number of patch patterns reported in literature[9,10,11,12,13,14,15,16]. Conventional shapes include square, rectangular, circular, ellipse, pentagon, ring, equilateral triangle, star etc. Rectangular and circular geometries are very common, but any shape that possess a reasonably well defined resonant mode and contribute effective radiation performance can be used. Rectangular microstrip is advantageous over circular one in the sense that, the antenna designer can enjoy more degrees of freedom with two parameters (length and breadth) available for tuning the operating frequency and hence are easily adaptable for applications. Accordingly intense researches were made on rectangular microstrip antennas[17,18,19,20,21]. A rectangular microstrip antenna element may be used as a stand alone or in combination with other like elements to form an array. In either case the antenna is to be designed to achieve a specific performance at a stipulated operating frequency. With this point of view rectangular microstrip patch antenna may be designed for a certain resonant frequency by choosing its elemental width and length. The design procedures and selection of

parameters for the better performance of rectangular microstrip patch antenna is discussed in detail elsewhere.[22]

For a substrate material of dielectric constant ($\varepsilon_{r\,sub}$) and thickness h, an antenna operating at a frequency of f_r should have a practical width W as

$$W = \frac{c}{2f_r}\left(\frac{\varepsilon_r + 1}{2}\right)^{-1/2} \tag{7.1}$$

The antenna radiation efficiency will be lower for decreased width, whereas increased width may result in better efficiency but with the excitation of higher order modes, which is not desirable.

Once the width of the patch W is known, the effective dielectric constant ε_e and the line extension Δl (length of the radiating slot) can be calculated using the following equations

$$\varepsilon_e = \frac{\varepsilon_r + 1}{2} + \frac{\varepsilon_r - 1}{2}\left(1 + \frac{12h}{W}\right)^{-1/2} \tag{7.2}$$

$$\frac{\Delta l}{h} = 0.412\left(\frac{(\varepsilon_e + 0.3)(W/h + 0.264)}{(\varepsilon_e - 0.258)(W/h + 0.8)}\right) \tag{7.3}$$

The length of the resonant element is given by

$$L = \frac{c}{2f_r\sqrt{\varepsilon_e}} - 2\Delta l \tag{7.4}$$

Or in other words, for rectangular microstrip patch antennas, the lowest order resonant frequency f_r can be accurately predicted using the equation,

$$f_r = \frac{c}{2}(L + \Delta l)\sqrt{\varepsilon_e} \qquad (7.5)$$

7.1.4 Advantages and Disadvantages of Microstrip Patch Antennas

Microstrip antennas possess many favourable characteristics such as light weight, low volume, and low profile. The planar configurations can also be made conformal by using flexible substrates. Microstrip antennas are low cost and very easy to fabricate which enables low cost mass production for industrial purposes. These antennas can be easily applied in aerospace vehicles, missiles, rockets and satellites without creating aerodynamical problems. Wide applications of the antennas are possible as they can radiate waves with linear as well as circular polarizations employing suitable feed mechanisms. Microstrip antennas can be easily used for dual frequency applications and they are very compatible with solid state devices such as oscillators, amplifiers, variable attenuators, switches, modulators, mixers, phase shifters etc.

However, microstrip patch antennas also have some major disadvantages from the application point of view in terms of their narrow bandwidth, comparatively lower gain and half plane radiation performance. Moreover, they have poor endfire radiation performance and poor isolation between the feed and radiating elements. The presence of the metallic conducting part increases the ohmic loss and hence the antennas have lower power handling capacity. In addition the possibility of surface waves will adversely affect the radiation performance of microstrip patch antennas. It is noteworthy that for many applications, the advantages of microstrip antennas far outweigh their disadvantages.

7.1.5 Bandwidth Enhancement of Microstrip Antennas

The main drawback associated with microstrip patch antennas is its inherent narrow impedance bandwidth. In most cases, the impedance bandwidth is not wide enough to handle the requirements of modern wireless communication systems.

The recent trends in improving the impedance bandwidth of microstrip antennas can be broadly divided into the following four categories:

(i) Various geometries and perturbations to introduce multiple resonances with better impedance matching,

(ii) Genetic Algorithm (GA) based optimization of antenna geometries,

(iii) Photonic Band Gap (PBG) structures used as printed antenna substrates,

(iv) Frequency Selective Surfaces (FSS) used as multilayered substrate or ground plane.

The first one is the leading of all four categories in numbers and varieties. A proximity-fed triangular patch in a circular slot is reported[23] which shows more than 90% of Standing Wave Ratio (SWR) < 2 bandwidth. A novel design of broad band stacked patch antenna has been proposed very recently by Ooi *et. al*[24] where they have used stacked patch with shaped slots and used probe compensation by metallic washer on the probe and obtained 44.9 % impedance bandwidth. Another new technique of impedance matching by capacitive loading of inverted microstrip has been recently proposed by the Guha *et al.*[25]. Stacked patch geometries with efficient feeding techniques were also explored to achieve large bandwidth[26,27].

Optimization of patch geometry is an ideal technique to have single or more optimized figures of merit like, impedance bandwidth. The genetic algorithm has been successfully applied by a number of researchers to improve the impedance bandwidth. The optimized shape however is too much irregular and unconventional and as such this can only be fabricated using the pattern produced in true scale by the genetic algorithm code.

The narrow impedance bandwidth of microstrip antennas can be ascribed to the thin substrates that are normally used to separate the patch and the ground plane. It was established that the impedance bandwidth increases with the thickness and decreases with the dielectric constant of the substrate used. Hence in order to increase the bandwidth of microstrip antennas, the substrate thickness has to be increased, while the dielectric constant has to be kept as low as possible.

The first option is more flexible for design purposes but, restricted by the generation of surface waves leading to low gain and efficiency. Moreover, it introduces further complications in terms of input impedance of the antenna. For thin substrates the

input impedance at the resonant frequency is purely real, but as the substrate thickness increases the input impedance becomes more inductive. In order to offset the inductive component of the input impedance, an alternative feeding mechanism is required. Use of the Photonic Band Gap (PBG) structures as antenna substrates is one promising solution to suppress the surface wave excitation employing thick substrates and thus attracts a large fraction of antenna people to work with PBG[28,29,30,31]. The PBG structure is basically a periodic metallic pattern printed on dielectric substrate for microwave and millimeter wave applications and this provides a stop band of electromagnetic waves propagating through it. The frequency range of the stop band depends on the pattern geometry and its dimensions. If the antenna operating frequency falls within this stop band, the surface waves are attenuated during propagating through the substrate. Thus the generation and propagation of surface wave is stopped.

Frequency selective surface (FSS) is another area of interest to antenna researchers. The FSS is also created by printing periodic patterns on microwave substrates to simulate equivalent inductance (L) and capacitance (C) to an electromagnetic wave and thus its basic characteristic is to scatter or reflect certain frequencies of electromagnetic waves incident on it. Out of various studies with FSS in the context of microstrip and printed antennas, increase in pass band of printed antenna or antenna arrays find a significant importance[32,33].

To date various other approaches to enhance the impedance bandwidth of microstrip patch antennas, have been suggested and implemented. These include wide band impedance-matching networks, edge coupled patches, stacked patches, shaped probes, capacitive coupling and slotted patches. However, not all of these solutions fulfill the requirements that are imposed by modern day telecommunication systems. Some of the solutions are not suitable for array substitutions, some requires multiple substrate layers, some are very complex to design, while others are very sensitive to alignment errors and manufacturing tolerances. The above mentioned methods will not only increase the complexity of the system but will adversely affect the gain of the antenna. As an alternative, a novel technique for the bandwidth enhancement of a microstrip patch antenna by loading a dielectric resonator disc on the patch surface is proposed.

7.1.6 DR loaded Microstrip Antennas

In 1998, George *et al.*[34] reported a probe fed broadband rectangular and circular dielectric resonator loaded microstrip patch antennas. Rectangular microstrip patch resonating at 2. 70 GHz and circular one operating at 4.01 GHz was reported with a bandwidth of about 10 % and 6 % respectively, when a dielectric resonator of $\varepsilon_{r\,dr} = 58$ was fixed on the nonradiating edge of the patch surface. It is reported[35] that suspended microstrip is a simplest and most widely used structure which, offers wide band and improved efficiency. The suspended microstrip patch antennas offer a bandwidth of about 5% to 6%.

Recently, Esselle *et al.*[36] reported an ultra wide band dielectric resonator-patch antenna. The authors proposed a structure which involves an aperture coupled dielectric resonator antenna placed over an aperture coupled microstrip patch antenna. The configuration had two coupling slots, one to couple the microstrip patch fields to the DR and the other to couple the microstrip – feed fields to the microstrip patch fields. Though the configuration presented a high bandwidth of 21% (at 5.5 GHz), multiple feeding in turn increased the complexity and size of the antenna system, which is not desirable. More recently Gupta *et al.*[37] reported DR loaded suspended circular and rectangular microstrip patch antennas with 18 % and 13 % respectively, which is nearly three and two fold compared with the bandwidth without loading a dielectric resonator. It is noteworthy that in DR loaded antennas the bandwidth remained unchanged even with sufficient enhancement in impedance bandwidth of the antennas.

Loading of a dielectric resonator disc envisages a novel technique for the bandwidth improvement of microstrip patch without much affecting the gain and radiation properties of the antenna. With this view it is expected that the resonant frequency and dielectric constant as well as the position of dielectric resonator disc loaded over the patch surface should play a major role in controlling the bandwidth and other antenna parameters. Keeping this in mind, detailed investigation was made on the optimization of the position of DR on the patch surface and the effect of its dielectric constant and resonant frequency on the antenna properties. The effect of loading DR on

the feedline (outside the patch surface) after fixing the microstrip patch at the optimized position for maximum impedance matching was also studied.

7.2 ANTENNA GEOMETRY

The geometry of the proposed DR loaded microstrip patch antenna is shown in Fig.7.1. Rectangular patch antenna of dimension L x W is etched on a substrate of thickness h_2 = 1.6mm and permittivity $\varepsilon_{r2\ sub}$ = 4.28 as described in section 7.1.3 of this chapter. The patch is electromagnetically coupled by a 50Ω microstrip feed fabricated on a substrate of thickness h_1 = 1.6mm and permittivity $\varepsilon_{r1\ sub}$ = 4.28. The antenna is loaded with a cylindrical DR of diameter d, height H and dielectric constant $\varepsilon_{r\ dr}$. The return loss, radiation pattern and gain of the antenna were measure as described in section 2.5 of Chapter 2.

7.3 EXPERIMENTAL RESULTS

7.3.1 DR over the patch surface

A rectangular microstrip antenna of L x W = 30mm x 39mm resonating at 2.3 GHz is fabricated on a dielectric substrate of permittivity ε_{r1sub} = 4.28 and height h_1 = 1.6mm as described in Fig. 7.1(a).

Table.7.1 Variation of percentage bandwidth of DR loaded antenna with position of DR on the microstrip patch
$\varepsilon_{r\ dr}$ = 48, H_{dr} = 7.21mm, D_{dr} = 24.15mm

Axial variation				Diagonal Variation		Variation along the edges	
x		y					
Position	%BW	Position	%BW	Position	%BW	Position	% BW
(0, 0)	5.50	(0, 0)	5.50	(0, 0)	5.50	(1.5, 0)	5.93
(0.5, 0)	5.62	(0, 0.5)	5.61	(0.5,0.5)	6.31	(1.5, 0.5)	6.21
(1, 0)	5.75	(0, 1)	5.85	(1, 1)	8.48	(1.5, 1)	7.39
(1.5, 0)	5.93	(0, 1.5)	6.22	(1.5,1.5)	10.57	(1.5, 1.5)	10.57
		(0, 2)	6.65			(1.5, 2)	8.33

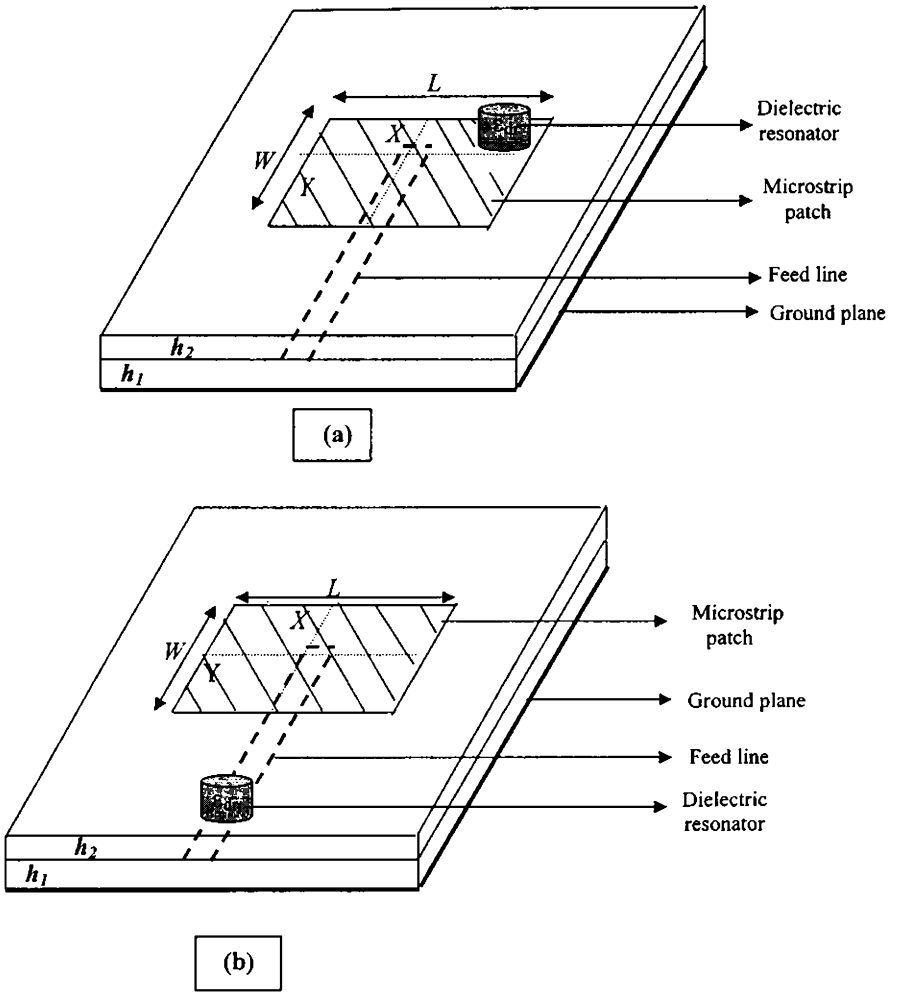

Fig.7.1 Geometry of DR loaded microstrip patch antenna
(a) DR over the patch (b) DR on the feedline

Dielectric resonator materials of different dielectric constant (9 – 92) were prepared by solid-state ceramic route as described in Chapter 2, Section 2.1.2. Their dimensions were so chosen to have the same resonant frequencies. The impedance bandwidth of the rectangular microstrip patch was noted first. The BW of the antenna was found to be

2.77% at 2.3 GHz. The DR of dielectric constant $\varepsilon_{r\,dr}$ = 48, height H_{dr} = 7.21mm and diameter D_{dr} = 24.15mm is fixed at different locations on the patch. The corresponding bandwidth is noted in each position and is shown in Table 7.1. Along *X* and *Y* direction the percentage bandwidth increases when the DR is moved from the center to the edge of the patch. The change in percentage bandwidth along the diagonal is more significant than any other intermediate position. It is clear from the table that along the diagonal the percentage bandwidth reaches a maximum at a position (1.5, 1.5). At this position, the DR is at the corner of the patch but it is completely within the boundary of the patch.

The DR is also moved along the edges of the microstrip patch to study the variation in percentage bandwidth. It is observed that the percentage bandwidth increases and reaches a maximum value at (1.5, 1.5) position and then decreased at the extreme corner. It was also noted that the maximum percentage bandwidth observed at the same position on all quadrants of the patch, as it is symmetrical. For all other intermediate positions of the DR on the microstrip patch the percentage bandwidth was less than that at the (1.5, 1.5) position. In a similar manner the optimum position for maximum percentage bandwidth was optimized using all DRs with different $\varepsilon_{r\,dr}$. It was observed that the position for maximum percentage bandwidth is the same for all DRs irrespective of their dielectric constant. This variation shown in Table 7.1 is for the DR of $\varepsilon_{r\,dr}$ = 48.

The variation of percentage bandwidth with dielectric constant $\varepsilon_{r\,dr}$ is tabulated in Table 7.2. It is clear from the table that as the dielectric constant of the loaded ceramic disk increases the percentage bandwidth of the antenna also increases and reaches a maximum value. It is inferred that significant bandwidth enhancement occurs when the dielectric constant of the DR is in the range 40 to 50. The maximum bandwidth is 10.57% for the material $Ca_5Nb_2TiO_{12}$. This material has a dielectric constant of 48, with a quality factor $Q_u \times f >$ 26000 GHz and low temperature variation of resonant frequency τ_f (See Chapter 3, Section 3.3.2). This confirms that the system is stable with temperature variations. More over the relatively low density (4.06 g/cm^3) of the material ensures that the weight and hence the complexity of the antenna system will not be much increased by DR loading. Above this value of ε_{dr}, the percentage bandwidth decreases.

Table 7.2 Variation of percentage bandwidth of DR loaded antenna with dielectric constant of DR

Sl. No	Dielectric Material	$\varepsilon_{r\,dr}$	Resonant frequency of the DR loaded antenna (GHz)	percentage bandwidth
1.	$5ZnO\text{-}Ta_2O_5\text{-}TiO_2$	9	2.31	3.23
2.	$CaO\text{-}4ZnO\text{-}Ta_2O_5\text{-}TiO_2$	10	2.31	3.26
3.	$Mg_5Nb_4O_{15}$	11	2.30	3.41
4.	$Mg_{4.5}Zn_{0.5}Nb_4O_{15}$	13	2.30	3.52
5.	$5CoO\text{-}Ta_2O_5\text{-}TiO_2$	14	2.30	3.55
6.	$Ca_5Ta_2HfO_{12}$	17	2.30	4.25
7.	$YTiTaO_6$	18	2.30	4.61
8.	$LaTiTaO_6$	20	2.30	4.92
9.	$Ca_5Ta_2ZrO_{12}$	21	2.30	4.95
10.	$5ZnO\text{-}2Nb_2O_5$	22	2.30	5.02
11.	$2CaO\text{-}3CoO\text{-}Ta_2O_5\text{-}TiO_2$	24	2.30	5.23
12.	$Ba\,(Mg_{1/3}Ta_{2/3})\,O_3$	25	2.30	5.56
13.	$CaO\text{-}4NiO\text{-}Nb_2O_5\text{-}TiO_{12}$	27	2.30	5.98
14.	$Ba\,(Zn_{1/3}Ta_{2/3})\,O_3$	29	2.30	6.48
15.	$2CaO\text{-}3NiO\text{-}Nb_2O_5\text{-}TiO_2$	31	2.29	6.59
16.	$Ca_4CoNb_2TiO_{12}$	34	2.29	6.98
17.	$EuTiTaO_6$	36	2.29	7.21
18.	$Ca_5Ta_2TiO_{12}$	38	2.28	7.95
19.	$TbTiTaO_6$	42	2.28	8.63
20.	$Ca_{4.36}Zn_{0.64}Nb_2TiO_{12}$	43	2.28	8.95
21.	$SrLa_4Ti_4O_{15}$	44	2.27	9.43
22.	$Ca_2Sr_3Ta_2TiO_{12}$	45	2.27	10.02
23.	$Ca_5Nb_2TiO_{12}$	48	2.27	10.57
24.	$CaLa_8Ti_9O_{31}$	50	2.27	9.94
25.	$Ca_4SrNb_2TiO_{12}$	52	2.28	9.56
26.	$CaLa_4Ti_5O_{17}$	54	2.28	8.86
27.	$Ca_4BaNb_2TiO_{12}$	58	2.28	8.41
28.	$Ba_{0.4}Sr_{0.6}InTi_5O_{14}$	62	2.28	7.90
29.	$Ca_3Ba_2Nb_2TiO_{12}$	66	2.29	7.23
30.	$BaPr_2Ti_4O_{12}\,(+Bi_2O_3)$	73	2.29	7.05
31.	$BaNd_2Ti_4O_{12}$	84	2.30	6.13
32.	$BaPr_2Ti_4O_{12}$	92	2.30	5.02

It is to be noted that the resonant frequency of the patch antenna is almost unaffected by loading a DR on it. A very small decrease in resonant frequency occurs when the value of $\varepsilon_{r\ dr}$ suits for maximum enhancement of percentage bandwidth. The variation of percentage bandwidth with dielectric constant of the DR is shown in Fig. 7.2.

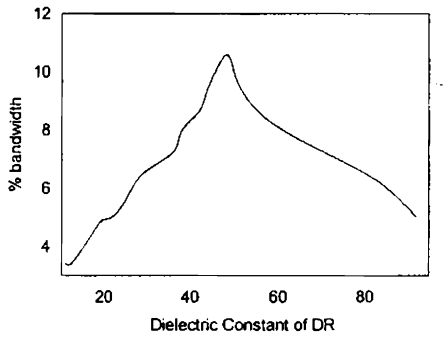

Fig. 7.2 Variation of percentage bandwidth of the DR loaded antenna with dielectric constant of DR

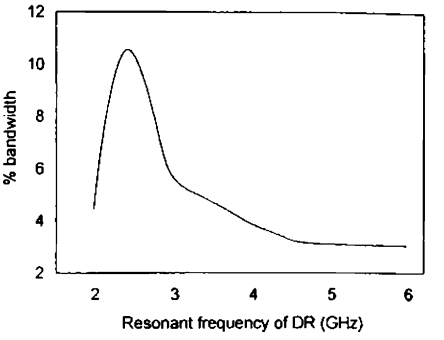

Fig. 7.3 Variation of percentage bandwidth of the DR loaded antenna with resonant frequency of DR

To study the effect of resonant frequency of the DR on the antenna properties we prepared $Ca_5Nb_2TiO_{12}$ samples of different dimensions so as to have different resonant frequencies (2 – 6 GHz). These samples were placed at the optimized position for maximum bandwidth and measured the percentage bandwidth of the antenna in each case. It is inferred that the DR loaded microstrip antenna attained a maximum bandwidth of 10.57% at 2.27 GHz when the resonant frequency (f_r = 2.4 GHz) of the DR approaches that of the rectangular microstrip patch alone. The variation of percentage bandwidth with resonant frequency of DR is depicted in Fig. 7.3.

The typical *E*-plane and *H*-plane radiation patterns of the DR loaded antenna in the operating band are given in Fig.7.4. The radiation patterns at start frequency (2.158 GHz), centre frequency 2.27 GHz and stop frequency 2.398 GHz are given. At the center frequency the *E*-plane half power beam width is 66° and *H*-plane half power beam width is 64° respectively. This confirms that the antenna is working like a conventional Microstrip Antenna with enhanced bandwidth. The cross polarization studies show that

the cross-polar isolation is better than -25 dB, which is also a desirable characteristic for communication antennas. The gain of the antenna was measured to be about 6.3 dBi.

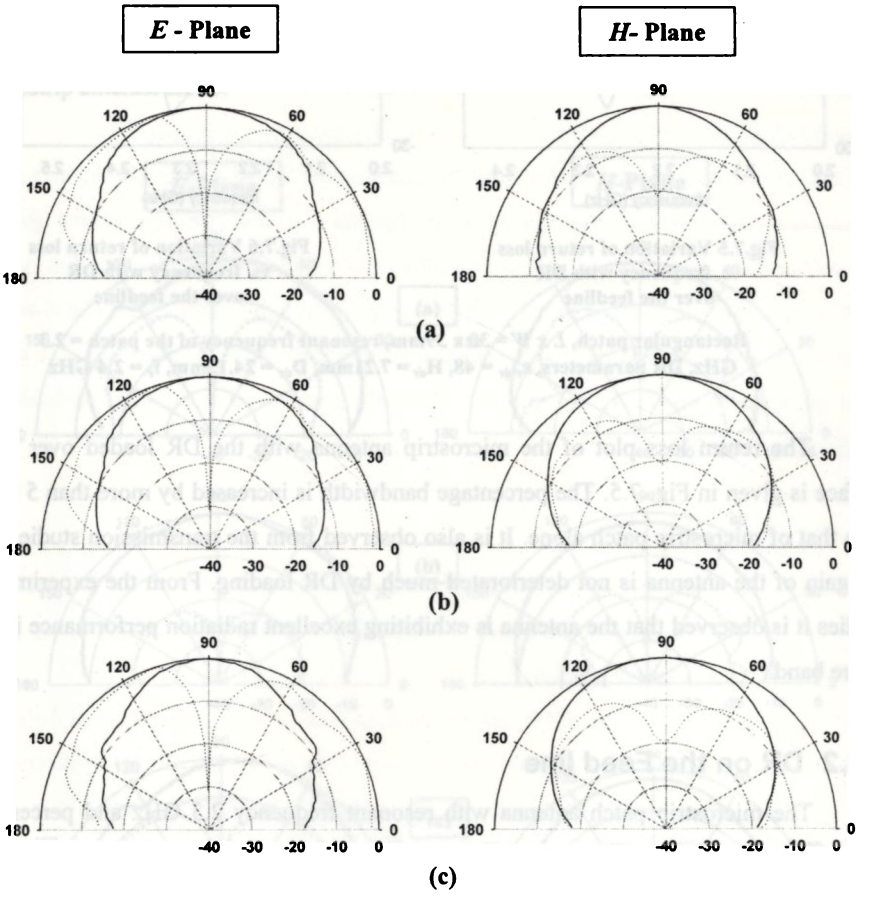

Fig.7.4.Radition pattern of the antenna with the DR loaded over the patch
____ co-polar ------cross-polar
(a) start frequency, 2.158GHz (b) center frequency, 2.27GHz and
(c) stop frequency, 2.398GHz
Rectangular patch, *L x W* = 30 x 39mm, resonant frequency of the patch = 2.3 GHz,
DR parameters, $\varepsilon_{r\,dr}$ = 48, H_{dr} = 7.21mm, D_{dr} = 24.15mm, f_r = 2.4 GHz

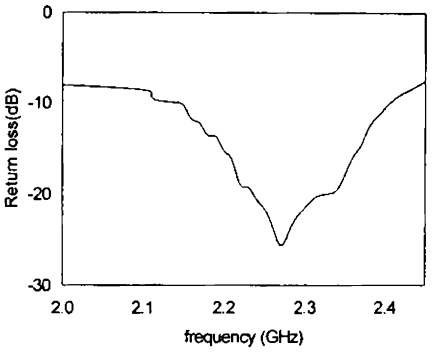

Fig.7.5 Variation of return loss vs. frequency with DR over the feedline

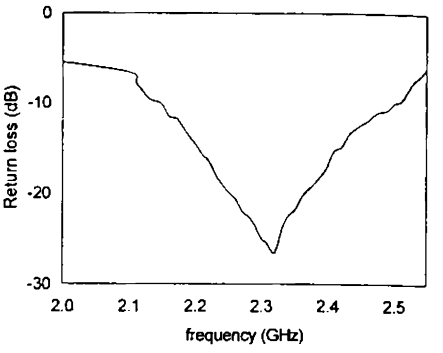

Fig.7.6 Variation of return loss vs. frequency with DR over the feedline

Rectangular patch, $L \times W$ = 30 x 39mm, resonant frequency of the patch = 2.3 GHz, DR parameters, $\varepsilon_{r\,dr}$ = 48, H_{dr} = 7.21mm, D_{dr} = 24.15mm, f_r = 2.4 GHz

The return loss plot of the microstrip antenna with the DR loaded over patch surface is given in Fig. 7.5. The percentage bandwidth is increased by more than 5 times than that of microstrip patch alone. It is also observed from the transmission studies that the gain of the antenna is not deteriorated much by DR loading. From the experimental studies it is observed that the antenna is exhibiting excellent radiation performance in the entire band.

7.3.2 DR on the Feed line

The microstrip patch antenna with resonant frequency 2.3 GHz and percentage bandwidth 2.77 is fixed on the feedline. The dielectric resonator material of ε_{dr} = 48 and f_r = 2.4 GHz is placed over the feedline at different positions [See Fig.7.1 (b)]. The percentage bandwidth and return loss is measured in each case. It is observed that as the DR moves away from the patch and approaches the feed point, the percentage bandwidth increases along with slight increase in the resonant frequency of the modified antenna. Near the feed point the bandwidth reached a maximum of 13.79% at 2.32 GHz with a negligible reduction in gain. The DR is fixed at this point on the feedline and the E -plane and H -plane radiation characteristics were studied.

The return loss of the antenna plotted against frequency is given in Fig. 7.6. The centre frequency slightly shifted towards the high frequency region when the DR was loaded on the feedline. In this case the bandwidth reached about 14% at 2.32 GHz with a 7-fold increase from that of microstrip patch alone. Moreover the transmission studies revealed that the gain of the antenna is nearly equal to that of conventional rectangular microstrip antenna alone.

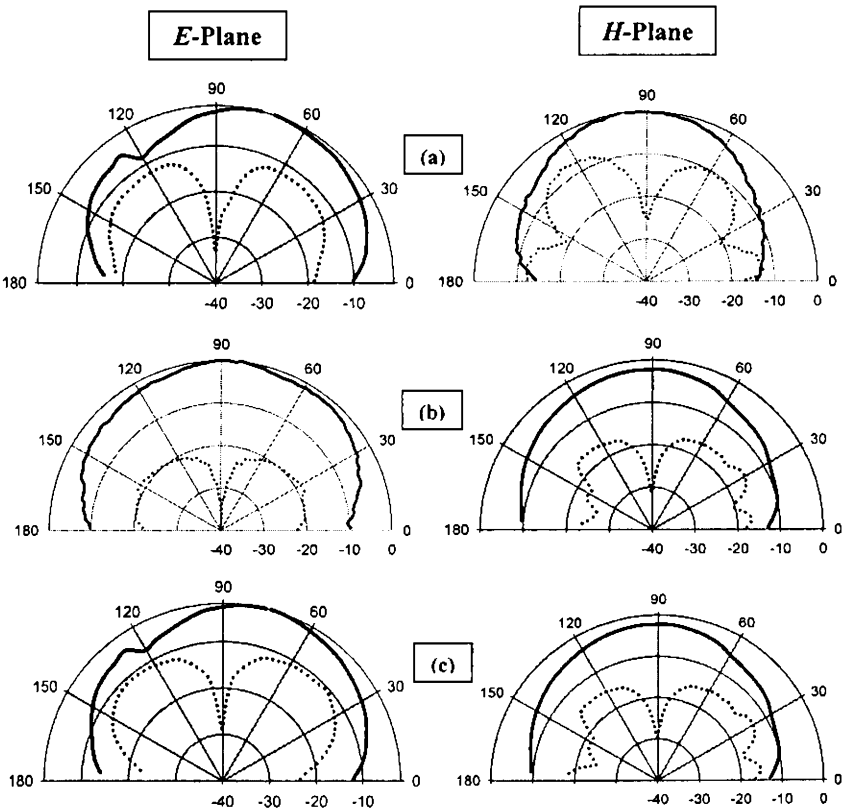

Fig.7.7 Radiation pattern of DR loaded antenna with DR on the feedline
_____ co polar ------- cross polar
(a) Start frequency, 2.188GHz (b) Center frequency, 2.32 GHz (c) Stop frequency, 2.508GHz
Rectangular patch, $L \times W$ = 30 x 39mm, resonant frequency of the patch = 2.3 GHz, DR parameters, $\varepsilon_{r\,dr}$ = 48, H_{dr} = 7.21mm, D_{dr} = 24.15mm, f_r = 2.4 GHz

Typical *E*-plane and *H*-plane radiation patterns at start frequency (2.188 GHz), centre frequency (2.32 GHz) and stop frequency 2.508 GHz are shown in Fig. 7.7. The antenna exhibits excellent cross-polar isolation of better than -30 dB, which is highly suitable for broadband applications in telecommunication purposes. However the cross-polar field of H-plane pattern is slightly distorted and side lobes are visible. The gain of the antenna was measured as described in Section 2.5.3 of Chapter 2 and was found to be about 6.9 dBi.

The investigations revealed that, the effect of DR loading on the microstrip patch is only to improve the performance of the antenna. It was found that the gain is comparable with that of conventional microstrip patch antennas and the radiation pattern study reveals that the antenna shows excellent properties in the entire band. The *E* and *H*-plane half power beam width is suitable enough for communication purposes. The cross-polar isolation is about -30 dB and it projects the antenna as a suitable candidate for practical applications.

7.4 CONCLUSIONS

- The cylindrical dielectric resonator loaded microstrip antenna for enhancing the impedance bandwidth of a conventional microstrip patch antenna is proposed.
- The position of DR on the patch surface as well as the value of dielectric constant and resonant frequency of DR needed for maximum percentage bandwidth is optimized. In addition the effect of fixing a high permittivity DR on the feedline was investigated. In both the cases it was observed that DRs with dielectric constant in the range 40 – 50 make maximum increase in the bandwidth of microstrip antennas. A wideband DR loaded microstrip patch antenna is fabricated with $Ca_5Nb_2TiO_{12}$ DR material of $\varepsilon_{r\,dr} = 48$.
- The effect of resonant frequency of DR on the antenna performance was also studied. Maximum increase in bandwidth of microstrip antenna was

attained when resonant frequency of DR was close to that of the patch radiator.

- ❖ In both cases the increase in bandwidth of microstrip patch antenna is achieved with excellent radiation characteristics. The studies also revealed that these methods will not adversely affect other properties of the antenna especially its gain and efficiency. These characteristics point towards the possibility of using these antennas for practical applications.
- ❖ A bandwidth of more than 10% is achieved by loading a dielectric resonator of $\varepsilon_{r\,dr} = 48$ over the patch and about 14% by loading the same DR on the feedline.

7.5 REFERENCES

[1] G. A. Deschamps, *3rd USAF Symp. on Antennas*, 1953.

[2] J. Q. Howell, *IEEE AP-S Int. Symp. Digest* (1972)177.

[3] R. E. Munson, *IEEE Trans. Antennas Propag.* **AP-22** (1974) 74.

[4] L. Lewin, *Proc. IEE* **107** (1960) 163.

[5] Mak C. L., K. M. Luk, K. F. Lee, and Y. L. Chow, *IEEE Trans. Antennas Propagat.* **48** (2002) 777.

[6] J.-C. Langer, J. Zou, C. Liu, and J. T. Bernhard, *IEEE Microwave and wireless components Lett.* **13** (2003) 120.

[7] G. P. Gauthier, J-P Raskin, L. P. B. Katehi, and G. M. Rebeiz, *IEEE Trans. Antennas Propagat.* **47** (1999) 1761.

[8] P.K. Singhal and L. Shrivastava, *J. Microwaves and Optoelectronics* **3** (2004) 87.

[9] J. T. Bernhard, Proc. *IEEE/URSI Antennas and Propagation Soc. International Symp.* **2** (2001) 696.

[10] K. M. Luk, K. F. Tong, S. M. Shum, K. F. Lee and R. Q. Lee, *IEEE AP-S Symposium Digest* (1997) 2111.

[11] J.-H. Lu, C.-L. Tang, and K. L. Wong, *Microwave and Opt. Technol. Lett.* **18** (1998) 345.

[12] S. S. Pattnaik, R. K. Mishra and N. Das, *Electron. Lett.* **26** (1990) 1906.

[13] H.-D. Chen and W.-S. Chen, *Microwave and Opt. Technol. Lett.* **30** (2001) 370.

[14] W.Y.Tam, A. K. Y. Lai, and K. M. Luk, *Microwave Opt. Tech. Lett.* **7** (1994) 371.

[15] A. Nachit and J. Foshi, *J. Microwaves and Optoelectronics* **2** (2000) 1.

[16] K. Parasnis, L. Shafai and G. Kumar, *Electron. Lett.* **22** (1986) 463.

[17] R. Garg and A. Ittipiboon, *Microstrip Antenna*, Design Handbook, Artech House, 2001.

[18] J. F. Zurcher and F. Gardiol *Broadband Patch Antenna*, A Handbook. Artech House, 1995.

[19] V. Schejbal, J. Novak and S. Gregora, *Radioengineering* **12** (2003) 12.

[20] V. Srinivasan, K.T.V. Reddy and G.Kumar, *Microwave and Opt. Tech. Lett.* **26** (2000) 8.

[21] B. Lethakumari, Sreedevi K Menon, C. K. Aanandan, K. Vasudevan and P. Mohanan, *Microwave Opt. Technol. Lett.* **35** (2004) 235.

[22] I. J. Bahl and P. Bhartia, *"Microstrp antennas"* (Artech house, Massachusetts, USA, 1982) pp. 46 – 57.

[23] Y. W. Jang, *Microwave Journal* **45** (2002) 288.

[24] B. L. Ooi, S. Qin and M. S. Leong, *IEEE Trans. Antennas Propagat.* **50** (2002) 1391.

[25] D. Guha and J. Y. Siddiqui, *IEEE AP-S Int. Symp.* (San Antonio, Texas, June 16-21, (2002) 534.

[26] K. Ghorbani, and R. B. Waterhouse, *IEEE Trans. Antennas Propagat.* **50** (2002) 1697.

[27] S. S. Iqbal, J. Y. Siddiqui, and D. Guha, *IEEE Int. Symp. on Antennas and propagation and USNC/CNC/URSI North American Radio Science Meeting*, (Columbus, OH, during June 22-27, 2003).

[28] H.Y.D. Yang, N.G. Alexopoulos, and E. Yablonovitch, *IEEE Trans. Antennas Propagat.* **45** (1997)185.

[29] V. Radisic, Y.X. Qian, R. coccioli, and T. Itoh, *IEEE Microwave Guided Wave Lett.* **8** (1998) 69.

[30] C. Cheype, C. Serier, M. Thevenot, T. Monediere, A. Reinix, and B. Jecko, *IEEE Trans. Antennas Propagat.* **50** (2002) 1285.

[31] Y. Horii, and M. Tsutsumi, *IEEE Microwave and Guided Wave Lett.* **9** (1999) 13.

[32] R. Mittra, C.H. Chan, T. Cwik, *Proc. IEEE* **76** (1998) 1593.

[33] Y. E. Erdemli, K. Sertel, R. A. Gilbert, D. E. Wright, and J. L. Volakis, *IEEE Trans. Antennas Propagat.* **50** (2002) 1716.

[34] Jacob George, C.K. Aanandan, P. Mohanan, K.G. Nair, H. Sreemoolanathan and M.T. Sebastian, *Microwave and Opt. Technol. Lett.* **17** (1998) 205.

[35] H. Iwasaki and Y. Suzuki, *IEEE Trans Antennas Propagat.* **AP-44** (1996) 777.

[36] K. P. Esselle, *Proc. IEEE International conference on Antennas and Propag.* April 17 – 20 (2001) 22.

[37] V. Gupta, S. Sinha, S. K. Koul, and B. Bhat, *Microwave and Opt. Technol. Lett.* **37** (2003) 300.

CHAPTER 8

BROADBAND DIELECTRIC RESONATOR ANTENNAS

This chapter describes a new technique for improving the bandwidth and radiation performances of dielectric resonator antennas. It is proposed that modification of conventional microstrip line into L- and T-shapes improve the antenna performance. Design, fabrication and characterization of cylindrical, elliptical and rectangular DRAs excited with microstrip line, L- and T-feeds are studied. Three dimensional Transmission Line Matrix method was employed to simulate the electric and magnetic field distribution of the DRA at resonance. Mode identification methods of the DRA are explained and experimental results were verified with simulation. The bandwidth, gain and radiation efficiency of each geometry of the antenna is investigated in detail.

8.1 INTRODUCTION

The boom market for wireless microwave/millimeter wave communication systems demand high performance, cost effective and low profile antennas for base station applications. Conventional antennas suffer from narrow bandwidth and low efficiency due to the ohmic loss of radiating elements and the bulky feeding networks at these frequencies. Ceramic dielectric resonator antennas have the inherent advantages like high radiation efficiency and large impedance bandwidth owing to their lower ohmic loss compared with conventional microstrip patch antennas. DRAs are very easy to design and fabricate and their operating bandwidth can be easily controlled by choosing the dielectric constant and dimensions of the dielectric resonator material used. In addition, DRAs can be excited in different modes to produce various radiation characteristics and can be easily integrated with other active or passive Microwave Integrated Circuit (MIC) components. DRAs with different shapes such as cylindrical, rectangular, hemispherical, conical, and cylindrical rings have been investigated[1,2,3,4,5] (See section 1.4.3 of Chapter 1).

Excitation techniques of DRAs employing conducting probe, microstrip slot, coplanar wave guide, aperture coupling etc. have also been studied[6] and is explained in detail in section 1.4.4 of Chapter 1. Microstrip feed line excitation of DR placed on a dielectric substrate provides a convenient coupling scheme[7] even though this may generate surface waves from the conducting plane. DRAs of different DR materials with dielectric constant ($\varepsilon_{r\,dr}$) ranging from 10 – 100 have been investigated by many researchers [1,2,5,7,8]. For very high $\varepsilon_{r\,dr}$ ($\varepsilon_{r\,dr} > 60$) even with the advantage of size reduction, the bandwidth and operating frequency of the antenna are found to be very low. For $\varepsilon_{r\,dr} <$ 30, though the bandwidth is relatively high, the antenna size and operating frequency will be high which is not desirable. Hence DRs with $30 < \varepsilon_{r\,dr} < 60$ are best suited for DRA applications[9], so that a compromise can be made between size, operating frequency and other antenna characteristics.

8.1.1 Bandwidth Enhancement Techniques of DRA

Bandwidth enhancement techniques for DRAs have been addressed by many researchers and have been the most popular and active topic in dielectric resonator antenna research. The various approaches adopted so far can be classified into three broad categories: (i) lowering the inherent radiation Q-factor of the resonator[10,11,12,13,14,15,16,17,18] (ii) using external matching networks and (iii) combining multiple resonators[19,20,21,22,23,24,25].

Several methods for reducing the radiation Q-factor of resonant antenna are available. One of the simplest methods to lower the Q-factor of DRA is by loading the antenna with other stray components. This method has got the advantage that, it will not increase the antenna dimension significantly. However parasitic elements will increase the complexity of the antenna configuration. The radiation Q-factor is related to the dielectric constant of DR, decrease in dielectric constant will cause a decrease in the radiation Q-factor and thus an increase in the bandwidth (See section 1.5.3 of Chapter). However, there is a lower limit on the value of the dielectric constant required to confine fields within the DRA in order to resonate. In addition this technique has got the disadvantage that as the dielectric constant is reduced, the size of the DRA will increase, for a given frequency, which is not desirable with the recent trends of miniaturization. Another simple technique is to use lower dielectric constant substrates. This method has got the disadvantage that, coupling to the antenna may become more difficult with low dielectric constant substrates and may lead to distorted radiation patters. In another approach, it is reported[26] that, a considerable degree of control over the bandwidth can be possible by adjusting the aspect ratio of DRAs. In general the bandwidth does not increase monotonically with the DRA volume. As DRA volume increases, the bandwidth initially decreases to reach a minimum value and then increases with volume. However one can not use very bulky antennas for broadband applications, as it will heavily load the device. The addition of an air gap between the ground plane and the DR was reported to be a simple and viable technique for enhancing the bandwidth of DRA and is advantageous as it does not take up extra real-estate in terms of additional matching network or parasitic element. But the design and fabrication and optimization of

thickness of air gap put additional constrains over the practical use of such antennas. Removal of the central portion of DR results in lowering the effective dielectric constant and hence radiation Q-factor is another promising strategy to increase the bandwidth of DRAs. This annular DRAs offer compact configuration and does not require the use of parasitic elements. However, only probe-fed excitation is the only effective mechanism to energize these DRAs.

Matching networks, such as quarter-wave transformers, matching stubs etc. can be used to increase the bandwidth of a resonant antenna by transforming its input impedance to better match with that of the coupling circuit. These are usually connected externally to the antenna, and are less desirable as they require additional real-estate and will increase the insertion loss to the system, which will degrade the radiation efficiency of the antenna.

Yet another approach to increase the bandwidth of DRAs involves the use of multiple resonant configurations. Employing DRA array with each resonator designed at a somewhat different but adjacent frequency, the antenna can be combined to give a wide band or multi-band operation. The main advantage of this mode of operation is that each resonator can be tuned more or less independently, which allows a great deal of design flexibility. The major disadvantage lies again in the added real-estate required in the array fabrication.

As described in section 1.4.4 of Chapter 1, direct microstrip line excitation of DRA is an attractive configuration, because of its simplicity and it allows the making use of all advantages offered by printed technology for implementing feed distribution network in array fabrication. The problem with feeding DRAs directly by a microstrip line is that, to achieve strong coupling, a DRA of high permittivity is required. Since DRA radiation Q-factor is directly proportional to the $\varepsilon_{r\,dr}$, the bandwidth of these DRAs is typically narrow. For wider band DRAs (with lower permittivity), only a small amount of coupling is achievable between the DR and microstrip line which results in poor radiation efficiency. Hence to overcome these difficulties, in the present work high ε_r dielectric resonators were prepared using $Ca_5Nb_2TiO_{12}$ of $\varepsilon_{r\,dr} = 48$. DRAs were fabricated in cylindrical, elliptical and rectangular geometries. A novel technique of

modifying the geometry of the microstrip feed line into L- and T-shape to increase the bandwidth of single DRA is employed here. The same method has been successfully experimented earlier[27,28] with microstrip patch antennas. This modified geometry excitation technique is advantageous over other conventional methods reported above as it does not need any additional stray elements, matching networks and is devoid of complexity of the antenna system. The experimental results were verified using 3D TLM[29,30,31] methods employing Microstripes 6.5 CAD simulation package[32].

8.2 CYLINDRICAL DIELECTRIC RESONATOR ANTENNAS

8.2.1 Antenna Geometry

The antenna is comprised of low loss $Ca_5Nb_2TiO_{12}$ cylindrical dielectric resonator material of diameter D = 24.15 mm and height H = 6.81 mm. The dielectric resonator material was prepared by conventional solid-state ceramic route as described in section 2.1.2 of Chapter 2. The low-loss $Ca_5Nb_2TiO_{12}$ material has a dielectric constant $\varepsilon_{r\,dr}$ = 48 with a quality factor $Q_u \times f$ > 26000 GHz and low temperature variation of resonant frequency τ_f = 40 ppm/°C (See section 3.3.2 of Chapter 3). The relatively low density (4.06 g/cm^3) of the material ensures lightweight of the antenna configuration.

Microstrip line excited DRA is designed as described in Section 2.4 of chapter 2. Accordingly, the DR is excited directly by a 50Ω microstrip line of width 3 mm, and length S_l = 50 mm, printed on a substrate (glass epoxy) of dielectric constant $\varepsilon_{r\,sub}$ = 4.28, and thickness h =1.6 mm. The geometry of the antenna configuration is shown in Fig. 8.1(a). The position of DR on the etched feed line was optimized to get best resonance with excellent radiation performance, gain and bandwidth. For this, the DR was placed at different positions near and over the feed line by moving along the X and Y directions. Maximum bandwidth with excellent radiation performance was obtained when the DR was placed over the feed line in centrally symmetric position as shown in Fig. 8.1(a). The DR was glued in the optimized position and the glue has negligible effect on the antenna characteristics. All the antenna characteristics were studied after fixing the DR in this position. To probe into the possibility of improving the impedance bandwidth, the conventional microstrip feedline for the excitation of DRs were modified in the form of L

and *T* as depicted in Figs. 8.1 (b) and (c). In the case of *L* and *T*-feed excitations, the arm length S_1 is kept at 50 mm and branch length (S_2) is varied from 0 to 40 mm.

8.2.2. Experimental Results

The simulated electric and magnetic field distributions of resonant mode of microstrip line excited cylindrical DRA at resonance is shown in Fig. 8.2. It is clear from the figure that, the electric field has major variations along the axial direction (*Z*), whereas the magnetic vector forms concentric circles around the axis (See modes and mode nomenclature in Section 1.1.4 of Chapter 1).

From the electric filed distribution, it can be seen that, the field is of transverse magnetic in nature and which have one full wave variation along the azimuthal and radial directions, whereas hardly any field variation along the axial (*Z*) direction. Hence the resonance mode of cylindrical DRA excited with microstrip line mechanism in this investigation is referred as TM_{110}.

The cylindrical DRA was characterized using HP 8510C network analyzer attached with a sweep oscillator and S-parameter test unit as explained Chapter 2, Section 2.5.1 to 2.5.3. The single-strip configuration (simple microstrip line) without any feed branching was tested first. The position of DR on the feed line was optimized for maximum bandwidth. A very good impedance match was obtained when the DR was placed symmetrically over the feed line with its geometric center at the point S_1 = 37 mm as shown in Fig.8.1 (a). A bandwidth of 12 % (2.459 – 2.775 GHz) at 2.625 GHz was obtained as depicted in Fig. 8.3. The simulated values of resonant frequency and impedance bandwidth agree very well with experimental results as is evident from the figure.

To study the effect of antenna characteristics with the modification in feed line geometry, two separate feed line shapes were tried. Microstrip lines in L [See Fig. 8.1 (b)] and T [Fig. 8.1 (c)] shapes with 50 Ω characteristic impedance were printed over the same substrate material. The position of DR on the feed line for maximum impedance match was optimized. It was observed that, optimum coupling of electromagnetic energy occurred when the DR was kept at the point of intersection of S_1 and S_2 as shown in Fig.

8.1 (b) and (c). To investigate the effect of feed length segment over the DRA properties, L- and T- feed lines of fixed arm length (S_1) and varying branch length (S_2) were fabricated on the same substrate material.

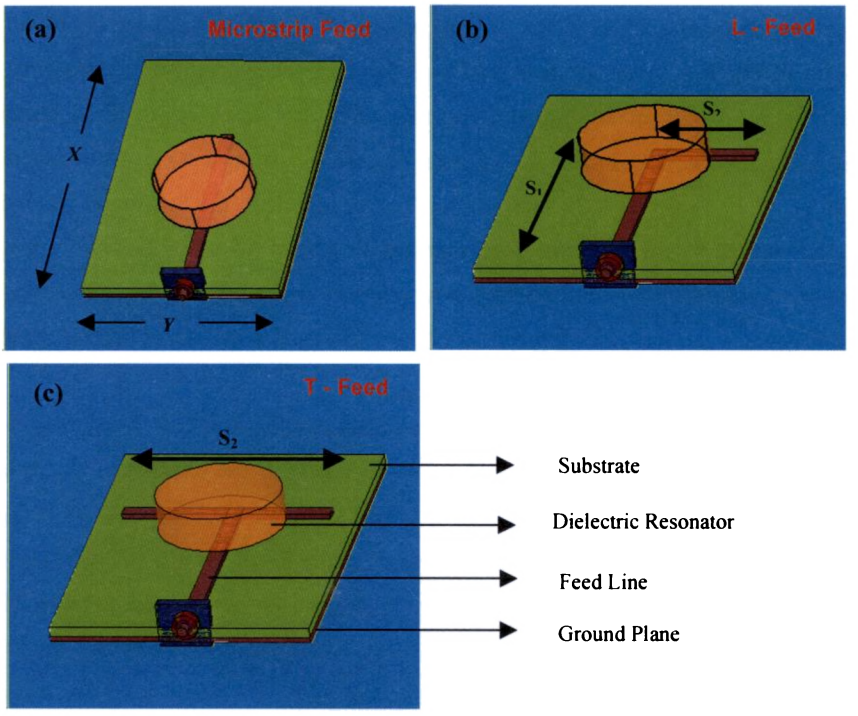

Fig. 8.1 Geometry of cylindrical DRA with conventional and geometry modified microstrip line excitations

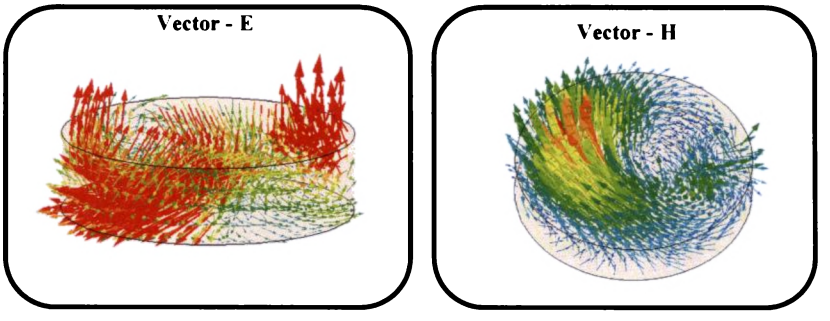

Fig. 8.2 Electric and magnetic field distributions of cylindrical DRA at resonance

The length of the straight feed (arm length, S_1) was fixed at 50 mm and feed segment length was varied from 0 – 40 mm in both the geometries. In all the cases the DR was placed over the feed line in the optimized position. The resonant frequency and percentage bandwidth of the DRA was measured in each case and the variations are depicted in Fig. 8.4. It can be seen that with the L-and T-shaped feed geometries, the percentage bandwidth of the antenna increases with the branch length up to a certain value and then decreases. For L-fed antenna, the percentage bandwidth reaches a maximum of 19 % for S_2 = 30 mm and for T-feed geometry, the maximum bandwidth obtained was 26 % for the same feed segment length (at 30 mm). L- and T- shaped microstrip lines with the optimum branch length was used to excite the cylindrical DR and the antenna parameters were measured after fixing DR on the optimized position with this geometry.

The resonant frequency and impedance bandwidth of L-and T-fed cylindrical DRAs are shown in Fig. 8.3. It can be seen that with L-fed excitation, the antenna resonates at a frequency of 2.68 GHz (2.545 - 3.04 GHz) with a bandwidth of 19 %. In the case of T-fed DRA, the operating frequency varies from 2.4 - 3.075 GHz (centre frequency at 2.6 GHz) and percentage bandwidth shows a further increase to reach 26 %. In both cases the experimental resonant frequencies and impedance bandwidth was found to be in excellent agreement with simulated values. It is evident that, the resonant frequency shifts to lower frequencies in the L-fed antenna, while increases with T-fed DRA when compared with the original simple microstrip line excitation. It is noteworthy that, with the branching of feed line geometry, the operating bandwidth of the antenna increases. The enhancement of bandwidth with feedline branching is believed to be due to the combined radiation from the DR and that from the non conventional discontinuous feedline.

Fig. 8.5 shows a convenient method of representing the input impedance of the antenna. Polar representation of the calculated input impedance of the antenna at the resonant frequency is given in the SMITH chart. The loci of the points are within the 2:1 VSWR value indicating an impedance matching. In all the three cases, maximum coupling between the feed line and antenna can be confirmed from the figure.

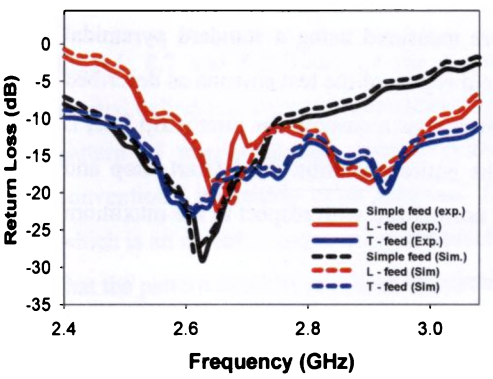

Fig. 8.3 Experimental and simulated return loss of simple, L and T- microstrip line fed cylindrical DRA

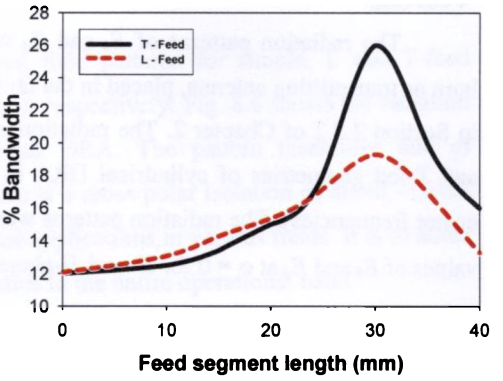

Fig. 8.4 variation of % bandwidth with arm length of L and T- microstrip line fed cylindrical DRA

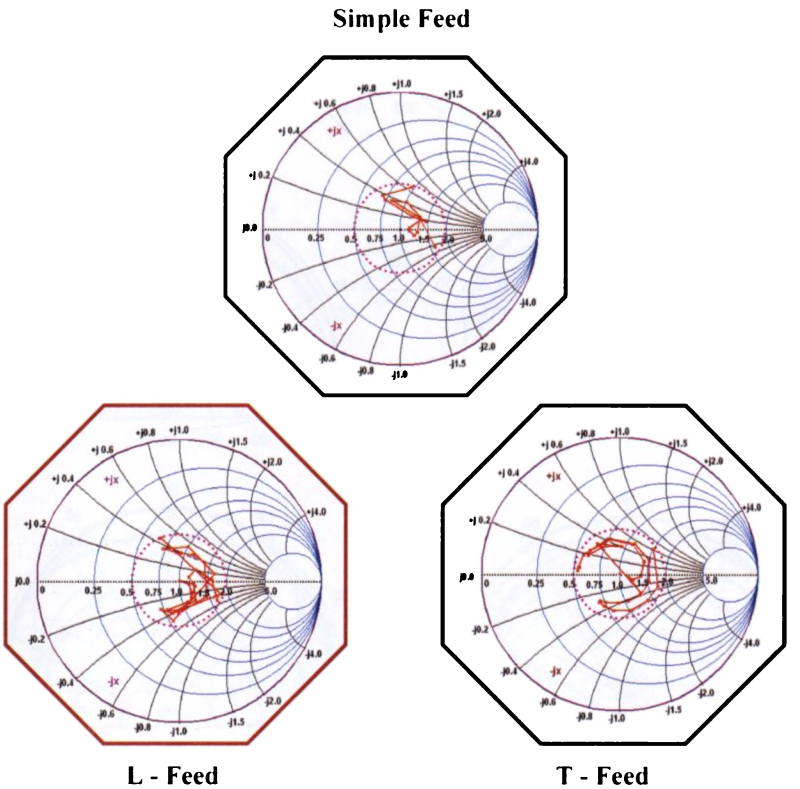

Fig. 8.5 Smith chart representation of input impedance of simple, L and T- microstrip line fed cylindrical DRA
$\varepsilon_{r\,dr}$ = 48, D = 24.15mm, H = 6.81 mm

The radiation patterns of E_θ and E_ϕ were measured using a standard pyramidal horn as transmitting antenna, placed in the far field region of the test antenna as described in Section 2.5.2 of Chapter 2. The radiation pattern was measured for microstrip line, L and T-fed geometries of cylindrical DRA in the entire operation band (start, stop and center frequencies). The radiation patterns were normalized with respect to the maximum values of E_θ and E_ϕ at $\varphi = 0$ for E- and H-planes.

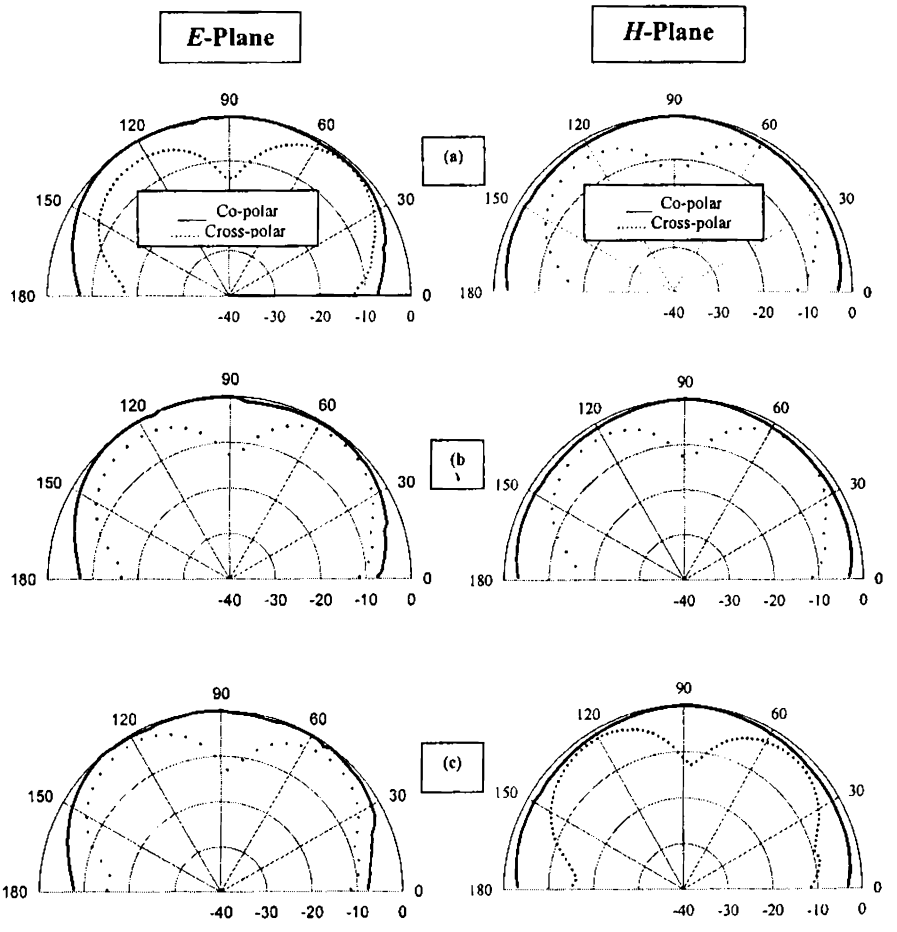

Fig. 8.6 Radiation pattern of microstrip line excited cylindrical DRA
(a) Start frequency (b) Centre frequency (c) Stop frequency
$\varepsilon_{r\,dr} = 48$, $D = 24.15$mm, $H = 6.81$ mm

Fig.8.6, 8.7 and 8.8 illustrates the measured field patterns for simple, L and T-feed excited cylindrical dielectric resonator antennas respectively. Fig. 8.6 shows the radiation pattern of microstrip line excited cylindrical DRA. The pattern resembles that of conventional microstrip patch antennas. There is a cross polar isolation of about –15 dB which is an essential requirement for practical applications in various fields. It is to noted that the pattern exhibits excellent characteristics in the entire operational band.

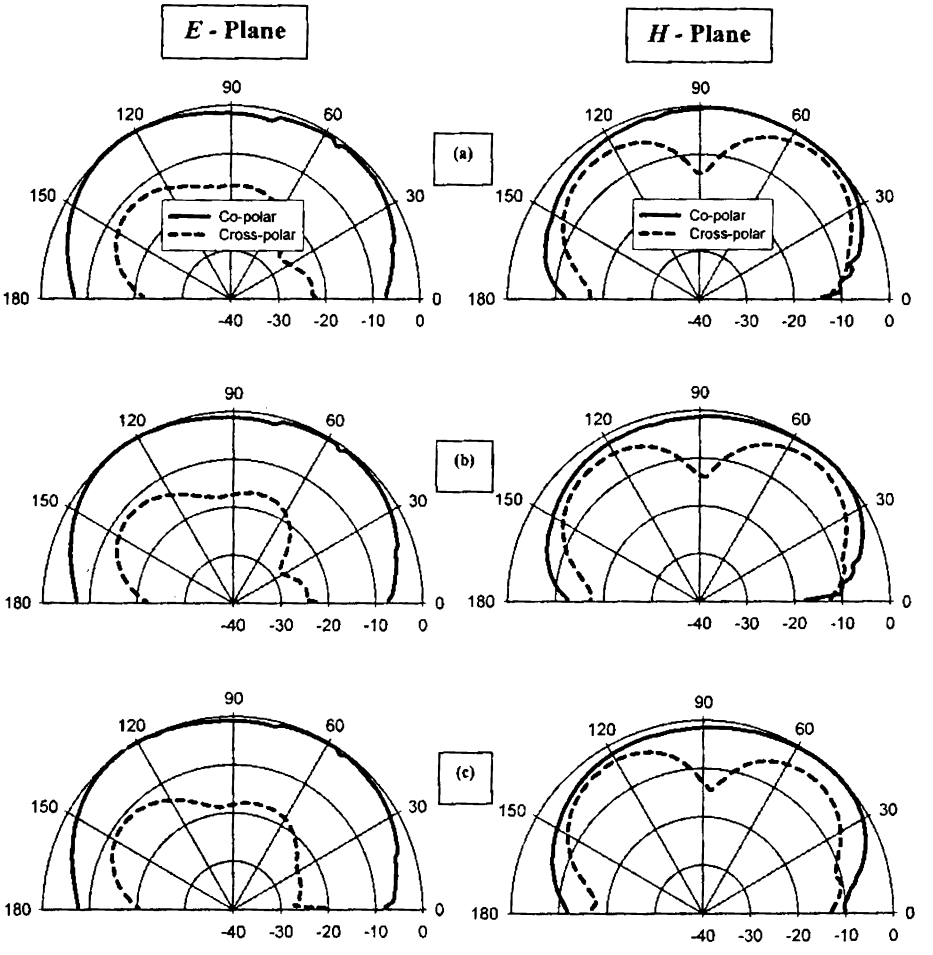

Fig. 8.7 Radiation pattern of L-strip excited cylindrical DRA
(a) Start frequency (b) Centre frequency (c) Stop frequency
$\varepsilon_{r\,dr}$ = 48, D = 24.15mm, H = 6.81 mm

Fig. 8.7 depicts the radiation patterns of L-strip fed cylindrical DRA. It is to be noted that the cross-polar pattern is slightly different in both *E* and *H*-field patterns. Though some scalloping and roll-off can be observed in the cross-polar pattern of *E*-field, the cross-polar isolation in this case is better than -20 dB, whereas that in *H*-field it is about -15 dB. The slight difference in the appearance of the patterns could be due to the asymmetrical feed structure.

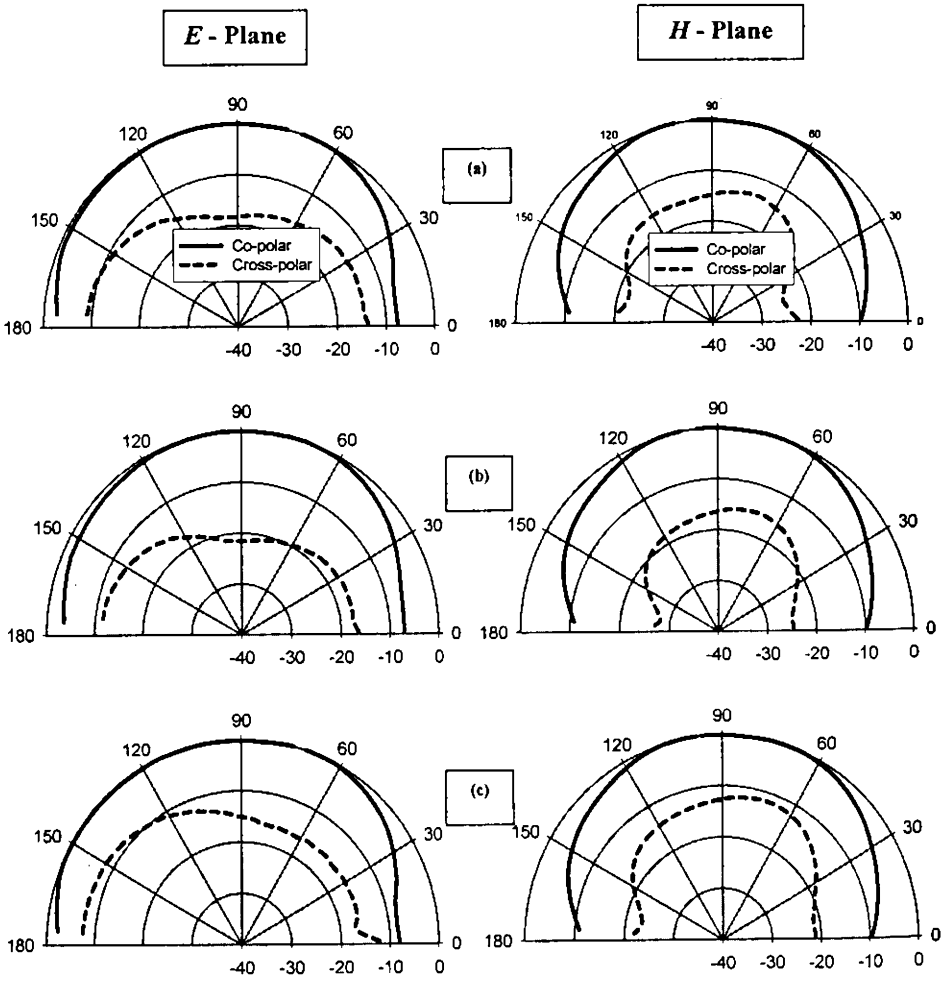

Fig. 8.8 Radiation pattern of T-strip excited cylindrical DRA
(a) Start frequency (b) Centre frequency (c) Stop frequency
$\varepsilon_{r\,dr}$ = 48, *D* = 24.15mm, *H* = 6.81 mm

The *E* and *H*-field radiation patterns of T-fed cylindrical DRA is depicted in Fig. 8.8. In this case, the cross-polar isolation is better than that observed in microstrip line and L-fed antennas and is more than -20 dB, which makes this antenna highly suitable for applications where high polarization is required. A significant change in the radiation patterns can also be observed with variation in feed line geometry. Moreover, the pattern symmetry is affected by the finite thickness of ground plane used.

The gain of the fabricated cylindrical DRAs were calculated using the same pyramidal horn used for the far field radiation measurements (See Chapter 2, Section 2.5.3). It was observed that at the centre of the operating band, microstrip line excited DRA has a gain of 8.2 dBi, L-strip excited DRA has 9.5 dBi and T-fed antenna has 7.9 dBi. The gain of the antenna was found to be maximum for L-feed and minimum for T-fed DRAs. The measured parameters of the investigated cylindrical DRAs are summarized in Table 8.1. It is to be noted that the gain and HPBW referred in the Table are those measured at the centre frequency of the operation band of the DRAs.

Table 8.1 Resonant frequency, bandwidth, gain and half power beam width of Microstrip line, L- and T-fed cylindrical DRAs

Feed Geometry	Resonant Frequency (GHz)	Operating Band (GHz)	2:1 VSWR Bandwidth (%)	Gain (dBi)	HPBW (E-plane) (Degrees)	HPBW (H-plane) (Degrees)
Simple Feed	2.625	2.459 - 2.775	12.00	8.2	120	100
L - Feed	2.680	2.545 - 3.040	19.00	9.5	120	105
T - Feed	2.600	2.400 - 3.075	26.00	7.9	115	95

As is evident from the table, with simple microstrip line excitation the antenna resonate at 2.625 GHZ, whereas that for L is higher and T-is lesser than that of simple feed energized DRAs. The bandwidth exhibits a direct proportionality with feedline branching. A maximum of 26 % at 2.6 GHz was obtained for T-fed cylindrical DRAs. It can also be observed that the gain is high for L-fed antenna compared with conventional microstrip line and T-feeding. The half power beam width of the antenna calculated from the

radiation patters are also tabulated in Table 8.1. As expected, the gain of the antenna varied inversely with HPBW. The measured gain and bandwidth was found to be better than that reported[33,34,35,36] for cylindrical DRAs even with low dielectric constant DRs. It is also worth to mention that, independent of the geometry of microstrip feed line, employed here, the gain and bandwidth of cylindrical DRA is reasonably high when compared with that of conventional patch antennas.

8.3 ELLIPTICAL DIELECTRIC RESONATOR ANTENNAS

8.3.1 Antenna Geometry

Elliptical[9] DRA geometry has not been investigated in detail because of the complexity involved in the DR fabrication, mode analysis etc. The elliptical antenna configurations considered in the present study are shown in Fig.8.9 (a), (b) and (c). The geometry comprises an elliptical dielectric disk resonator of $Ca_5Nb_2TiO_{12}$ material synthesized by conventional solid state ceramic route. The DR of relative permittivity $\varepsilon_{r\,dr}$ = 48, major axis dimension $2a$ = 33 mm, minor axis $2b$ = 27 mm and height H = 11.5 mm is energized by microstrip line methods. In Figure 8.9 (a), the DR is electromagnetically coupled with a 50 Ω microstrip feed line of width 3 mm and length S_1 = 50 mm, fabricated on a substrate of dielectric constant $\varepsilon_{r\,sub}$ = 4.28 and thickness h = 1.6 mm backed by a conducting plane. The geometry of the microstrip line is modified into L and T-shapes as shown in Fig. 8.9(b) and 8.9(c) to study its effect on the antenna characteristics of DR. As shown in Fig.8.9 (b), L-shaped microstrip lines with feed length S_1 fixed at 50 mm and branch segment lengths S_2 of 0 – 40 mm were fabricated on the same substrate. Similarly T-shaped microstrip lines of various arm lengths were also fabricated as shown in Fig.8.9 (c).

8.3.2 Experimental Results

Fig. 8.10 shows the simulated electric and magnetic field distributions of an elliptical DRA at its resonant frequency. It can be seen from the figure that, the electric vector has major field variations along the axial direction (Z), whereas the magnetic vector forms concentric circles around the axis as in the case of cylindrical DRA (See

modes and mode nomenclature in Section 1.1.4 of Chapter 1). From the electric field distribution pattern, it can be seen that, the field is of transverse magnetic in nature and which have one full wave variation along the azimuthal and radial directions, whereas the

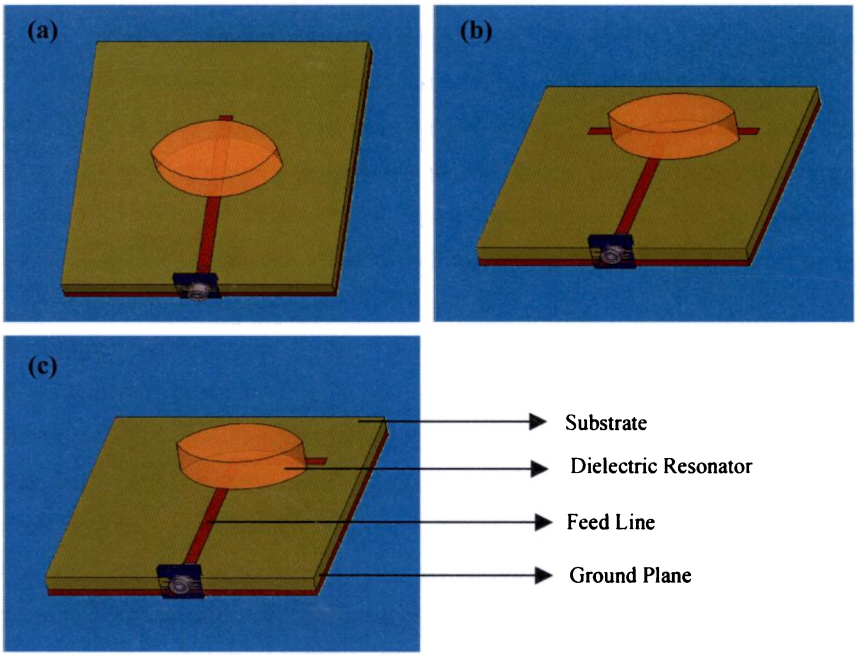

Fig. 8.9 Geometry of elliptical DRA with conventional and geometry modified microstrip line excitations

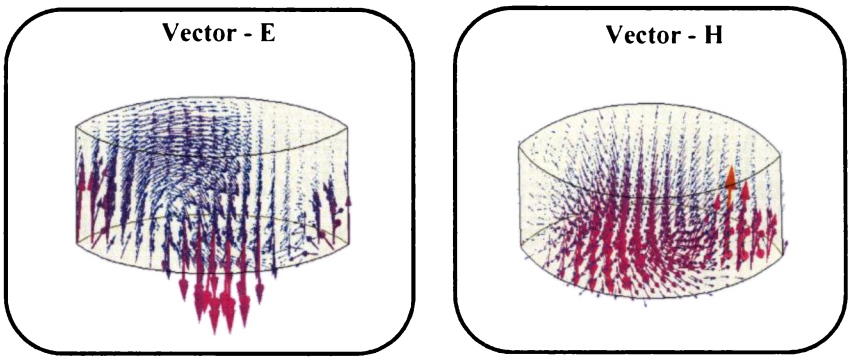

Fig. 8.10 Electric and magnetic field distributions of elliptical DRA at resonance

field variation along the axial (Z) direction is less than half a wavelength. Hence the resonance mode of cylindrical DRA excited with microstrip line mechanism, in this investigation is referred as $TM_{11\delta}$. The field distribution is compared with that described by Luk *et al.*[26] and confirmed the identity of the observed mode.

The elliptical DRA was characterized as explained in Chapter 2, Section 2.5.1 to 2.5.3. The single-strip configuration (simple microstrip line) without any feed branching was tested first. The position of DR on the feed line was optimized for maximum bandwidth. A very good impedance match was obtained when the DR was placed symmetrically with its major axis perpendicular to the feed line and its geometric center at the point S_1 = 35 mm as shown in Fig.8.9 (a). A bandwidth of 10 % (1.76 – 1.945 GHz) at 1.85 GHz was obtained as depicted in Fig.8.11. Based on the single strip design, the simple microstrip feed line was branched into L and T-shapes as shown in Fig. 8.9 (b) and 8.9 (c). The feed length S_1 is fixed at 50 mm and segment length S_2 is varied from 0 to 40 mm. The segment length S_2 was optimized for maximum impedance bandwidth.

The percentage bandwidth of elliptical DRA excited with L-shaped microstrip line increases with feed segment length, reaches a maximum when S_2 = 35 mm and then decreases gradually as shown in Fig.8.12. Similarly for T-shape feed geometry the bandwidth shows a maximum value for S_2 = 30 mm as is evident from Fig.8.12. For both the geometries, the antenna has maximum impedance bandwidth when the DR was fixed with its geometric center at the junction of the feed line (S_1 = 50 mm and S_2 = 0 mm).

The return loss characteristics of elliptical DRA excited using L and T-shaped strip line mechanisms are plotted in Fig.8.11. With L-shape feed excitation, the antenna resonates at 1.9 GHz with an operation bandwidth of 230 MHz (1.81 – 2.04 GHz, 12.11%). In the case of elliptical DRA energized with T-shape feed line, the bandwidth is 325 MHz (2.075 – 2.40 GHz, 14.77%) at 2.2 GHz. It is noteworthy that, the resonant frequency as well as percentage bandwidth increases with branching of the feed line geometry in elliptical DRA as that observed in cylindrical DRAs.

The SMITH chart representation of the input impedance of microstrip line, L-and T-fed elliptical DRAs are shown in Fig. 8.13. It is evident that, the curve lies well within

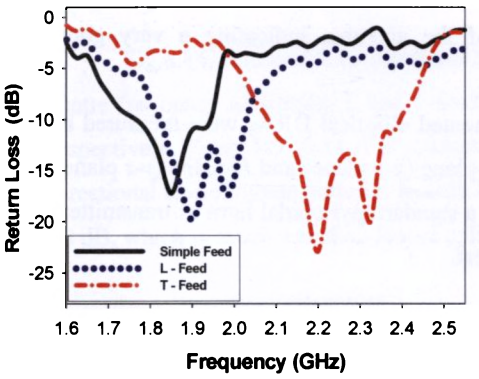

Fig. 8.11 Experimental and simulated return loss of simple, L and T- microstrip line fed elliptical DRA

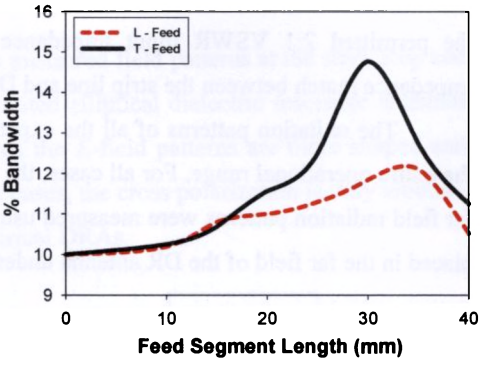

Fig. 8.12 variation of % bandwidth with arm length of L and T- microstrip line fed elliptical DRA

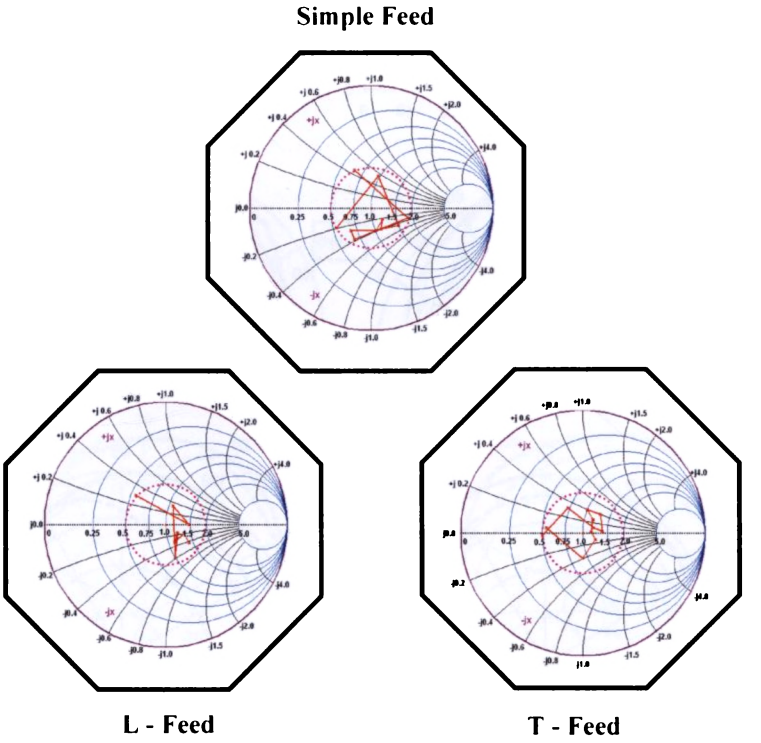

Fig. 8.13 Smith chart representation of input impedance of simple, L and T- microstrip line fed elliptical DRA
$\varepsilon_{r\,dr}$ = 48, $2a$ = 33mm, $2b$ = 27mm, H = 11.5mm

the permitted 2:1 VSWR input impedance of the antenna, indicating a very good impedance match between the strip line and DR.

The radiation patterns of all the experimented elliptical DRAs were measured in the entire operational range. For all cases, the *E*-plane (*x*-*y* plane) and *H*-plane (*y*-*z* plane) far field radiation patterns were measured using a standard pyramidal horn as transmitter, placed in the far field of the DR antenna under test.

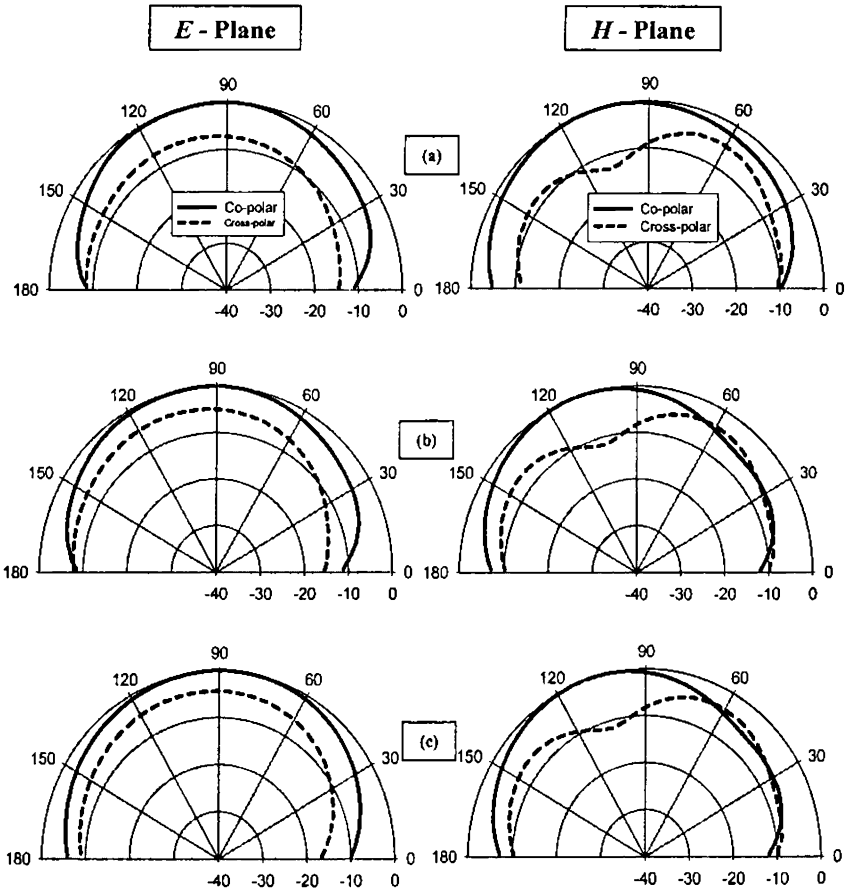

Fig. 8.14 Radiation pattern of microstrip line excited elliptical DRA
(a) Start frequency (b) Centre frequency (c) Stop frequency
ε_r dr = 48, $2a$ = 33mm, $2b$ = 27mm, H = 11.5mm

Fig.8.14, 8.15 and 8.16 illustrates the measured field patterns at the start, stop and centre frequency of simple, L and T-feed excited elliptical dielectric resonator antennas respectively. From Fig. 8.14 it is evident that the *E*-field patterns are more shaped and directional than *H*-plane patterns. In both the cases, the cross polarization is only around -10 dB, which is much less than that of cylindrical DRAs.

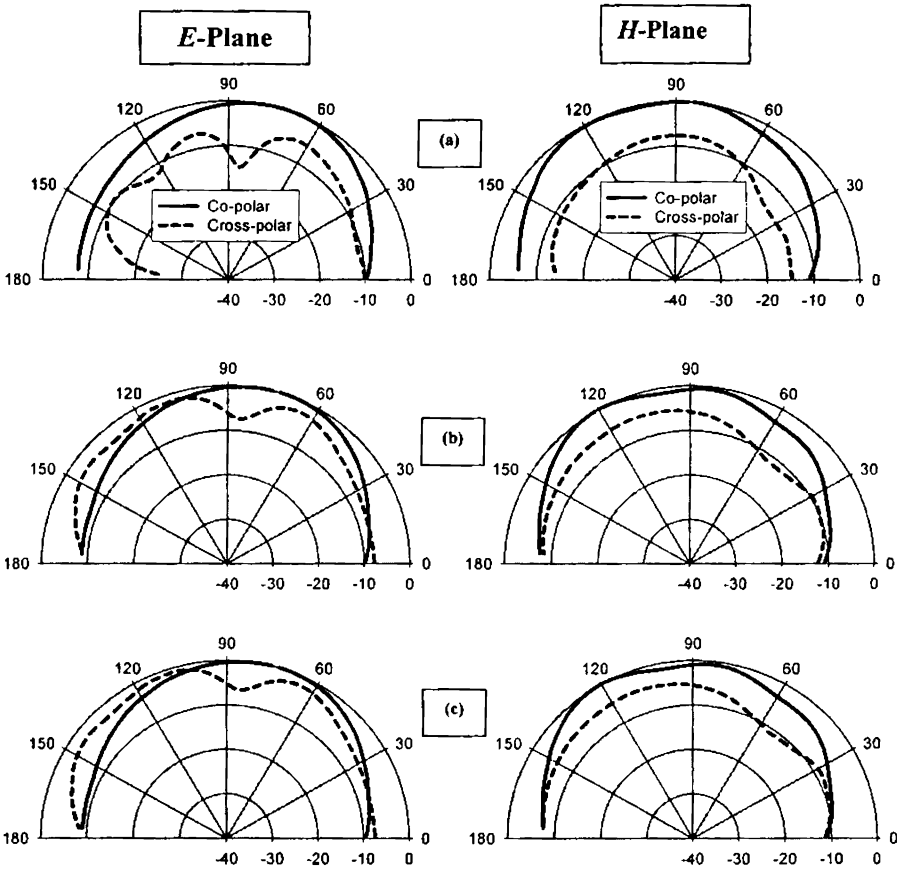

Fig. 8.15 Radiation pattern of L-strip line excited elliptical DRA
(a) Start frequency (b) Centre frequency (c) Stop frequency
ε_r dr = 48, $2a$ = 33mm, $2b$ = 27mm, H = 11.5mm

Fig. 8.15 depicts the field patterns for L-strip elliptical DRA. In this case the pattern becomes more symmetric for H-field where as better isolation occurs for E-field. The polarization discrimination is better than -15dB, which is more than that of elliptical microstrip line DRA, but still less than that of their cylindrical analogue.

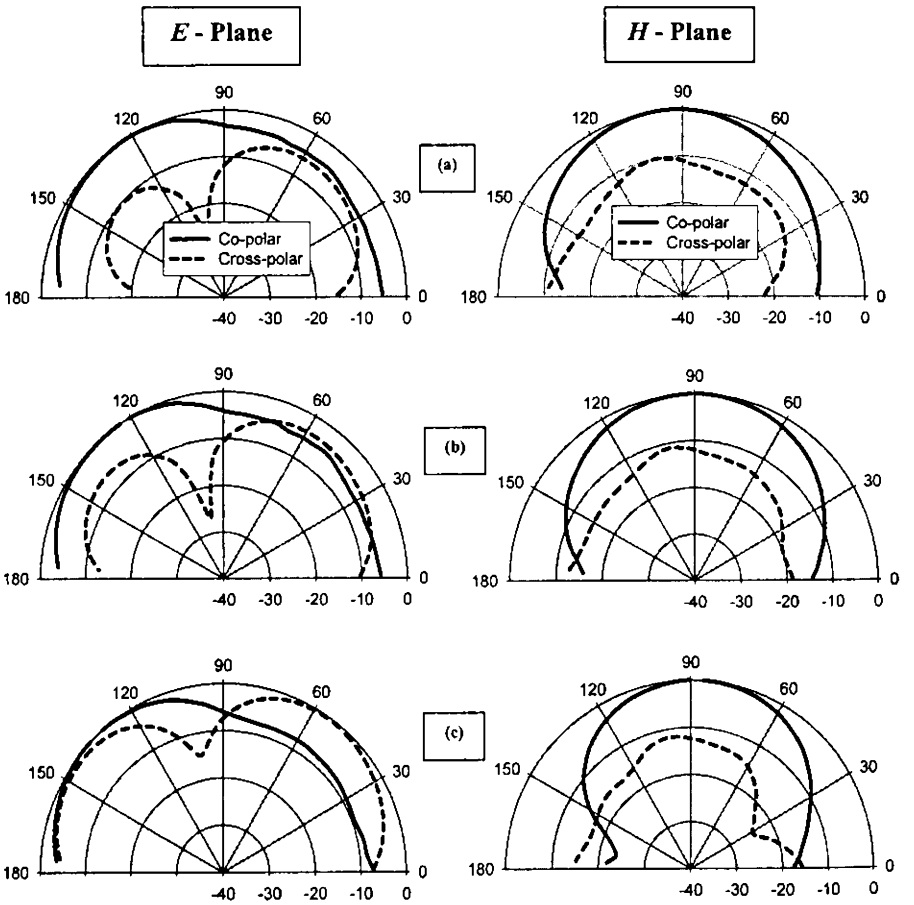

Fig. 8.16 Radiation pattern of T-strip line excited elliptical DRA
(a) Start frequency (b) Centre frequency (c) Stop frequency
ε_r dr = 48, $2a$ = 33mm, $2b$ = 27mm, H = 11.5mm

The far field radiation patterns of elliptical DRA excited using T-shaped microstrip line mechanism is shown in Fig. 8.16. It is interesting to note that, the cross-polar isolation increases in the *E*-plane pattern to reach more than -25 dB, which is highly desirable for communication antennas. However the pattern is more symmetric in the *H*-plane, though the cross-polarization is lesser.

With all types of feed geometry, the co-polar pattern is broad and almost omnidirectional both in *E* and *H*-planes. In all cases the cross-polar isolation is only about -10 to -15 dB, which is less than that of conventional antennas and other DRA geometries. The ripple appeared in the radiation pattern as well as the discrepancy at small elevation angles are due to the finite size of the ground planes used. One should also note that the symmetry of the radiation pattern depends on the symmetry of geometry of DR, feed line and the position of DR over the feed line. Hence it is evident that the radiation pattern becomes more symmetric for cylindrical DRA than for elliptical one. Also the pattern became more symmetric for microstrip line feed compared with L- and T-shapes for both cylindrical and elliptical DRA. The same receiving antenna as that used for the radiation pattern measurement was used to calculate the gain at several distances away from DRA under test. The comparative gain and other experimental results of elliptical DRA energized with various geometries of microstrip line feed techniques are summarized in Table 8.2.

Table 8.2 Resonant frequency, bandwidth, gain and half power beam width of Microstrip line, L- and T-fed elliptical DRAs

Feed Geometry	Resonant Frequency (GHz)	Operating Band (GHz)	2:1 VSWR Bandwidth (%)	Gain (dBi)	HPBW (E-plane) (Degrees)	HPBW (H-plane) (Degrees)
Simple Feed	1.85	1.760 - 1.945	10.00	8.0	115	90
L - Feed	1.90	1.810 - 2.040	12.11	9.2	110	85
T - Feed	2.20	2.075 - 2.400	14.77	6.5	120	100

As is evident from the Table, with simple microstrip line excitation the gain of the antenna is about 8 dBi, whereas that for L and T-feed energized DRAs are 9.2 dBi and 6.5 dBi respectively. The half power beam width (HPBW) of elliptical DRA excited using simple feed is 115° in the *E*-plane and 90° in *H*-plane whereas that in the case of L and T-feed antennas are 110° & 85° and 120° & 100° in the *E* and *H*-planes respectively. As expected the gain of the antenna varied inversely with HPBW. The measured gain was found to be better than that reported in many other broadband DRAs. However it is to be noted that for the same ε_r the impedance bandwidth is higher for cylindrical DRA compared with that for elliptical DRA. It is worth to mention that, independent of the geometry of microstrip feed line employed here, the gain and bandwidth of elliptical DRA is reasonably high when compared with that of conventional patch antennas.

8.4 RECTANGULAR DIELECTRIC RESONATOR ANTENNAS

8.4.1 Antenna Geometry

The rectangular DRA is more difficult to analyze than cylindrical one because of the increase in edge shaped boundaries[37,38,39]. At the same time, rectangular DRA is more versatile as it has got more degrees of freedom than cylindrical and elliptical geometries. For any given resonant frequency and fixed dielectric constant, the three dimensions of rectangular DRA can be chosen independently, where as cylindrical and elliptical DRA has got only one and two dimensions respectively.

The configuration of Microstrip line, L-and T-strip excited rectangular DRAs are shown in Fig. 8.17. High dielectric constant, low loss $Ca_5Nb_2TiO_{12}$ ceramic dielectric resonator material, which used for the fabrication of cylindrical and elliptical DRAs was used for the formulation of rectangular DRA also. The microwave dielectric properties of the material are described in section 3.3 of Chapter 3. A rectangular DR of $Ca_5Nb_2TiO_{12}$ material with length l = 22.50 mm, breadth b = 11.90 mm and height h = 5.55 mm was prepared by solid state ceramic route. The DR was energized by a conventional 50 Ω microstrip line of width 3 mm, extends a length of S_l = 50 mm printed on a substrate of thickness h = 1.6 mm and dielectric constant $\varepsilon_{r\,sub}$ = 4.28. The position of DR on the feed line was optimized to provide best coupling between microstrip line and rectangular DR

and hence maximum matching at the desired frequency. Excellent matching was observed when the DR was placed symmetrically over the feed line at the point where S_1 = 45 mm with its length perpendicular to the length of feed line See Fig. 8.17 (a).

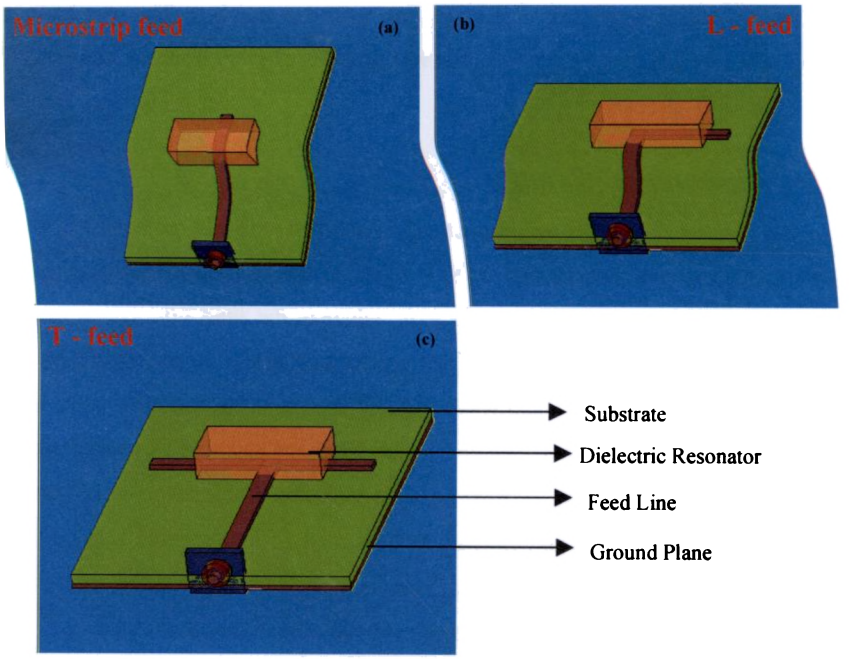

Fig. 8.17 Geometry of rectangular DRA with conventional and geometry modified microstrip line excitations

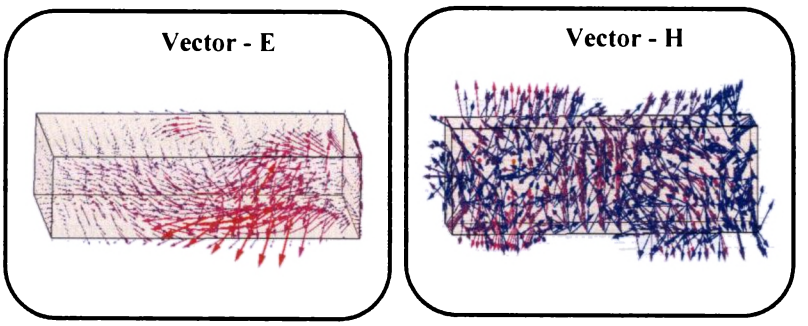

Fig. 8.18 Electric and magnetic field distributions of rectangular DRA at resonance

To study the effect of L-and T-feed excitation methods, microstrip lines of S_1 fixed at 50 mm and arm lengths S_2 varying from 0 – 40 mm were fabricated in the desired shape. For optimum arm length and position on the feed line for maximum coupling and bandwidth, the DR was glued to the substrate over the feed line. The glue had negligible effect on the frequency of operation, but was found to slightly improve coupling.

8.4.2 Experimental Results

The simulated electric and magnetic field distributions of a rectangular DRA at its resonant frequency is shown in Fig. 8.18. It is evident from the figure that, the electric field forms concentric circles around the axis, whereas the magnetic vector has major variations along the axial direction (*Z*) (See modes and mode nomenclature in section 1.1.4 of Chapter 1). From the electric filed distribution pattern, it can be seen that, the field is of transverse electric in nature and which have one full wave variation along the azimuthal and radial directions, whereas no field variation along the axial (*Z*) direction. Hence the resonance mode of rectangular DRA excited with microstrip line mechanism in this investigation is referred as TE_{110}. This field distribution is compared with that reported by Luk *et al.*[26] and confirmed the correctness of the identified mode.

The variation of percentage bandwidth with arm length of L-and T-fed rectangular DRA is illustrated in Fig. 8.19. The bandwidth increases initially with arm length, reaches a maximum at S_2 = 35 mm for L- and 30 mm for T-fed DRAs and then decreases. This is taken as the optimum feed length dimension and all the antenna characteristics were measured after fixing DR over the feed line in the optimized position. The experimental and simulated return loss of simple, L- and T-shaped microstrip line excited rectangular DRA is shown in Fig. 8.20. With simple microstrip line excitation, the antenna resonates at 3.115 GHz with a percentage impedance bandwidth of 14.9 (2.995 - 3.45 GHz). The simulated resonant frequency is slightly less than that of experimental value but both are in agreement within experimental error. With L-feed excitation the resonant frequency shifts to low values to reach 2.9 GHz, but with an enhancement of bandwidth to reach 17.6 % (2.69 - 3.20 GHz). As is evident from Fig.

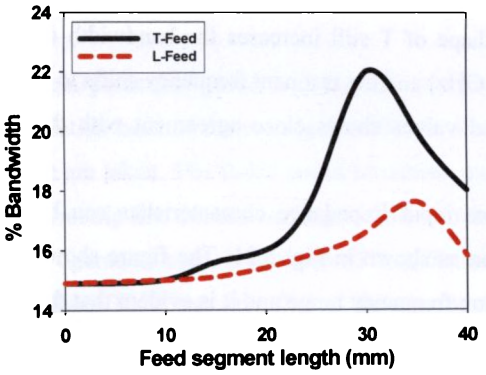

Fig. 8.19 variation of % bandwidth with arm length of L and T- microstrip line fed rectangular DRA

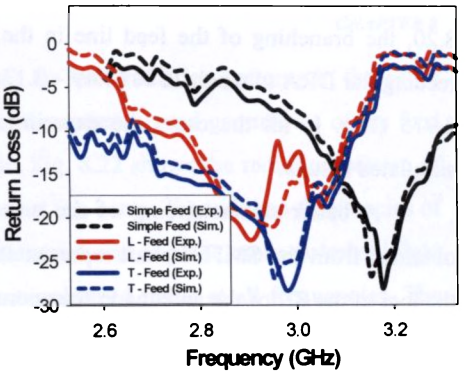

Fig. 8.20 Experimental and simulated return loss of simple, L and T- microstrip line fed rectangular DRA

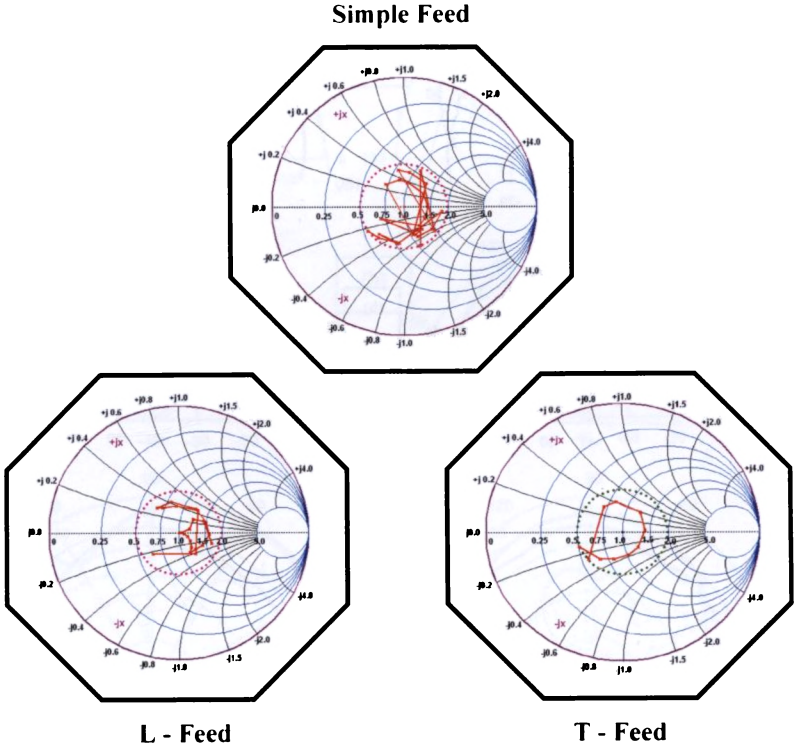

Fig. 8.21 Smith chart representation of input impedance of simple, L and T- microstrip line fed rectangular DRA
$\varepsilon_{r\,dr} = 48$, $l = 22.50$mm, $b = 11.90$mm, $h = 5.55$mm

8.20, the branching of the feed line in the shape of T still increases the bandwidth of rectangular DRA to reach 22 % (2.49 – 3.125 GHz) and the resonant frequency shifts to 2.975 GHz. In all the cases the experimental values shows close agreement with the simulated results.

A better understanding of the antenna input impedance characteristics can be obtained from the SMITH chart representation as shown in Fig. 8.21. The figure shows the loci of the S_{11} of the antenna in the operation frequency range and it is evident that the curve lies well within the 2:1 VSWR input impedance represented in SMITH chart and hence confirms a very good impedance match between the strip line and DR.

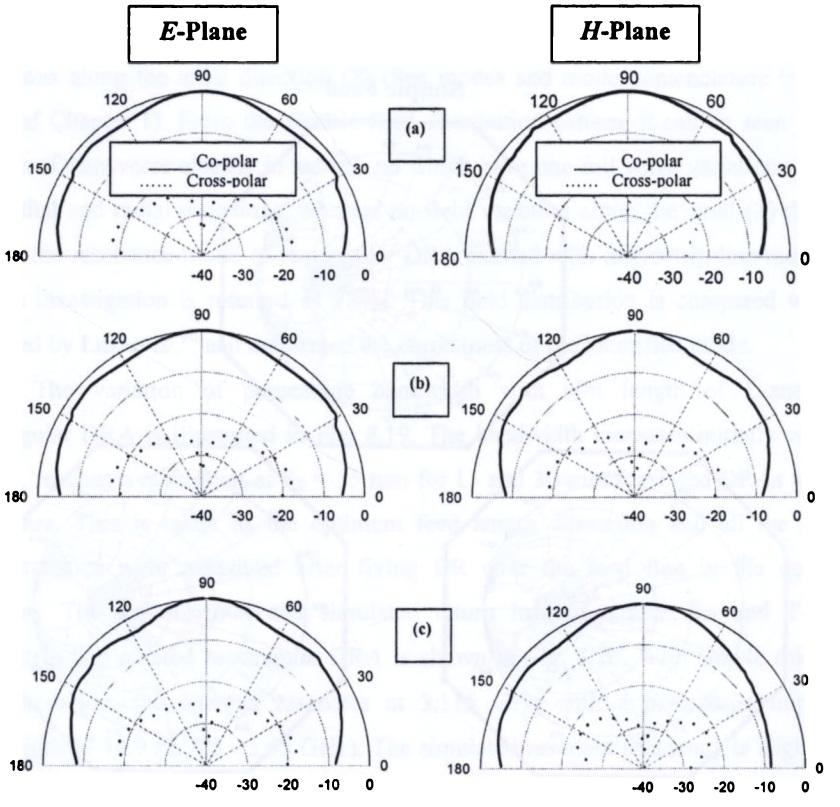

Fig. 8.22 Radiation pattern of microstrip line excited rectangular DRA
(a) Start frequency (b) Centre frequency (c) Stop frequency
$\varepsilon_{r\,dr} = 48$, $l = 22.50$mm, $b = 11.90$mm, $h = 5.55$mm

The *E*-plane (*x*-*y* plane) and *H*-plane (*y*-*z* plane) far field radiation patterns in the entire radiation band of the rectangular DRAs with all the experimented geometries of the feed line are taken. The fields are of broadside mode. Fig. 8.22 shows the radiation pattern of microstrip line excited rectangular DRA in the start (a), centre (b) and stop frequencies of the operation band. It is observed that, the maximum *E* and *H*-plane cross-polarized field is about 30dB less than that of the maximum co-polarized fields at all frequencies. The patterns are symmetric and resemble that of a microstrip patch antenna.

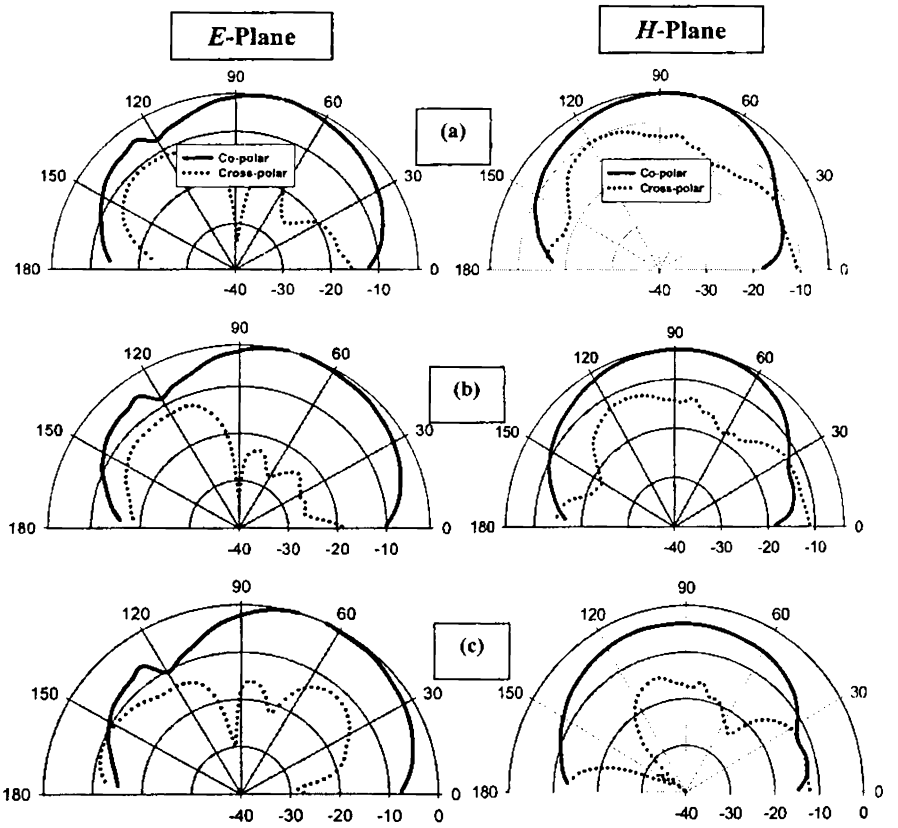

Fig. 8.23 Radiation pattern of L-strip line excited rectangular DRA (b) Start frequency (b) Centre frequency (c) Stop frequency $\varepsilon_{r\,dr} = 48$, $l = 22.50$mm, $b = 11.90$mm, $h = 5.55$mm

The radiation pattern of L-fed rectangular DRA is depicted in Fig. 8.23. It is evident from the figure that, the symmetry of the pattern is highly disturbed and the cross-polar isolation decreased with asymmetric feeding mechanism. The cross-polar isolation in *E*-plane is about -30dB whereas its magnitude significantly reduces in the *H*-field to reach about -15 dB.

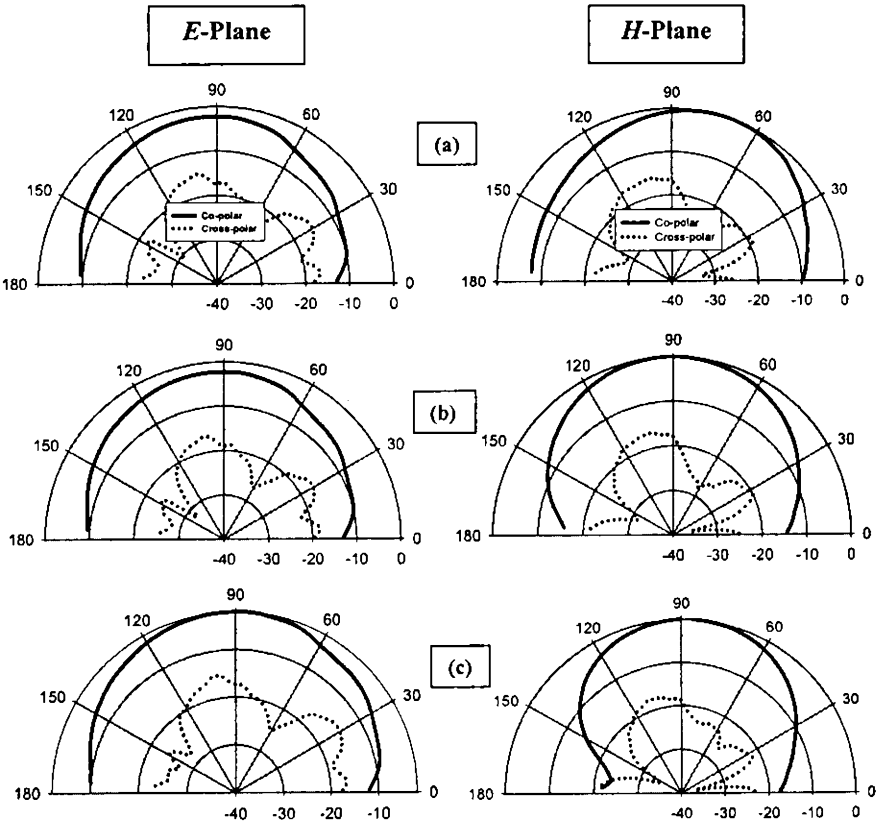

Fig. 8.24 Radiation pattern of T-strip line excited rectangular DRA
(c) Start frequency (b) Centre frequency (c) Stop frequency
$\varepsilon_{r\,dr} = 48$, $l = 22.50$mm, $b = 11.90$mm, $h = 5.55$mm

The radiation performance of T-shape microstrip line excited rectangular DRA is shown in Fig. 8.24. It is readily readable from the figure that, T-fed excitation still badly affected the pattern symmetry compared with simple microstrip line and L-shaped feed mechanisms. The cross-polarization levels in the radiation patterns remained about -20dB in both the *E*- and *H*-planes, while the cross polar patterns were found to have side lobes in either cases.

The gain of rectangular DRA energized using different feeding methods were measured in the transmission mode at their resonant frequency. It was observed that the gain value was higher for L-fed rectangular DRA compared with simple microstrip line and T-fed geometries. The HPBW of the antenna geometry was calculated from the radiation pattern at the centre frequency. The gains of the antennas were also measured at the resonant frequency. The characteristics of rectangular DRA with the experimented feed line geometries are given in Table 8.3.

Table 8.3 Resonant frequency, bandwidth, gain and half power beam width of Microstrip line, L- and T-fed rectangular DRAs

Feed Geometry	Resonant Frequency (GHz)	Operating Band (GHz)	2:1 VSWR Bandwidth (%)	Gain (dBi)	HPBW (E-plane) (Degrees)	HPBW (H-plane) (Degrees)
Simple Feed	3.115	2.995 - 3.450	14.9	8.8	120	100
L - Feed	2.900	2.690 - 3.200	17.6	10.0	110	85
T - Feed	2.975	2.490 - 3.125	22.0	9.0	120	100

It can be seen from the Table 8.3 that, the percentage bandwidth increases with branching of the feed line. The gain of the antenna is 8.8 dBi for microstrip line and increases to 10 and 9 dBi for L- and T-fed antennas. The least value of HPBW implies better gain. Simple microstrip line fed rectangular DRA has a HPBW of 120 & 100° at *E*- and *H*-planes respectively. At the same time the values are 110 & 85 and 120 & 100 for L- and T-fed geometries.

In cylindrical, elliptical and rectangular DRAs excited with microstrip line, L-and T-feed, certain general observations were made. In all the investigated geometries of DRA, the bandwidth is increased with branching of the feed line. In all cases, the experimental resonant frequency and bandwidth was higher than that obtained by simulation. In all microstrip line excitation mechanisms, a thin layer will be trapped between the DR and feed line. This will decrease the effective dielectric constant and hence the resonant frequency will be shifted towards higher values during experiment. Junker *et al.*[40,41] reported that, deliberate inclusion of air gap between the DRA and the ground plane will increase the resonant frequency, decrease the resonance resistance and hence the bandwidth will be broadened with size of the air gap. It was also pointed out[42,43] that, the air gap can be used to tune the operating frequency and for fabricating wider bandwidth DRAs. Hence in practical cases, the thin air layer trapped between the DR and microstrip line will decrease the radiation Q-factor to increase the bandwidth. It is also observed that, with the modifications in the feed line geometry, the symmetry of the radiation pattern is destroyed. This is believed to be because of the fact that, the current through the asymmetric feed line also contributes to the antenna radiation to distort its symmetry. At the same time the ripples appeared in all the radiation patterns is due to scattering from edges of the finite ground plane on which the DR is mounted.

8.5 CONCLUSIONS

- Wideband dielectric resonator antennas of cylindrical, elliptical and rectangular geometries were designed, fabricated and characterized using high permittivity $Ca_5Nb_2TiO_{12}$ dielectric material. The effect of feed line geometry on the antenna performance was studied. For this the DRAs were energized employing simple, L and T-shaped microstrip lines.
- The excited resonance mode of each and every antenna geometry was identified using Micro-stripes 6.5 version of CAD simulation software working based on 3D TLM methods. The simulated resonant frequency and impedance bandwidth shows excellent match with experimental results.

- Broadband microstrip line energized cylindrical DRA was formulated. The antenna has a bandwidth of 316 MHz (12%, at 2.625 GHz) and a gain of 8.2 dBi. The bandwidth increased to 495 MHz (19%, at 2.68 GHZ) and 675 MHz (26%, at 2.6 GHz) for L- and T-strip excitations respectively. Whereas the gain of the DRA shifted to 9.5 and 7.9 dBi for L- and T-strip energized cylindrical DRAs. Slight distortions in the radiation patterns and improved cross-polar isolation were observed with modified geometry of the excitation techniques.
- Elliptical DRA excited with microstrip line methods was fabricated. The antenna has a resonance at 1.85 GHz with a bandwidth of 185 MHz (10 %) and a gain of 8 dBi. The performance of the antenna was improved by L-and T-fed excitations. L-fed elliptical antennas exhibit a wider bandwidth of 230 MHz (12.11 %, at 1.9 GHz) and enhanced gain of 9.2dBi. At the same time the T-fed DRA still have better bandwidth than the simple and L-fed DRA to reach 325 MHz (14.77 %, at 2.2 GHz) and a gain of 6.5 dBi. As in the case of cylindrical DRA, the symmetry of the radiation pattern is affected by variations in excitation techniques. However, the cross-polar isolation was found to be higher for T-fed antennas compared with microstrip line and L-fed elliptical DRAs.
- Microstrip line excited wide band rectangular DRA was fabricated using the same $Ca_5Nb_2TiO_{12}$ dielectric material. As in the case of cylindrical and elliptical DRAs, the performance of rectangular DRA was improved with L-and T-feed excitations. Microstrip line fed rectangular DRA has a bandwidth of 455 MHz (14.9 %, at 3.115 GHz), whereas L- and T-fed antennas has 510 MHz (17. 6 %, at 2.9 GHz) and 635 MHz (22 %, 2.975 GHz) respectively. The gain of the antennas are 8.8, 10 and 9 dBi respectively for the simple, L- and T-configurations. Radiation performance of rectangular DRAs were also found to be affected by variation in feed line shape as in the case of cylindrical and elliptical DRAs.

- In cylindrical, elliptical and rectangular DRAs, the impedance bandwidth increases linearly with branching of feed line. Compared with microstrip line methods, resonant frequency and gain of the antenna increased for L-feeding, while decrease of resonant frequency and gain was observed with T-feed excitation methods.
- Thus L-and T-feed microstrip line excitation offers a convenient method for the bandwidth enhancement of DRAs. The high permittivity DR material offers miniaturization and are advantageous over currently employed such antennas for practical applications. In addition the relatively low density of the DR material used points towards the possibility of fabrication of light weight antennas.

8.6 REFERENCES

[1] S. A. Long, M. McAllister and L. C. Shen, *IEEE. Trans. Antennas. Propag.* **AP-31** (1983) 406.

[2] M. McAllister, S. A. Long and G.L Conway, *Electron. Lett.* **19** (1983) 219.

[3] M. McAllister and S. A. Long, *Electron. Lett.* **24** (1988)1156.

[4] A. A. Kishk, Y. Yin and A. W. Glisson, *IEEE. Trans. Antennas. Propag.* **AP-50** (2002) 469.

[5] R. K. Mongia, A. Ittipiboon, P. Bhartia and M. Cuhaci, *Electron. Lett.* **29** (1993)1530.

[6] R. K. Mongia, and P. Bhartia, *Inter. J. for Microw. and Millim. Wave Comput. Aided Engg.* **4** (1994) 230.

[7] R. A. Kranenburg, and S. A. Long, *Electron. Lett.* **24** (1998) 1156.

[8] R. K. Mongia, A. Ittipiboon, and M. Cuhaci, *Electron. Lett.* **30** (1994) 163.

[9] S. Mridula, Sreedevi K. Menon, P. Mohanan, P.V. Bijumon and M.T. Sebastian, *Microwave Opt. Technol. Lett.* **40** (2004) 316.

[10] K.-L. Wong, N.-C. Chen and H.-T. Chen, *IEEE Microwave and Guided Wave Lett.* **3** (1993) 355.

[11] A. Ittipiboon, A. Petosa, D. Roscoe and M. Cuhaci, *IEEE Antennas and Propagattion Soc. International Symp. Digest,* Baltimore, USA, (1996) 2038.

[12] S. M. Shum and K. M. Luk, *Electron. Lett.* **30** (1994) 277.

[13] K. W. Leung, *IEEE Trans. Microwave Theoty and Tech.* **MTT-49** (2001) 524.

[14] N. C. Chen, H. C. Su, K. L. Wong and K. W. Leung, *Microwave and Opt. Technol. Lett.* **8** (1995) 13.

[15] S. M. Shum and K. M. Luk, *IEE Proc. Microwave Antennas Propagat.* **142** (1995) 189.

[16] H. K. Ng and K. W. Leung, *IEEE Antennas and Propagation Society International Symp. Digest.*, Salt Lake City, USA, **4** (2000) 2080.

[17] R. T. Long, R. J. Dorris, S. A. Long, M. A. Khayat and J. T. Williams, *Electron. Lett.* **27** (2001) 406.

[18] K. W. Leung and S. K. Mok, *Electron. Lett.* **37** (2001) 934.

[19] A. A. Kishk, B. Ahn and D. kajfez, *Electron. Lett.* **25** (1989) 1232.

[20] A, sangiovanni, J. Y. Dauvignac and Ch. Pichot, *Microwave and Opt. Technol. Lett.* **18** (1998) 303.

[21] K. W. Leung, K. M. Luk, K. Y. Chow and E. K. N. Yung, *Electron. Lett.* **33** (1997) 725.

[22] G. P. Junker, A. W. Glisson and A. A. Kishk, *Microwave and Opt. Technol. Lett.* **9** (1995) 204.

[23] R. N. Simons and R. Q. Lee, *IEE Proc.-H* **140** (1993) 336.

[24] K. W. Leung, K. Y. Chow, K. M. Luk and E. K. N. Yung, *Electron. Lett.* **32** (1996) 2038.

[25] K. K. Pang, H. Y. Lo, K. W. Leung, K. M. Luk and E. K. N. Yung, *Microwave and Opt. Technol. Lett.* **27** (2000) 377.

[26] K. M. Luk and K. W. Leung, "*Dielectric Resonator Antennas*", Ed. J. R. James (Resrach Studies Press Ltd. Baldock, Hertfordshire, U. K., 2003.

[27] B. Lethakumary, Sreedevi K Menon, C. K. Aanandan, K. Vasudevan and P. Mohanan, *Microwave Opt. Technol. Lett.* **35** (2004) 235.

[28] B. Lethakumary, *PhD thesis* submitted to Cochin University of Science and Technology, India (2005).

[29] P. B. Johns and R. L. Beurle, "*Numerical solution of two-dimensional scattering problems using a transmission-line matrix*", *Proc. IEE* **118** (12) (1971)1203.

[30] J. Paul, V. Podliozny, D. W. P. Thomas and C. Chrstopoulos, *Turk. J. Elec. Engin.* **10** (2002) 185.

[31] I. Salama and S.M. Riad, *IEEE Trans. On Microwave Teory and Technol.* **48** (2000) 1089.

[32] Micro-stripes 6.5 Reference manual, Flomerics Limited, Surrey, UK.

[33] B. J. Fasenfest, A. G. Walsh, C. S. De Yong, T. F. Kennedy, S. A. Long and J. T. Williams, *Electron. Lett.* **39** (2003) 12.

[34] K. Y. Chow and K. W. Leung, *IEEE Trans. on Antennas and Propagat.* **50** (2002) 404.

[35] M. H. Neshati and Z. Wu, *11th International Conference on Antennas and Propagat.* **480** (2001) 866.

[36] S.-C. Gao, L.-W. Li, M.-S. Leong, and T.-S. Yeo, *IEEE Trans. on Vehicular Technol.* **51** (2002) 17.

[37] R. K. Mongia and A. Ittipiboon, *IEEE Trans. Antennas and Propagat.* **45** (1997) 1348.

[38] Y. M. M. Antar and Z. Fan, *IEE Proc.-Microwave Antennas Propagat.* **143** (1996) 113.

[39] A. Petosa, N. R. S. Simons, R. Siushansian, A. Ittipiboon and M. Cuhaci, *IEEE Trans. Antennas. Propagat.* **48** (2000) 738.

[40] G. P. Junker, A. A. Kishk, A. W. Glisson and D. kajfez, *IEEE Antennas and Propagatation Magazine.* **37** (1995) 40.

[41] G. P. Junker, A. A. Kishk, A. W. Glisson and D. Kajfez, *Electron. Lett.* **30** (1994) 97.

[42] D. Drossos, Z. Wu and J. Litava, *Electron. Lett.* **32** (1999) 36.

[43] Z. Li, C. Wu and J. Litva, *Electron. Lett.* **32** (1996) 606.

CHAPTER 9

CONCLUSIONS AND SCOPE FOR FUTURE WORK

This chapter features summary of the research work described in this thesis. The highlights of the results presented in each chapter are outlined in chronological order. The scope for extending the work in future directions such as in the area of dielectric resonators and antennas are also discussed.

This thesis presents the microwave dielectric properties of two novel dielectric resonator materials with the composition $Ca(Ca_{1/4}Nb_{2/4}Ti_{1/4})O_3$ and $Ca(Ca_{1/4}Ta_{2/4}Ti_{1/4})O_3$ ceramics and their application in the fabrication of wideband antennas. The microwave dielectric properties of the ceramics were tailored by several techniques such as doping, glass addition and solid solution formations in the complex perovskite *A* and *B*-sites with suitable substitutions. Among the wide variety of DRs developed, ceramic resonators with optimum properties were identified to fabricate broadband dielectric resonator loaded microstrip patch antennas. Furthermore, wideband, high permittivity dielectric resonator antennas were fabricated and explored the possibility of tuning their characteristics by modifying the feed line geometries.

The first two chapters of this thesis explain the fundamental concepts related to dielectric resonators, antennas, their design, fabrication and characterization methods. Chapter 3 of the thesis outlines a general introduction about complex perovskite materials and a brief history and literature survey related to the evolution of $Ca(Ca_{1/4}Nb_{2/4}Ti_{1/4})O_3$ and $Ca(Ca_{1/4}Ta_{2/4}Ti_{1/4})O_3$ ceramics. The influence of synthesizing conditions on the microwave dielectric properties of both the ceramics were investigated. $Ca_5Nb_2TiO_{12}$ has $\varepsilon_r = 48$, $Q_u x f > 26000$ (at 3.68 GHz) and $\tau_f = +40$ppm/°C, when sintered at 1550°C/4h whereas $Ca_5Ta_2TiO_{12}$ has $\varepsilon_r = 38$, $Q_u x f > 33000$ (at 4.18 GHz) and $\tau_f = +10$ppm/°C at a sintering temperature of 1625°C/4h. Annealing at lower temperatures for different durations could not make any improvement in the microwave dielectric properties of the complex perovskite materials. Solid solution phases in the $Ca_5Nb_{2-x}Ta_xTiO_{12}$ ($0 \le x \le 2$) system has been prepared and found that the density and dielectric properties shows a linear variation between that of the end members for all compositions. The effect of dopants on the structure, microstructure and microwave dielectric properties of $Ca(Ca_{1/4}Nb_{2/4}Ti_{1/4})O_3$ and $Ca(Ca_{1/4}Ta_{2/4}Ti_{1/4})O_3$ dielectrics were investigated. Divalent dopants in general, trivalent Cr_2O_3, In_2O_3 and pentavalent Sb_2O_3 were identified as the efficient candidates for improving the microwave dielectric properties of $Ca(Ca_{1/4}Nb_{2/4}Ti_{1/4})O_3$ and $Ca(Ca_{1/4}Ta_{2/4}Ti_{1/4})O_3$ ceramics. With the doping of 0.5 mole % of MgO, the dielectric properties of $Ca(Ca_{1/4}Nb_{2/4}Ti_{1/4})O_3$ was improved to $\varepsilon_r = 48$, $Q_u x f = 33000$ GHz and $\tau_f = 38$ ppm/°C, whereas for $Ca(Ca_{1/4}Ta_{2/4}Ti_{1/4})O_3$ the values are $\varepsilon_r =$

38, $Q_u \times f$ = 40500 GHz and τ_f = 6 ppm/°C. The doping of 1 mole % each of Co_3O_4 and Sb_2O_5 imparted 15 – 20 % increase in quality factor of $Ca(Ca_{1/4}Nb_{2/4}Ti_{1/4})O_3$ and $Ca(Ca_{1/4}Ta_{2/4}Ti_{1/4})O_3$ ceramics without much affecting their ε_r and improved the τ_f. Cr_2O_3 was identified as the most effective dopant for reducing the microwave loss factor of both the ceramics. With 1 mole % Cr_2O_3, $Ca(Ca_{1/4}Nb_{2/4}Ti_{1/4})O_3$ has ε_r = 49 and $Q_u \times f$ = 34000 GHz, whereas $Ca(Ca_{1/4}Ta_{2/4}Ti_{1/4})O_3$ has ε_r = 39 and $Q_u \times f$ = 41000 GHz. However this dopant increased the τ_f of both the ceramics. Temperature stable dielectric resonators were obtained with the addition of about 1.6 mole % each of MgO, Co_3O_4, Al_2O_3 and ZrO_2 to $Ca(Ca_{1/4}Ta_{2/4}Ti_{1/4})O_3$ material. A correlation between the radius of the dopant ion and quality factor of the parent materials were established. It was found that dopants with ionic radii comparable to that of the average *B*-site radius of the perovskite structure became more efficient in improving the microwave dielectric properties of $Ca(Ca_{1/4}Nb_{2/4}Ti_{1/4})O_3$ and $Ca(Ca_{1/4}Ta_{2/4}Ti_{1/4})O_3$ ceramics.

Chapter 4 deals with the microwave dielectric properties of glass fluxed $Ca(Ca_{1/4}Nb_{2/4}Ti_{1/4})O_3$ and $Ca(Ca_{1/4}Ta_{2/4}Ti_{1/4})O_3$ ceramics. Different weight percentage of glasses such as B_2O_3, SiO_2, $B_2O_3 - SiO_2$, $ZnO - B_2O_3$, $Al_2O_3 - SiO_2$, $Al_2O_3 - B_2O_3 - SiO_2$, $BaO - B_2O_3 - SiO_2$, $MgO - B_2O_3 - SiO_2$, $ZnO - B_2O_3 - SiO_2$, $PbO - B_2O_3 - SiO_2$ and $2MgO - Al_2O_3 - 5SiO_2$ were added to calcined $Ca(Ca_{1/4}B_{2/4}Ti_{1/4})O_3$ [B = Nb, Ta] precursor. Boron oxide based glasses were found to be more effective in lowering the sintering temperature and 2 wt % addition of such glasses reduced the sintering temperature of both the ceramics by about 250-300°C. Al_2O_3 based glasses were more effective in reducing the τ_f of $Ca(Ca_{1/4}Nb_{2/4}Ti_{1/4})O_3$ and $Ca(Ca_{1/4}Ta_{2/4}Ti_{1/4})O_3$ ceramics. The improvement of microwave dielectric properties were more pronounced with ternary glasses than that with primary and binary glasses. Marginal increase of 2 % density, 14 % quality factor and 4 % dielectric constant was attained when $Ca_5Nb_2TiO_{12}$ ceramics were fluxed with small amount of SiO_2, $Al_2O_3 - SiO_2$, $Al_2O_3 - B_2O_3 - SiO_2$, $MgO - B_2O_3 - SiO_2$ and $2MgO - Al_2O_3 - 5SiO_2$. 0.1 wt % $2MgO - Al_2O_3 - 5SiO_2$ glass added $Ca_5Nb_2TiO_{12}$ ceramics sintered at 1520°C/4h has ε_r = 50, $Q_u \times f$ > 30 000 GHz and τ_f = +38 ppm/°C. 0.1 - 0.2 wt % addition of Al_2O_3-SiO_2, $Al_2O_3 - B_2O_3 - SiO_2$, MgO-B_2O_3-SiO_2 and $2MgO$-Al_2O_3-$5SiO_2$ to $Ca_5Ta_2TiO_{12}$, produced an enhancement of 4 % in ε_r and

22 % in $Q_u x f$ values. With 0.2 wt % of Al_2O_3 - B_2O_3 – SiO_2, the microwave dielectric properties of $Ca(Ca_{1/4}Ta_{2/4}Ti_{1/4})O_3$ ceramics are $\varepsilon_r = 38$, $Q_u x f = 38000$ GHz and $\tau_f = 8$ ppm/°C, whereas for 0.1 wt % addition of $2MgO\text{-}Al_2O_3\text{-}5SiO_2$ $\varepsilon_r = 38$, $Q_u x f = 40000$ GHz and $\tau_f = 5$ ppm/°C. Addition of B_2O_3, $Al_2O_3\text{-}B_2O_3\text{-}SiO_2$, $MgO\text{-}B_2O_3\text{-}SiO_2$ and $2MgO\text{-}Al_2O_3\text{-}5SiO_2$ glasses to $Ca_5Ta_2TiO_{12}$ in 1 – 2 wt % shifted the τ_f of the ceramics from positive to negative values forming temperature stable compositions.

The effect of substitution of *A* and *B*-site ions on the microwave dielectric properties of $Ca(Ca_{1/4}Nb_{2/4}Ti_{1/4})O_3$ ceramics are described in Chapter 5. Structural and dielectric properties of solid solution phases such as $Ca_{5-x}Ba_xNb_2TiO_{12}$, $Ca_{5-x}Sr_xNb_2TiO_{12}$, $Ca_{5-x}Mg_xNb_2TiO_{12}$, $Ca_{5-x}Zn_xNb_2TiO_{12}$, $Ca_{5-x}Ni_xNb_2TiO_{12}$, $Ca_{5-x}Co_xNb_2TiO_{12}$, $Ca_5Nb_2Ti_{1-x}Zr_xO_{12}$ and $Ca_5Nb_2Ti_{1-x}Hf_xO_{12}$ were investigated. $Ca_{5-x}A_xNb_2TiO_{12}$ (A = Ba, Sr) ceramics undergo a structural transformation with increasing x and a complete solid solution was formed only for x up to 4. With compositional variations the structure evolved into a pseudo-cubic form from true orthorhombic symmetry. This was verified by employing Raman and FTIR spectroscopic studies. Q_u showed a linear decrease with increasing Ba-content, where as in Sr-based system, Q_u showed a gradual decrease for $x = 0$ to 3 (26,000 – 6,000 GHz) and then increased for $x = 4$ (11,500 GHz). The ε_r and τ_f exhibited a linear increase with Ba/Sr content in $Ca_{5-x}A_xNb_2TiO_{12}$ (A = Ba, Sr) ceramics. $Ca_{5-x}A'_xNb_2TiO_{12}$ (A' = Mg, Zn, Ni and Co) ceramics form solid solutions only for x up to 1 and beyond this limit they form as mixture phases. However the microwave dielectric properties of the ceramics were improved for $0 \leq x \leq 1$. In all the four systems with $0 \leq x \leq 1$, an inverse linearity was established between mole fractions of substituted ions and unit cell volume. Within the solid solution range, Mg, Zn, Ni and Co substitution in $Ca(Ca_{1/4}Nb_{2/4}Ti_{1/4})O_3$ ceramics resulted in the enhancement of quality factor, decrease in ε_r and improvement in τ_f. $Ca_{4.35}Mg_{0.65}Nb_2TiO_{12}$ has $\varepsilon_r = 41$, $Q_u x f = 33000$ GHz, $Ca_{4.36}Zn_{0.64}Nb_2TiO_{12}$, has $\varepsilon_r = 43$, $Q_u x f = 29000$ GHz, $Ca_{4.38}Ni_{0.62}Nb_2TiO_{12}$ has $\varepsilon_r = 42$, $Q_u x f = 28200$ GHz and $Ca_{4.18}Co_{0.82}Nb_2TiO_{12}$ has $\varepsilon_r = 37$, $Q_u x f = 30000$ GHz. All these compositions were fond to have near zero temperature coefficient of resonant frequency. With $2 \leq x \leq 5$, all the compositions formed mixture phases with low ε_r and high negative τ_f. However compositions with $x = 5$, like $5MgO\text{-}Nb_2O_5\text{-}TiO_2$ has $\varepsilon_r = 15$, $Q_u x f = 59000$

GHz and τ_f = -77ppm/°C (sintered at 1325°C), whereas 5CoO-Nb_2O_5-TiO_2 has ε_r = 9, $Q_u x f$ = 41000 GHz and τ_f = -59 ppm/°C (sintered at 1010°C). These low loss, low ε_r materials may find applications as substrates for Microwave Integrated Circuits. The ability of 3D Transmission Line Matrix method to compute the resonant frequency and dielectric properties of a shielded cylindrical ceramic resonator was established by simulating their transmission mode resonance spectrum. The microwave dielectric properties calculated from the simulated resonance spectrum showed excellent agreement with experimental results. $Ca_5Nb_2Ti_{1-x}Zr_xO_{12}$ and $Ca_5Nb_2Ti_{1-x}Hf_xO_{12}$ ($0 \leq x \leq 1$) complex perovskites yielded temperature stable compositions with decreased ε_r and Q_u compared with the parent material. The density and cell volume were found to be increased with increase in Zr/Hf content. $Ca_5Nb_2Ti_{0.2}Zr_{0.8}O_{12}$ has ε_r = 34, $Q_u x f$ = 24,000 GHz and $\tau_f \approx 0$ ppm/°C and $Ca_5Nb_2Ti_{0.4}Hf_{0.6}O_{12}$ has ε_r = 32, $Q_u x f$ = 22000 GHz and $\tau_f \approx 0$ ppm/°C.

The influence of cationic substitutions in $Ca(Ca_{1/4}Ta_{2/4}Ti_{1/4})O_3$ ceramics are outlined in Chapter 6. Accordingly, solid solution phases in the $Ca_{5-x}Ba_xTa_2TiO_{12}$, $Ca_{5-x}Sr_xTa_2TiO_{12}$, $Ca_{5-x}Mg_xTa_2TiO_{12}$, $Ca_{5-x}Zn_xTa_2TiO_{12}$, $Ca_{5-x}Ni_xTa_2TiO_{12}$, $Ca_{5-x}Co_xTa_2TiO_{12}$, $Ca_5Ta_2Ti_{1-x}Zr_xO_{12}$ and $Ca_5Ta_2Ti_{1-x}Zr_xO_{12}$ ceramics have been synthesized and their structural aspects and microwave dielectric properties were studied as a function of mole fraction of substituted cations. As in the case of niobium analogue, Ba and Sr substitution has resulted a structural evolution from orthorhombic to pseudo-cubic symmetry. The solid solution phases were formed only for x up to 4. For x = 5, $Ca_{5-x}A_xTa_2TiO_{12}$ (A = Ba, Sr) ceramics form mixture phases of $(Ba/Sr)_4Ta_2O_9$ - $(Ba/Sr)TiO_3$. Regarding the microwave dielectric properties, in Ba-substituted ceramics, Q_u showed a linear decrease with increase in Ba-content, where as in Sr-based system, Q_u showed a gradual decrease for x = 0 to 3 (33000 – 8500 GHz) and then increased for x = 4 (16000 GHz). The ε_r and τ_f increased with mole fraction of barium/strontium content in $Ca_{5-x}A_xTa_2TiO_{12}$ (A = Ba, Sr) dielectrics. The discrepancy observed in microwave dielectric properties due to structural transformations in $Ca_{5-x}A_xTa_2TiO_{12}$ (A = Ba, Sr) system was investigated based on Raman and FTIR spectroscopic methods. The structural evolution observed in the XRD was confirmed, by spectroscopic methods as the shift of modes and distortions occurred. Dielectric resonators with improved properties were identified in

$Ca_{5-x}A'_xTa_2TiO_{12}$ (A' = Mg, Zn, Ni & Co) ceramics. With the substitution of Mg, Zn, Ni and Co in $Ca_5Ta_2TiO_{12}$ ceramics for $0 \leq x \leq 1$, the ε_r decreased, Q_u increased and τ_f shifted from positive to negative values. The microwave dielectric properties were highly affected by the polarizability and ionic radius of the substituted cations. The temperature stable compositions identified in the system are $Ca_{4.82}Mg_{0.18}Ta_2TiO_{12}$ with $\varepsilon_r = 37$, $Q_u \times f$ = 36000 GHz, $Ca_{4.85}Zn_{0.15}Ta_2TiO_{12}$ which has ε_r = 37, $Q_u \times f$ = 35000 GHz. $Ca_{4.75}Ni_{0.25}Ta_2TiO_{12}$ with $\varepsilon_r = 35$, $Q_u \times f = 34000$ GHz and $Ca_{4.88}Co_{0.12}Ta_2TiO_{12}$ with, ε_r = 36, $Q_u \times f = 35000$ GHz. For $2 \leq x \leq 5$, the ceramics form a mixture of various phases with a decrease in ε_r and negative τ_f. With x = 5, Mg and Co-based materials have high quality factor and low dielectric constant. $5MgO\text{-}Ta_2O_5\text{-}TiO_2$ has $\varepsilon_r = 18$, $Q_u \times f = 114000$ GHz and τ_f = -56 ppm/°C (when sintered at 1325°C) whereas $5CoO\text{-}Ta_2O_5\text{-}TiO_2$ has ε_r = 14, $Q_u \times f = 48000$ GHz and τ_f = -43 ppm/°C (sintered at 1150°C). These properties enable them as potential candidates for substrate applications in microelectronic technology. The transmission mode resonance spectrum of $Ca_{5-x}A'_xTa_2TiO_{12}$ (A' = Mg, Zn, Ni & Co) ceramics for $0 \leq x \leq 5$ was simulated by means of 3D-Transmission Line Matrix methods. The simulated values of microwave dielectric properties were found to be in excellent agreement with experimental results with less than 2 % error. Further $Ca_5Ta_2Ti_{1-x}Zr_xO_{12}$ and $Ca_5Ta_2Ti_{1-x}Hf_xO_{12}$ ($0 \leq x \leq 1$) solid solutions were formed with an improvement in dielectric properties (especially τ_f) of $Ca_5Ta_2TiO_{12}$ ceramics. The density and cell volume were found to be increased with increase in Zr/Hf content. In both the solid solutions, ε_r and Q_u were decreased whereas τ_f shifted its sign. Two potential compositions with temperature compensation of resonant frequency were identified. In the Zr-based system, $Ca_5Ta_2Ti_{0.7}Zr_{0.3}O_{12}$ has ε_r = 36, $Q_u \times f = 28000$ GHz and τ_f = 0, whereas in the Hf substituted composition $Ca_5Ta_2Ti_{0.6}Hf_{0.4}O_{12}$ has $\varepsilon_r = 34$, $Q_u \times f = 26000$ GHz and $\tau_f \approx 0$ ppm/°C.

The following table comprises important and selective dielectric resonator materials developed in the course of this PhD work.

$A(A_{1/4}B_{2/4}C_{1/4})O_3$ [A = Ca, Ba, Sr, Mg, Zn, Ni & Co; B = Nb, Ta; C = Ti, Zr & Hf] DIELECTRIC RESONATORS

Sl. No	Material	ST (°C/ 4h)	Den-sity (g/ cm^3)	$Q_u x f$ (GHz)	f (GHz)	ε_r	τ_f (ppm/ °C)
1	$Ca_5Nb_2TiO_{12}$	1550	4.06	26000	3.6830	48	40
2	$Ca_{4.35}Mg_{0.65}Nb_2TiO_{12}$	1550	4.20	33000	4.1060	41	≈ 0
3	$5MgO - Nb_2O_5-TiO_2$	1325	4.17	59000	6.8010	15	-77
4	$Ca_{4.36}Zn_{0.64}Nb_2TiO_{12}$	1550	4.36	29000	4.0037	43	≈ 0
5	$Ca_{4.38}Ni_{0.62}Nb_2TiO_{12}$	1550	4.33	28200	4.0735	42	≈ 0
6	$Ca_{4.18}Co_{0.82}Nb_2TiO_{12}$	1550	4.42	30000	4.3079	37	≈ 0
7	$5CoO-Nb_2O_5-TiO_2$	1010	4.32	41000	7.4589	9.0	-59
8	$Ca_5Nb_2Ti_{0.2}Zr_{0.8}O_{12}$	1670	4.14	24000	4.4124	34	≈ 0
9	$Ca_5Nb_2Ti_{0.4}Hf_{0.6}O_{12}$	1675	4.42	22000	4.4578	32	≈ 0
10	$Ca_5Ta_2TiO_{12}$	1625	5.26	33000	4.2530	38	+10
11	$Ca_{4.82}Mg_{0.18}Ta_2TiO_{12}$	1625	5.31	36000	4.3561	37	≈ 0
12	$5MgO-Ta_2O_5-TiO_2$	1325	5.41	114000	6.6103	18	-56
13	$Ca_{4.85}Zn_{0.15}Ta_2TiO_{12}$	1625	5.36	35000	4.1537	37	≈ 0
14	$Ca_{4.75}Ni_{0.25}Ta_2TiO_{12}$	1625	5.33	34000	4.4959	35	≈ 0
15	$Ca_{4.88}Co_{0.12}Ta_2TiO_{12}$	1625	5.26	35000	4.4879	36	≈ 0
16	$5CoO-Ta_2O_5-TiO_2$	1150	6.15	48000	6.5276	14	-43
17	$Ca_5Ta_2Ti_{0.7}Zr_{0.3}O_{12}$	1650	5.45	28000	4.4124	36	≈ 0
18	$Ca_5Ta_2Ti_{0.6}Hf_{0.4}O_{12}$	1675	5.48	26000	4.3574	34	≈ 0

As is evident from the table, dielectric resonators with $9 \leq \varepsilon_r \leq 83$, $1200 \leq Q_u \times f \leq 1\ 14000$ GHz and $+60 \leq \tau_f \leq -77$ ppm/°C have been developed during this investigation.

The fabrication of broadband dielectric resonator loaded microstrip patch antenna is described in Chapter 7. Two separate techniques were employed to fulfill the aim. DRs were placed over the patch and as an alternate method they were positioned over the feed line. In both cases the position of DR on the patch surface/feedline as well as the value of dielectric constant and resonant frequency of DR needed for maximum percentage bandwidth is optimized. Cylindrical dielectric resonators developed as explained in Chapters 3 – 6 were used with ε_r varying from 9 – 92. $Ca_5Nb_2TiO_{12}$ material with $\varepsilon_r = 48$ was found to be best suited for maximum enhancement of impedance bandwidth of the antenna. Furthermore it was confirmed that, maximum coupling of the electromagnetic energy between the feed and DR occurs when the resonant frequency of the DR matches with that of the patch antenna. A bandwidth of more than 10% is achieved by loading a dielectric resonator of $\varepsilon_{dr} = 48$ over the patch and about 14% by loading the same DR on the feed line. DR loading produced microstrip patch antennas with 5-7 fold enhancement in their impedance bandwidth. The studies also revealed that these methods will not adversely affect other properties of the antenna especially its gain and radiation efficiency.

Eighth Chapter probes into the design and fabrication of wideband dielectric resonator antennas of various geometries like cylindrical, elliptical and rectangular ones using high permittivity $Ca_5Nb_2TiO_{12}$ material. A novel method for bandwidth enhancement viz. modification of microstrip line geometry was also explored. Hence cylindrical DRA was excited using conventional microstrip line method to resonate at 2.625 GHz with a percentage bandwidth of 12 and a gain of 8.2 dBi was fabricated. The performance of the antenna was improved when it was excited with L-and T-shape microstrip lines. The bandwidth increased to 495 MHz (19%, at 2.68 GHZ) and 675 MHz (26%, at 2.6 GHz) for L- and T-strip excitations respectively. Whereas the gain of the DRA shifted to 9.5 and 7.9 dBi for L- and T-strip energized cylindrical DRAs. Microstrip line excited elliptical DRA was fabricated to resonate at 1.85 GHz with a bandwidth of 10 % and a gain of 8 dBi. The impedance bandwidth was made wider by exciting it with

L- and T-feed line methods. With L-feed the antenna has a bandwidth of 12.11 % (at 1.9 GHz) and enhanced gain of 9.2dBi. At the same time the T-fed DRA still have better bandwidth than the simple and L-fed DRA to reach 14.77 % (at 2.2 GHz) and a gain of 6.5 dBi. As in the case of cylindrical and elliptical DRAs, the performance of rectangular DRA was also improved with L-and T-feed excitations. Microstrip line fed rectangular DRA has a bandwidth of 14.9 % (at 3.115 GHz), whereas L- and T-fed antennas has 17. 6 % (at 2.9 GHz) and 22 % (at 2.975 GHz) respectively. The gain of the antennas are 8.8, 10 and 9 dBi respectively for the simple, L- and T-configurations. It is to be noted that regardless of the antenna geometry, the impedance bandwidth increases with branching of the feed line. A general behavior of shifting the resonant frequency towards the higher values was observed with L-fed DRAs, where as the reverse effect was detected with T-fed antennas in all the geometry of DRAs investigated in this work. Slight distortion and ripples in the radiation pattern was observed due to the finite size of the ground plane and the same was found to increase with excitation of asymmetric feed lines (L- and T). Cross-polarization levels vary from 15 – 25 dB depending upon the DRA and feed line geometries and was within the acceptable range for practical applications.

The following tables summarizes the geometry and important characteristics of ceramic antennas developed in the course of this PhD work.

Geometry, resonant frequency, operating bandwidth and gain of DR loaded microstrip patch antennas

Antenna Geometry	Resonant Frequency (GHz)	Operating Band (GHz)	2:1 VSWR Bandwidth (%)	Gain (dBi)
DR Loaded Antenna (DR over the patch)	2.27	2.158 – 2.398	10.57	6.3
DR Loaded Antenna (DR over the feed line)	2.32	2.188 - 2.508	13.79	6.9

Geometry, resonant frequency, operating bandwidth and gain of DRAs

Antenna Geometry	Resonant Frequency (GHz)	Operating Band (GHz)	2:1 VSWR Bandwidth (%)	Gain (dBi)
Simple Feed CDRA	2.625	2.459 - 2.775	12.00	8.2
L - Feed CDRA	2.680	2.545 - 3.040	19.00	9.5
T - Feed CDRA	2.600	2.400 - 3.075	26.00	7.9
Simple Feed EDRA	1.850	1.760 -1.945	10.00	8.0
L - Feed EDRA	1.900	1.810 - 2.040	12.11	9.2
T - Feed EDRA	2.200	2.075 - 2.400	14.77	6.5
Simple Feed RDRA	3.115	2.995 - 3.450	14.90	8.8
L - Feed RDRA	2.900	2.690 - 3.200	17.60	10.0
T – Feed RDRA	2.975	2.490 - 3.125	22.00	9.0

The scope for the extension of the work described in this thesis lies mainly in two areas. The primary one is to synthesize $Ca(Ca_{1/4}Nb_{2/4}Ti_{1/4})O_3$ and $Ca(Ca_{1/4}Ta_{2/4}Ti_{1/4})O_3$ ceramics at low temperatures without much deteriorating its dielectric properties to facilitate its mass production for industrial applications. Though glass additives could reduce the sintering temperature, it also negatively affected the microwave dielectric properties. Hence chemical synthesizing techniques like hydrothermal, co-precipitation, citrate-gel, sol-gel etc. would be of great interest. It is established that the dielectric properties of single crystals are superior to their polycrystalline counterparts. Hence another future direction in dielectric resonator research is to grow single crystals of $Ca(Ca_{1/4}Nb_{2/4}Ti_{1/4})O_3$ and $Ca(Ca_{1/4}Ta_{2/4}Ti_{1/4})O_3$ ceramics for microwave applications.

In the current work DRAs were excited by microstrip line methods. Though this is the simplest method, various applications need the antenna to be excited using different methods. Hence excitation of $Ca_5Nb_2TiO_{12}$ using coaxial feed line, conducting probe,

slotline, aperture coupling etc. may be tried. Surface Mountable Antennas for WLAN applications, like ceramic chip antennas and dielectric resonator antennas fabricated using Low Temperature Co-fired Ceramic Technology can provide miniaturization as well as efficiency. The potential dielectric properties of $Ca_5Nb_2TiO_{12}$ material make them competent of use in such applications. The possibility of fabricating antennas of this category could be tried as an extension of the work did in this thesis. For applications requiring enhanced bandwidth and high-gain antennas, dielectric resonator antenna arrays would be a good choice. Single element DRAs experimented in this work yielded better properties than that reported earlier. Hence DRA arrays employing $Ca_5Nb_2TiO_{12}$ dielectric resonator excited using branched microstrip lines printed over the substrate may be investigated to produce still improved results. Consequent to the emergence of tunable dielectrics, phase shifter connected DRAs would serve as an added advantage to the devices employing dielectric resonator antennas. The use of ferroelectric film could enable the integration of phase shifters with antenna array on the same substrate by substantially aiding miniaturization, mass and cost reduced production of microwave and RF devices. Hence investigations based on the phase shifter coupled integrated beam steerable single element and DRA array using ferroelectric technology would be of great scientific and technological importance.

LIST OF PATENTS AND PUBLICATIONS

International Patents

1. M. T. Sebastian, **P. V. Bijumon**, P. Mohanan and Sreedevi. K. Menon *"Development of novel cylindrical dielectric resonator antenna and other devices based on new microwave dielectric ceramic compositions in the $Ca_5A_2TiO_{12}$[A=Nb, Ta] system"* (Applied: File No: NF 382/02)

2. M. N. Suma, **P. V. Bijumon**, M. T. Sebastian and P. Mohanan *"Novel Wideband Dielectric Resonator Loaded Printed Monopole Antennas"* (Applied: File No: NF 0230/05)

Publications in SCI Journals

1. **P. V. Bijumon**, Sreedevi. K. Menon, M. N. Suma, M. T. Sebastian and P. Mohanan, "Broad band cylindrical dielectric resonator antenna excitated by modified microstrip line" ***Electron. Lett.*** 41 (7) (2005).

2. **P. V. Bijumon**, A. Dias, R. L. Moreira, P. Mohanan and M. T. Sebastian, "New low loss ceramics in $Ca_{5-x}Sr_xA_2TiO_{12}$ [A = Nb, Ta] system: Microwave dielectric properties and vibrational spectroscopic analysis", ***J. Appl. Phys.*** 97 (2005).

3. M. N. Suma, Sreedevi K Menon, **P.V. Bijumon**, M.T. Sebastian and P.Mohanan, "Rectangular Dielectric Resonator Antenna on a Conductor Backed Co-planar Waveguide" ***Microwave Opt. Technol. Lett.*** 45 (2) (2005) 154 – 156.

4. **P. V. Bijumon** and M. T. Sebastian "Temperature Stable Microwave Dielectric Ceramics in the $Ca_5A_2Ti_{1-x}Zr_xO_{12}$ (A = Nb, Ta) System" ***J. Mater. Res.*** 19 (2004) 2922 – 2928.

5. Binu Paul, S. Mridula, P. Mohanan, **P.V. Bijumon**, and M. T. Sebastian, "A compact very-high-permittivity dielectric-eye resonator antenna for multiband wireless applications" ***Microwave Opt. Technol. Lett.*** 43 (2004) 118 – 121.

6. S. K Menon, B. Lathakumari, P. Mohanan, **P.V. Bijumon**, and M. T. Sebastian, "Wideband cylindrical dielectric resonator antenna excited using an L-strip feed" ***Microwave Opt. Technol. Lett.*** 42 (2004) 293 – 294.

7. S. Mridula, Sreedevi K. Menon, P. Mohanan, **P.V. Bijumon** and M.T.

T40-

Sebastian, "Characteristics of a microstrip excited high permittivity rectangular Dielectric resonator antenna" ***Microwave Opt. Technol. Lett.*** 40 (2004) 316-318.

8. M.T. Sebastian, N. Santha, **P. V. Bijumon**, Anna Axelsson and Neil McN. Alford "Microwave dielectric properties of $(1-x)\ CeO_2 - xCaTiO_3$ and $(1-x)CeO_2 - xSm_2O_3$ ceramics. ***J. Eur. Ceram. Soc.*** 24 (2004) 2583-2589.

9. **P. V Bijumon**, V. Kohli, Om Prakash, M. R. Varma and M. T. Sebastian "Dielectric properties of $Ba_5RETi_3A_7O_{30}$ [RE = Ce, Pr, Nd, Sm, Gd, Dy, and Bi, A=Nb, Ta] ceramics" ***Mater. Science and Engineering B*** 113 (2004)13 - 18.

10. **P.V. Bijumon**, P. Mohanan and M. T. Sebastian "High Dielectric Constant Low loss Microwave Dielectric Ceramics in the $Ca_5Nb_{2-x}Ta_xTiO_{12}$ System" ***Mater. Lett.*** 57 (2003)1380-1384.

11. **P. V. Bijumon**, S. Solomon, P. Mohanan and M. T. Sebastian "A new group of microwave dielectric ceramics in the $RE(Ti_{0.5}W_{0.5})O_4$ [RE = Pr, Nd, Sm, Gd, Tb, Dy, and Y] system" ***J. Mater. Sci. Mater. Electron.*** 14 (2003) 5 – 8.

12. **P. V. Bijumon**, Sreedevi. K. Menon, P. Mohanan and M. T. Sebastian "Enhanced bandwidth microstrip patch antennas loaded with high permittivity dielectric resonators" ***Microwave Opt. Technol. Lett.*** 35 (2002) 327 – 330.

13. **P. V. Bijumon**, P. Mohanan and M. T. Sebastian "Microwave Dielectric Properties of $LaMgAl_{11}O_{19}$ Ceramics" ***Mater. Res. Bull.*** 37 (2002) 2129 – 2133.

14. **P. V. Bijumon**, P Mohanan and M. T. Sebastian. "Synthesis, Characterization and Properties of $Ca_5A_2TiO_{12}$ (A=Nb, Ta) Ceramic Dielectric Materials for Applications in Microwave Telecommunication Systems" ***Jpn. J. Appl. Phys.*** Part I, 41(6A) (2002) 3384 – 3385.

15. M.T. Sebastian, Manoj Raama Varma, N. Santha, I. N. Jawahar, K. P. Surendran and **P. V. Bijumon** "Ceramic Dielectric Resonators for Microwave Telecommunication Systems" ***Metals, Materials and Processes*** 13 (2001) 327-338.

16. **P. V. Bijumon** and M. T. Sebastian, "Tailoring the microwave dielectric properties of $Ca_5Ta_2TiO_{12}$ ceramics through glass addition", ***J. Am. Ceram. Soc.*** (in press).

17. **P. V. Bijumon** and M. T. Sebastian, "Low temperature sintering and

microwave dielectric properties of glass added $Ca_5Nb_2TiO_{12}$ ceramics", ***Mater. Sci. Eng. B.*** (in press).

18. **P. V. Bijumon**, Sreedevi. K. Menon, B. Lethakumari, M. T. Sebastian and P. Mohanan, "T-strip fed high permittivity rectangular dielectric resonator antenna for broad band applications" ***Microwave Opt. Technol. Lett.*** (in press).

19. K. P. Surendran, **P. V. Bijumon**, P. Mohanan and M. T. Sebastian " $(1 - x)MgAl_2O_4$-$xTiO_4$ Dielectrics for Microwave and Millimeter wave applications" ***Appl. Phys. A*** (in press).

20. Sreedevi K Menon, B Lethakumary, **P V Bijumon**, M.T. Sebastian and P Mohanan, "L-Strip Fed Wide Band Rectangular Dielectric Resonator Antenna" ***Microwave Opt. Technol. Lett.*** (in press).

Papers Communicated

21. **P. V. Bijumon**, P. Mohanan and M. T. Sebastian "Experimental investigations and 3D TLM simulation of microwave dielectric resonators: Part I - $Ca_{5-x}A_xNb_2TiO_{12}$ (A = Mg, Zn, Ni & Co) Ceramics", ***J. Appl. Phys.*** (April 2005,

22. **P. V. Bijumon**, P. Mohanan and M. T. Sebastian "Experimental investigations and 3D TLM simulation of microwave dielectric resonators: Part II - $Ca_{5-x}A_xTa_2TiO_{12}$ (A = Mg, Zn, Ni & Co) Ceramics", ***J. Appl. Phys.*** (April 2005).

23. **P. V. Bijumon**, Sreedevi. K. Menon, B. Lethakumari, M. T. Sebastian and P. Mohanan, "Broad band elliptical dielectric resonator antennas excited with geometry modified microstrip lines" ***Microwave Opt. Technol. Lett.*** (April 2005).

24. **P. V. Bijumon** and M. T. Sebastian, "Effect of dopants on the microwave dielectric properties of $Ca(Ca_{1/4}A_{2/4}Ti_{1/4})O_3$ [A = Nb, Ta] ceramics", ***J. Eur. Ceram. Soc.*** (March 2005).

25. **P. V. Bijumon** and M. T. Sebastian, "Microwave dielectric properties of temperature stable $Ca_5A_2Ti_{1-x}Hf_xO_{12}$ (A = Nb, Ta) ceramics", ***J. Electroceramics*** (March 2005).

26. A. Dias, **P. V. Bijumon**, M. T. Sebastian P. Mohanan and R. L. Moreira "Microwave dielectric properties and vibrational spectroscopic analysis of $Ca_{5-x}Ba_xA_2TiO_{12}$ (A = Nb, Ta) Ceramics" ***J. Appl. Phys.*** (March 2005).

27. V. George, J. Philip, **P. V. Bijumon** and M. T. Sebastian, "Elastic properties of $Ca_{5-x}A_xNb_2TiO_{12}$ (A = Mg, Zn) microwave ceramics", ***Mater. Lett.*** (July 2005).

International Conference Proceedings

28. **P.V. Bijumon**, P. Mohanan and M. T. Sebastian "Microwave dielectric properties of $Ca_{5-x}A_xB_2Tio_{12}$ [A = Ba, Sr; B = Nb, Ta] ceramics" presented at the international conference on *Microwave Materials and Their Applications (2002)[MMA- 2002]* held at York, UK from 1-3, September 2002.

29. S. Mridula, Sreedevi. K. Menon, K. Vasudevan, P. Mohanan, **P. V. Bijumon** and M. T. Sebastian "Microstrip Fed Compact Rectangular Dielectric Resonator Antenna". Proc., *First International Conference on Microwaves, Antennas, Propagation and Remote Sensing (ICMARS 2003),* International Centre for Radio Science, Jodhpur, Dec. 15 – 19, 2003.

30. S. Mridula, Sreedevi. K. Menon, Binu Paul, C. K. Anandan, K. Vasudevan, P. Mohanan, **P. V. Bijumon** and M. T. Sebastian "Experimental investigations on a Microstrip fed Compact Rectangular Dielectric Resonator Antenna" Proc., *International Conference on Computers and Devices for Communication (CODEC – 04)*, Institute of Radio Physics and Electronics, University of Calcutta, Jan. 1 – 3, 2004.

31. Binu Paul, S. Mridula, Sreedevi. K. Menon, C. K. Anandan, P. Mohanan, **P. V. Bijumon** and M. T. Sebastian "Time Domain Analysis of a Microstrip Line Excited Compact Rectangular Dielectric Resonator Antenna" Proc., 20th Annual Review of Progress in Applied Computational Electromagnetics, Syracuse, New York, April 19 – 23, 2004.

32. **P. V. Bijumon** and M. T. Sebastian "Studies on the Microwave Dielectric Properties of Glass Fluxed $Ca_5Ta_2TiO_{12}$ Ceramics" presented at the international conference on *Microwave Materials and Their Applications (2004) [MMA- 2004]* held at Inuyama, Japan from 25 – 28 October, 2004.

33. **P. V. Bijumon** and M. T. Sebastian "Glass Fluxed $Ca_5Ta_2TiO_{12}$ Ceramics for Microwave Telecommunication Applications" Proc., 2nd International Conference on "*Microwaves, Antennas, Propagation and Remote Sensing*" held at International Centre for radio Science, Jodhpur, India from 23 – 25th November, 2004.